

Multi-Physics Modelling of a Grid Connected
Diesel Engine Driven Synchronous Generator Set
for the Analysis of Transient Low Voltage Ride
Through Performance

Oliver Tweedy

A thesis submitted to the University of Nottingham
for the degree of Doctor of Philosophy

Faculty of Engineering

March 2020

Abstract

Understanding the electromechanical behaviour of synchronous generators during severe low voltage fault conditions is vital to measure the potential performance impact and damage that may occur as a result to both connected equipment and the generator set. The work outlined in this paper addresses the process of developing a multi-physics model of a grid connected synchronous generator utilising 2D transient electromagnetic modelling with co-simulation of a 1D torsional beam element model. A 3D finite element model of a synchronous generator rotor is created and analysed using the ANSYS modal solver to obtain the orthotropic elastic properties of the laminated generator rotor core using a parametric modal analysis technique. The first 8 modes are obtained with a mean error of 1.3%, proving the accuracy of the method as the first contribution to knowledge.

The dynamically validated rotor model is used to obtain the torsional stiffness values for an equivalent 1D torsional model which is coupled to a 2D transient magnetic model of the generator (ANSYS Maxwell and Simplorer), completing the multi-physics generator set model. Three phase short circuit simulation results are compared with experimental test results to validate the model for use in low voltage ride through simulations.

The relationship between the relative angular position of the rotor and stator fields and the peak electromagnetic torque transient is obtained. In the case of an unprotected generator, a peak torque of 16.5 pu is observed with a relative angular shift of 360° . Five distinct peak torques were discovered over the 360° range that was simulated,

occurring in steps of 90° owing to the four-pole configuration of the rotor. The discovery of this relationship provides the second contribution to knowledge in this research.

Finally, three modifications are made to the generator set model subjected to the worst-case transient, an increase in rotor inertia, inclusion of controlled series braking resistors and a clutch to reduce the angular displacement of the flexible coupling between the two machines. The peak electromagnetic torque is reduced by 0.88 kNm (32.2%) and 4.17 kNm (73.8%) respectively. Ultimately, the peak stress in the generator shaft keyway is reduced by 77.4%. The relative impact of the modifications on low voltage fault ride through performance represents the third contribution to knowledge.

Acknowledgements

I would like to thank my supervisors, Seamus Garvey and Michael Galea for their support and advice throughout the project.

I wish to thank Cummins Generator Technologies for providing funding for the project and I extend special thanks to Philip Bend of CGT for his technical support and assistance.

I also express my thanks to my fellow PhD students and the University of Nottingham technicians working with the Cummins Innovation Centre for their help in setting up the lab tests and providing suggestions and feedback on experimental results.

Contents

Abstract.....	i
Acknowledgements.....	iii
Contents	iv
Nomenclature.....	x
List of tables.....	xii
List of figures.....	xiii
Chapter 1 Introduction.....	1
1.1 Problem definition.....	2
1.2 Objectives.....	3
1.3 Literature review	4
1.3.1 Finite element modelling of rotors	4
1.3.2 Existing examples of experimentally validated finite element rotor- dynamic analyses	4
1.3.3 Laminated rotors.....	8
1.3.4 Existing electro-mechanical models used for low voltage ride through simulations of generator sets	9
1.3.5 Potential solutions for improving fault ride through performance	10
1.3.6 Stress analysis of rotors	12
1.3.7 Literature review summary.....	14
Chapter 2 Background and theory.....	16
2.1 Synchronous generator sets and low voltage ride through.....	16
2.1.1 Generator set control	17
2.1.2 Generator electrical faults.....	19
2.1.3 Grid stability	20
2.1.4 Power plants and distributed generation.....	21
2.1.5 Low voltage ride through	23
2.1.6 Fault ride through requirements and grid codes	24
2.1.7 Fault clearing	27
2.1.8 FRT generator parameters	30
2.1.8.1 Short circuit ratio	30

2.1.8.2 SCR and transient reactance	30
2.1.8.3 Sub-transient reactance	31
2.1.8.4 Exciter ceiling voltage	32
2.1.9 FRT Design considerations for synchronous generators	33
2.1.9.1 Design for compliance	34
2.1.9.2 Design for robustness.....	35
2.1.9.3 Electrical damage.....	35
2.1.9.4 Mechanical and thermal damage, stator windings and bracing	36
2.1.9.5 Damper bars	37
2.1.9.6 Rotor shaft.....	38
2.1.9.7 Genset control	39
2.1.10 Design practices for LVRT.....	40
2.1.10.1 Reactance and load angle.....	41
2.1.10.2 Reducing synchronous reactance	42
2.2 Rotor dynamics	44
2.2.1 Vibration in electrical machines	45
2.2.2 Transverse vibrations of rotors	47
2.2.3 Cylindrical and conical mode shapes	50
2.2.4 Torsional vibration of rotors.....	50
2.2.5 Free vibration.....	52
2.2.6 Multi-inertia model and forced vibration	54
2.2.7 Modal analysis and testing of rotors.....	56
2.2.8 Model updating.....	56
2.3 Dynamic modelling of rotors	61
2.3.1 Finite element approach	61
2.3.2 Finite elements.....	64
2.3.3 Stiffness matrix.....	65
2.3.4 1D Finite element calculation for torsional modal analysis (un- damped)	65
2.4 Rotor structural characteristics and modelling challenges	68
2.4.1 Main rotor core	70
2.4.2 Exciter.....	72
2.4.3 Shaft and shaft features	73
2.4.4 Fan	73
2.4.5 Material properties of laminated cores	74
2.4.6 Electromagnetic finite element modelling.....	76

Chapter 3	Generator modelling and dynamic validation.....	78
3.1	Construction of 3DFE rotor model.....	78
3.2	Modal analysis setup	81
3.2.1	Rotor mesh.....	82
3.2.2	Boundary conditions.....	83
3.2.3	Contact settings	84
3.2.4	Known elastic material properties	85
3.2.5	Windings.....	85
3.2.6	Updating material properties	86
3.2.7	ANSYS parametric modal analysis	88
3.3	Experimental testing and modal analysis results.....	89
3.3.1	Rig setup and instrumentation	89
3.3.2	Modal test and modal analysis results	91
3.3.3	Influence of elastic variables on modes.....	92
3.3.4	Observations for UC22F modes	94
3.3.5	Selection of elastic properties for parametric analysis	95
3.3.6	Mode shapes	97
3.3.7	Discussion of results.....	101
3.3.8	Chapter 3 summary.....	101
3.3.9	Chapter 3 contributions to the literature	104
Chapter 4	Electromagnetic modelling and transient short circuit testing	105
4.1	Model construction and features	105
4.1.1	Geometry setup.....	105
4.1.2	Stator field	107
4.1.3	Electrical materials	108
4.1.4	Simulation setup and adjustable variables.....	109
4.1.5	Circuit setup for steady state simulations.....	112
4.2	Experimental setup.....	113
4.2.1	Operation and test procedure.....	115
4.2.2	Results from the electromagnetic model: steady state simulation and validation	116
4.2.3	Chapter 4 summary.....	123
Chapter 5	Multi-physics modelling.....	125
5.1	Model construction and simulation setup.....	125
5.1.1	Co-simulation	125

5.1.2 1D torsional mechanical model	128
5.1.3 Three-phase short circuit co-simulation setup.....	131
5.2 Short circuit experimental test and simulation results	132
5.2.1 Half voltage (110 V RMS), full load three-phase short circuit	133
5.2.2 Half voltage (110V RMS), no load three-phase short circuit.....	135
5.2.3 Full voltage (220 V RMS), full load three-phase short circuit.....	138
5.2.4 Full voltage (220 V RMS), no load three-phase short circuit	141
5.3 Simpler transient short circuit testing: Influence of variables on results.....	144
5.3.1 Voltage and field current	144
5.3.2 Simulation time step	146
5.3.3 Line resistance and load	147
5.3.4 Fault resistance	147
5.3.5 Rotor inertia.....	148
5.3.6 Component torsional stiffness	149
5.3.7 Motor speed control.....	150
5.3.8 Fault start time	150
5.3.9 Chapter summary.....	150

Chapter 6 Low voltage fault testing with the multi-physics generator set model.... 153

6.1 LVRT tests with the grid connected model.....	153
6.1.1 100% voltage drop: 40 ms fault ride through.....	155
6.1.2 100% voltage drop fault: 180 ms ride through.....	159
6.1.3 100% voltage drop fault: 320 ms ride through.....	162
6.1.4 Observations and typical fault ride through characteristics.....	165
6.2 Effect of Reduced Circuit Resistance on LVRT response	175
6.2.1 Minimum grid code: 140 ms FRT	176
6.3 Case study model	182
6.3.1 Symmetric fault simulation: Motor/generator set.....	186
6.3.2 Symmetric fault simulation: Motor/diesel engine set.....	189
6.3.3 Flexible coupling	192
6.3.4 Diesel engine generator set with flexible coupling	195
6.3.5 Diesel engine speed correction delay	197
6.4 Rotor angle and reconnection electromagnetic torque of the engine generator set model	201
6.4.1 Rotor angle shift	201
6.4.2 Relationship between the relative angular position of the rotor and peak electromagnetic torque at the point of grid reconnection	204
6.4.3 Post grid reconnection torque	209

6.4.4 Comparison of rotor angular position.....	211
6.4.5 Worst-case scenario.....	212
6.4.6 Chapter 6 summary.....	215
6.4.7 Chapter 6 contributions to the literature.....	217
Chapter 7 Transient torsional analysis	219
7.1 ANSYS 3DFE genset model.....	219
7.1.1 Modal superposition method	221
7.1.2 Full transient analysis method	225
7.1.3 Engine generator set transient analysis.....	228
7.1.4 Flexible coupling model.....	230
7.1.5 Impact of coupling stiffness on modal results	234
7.2 Dynamic Stress analysis.....	240
7.2.1 Full transient analysis of the engine generator set with a flexible coupling	241
7.2.2 Initial disconnection transient torque	242
7.2.3 Equivalent stress and maximum shear stress over 40 ms with 0.5 ms time step.....	246
7.2.4 Stress analysis for grid reconnection at 140 ms	250
7.2.5 Keyway and key contact stress.....	256
7.2.6 Chapter 7 summary.....	257
Chapter 8 Design optimisation for low voltage ride through performance improvement	260
8.1 Generator set modifications	260
8.1.1 Braking resistors.....	262
8.1.2 Increased braking resistance: 1 Ω per phase.....	266
8.1.3 Series braking resistors: 0.5 Ω per phase.....	270
8.1.4 Increased inertia.....	273
8.1.4.1 Increased coupling inertia of 0.67 kgm ²	273
8.1.4.2 Adding inertia to the generator and engine and auxiliary inertia components	275
8.1.5 Increased rotor to generator stiffness: Coupling clutch.....	281
8.1.5.1 Clutch engaged at the point of grid reconnection only	285
8.2 Combined fault ride through modifications	287
8.2.1 Dynamic stress analysis for the improved LVRT performance generator set versus the standard generator set	292
8.2.2 Additional design alterations	297

8.2.3 Chapter 8 summary.....	298
8.2.4 Chapter 8 contributions to the literature.....	300
Chapter 9 Conclusions.....	302
9.1 Overview of Work.....	303
9.2 Contributions to knowledge.....	304
9.2.1 Contribution 1: Relationship between the relative angular position and fault torque for a synchronous generator during a LVRT fault.	305
9.2.2 Contribution 2: Modifications to improve LVRT performance.	306
9.2.3 Contribution 3: Parametric modal analysis method for laminated rotors.....	309
9.3 Future work.....	310
9.3.1 Direct future work.....	310
9.3.2 Potential future work.....	311
9.3.3 Concluding remarks.....	312
References.....	315
Appendix A: Raw frequency analyser results for UC22F/G rotors.....	322
Appendix B: Torsional mode calculation for equivalent shaft model of the motor driven generator set.....	325
Appendix C: Torsional mode calculation for equivalent shaft model of diesel engine driven generator set.....	327
Appendix D: Shear modulus values used in the 3DFE model.....	330
Appendix E: Simplorer model of the improved diesel engine generator set.....	332

Nomenclature

A	Magnetic vector potential
B	Magnetic flux density
C	Damping factor
D	Diameter
e	Electromotive force
E	Young's modulus
f	Frequency
f_n	Natural frequency
F	Force
G	Shear modulus
h	Inertia constant
H	Magnetic field intensity
H_c	Coercivity of a permanent magnet
I	Mass moment of inertia
J	Second moment of area about axis of rotation
J_s	Current source density
[J]	Inertia matrix
k	Spring constant
k_e	Element stiffness matrix
k_T	Torsional stiffness
[K]	Stiffness matrix
l	Length
l_L	Laminated stack length

L	Inductance
n_L	Number of laminations
[M]	Mass matrix
p	Number of poles
s_f	Stacking factor
t	Time
t_L	Lamination thickness
T	Torque
V	Voltage
X_d	Direct axis reactance
X_L	Leakage reactance
X_q	Quadrature axis reactance
X_s	Synchronous reactance

Greek symbols

θ	Angular displacement
$\dot{\theta}, \omega$	Angular velocity
$\ddot{\theta}$	Angular acceleration
μ	Electromagnetic permeability
σ	Conductivity (S/m)
ν	Reluctivity (H^{-1})

List of tables

Table 3.1: Mass properties and dimensions of the UC22F and UC22G generator rotors	79
Table 3.2: Solid G core rotor modal analysis frequencies vs. modal test frequencies	92
Table 3.3: Final elastic property combinations for the UC22G rotor	95
Table 3.4: Final elastic property combinations for the UC22F rotor.....	96
Table 4.1: Target simulation results for steady state operating conditions of the generator for full and half voltage operation (power factor 1).	117
Table 5.1: Mechanical properties of the motor/generator test genset.....	128
Table 5.2: Mechanical properties of the diesel engine/generator genset.....	129
Table 6.1: Simulation results for LVRT testing of the validated UC22F motor/generator Simplorer model.....	175
Table 6.2: Electromagnetic torque for reconnection at various values of rotor angle shift.....	206
Table 7.1: Torsional modes for the 3DFE equivalent motor driven generator set - modal frequencies and shapes for various coupling stiffness.....	234
Table 7.2: Torsional modes for the 3DFE equivalent engine driven generator set - modal frequencies and shapes for various coupling stiffness.....	236
Table 7.3: Peak equivalent stress and shear stress in the coupling key/keyway following reconnection after 140 ms FRT	255
Table 8.1: Peak equivalent stress and shear stress in the coupling key/keyway following reconnection at 15° rotor angle shift for the standard genset and the improved genset	293
Table D.1: Shear modulus values for full 3DFE equivalent stiffness engine model.....	330

List of figures

Figure 1.1: Synchronous generator behaviour under normal conditions and when subjected to a fast transient torque due to a low voltage fault.	2
Figure 2.1: Separately excited synchronous generator coupled to a diesel engine.....	18
Figure 2.2: Voltage curve during a grid fault (30).....	25
Figure 2.3: LVRT Requirements of international grid codes (33).....	26
Figure 2.4: Voltage curves for LVRT Requirements of international grid codes (15).....	27
Figure 2.5: Synchronous generator response to a 110 ms low voltage fault (14).....	29
Figure 2.6: Current following a fault event, showing the sub-transient, transient and steady state regions (36).....	32
Figure 2.7: Damper bar placement in a salient pole rotor (44)	37
Figure 2.8: Damage to rotor shaft key following an out of phase synchronisation event (22)	39
Figure 2.9: Synchronous generator phasor diagram (47).....	42
Figure 2.10: Effects of stress stiffening and spin softening (53)	49
Figure 2.11: Multi-mass torsional model (55)	55
Figure 2.12: Combin14 spring-damper (60)	63
Figure 2.13: COMBI214 2-D spring-damper bearing (61).....	63
Figure 2.14: Types of finite elements (59).....	64
Figure 2.15: Rotor with four masses attached to a shaft.....	66
Figure 2.16: Generator rotor components.	69
Figure 3.1: UC22F Rotor geometry, view from the non-drive end	80
Figure 3.2: Initial meshing on the rotor core and fan of the UC22F rotor.....	82
Figure 3.3: Suspended F Core Rotor. Accelerometer positioned for torsional mode acquisition from the core.....	90
Figure 3.4: Modal test impact locations.....	90
Figure 3.5: Dismantled UC22G rotor (bearings, fan and exciter removed)	90

Figure 3.6: G core parametric variation of E_{zz} with constant $G_{xz}/G_{yz} = 1.6e^{10}$ Pa.....	93
Figure 3.7: G core parametric variation of G_{xz}/G_{yz} with constant $E_{zz} = 1.4e^{10}$ Pa.....	94
Figure 3.8: Lateral mode shapes of the G core rotor	97
Figure 3.9: Lateral mode shapes of the F core rotor	98
Figure 3.10: Torsional mode shapes of the F core rotor	99
Figure 3.11: Exaggerated deflections of torsional and lateral rotor modes: (a) first torsional mode, (b) first torsional mode with the fan hidden, (c) axial view of the rotor core in the first torsional mode, (d) first lateral mode, (e) fifth lateral mode, (f) axial view of the fan in the fifth lateral mode.....	99
Figure 4.1: Maxwell model of 2D slice through UC22F rotor	106
Figure 4.2: UC22F Stator Windings	107
Figure 4.3: All stator phases, U = red, V = blue, W = green.	108
Figure 4.4: B-H curve for stator and rotor core electrical steel	109
Figure 4.5: Simple resistive load connected circuit diagram for UC22F model	112
Figure 4.6: UC22F generator and electric motor test rig prepared for steady state and three phase short circuit experimental tests	114
Figure 4.7: Experimental results for half voltage (left) and full voltage (right) operation. Rotor speed and rotor torque at full load	118
Figure 4.8: Experimental results for full voltage operation. Terminal current and voltage for U phase (power factor 1, full load).....	118
Figure 4.9: Steady state, full voltage simulation results. Terminal current (PF = 1, full load).....	119
Figure 4.10: Steady state, full voltage simulation results. Terminal voltage (PF = 1, full load).....	119
Figure 4.11: Steady state, full voltage simulation results. Electromagnetic torque (PF = 1, full load).....	120
Figure 4.12: Steady state, half voltage experimental results. Terminal current and voltage for U phase (PF = 1, full load).....	121
Figure 4.13: Steady state, half voltage simulation results. Terminal current (PF = 1, full load).....	122
Figure 4.14: Steady state, half voltage simulation results. Terminal voltage (PF = 1, full load).....	122

Figure 4.15: Steady state, half voltage simulation results. Electromagnetic torque (PF = 1, full load).....	123
Figure 5.1: Block diagram for general co-simulation setup of the synchronous generator set.	126
Figure 5.2: Torsional model of the diesel engine/generator set.....	130
Figure 5.3: Steady state combined engine torque	131
Figure 5.4: Experimental full load 110V 3-phase short circuit terminal current.....	133
Figure 5.5: Simulation full load 110V 3-phase short circuit terminal current.....	134
Figure 5.6: Simulation full load 110V 3-phase short circuit transducer torque versus experimental transducer torque.....	134
Figure 5.7: Simulation full load 110V 3-phase short circuit transducer speed versus experimental transducer speed.....	134
Figure 5.8: Experimental no load 110V 3-phase short circuit terminal current	136
Figure 5.9: Simulation no load 110V 3-phase short circuit terminal current	136
Figure 5.10: Simulation no load 110 V 3-phase short circuit transducer torque versus experimental transducer torque.....	137
Figure 5.11: Simulation no load 110 V 3-phase short circuit transducer speed versus experimental transducer speed.....	137
Figure 5.12: Experimental full load 220 V 3-phase short circuit stator current	139
Figure 5.13: Simulation of full load 220 V 3-phase short circuit stator current.....	139
Figure 5.14: Simulation of full load 220 V 3-phase short circuit transducer torque versus experimental transducer torque (scaled).....	140
Figure 5.15: Simulation full load 220 V 3-phase short circuit transducer speed versus experimental transducer speed (scaled)	140
Figure 5.16: Experimental no load 220V 3-phase short circuit stator current.....	142
Figure 5.17: Simulation no load 220V 3-phase short circuit stator current.....	142
Figure 5.18: Simulation no load 220V 3-phase short circuit transducer torque versus experimental transducer torque.....	142
Figure 5.19: Simulation no load 220V 3-phase short circuit transducer speed versus experimental transducer speed.....	143
Figure 6.1: Grid connected generator set Simplorer model.....	153

Figure 6.2: 100% voltage drop fault applied to motor driven generator set, PF = 1. Air gap electromagnetic torque for 40 ms FRT.	156
Figure 6.3: 100% voltage drop fault applied to motor driven generator set, PF = 1. Transducer speed for 40 ms FRT.	156
Figure 6.4: 100% voltage drop fault applied to motor driven generator set, PF = 1. Fault current for 40 ms FRT.	157
Figure 6.5: 100% voltage drop fault applied to motor driven generator set, PF = 1. Line current for 40 ms FRT.	157
Figure 6.6: 100% voltage drop fault applied to motor driven generator set, PF = 1. Transducer torque for 40 ms FRT.	158
Figure 6.7: 100% voltage drop fault applied to motor driven generator set, PF = 1. Motor torque control response for 40 ms FRT.	158
Figure 6.8: 100% voltage drop fault applied to motor driven generator set, PF = 1. Electromagnetic air gap torque for 180 ms FRT.	160
Figure 6.9: 100% voltage drop fault applied to motor driven generator set, PF = 1. Transducer speed for 180 ms FRT.	160
Figure 6.10: 100% voltage drop fault applied to motor driven generator set, PF = 1. Transducer torque for 180 ms FRT.	160
Figure 6.11: 100% voltage drop fault applied to motor driven generator set, PF = 1. Fault current for 180 ms FRT.	161
Figure 6.12: 100% voltage drop fault applied to motor driven generator set, PF = 1. Line current for 180 ms FRT.	161
Figure 6.13: 100% voltage drop fault applied to motor driven generator set, PF = 1. Air gap electromagnetic torque for 320 ms FRT.	162
Figure 6.14: 100% voltage drop fault applied to motor driven generator set, PF = 1. Transducer speed for 320 ms FRT.	163
Figure 6.15: 100% voltage drop fault applied to motor driven generator set, PF = 1. Transducer torque for 320 ms FRT.	163
Figure 6.16: 100% voltage drop fault applied to motor driven generator set, PF = 1. Motor torque control response for 320 ms FRT.	164
Figure 6.17: 100% voltage drop fault applied to motor driven generator set, PF = 1. Fault current for 320 ms FRT.	164
Figure 6.18: 100% voltage drop fault applied to motor driven generator set, PF = 1. Line current for 320 ms FRT.	165

Figure 6.19: Field current input for Maxwell LVRT Simulation (100% voltage drop).....	166
Figure 6.20: Transducer torque immediately following fault initiation.	167
Figure 6.21: Rotor angular position for 40 ms LVRT vs. steady state angular position.....	169
Figure 6.22: Magnified rotor angular position for 40 ms LVRT vs. steady state angular position.....	169
Figure 6.23: Rotor angular position for 180ms LVRT vs. steady state angular position.....	170
Figure 6.24: 100% voltage drop fault applied to motor driven generator set, PF = 1. Air gap electromagnetic torque for 163.6 ms FRT.....	171
Figure 6.25: 100% voltage drop fault applied to motor driven generator set, PF = 1. Transducer speed for 163.6 ms FRT.....	172
Figure 6.26: 100% voltage drop fault applied to motor driven generator set, PF = 1. Transducer torque for 163.6 ms FRT.	172
Figure 6.27: 100% voltage drop fault applied to motor driven generator set, PF = 1. Fault current for 163.6 ms FRT.	173
Figure 6.28: 100% voltage drop fault applied to motor driven generator set, PF = 1. Line current for 163.6 ms FRT.	173
Figure 6.29: Rotor angular position for 320 ms LVRT vs. steady state angular position.....	174
Figure 6.30: 100% voltage drop fault applied to motor driven generator set, PF = 1. Air gap electromagnetic torque for 140 ms FRT with reduced resistance.....	176
Figure 6.31: 100% voltage drop fault applied to motor driven generator set, PF = 1. Transducer speed for 140 ms FRT with reduced resistance	177
Figure 6.32: 100% voltage drop fault applied to motor driven generator set, PF = 1. Transducer torque for 140 ms FRT with reduced resistance.....	177
Figure 6.33: 100% voltage drop fault applied to motor driven generator set, PF = 1. Line / fault Current for 140 ms FRT with reduced resistance.	178
Figure 6.34: 100% voltage drop fault applied to motor driven generator set, PF = 1. Rotor angle for 140 ms FRT with reduced resistance.	178
Figure 6.35: UK grid code voltage limits for 'Type D' synchronous machines (67).....	179
Figure 6.36: Minimum and maximum fault voltage against time curves (68).....	179

Figure 6.37: Transducer torque comparison for low resistance circuit versus high resistance circuit	181
Figure 6.38: 100% voltage drop fault applied to the case study model, PF = 0.8. Electromagnetic torque for 140 ms FRT.	183
Figure 6.39: 100% voltage drop fault applied to the case study model, PF = 0.8. Speed for 140 ms FRT.	183
Figure 6.40: 100% voltage drop fault applied to the case study model, PF = 0.8. Torque for 140 ms FRT.	184
Figure 6.41: 100% voltage drop fault applied to the case study model, PF = 0.8. Current for 140 ms FRT.	184
Figure 6.42: Electromagnetic torque following disconnection for 140 ms ride through at power factor 1 and power factor 0.8.....	185
Figure 6.43: 100% voltage drop fault applied to the case study model, PF = 0.8. Electromagnetic torque for 140 ms FRT. Reduced field.	187
Figure 6.44: 100% voltage drop fault applied to the case study model, PF = 0.8. Speed for 140 ms FRT. Reduced field.	187
Figure 6.45: 100% voltage drop fault applied to the case study model, PF = 0.8. Torque for 140 ms FRT. Reduced field.	188
Figure 6.46: 100% voltage drop fault applied to the case study model, PF = 0.8. Current for 140 ms FRT. Reduced field.	188
Figure 6.47: 100% voltage drop fault applied engine driven generator set, PF = 0.8. Air gap electromagnetic torque for 140 ms FRT. Reduced field.....	190
Figure 6.48: 100% voltage drop fault applied engine driven generator set, PF = 0.8. Transducer torque for 140 ms FRT. Reduced field.	190
Figure 6.49: 100% voltage drop fault applied engine driven generator set, PF = 0.8. Transducer speed for 140 ms FRT. Reduced field.	190
Figure 6.50: Non-linear static torsional stiffness versus applied torque for the flexible coupling.	194
Figure 6.51: Simplorer model for flexible coupling testing on the motor/generator torsional model.....	194
Figure 6.52: Electromagnetic torque in the case study diesel engine generator set versus coupling torque in the same model with the flexible coupling.....	196
Figure 6.53: Coupling angular speed in the case study diesel engine generator set versus coupling torque in the same model with the flexible coupling.....	196

Figure 6.54: Coupling torque in the case study diesel engine generator set versus coupling torque in the same model with the flexible coupling.....	197
Figure 6.55: Case study simulation of diesel engine genset with reduced speed control gain vs existing speed control response. Motor torque.	198
Figure 6.56: Case study simulation of diesel engine genset with reduced speed control gain vs existing speed control response. Angular speed.	199
Figure 6.57: Case study simulation of diesel engine genset with reduced speed control gain vs existing speed control response. Electromagnetic torque.	199
Figure 6.58: Case study simulation of diesel engine genset with reduced speed control gain vs existing speed control response. Coupling torque.....	200
Figure 6.59: Rotor angle vs. steady state angle for final diesel engine generator set	201
Figure 6.60: Magnitude of rotor angle shift over time (180° maximum shift)	202
Figure 6.61: Electromagnetic air gap torque for the engine generator set reconnecting at rotor angle shift of 90°	203
Figure 6.62: Coupling angular speed for the engine generator set reconnecting at rotor angle shift of 90°	204
Figure 6.63: Electromagnetic torque for reconnection at various values of rotor angular shift. Peaks appear in order of increasing rotor angle shift.....	205
Figure 6.64: Electromagnetic torque for reconnection at various values of rotor angle shift over post reconnection time period	210
Figure 6.65: Physical shift in rotor angular position at 0°, 15° and 180° shift	212
Figure 6.66: Electromagnetic torque for rotor angle shift of 180° and 360° extended	213
Figure 6.67: Coupling angular speed for rotor angle shift of 180° and 360° extended	214
Figure 7.1: Motor/generator set equivalent shaft ANSYS model.....	221
Figure 7.2: Modal analysis results for the 3D equivalent shaft model of the motor/generator set (rotational displacement for 106.87 Hz mode shown).....	222
Figure 7.3: Raw directional velocity results for the 3D equivalent shaft model of the motor/generator set. (Results obtained at the end with minimum displacement, in blue, where the coupling inertia is positioned).....	222

Figure 7.4: Equivalent ANSYS model angular speed vs. Simplorer model angular speed	223
Figure 7.5: View of moment reaction probe results at the motor/generator set coupling.....	223
Figure 7.6: Coupling torque for the 1D Simplorer model versus torque for the 3DFE equivalent shaft model. Motor genset	224
Figure 7.7: Un-damped transducer angular speed results from Simplorer model versus 3DFE equivalent shaft model of the motor genset (311 ms fault start time, zeroed)	225
Figure 7.8: Un-damped transducer torque results from Simplorer model versus 3DFE equivalent shaft model of the motor genset.....	226
Figure 7.9: 3DFE model angular speed for damped coupling vs. un-damped coupling. Motor genset	227
Figure 7.10: ANSYS torque for damped coupling vs. un-damped coupling. Motor genset	227
Figure 7.11: Modal results for equivalent shaft model of engine generator set. Original coupling stiffness of 2.11MNm/rad. (107.83Hz mode with large displacement of engine inertia ring shown)	229
Figure 7.12: Coupling torque results from Simplorer model versus 3DFE equivalent shaft model of the motor genset	229
Figure 7.13: Coupling angular speed results from Simplorer model versus 3DFE equivalent shaft model of the motor genset	230
Figure 7.14: Shear modulus vs. time curve for coupling material for transient analysis of 3DFE engine genset.....	231
Figure 7.15: Equivalent geometry of inertia ring in engine damper hub and applied joint boundary conditions. (A) Inertia ring to damper hub joint, (B) inertia ring to ground joint	232
Figure 7.16: Full transient analysis results of coupling torque for the engine generator set with flexible coupling.....	232
Figure 7.17: Full transient analysis results of coupling angular speed for the engine generator set with flexible coupling.....	233
Figure 7.18: Mass normalised torsional mode shapes for 50 kNm/rad coupling stiffness (T1 left, T2 right).....	235
Figure 7.19: Mass normalised torsional mode shapes for 1000 kNm/rad coupling stiffness (T1 left, T2 right).....	235

Figure 7.20: motor genset mass normalised torsional mode shapes for 50 kNm/rad coupling stiffness (T1 left, T2 right).....	237
Figure 7.21: Motor genset mass normalised torsional mode shapes for 50 kNm/rad coupling stiffness (T3 left, T4 right).....	238
Figure 7.22: Engine genset mass normalised torsional mode shapes for 1000 kNm/rad coupling stiffness (T1 left, T2 right).....	238
Figure 7.23: Engine genset mass normalised torsional mode shapes for 1000 kNm/rad coupling stiffness (T3 left, T4 right).....	238
Figure 7.24: View of generator shaft connected to the engine coupling with extended key.	241
Figure 7.25: Coupling torque (moment reaction), angular speed and average von Mises stress in the keyway during grid disconnection over 10ms period. Comparison of results with 0.05ms, 0.5ms and 1ms time steps.....	243
Figure 7.26: Equivalent von Mises and shear stress in the key/keyway at 10 ms following during grid disconnection.	245
Figure 7.27: Equivalent stress at peak coupling torque (14 ms).....	246
Figure 7.28: Peak disconnection coupling torque over 40 ms time period.....	247
Figure 7.29: Magnitude of electromagnetic torque at 14 ms	247
Figure 7.30: Equivalent stress at 28.5 ms.....	248
Figure 7.31: Plot of maximum equivalent stress over 40 ms time period	248
Figure 7.32: Maximum shear stress in the key at 28.5 ms.....	249
Figure 7.33: Maximum shear stress in the shaft keyway at 28.5 ms	249
Figure 7.34: Electromagnetic torque applied to the generator core over 80 ms. Obtained from 140 ms LVRT Simplorer simulation of the engine genset	250
Figure 7.35: Coupling torque over 80 ms obtained from 140 ms LVRT Simplorer simulation of the engine genset.....	251
Figure 7.36: Coupling torque in the 3DFE transient model over 80 ms following grid reconnection	251
Figure 7.37: Equivalent stress in the key and keyway over 80 ms following grid reconnection	252
Figure 7.38: Maximum shear stress at the key and keyway over 80ms following grid reconnection.	253

Figure 7.39: Coupling moment reaction over 80 ms, torque applied at the shaft instead of the core. (Time step increased to 1 ms).....	254
Figure 7.40: Stress locations on the key and keyway	255
Figure 8.1: Simplorer generator circuit with braking resistor branches	263
Figure 8.2: Stator current with braking resistors 0.5 Ω per phase	263
Figure 8.3: Electromagnetic torque with braking resistors 0.5 Ω per phase.....	264
Figure 8.4: Coupling torque with braking resistors 0.5 Ω per phase	264
Figure 8.5: Coupling angular speed with braking resistors 0.5 Ω per phase	265
Figure 8.6: Stator current with braking resistors, 1 Ω per phase	267
Figure 8.7: Electromagnetic torque with braking resistors, 1 Ω per phase.....	267
Figure 8.8: Coupling torque with braking resistors, 1 Ω per phase	268
Figure 8.9: Coupling angular speed with braking resistors, 1 Ω per phase	268
Figure 8.10: Braking resistors connected with series with grid supply	271
Figure 8.11: Electromagnetic torque for increased inertia (0.67 kgm^2) vs. original inertia (0.067 kgm^2).....	274
Figure 8.12: Coupling torque with increased inertia (0.67 kgm^2) vs. original inertia (0.067 kgm^2)	274
Figure 8.13: Coupling angular speed with increased inertia (0.67 kgm^2) vs. original inertia (0.067 kgm^2).....	275
Figure 8.14: Coupling torque for the increased inertia generator set and balanced inertia ratio to 1 vs. standard genset model	277
Figure 8.15: Coupling angular speed for the increased inertia generator set and balanced inertia ratio to 1 vs. standard genset model.	278
Figure 8.16: Auxiliary 0.5 kgm^2 inertias, end of generator shaft (left) and connected in parallel with the damper hub of the engine (right)	279
Figure 8.17: Coupling torque for the increased inertia generator set (Series2) and balanced inertia ratio to 1 vs. standard genset model. 0.5 kgm^2 inertias removed 50 ms after grid reconnection.....	279
Figure 8.18: Coupling angular speed for the increased inertia generator set and balanced inertia ratio to 1 vs. standard genset model. 0.5 kgm^2 inertias removed 50 ms after grid reconnection.....	280
Figure 8.19: Simplorer torsional model with 'clutch' torsional stiffness element (S7kt1).....	281

Figure 8.20: Electromagnetic torque for coupling with clutch vs. electromagnetic torque for standard flexible coupling	283
Figure 8.21: Engine flywheel torque for coupling with clutch vs. engine flywheel torque standard flexible coupling.....	283
Figure 8.22: Engine flywheel speed for coupling with clutch vs. engine flywheel speed standard flexible coupling.....	284
Figure 8.23: Electromagnetic torque for coupling with clutch vs. electromagnetic torque for standard flexible coupling. Activated at the point of reconnect.....	285
Figure 8.24: Engine flywheel torque for coupling with clutch vs. engine flywheel torque standard flexible coupling. Activated at the point of reconnect	286
Figure 8.25: Engine flywheel speed for coupling with clutch vs. engine flywheel speed standard flexible coupling. Activated at the point of grid reconnection	286
Figure 8.26: Standard genset stator current (A) reconnection at rotor angle shift of 15° (178.8 ms FRT)	289
Figure 8.27: Combined FRT improvements genset stator current (A) reconnection at rotor angle shift of 15° (276.35 ms FRT)	289
Figure 8.28: Combined fault ride through improvements versus standard genset electromagnetic torque (kNm) at 15° rotor angle shift	290
Figure 8.29: Combined fault ride through improvements versus standard genset coupling torque (kNm) at 15° rotor angle shift.....	290
Figure 8.30: Combined fault ride through improvements versus standard genset coupling speed (rad/s) at 15° rotor angle shift	291
Figure 8.31: Combined fault ride through improvements versus standard genset flywheel torque (kNm) at 15° rotor angle shift.....	291
Figure 8.32: Combined fault ride through improvements versus standard genset clutch torsional stiffness (Nm/rad) at 15° rotor angle shift.....	292
Figure 8.33: Maximum equivalent stress in standard genset key at 15° rotor angle shift.....	293
Figure 8.34: Average equivalent stress in standard genset key at 15° rotor angle shift	294
Figure 8.35: Maximum equivalent stress in standard genset keyway at 15° rotor angle shift.....	294

Figure 8.36: Average equivalent stress in standard genset keyway at 15° rotor angle shift.....	294
Figure 8.37: Maximum equivalent stress in improved genset key at 15° rotor angle shift.....	295
Figure 8.38: Average equivalent stress in improved genset key at 15° rotor angle shift	295
Figure 8.39: Maximum equivalent stress in improved genset keyway at 15° rotor angle shift.....	296
Figure 8.40: Average equivalent stress in improved genset keyway at 15° rotor angle shift.....	296
Figure A.1: FRF plot for UC22F rotor. Lateral modes measured at impact point 2.....	322
Figure A.2: FRF plot for UC22F rotor. Torsional modes measured at impact point 5 (end of core).....	322
Figure A.3: FRF plot for UC22G rotor. Lateral modes measured at impact point 2.....	323
Figure A.4: FRF plot for UC22F rotor. Torsional modes measured at impact point 5 (end of core).....	323
Figure E.1: Complete Simplorer model of the improved generator set.....	332
Figure E.2: Electromagnetic generator model connected to stator/terminal circuit in the improved generator set model	333
Figure E.3: Torsional model within the improved generator set model	334

Chapter 1 Introduction

The outline of this project was conceived through the collaborative efforts of University of Nottingham and Cummins Generator Technologies via the Cummins Innovation Centre in response to the introduction of new grid code requirements for low voltage fault ride through for grid connected generators. The goal of this research project is to develop a solution to predict the electromechanical behaviour of synchronous generators during low voltage grid faults and better understand the resulting potential physical damage to the rotor assembly.

Synchronous generator sets consist of two machines coupled together, a synchronous generator and a prime mover. Diesel engines are often used as the prime mover to drive the generator and convert mechanical energy to electrical energy for distribution to a local or national grid. When the grid voltage drops due to faults in the network, synchronous generators are subjected to high transient currents at both the point of voltage drop, and when the grid voltage is restored as shown in Figure 1.1. This produces a transient torque between the two machines in the generator set which can be several orders of magnitude greater than the normal operating torque and capable of causing damage to the rotors and coupling.

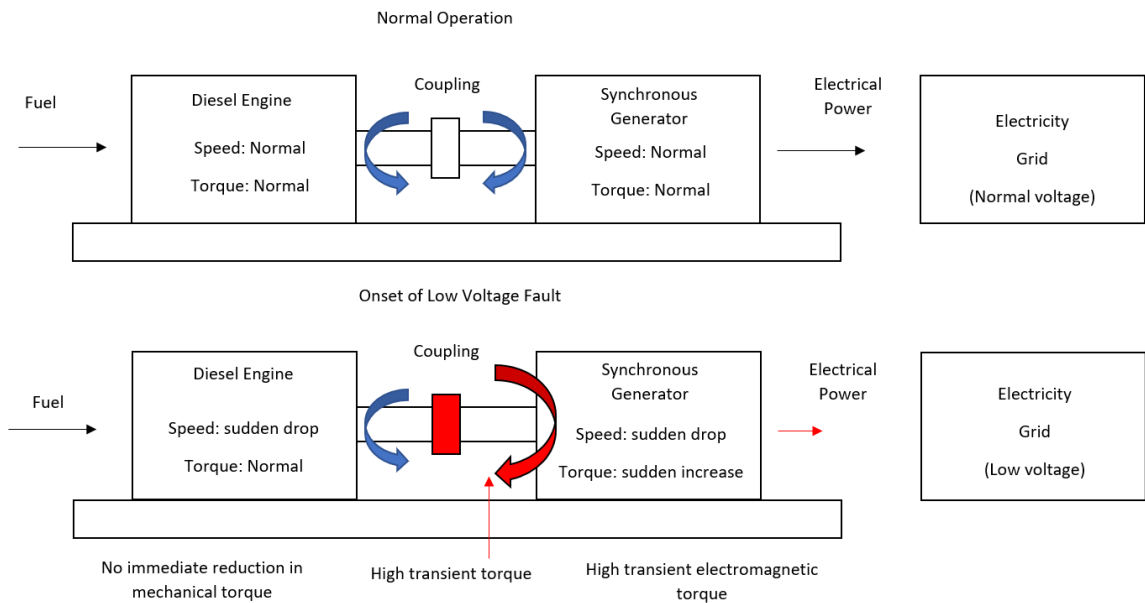


Figure 1.1: Synchronous generator behaviour under normal conditions and when subjected to a fast transient torque due to a low voltage fault.

1.1 Problem definition

There is a growing need to develop the existing design of synchronous generators to meet increasingly demanding grid codes which require generator sets to remain connected to the grid throughout low voltage faults for longer periods of time and increased levels of voltage drop. The problem in doing so is that the fast transient (10 to 20 ms) torque and thus the peak stress in the machine rotors is not well defined in existing research which typically focuses on the rotor speed / angular displacement over the entire low voltage fault period rather than the magnitude and behaviour of the fast transients at the beginning and end of the fault. As a result, the likelihood and severity of damage due to low voltage faults is largely unknown and, if addressed at all in the machine design, is remedied by overengineering the shafts and couplings. Ultimately, a generator designed to endure extended voltage drop faults may still be damaged by the fast transients. This research intends to address this problem by simulating a

synchronous generator subjected to low voltage faults and observing the fast transient behaviour and the resulting structural stresses. The need to reduce the severity of these fast transients is also addressed by the introduction of some new and existing modifications to the generator set model.

1.2 Objectives

The following objectives for this thesis are met to achieve the aim of improving understanding of the impact of LVRT faults on grid connected synchronous generators.

- Create a multi-physics model of a synchronous generator set. Focusing on its use in electromechanical analysis.
- Validate the mechanical and electrical components of the model using three-phase short circuit testing and suspended rotor modal testing.
- Investigate the stator current, electromagnetic air gap torque, coupling/shaft torque, rotor speed and shift in rotor angular position for various low voltage fault conditions using transient analysis. Determine the driving factors for each of these performance parameters.
- Analyse the dynamic stress in the rotor coupling using the electromagnetic and engine torques obtained from the multi-physics model.
- Determine the severity of the different possible faults and investigate the impact of potential design modifications on fault ride through performance improvement.

1.3 Literature review

This literature review is conducted to observe the existing research on modelling of synchronous generators sets and simulation of low voltage ride through faults. Co-simulation or multi-physics models that simulate both electromagnetic and mechanical systems in the generator are of particular interest here. A summary of the research is provided at the end of this section which explains how it is used in this thesis.

1.3.1 Finite element modelling of rotors

Modern research typically focuses on developing models of rotors and rotating components that accurately reproduce the dynamic characteristics of their real-life counterparts. The most popular methods of dynamic analysis are based on finite element (FE) calculations. The finite element method effectively solves the equations of motion for structures discretised into many small elements. The FE method is well suited for solving distributed parameter models, especially given the increase in available computing power since its inception (1).

1.3.2 Existing examples of experimentally validated finite element rotor-dynamic analyses

Any rotor model which is intended for use in detailed rotor-dynamic analysis must have dynamic properties (characterised through mode shapes and their corresponding eigenfrequencies) matching those of the real rotor it is modelled upon. In this section

of the literature review, existing research that utilises 1D and 3D finite element modelling techniques and modal testing for model validation purposes is explored.

One dimensional torsional models are historically used for dynamic analysis of rotating structures including synchronous generators, these models use a simplified representation of the rotor geometry rendered down to the equivalent torsional stiffness and inertia elements of the assembly. Such low order models can be solved quickly with modern PCs but are limited due to the simplifications required to reduce the complexity of the true rotor geometry. This becomes particularly apparent when comparing 1D and 3D torsional models for rotors that include fan blades and abrupt changes in diameter between components (1). Fan blade modes are absent from dynamic analysis of 1D torsional models and mode shapes for complex geometries can differ significantly. 3D torsional models have not completely replaced 1D models, the latter will always be required for validation of the former and when used in conjunction with each other can be used to break down larger more complex assemblies to better understand its dynamic behaviour.

3D solid finite element models are already utilised in industry to determine the rotordynamic properties of rotating machinery. During the early stages of their adoption within the industry Bellamy et. al (2) discusses one such application of solid 3D models for aero gas turbines and highlights the positive benefits of using such models over 1D beam models, particularly their capability to incorporate more detailed rotor dynamic criteria into the analysis and ultimately provide more accurate results.

Rao (3) considers the problem of modelling asymmetric rotors with 1D beam elements, requiring the determination of asymmetry parameters from model analysis of a real equivalent rotor. The researchers create a 3D solid model of a Jeffcott type rotor and conduct a modal analysis with ANSYS mechanical analysis software accounting for stress stiffening and spin softening.

In a more recent example of 3D solid element modelling, Meng et al (4) analysed a 3D solid element model of an industrial turbo engine with ANSYS including the casing and bearings along with the rotor itself by utilising transfer functions to represent the coupling effects between the rotating and stationary components. Unbalance forces are simulated in this analysis and the unbalance response results are compared with the modal results of the rotor system (in the form of a Campbell diagram).

Mudau et al. (1) constructed a 3D finite element model of a large steam turbine connected to a synchronous generator and performed a dynamic torsional analysis using ANSYS workbench to determine the modal frequencies and shapes. A simple 1D lumped mass model is used to validate the ANSYS results, and the modal frequencies are checked against the 50 Hz and 100 Hz (second order) grid frequencies. The first three torsional modes of the 3DFE model closely match those calculated using the 1D lumped mass model. The torsional modes close to the grid frequencies are analysed further and it is noted that the generator modes (where torsional displacement of the generator rotor is dominant) must not be excited at orders of the grid frequency. The mode shapes confirmed that neither of these modes contain excessive generator rotor displacement. Note that bonded contacts are used throughout this analysis to prevent sliding or separation of contacts. The paper also suggests that the dynamically validated

model will be useful for further torsional analysis of excitation due to three-phase short circuits and plans to conduct transient stress analysis to obtain the maximum shear stress near the generator coupling.

Hadi et al. (5) conducts a dynamic analysis of a high speed rotor which includes modal analyses of a 3D finite element model of a rotor assembly and a one dimensional beam element model. The natural frequencies obtained from the modal analyses are compared with a modal test to validate the models. This research, along with many other similar examples determines that the 3D solid finite element method is viable for producing simulated modal analysis results that compare well with experimental modal results.

Dynamic analysis of entire rotating machines includes the stationary components such as the frame and casing in which the rotor is contained. The connection between rotating and stationary components is established through the bearings. Cao et al. (6) present a review of a range of different models for roller bearings. The range of physical conditions that must be considered to accurately model such a complex non-linear component, such as contact stress and non-Hertzian contact simulation evidently requires a large amount of computing resources (high mesh density, iterative non-linear calculations etc.) for a viable FE model. 3D detailed dynamic analyses of bearings are therefore rarely coupled to dynamic analyses of the rotors they support and require assumed boundary conditions for interaction between the two models or simplification of one component (for example, 2D bearings supporting a 3D rotor). The study of bearing performance is determined to be out of scope for this project.

1.3.3 Laminated rotors

The laminated structure of the rotor core is a well-known problem when performing any dynamic analysis for electrical machine rotors. Any study that attempts to validate the modal results for a generator rotor with a laminated core requires some correction of the elastic properties of the rotor core. In the absence of such an analysis, the work will at least acknowledge that reason why experimentally obtained modes will be shifted by a given factor from analytically obtained results performed on a uniform, solid rotor core.

Garvey et al. (7) describes how the laminated core can be treated as single structure with orthotropic material properties. The orthotropic properties as measured from experimental tests are applied to an ‘un-branched’ beam element model. A similar study is undertaken by Santos et al. (8) with an un-branched beam-element model whereby the Young’s modulus of the rotor core is applied to a cylinder, added to the circumference of the shaft to represent the additional stiffness added to the rotor by the laminated core.

Both the lateral and torsional stiffness of a laminated rotor vary depending on several factors. Considering the laminated core and shaft assembly alone, the pressing process, core geometry, stacking factor and lamination varnish material all impact the stiffness of the rotor. The laminations are pressed together and onto the rotor shaft at a particular pressure. The pressure applied partly determines the flexibility of the rotor assembly. Existing studies confirm that an increase in inter-lamination pressure results in a significant increase in modal frequency, particularly at higher orders (9), (10). The

interference depth between the core and shaft determines the interface stiffness, which also alters the modal results. Chen et al. (11), (12) studied interference between hot fit shaft and core assemblies and demonstrates a noticeable decrease in modal frequencies at lower interference depths. In addition, the windings, damper cage and support bars that compose the fully assembled core all impact the structural stiffness of the rotor. When considering the fully assembled rotor structure, secondary rotor components, namely the shaft mounted fan and exciter significantly influence the modal properties of the rotor.

1.3.4 Existing electro-mechanical models used for low voltage ride through simulations of generator sets

Electro-mechanical models are commonly used for research and development of generators and there exists examples of simulations performed for three-phase short circuit and low voltage ride through faults that utilise coupled electromagnetic and mechanical simulations. Cummins Generator Technologies has developed such a solution using MATLAB to build a Simulink model (13) and simulate a 100% voltage drop in voltage for a large synchronous generator (14). Ostman et al. (15), (16) uses a Simulink model of a grid connected generator to simulate three phase short circuit and low voltage ride through faults based on voltage curves designated by grid codes. The same rotor acceleration and increase in rotor angle behaviour occurs in both models and is seen as the characteristic low voltage/three-phase short circuit behaviour throughout the analysis chapters in this thesis. The same ride through behaviour is shown in the simulation of three-phase low voltage faults by Abed et al. (17).

1.3.5 Potential solutions for improving fault ride through performance

Listed here are some of the potential solutions, including solutions for the electrical circuit that may also reduce the torsional load on the system. Generator set variables that affect fault ride through performance are outlined in (15) as follows; Rotor inertia, generator reactance, exciter and automatic voltage regulator (AVR) control design, engine response time/speed. Factors related to the electrical circuit and grid conditions that affect fault ride through performance are noted as follows. Voltage drop shape and magnitude, type of fault (1, 2, 3 phase etc.), fault clearance time or recovery period, fault location, grid strength (capability of returning to pre-fault parameters), active and reactive power (power factor) prior to fault and load requirements following the fault. Specific interest is paid to the generator set variables that affect the fault ride through and fault clearance performance in this project.

Shicong Y et al. (18) utilises a Simulink model of a synchronous generator for simulation of various low voltage ride through conditions, include a 100% voltage drop. The author suggests two possible methods to improve the low voltage ride through performance of the generator, braking resistors and a power flow controller. Crowbar and DC chopper circuits are used in the analysis of low voltage protection techniques by Abed et al. (17), a series dynamic resistor circuit is also utilised in a similar manner to the braking resistors scheme to limit high rotor current during LV faults. With the dynamic resistor circuit and chopper circuits active during the LV fault, the peak rotor currents at the initiation of the fault are greatly reduced thus reducing the initial peak generator torque. Series braking resistors are also included in a synchronous generator circuit in a study carried out by Norbert (19) to improve the LVRT capability of the

machine. With the activation of the series braking resistors, the simulated rotor acceleration is significantly reduced to the point where near pre-fault speed is maintained throughout the entire fault period of 250 ms. The study also suggests that the braking resistors only be engaged during the beginning of the fault and must be disengaged to avoid intensifying the backswing effect.

Johal H et al. (20) provides additional methods of increasing the critical clearing time (CCT). The critical clearing time is defined as the maximum fault period for which the generator remains in synchronism with the grid. These methods include the following: increasing the excitation ceiling voltage to improve post fault power transfer and oversizing the generator, thus decreasing the initial rotor angle and therefore increasing the maximum rotor shift angle available either side of full synchronism with the grid. Increasing the rotor inertia by redesigning the shaft or adding a flywheel or other mass to the system is also suggested. Increasing the rotor inertia leads to a reduction in rotor acceleration during a low voltage fault, thus improving the transient stability margin. The inertia present in a generator plays a key role in determining its low voltage ride through performance and is a major factor in maintaining grid stability following the loss of generation equipment (21). In the simulations performed in (20), the CCT is almost doubled when the generator inertia is increased seven fold. The impact of increased generator inertia is not well studied regarding analysing the impact in the electro-mechanical LVRT performance of the generator. The electromagnetic air gap torque and thus the shaft torque through the generator set needs to be thoroughly investigated in order to better understand the potential damage to the rotor.

1.3.6 Stress analysis of rotors

Identifying the potential damage to the generator requires knowledge of the components that are exposed to high magnitude torque during low voltage ride through faults. Narayanan et al. (22) provides an image of the drive end of a generator following a severe low voltage fault event as shown in Figure 2.8. Both the key and keyway have deformed in the shaft due to the twisting motion between the two machines and the keyway in the coupling has also cracked and deformed. Such a component that is designed with transient torque in mind failing in this manner indicates just how damaging low voltage ride faults can be. The ratio of inertias between the generator and prime mover determines the magnitude of the fault torque applied at the coupling between the two machines.

The stress in a shaft keyway can be obtained by multiplying the nominal maximum shear stress or nominal maximum von Mises stress in the shaft with a stress concentration factor (SCF) which is determined by the geometry of the keyway. The SCF for a keyway under torsion can vary between 2 and 3 as discussed in (23), (24). Hearn (24) notes that the presence and fit of a key within the keyway can significantly affect the stress distribution within the keyway and no general solution exists to determine the stress in a keyed assembly.

The initial electromagnetic air gap torque that occurs during the sub-transient period following grid reconnection rapidly peaks to a high value, greater than that at the point of grid disconnection. In the case of the 100% voltage drop simulated in (14), the reconnection torque reaches a magnitude of 4 kNm. Three-phase short circuits can

produce transient electromagnetic air gap torque up to twelve times larger than the rated electromagnetic torque, potentially resulting in damage to couplings and turbine/fan blades (21). Additionally, high magnitude torsional vibrations induced by oscillations in electromagnetic torque during low voltage faults are capable of exciting torsional modes of generator set drive shafts (25). Repeated low voltage faults can lead to structural fatigue and eventually failure of the rotor.

Dongxiang et al. (26) study a 600 MW steam turbine coupling that cracked due to torsional vibrations caused by power system disturbances. The system was exposed to a two-phase short circuit event alongside load induced torsional vibration throughout periods of its life installed in the plant. Stress analysis was performed using ANSYS to locate the area of maximum stress in the keyways of the coupling during the two-phase short circuit and sustained average stress for torsional vibration close to a torsional mode of the assembly. The author notes that the stress obtained due to the applied two-phase short circuit exceeds the yield strength of the material and likely contributed to the failure of the coupling.

Additionally, other components that are affected by low voltage ride through include the following as listed by Pillai et al. (27). Stator and rotor windings can physically move and flex when exposed to high inrush fault currents during low voltage faults, this can lead to cracking of the insulating varnish and potential short circuits in individual strands. The rotor rectifier may also be damaged due to high transient voltages. Indeed the forces applied to the generator stator windings during out of phase synchronisation or a three phase short circuit may be up to 100 times larger than steady

state values (28), but such faults are significantly less likely than thermal expansion or start-stop cycles that occur thousands of times over the life span of the machine.

1.3.7 Literature review summary

The research in section 1.3.2 provides evidence that analysis of 3D finite element models can produce accurate modal results with the use of FE programs such as ANSYS. These observations are utilised in this project to justify the creation of a dynamically validated 3D model of a synchronous generator. The research in (1) also suggests future work on simulating the torsional response to three-phase short circuits applied to the 3DFE rotor model. The work performed in this thesis follows the existing research by using the 3DFE modal analysis technique with ANSYS to create a model of a synchronous generator rotor, and it advances the existing research by analysing the torsional stress response in this model to low voltage ride through faults (which in the case of the examples simulated in this thesis are similar to three-phase short circuit faults, i.e. 100% voltage drop faults).

Existing literature (7) shows that it is possible to use the modal frequencies and shapes obtained from a modal analysis of the 3D laminated rotor core geometry to determine its orthotropic elastic properties. This research uses the example of a laminated rotor core pressed to a shaft, however when it comes to obtaining the modes of a fully assembled generator rotor there are additional components to consider. This research into using a 3DFE model to obtain the elastic properties of the rotor core is advanced in this thesis by extending the technique to a fully assembled rotor. The accuracy of the

approach is analysed and used to validate the dynamic 3DFE model of the generator rotor.

The research covered in section 1.3.4 on existing electro-mechanical models provides some good examples of coupled electro-mechanical simulations of engine driven synchronous generator sets subjected to low voltage ride through events. This thesis builds off this existing research by using the LVRT behaviour shown in these results to provide an indication of the expected response (in terms of torque, speed, current etc.) to low voltage faults. The research is advanced further by exploring the behaviour of several different LVRT conditions, and ultimately obtaining the relationship between the relative angular position of the rotor and the peak electromagnetic torque observed at the point of grid reconnection (full voltage restoration).

The research on the potential solutions for improving FRT performance in 1.3.5 is performed to investigate existing methods that can reduce the severity of LVRT faults and gauge how effective they are. The two common solutions that appear in the research are braking resistors and increasing the rotor inertia. This work advances the existing research by adding braking resistors directly to the synchronous generator's stator circuit, balancing the inertia between the generator and engine and adding additional inertia to the rotor. The performance contribution of each modification is analysed and compared with an unprotected generator set to determine how effective they are when applied to a grid connected engine driven generator set. This research outcome is intended to form a foundation for further research into the development of such devices that may be added to the generator set to enable both improved LVRT performance and ensure grid code compliance into the future. The short coming of this research is that

the peak electromagnetic torque is not a strong focus, as a result there is no analyses that show if the modifications reduced the torque and therefore the stress in the generator set rotors.

The research outlined in section 1.3.6 provides existing examples of the damage that synchronous generators may sustain following low voltage fault events and suggests that the shaft torque can increase during out of phase synchronisation by up to 12 pu. Additional research showed that 3DFE transient stress analysis could be performed using ANSYS to obtain stress results in generator rotors subjected to short circuit faults. In this thesis, transient 3DFE analysis is used to further the knowledge on low voltage ride through effects as highlighted in (21) by obtaining the peak stress in the shaft keyway of a generator for an extreme LVRT scenario.

Chapter 2 Background and theory

2.1 Synchronous generator sets and low voltage ride through

When analysing the alternator to determine its suitability to meet grid code requirements, it is vital to also consider the impact that the prime mover and interconnected control systems have on fault ride through (FRT) stability. Diesel engine generator sets range in size and rated power from a few kVA to multi MVA machines and are utilised in a wide range of power supply systems for stand-by emergency power or prime power. Diesel driven generator sets (gensets) are frequently used to supply power to local infrastructure due to the convenience and availability of diesel fuel, as a result they form a substantial portion of distributed generation capacity around the world alongside renewable energy generation.

In many countries around the world, including the UK, diesel generators that are normally used as standby systems by consumers to support industrial and commercial infrastructure such as hospitals and airports can be called upon to support the electrical grid during periods of high demand. Around a quarter of the backup power in the UK is supplied by standby diesel gensets. Both localised and power plant gensets are required to stay connected to the grid during faults in order to stabilise the grid and prevent a cascading loss of generation on the network.

Smaller diesel gensets (10's to 100's kVA) that are connected to the national grid have a low rotational inertia and electrical power output when compared to the larger gensets that are providing primary power to the grid in power plants. Whilst these gensets serve to support the grid during periods of high demand, they also add to the problem of grid instability introduced by distributed generation. At the same time, the prime mover (the diesel engine) contributes to this instability due to delays in speed recovery following severe supply faults which increases the period of time before the machine is resynchronised with the grid.

2.1.1 Generator set control

The separately excited machine uses a small pilot generator which typically consists of a permanent magnet rotor with a three-phase winding on the stator. The pilot generator, also often referred to as a permanent magnet generator (PMG) produces power for the field circuit of the exciter, thus avoiding the dependency of starting the generator using its residual magnetic field. No external electric power source is required to run the

machine as the permanent magnets always produces a magnetic field. Voltage induced in the PMG rotor is supplied directly to the automatic voltage regulator, AVR, which rectifies the three phase AC to DC and supplies it to the stator of the exciter. As with the self-exciter generator, the current from the exciter rotor is rectified and supplied to the main rotor as DC and the stator induced AC voltage is connected to the sensor input of the AVR.

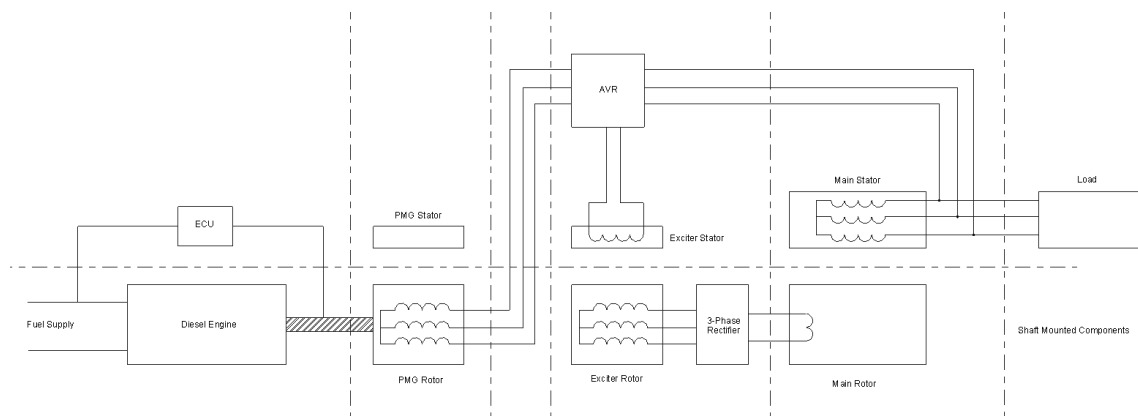


Figure 2.1: Separately excited synchronous generator coupled to a diesel engine.

Figure 2.1 shows a block diagram of the two basic control systems that are implemented to control the genset. The AVR maintains the correct voltage level at the generator terminals by controlling the field voltage in the exciter, which directly controls the armature voltage and current. The engine control unit (ECU) contains a speed controller and governor which directly controls the fuel injection (throttle control) into the engine in order to correct the rotational speed of the shaft. Speed measurements are taken from the shaft between the diesel engine (DE) and the synchronous generator (SG) and compared with a reference speed, which in this case is fixed at the grid frequency. The DE control system will always attempt to maintain a constant speed, though the torque

will vary with changes in the electrical loading on the SG and thus the mechanical power from the DE will vary to match the electrical power demand.

Both the ECU and generator control systems are linked to the genset control panel. From here, system parameters can be controlled manually such as the reference speed and voltage. System parameters are automatically monitored by the control panel and emergency shutdowns are triggered when maximum/minimum limits are breached such as high temperature or over current. Ultimately the ECU controls or responds to the kW loading on the generator and the AVR and exciter system control or respond to the apparent power (kVA) and therefore the reactive power (kVAR) loading.

2.1.2 Generator electrical faults

An electrical fault in a generator is typically considered to be caused by one or more of the following;

- Generator insulation breakdown caused by lightning strikes and switching surges, manufacturing defects, installation defects and poor quality or damaged insulation causing overvoltage in the machine.
- Mechanical contact or damage to the generator or the electricity distribution equipment (lines, transformers etc.) including fallen tree branches, collisions with heavy equipment, poor weather conditions, and natural disasters.
- Thermal damage to the generator due to improper loading or sizing of the machine leading to excessive time spent operating in the over current condition (above rated current).

These fault sources are permanent faults, ordinarily, generators connected to the grid which experience these faults will shut down to protect themselves when the operating characteristics of the system (voltage, current, frequency etc.) deviate too far from normal operating levels. If there is enough generation capacity to compensate for one or more generator failures then the grid may continue to supply electrical power, though this may be at a reduced voltage (brown out) which will adversely affect the operation of all machinery connected to the grid. If the fault causes multiple generator shutdown and a significantly large proportion of the generating capacity of the grid is lost, it is likely that the remaining generators will also shut down as they will be incapable of supplying the electrical load, resulting in a black out.

2.1.3 Grid stability

A stable electricity grid maintains a steady balance between production and consumption of electrical power. The frequency of a stable grid remains constant at either 50 Hz or 60 Hz despite changes in load caused by consumer activity. When periods of peak electricity consumption are expected, for example in the evening when power demand for residential heating and appliances increases, additional generators can be brought online in advance to ensure that supply meets demand at all times.

Grid instability occurs when generation capacity does not meet the load requirement. As mentioned previously, electrical faults are one source of such conditions, another source of grid instability is unbalanced power generation across the grid.

2.1.4 Power plants and distributed generation

Electricity grids around the world are designed around a centralised power generation system, where large power plants supply the majority of power to the network via large multi-megawatt generators that are typically powered by gas turbines or steam turbines (nuclear, coal and oil plants). The large size and weight of the rotors in generators of this scale lend a high inertia to the system, which results in a very slow dynamic response to sudden changes on the grid such as electrical faults. In effect, the high inertia of this power generation machinery promotes excellent grid stability, as the system has the capacity to absorb power fluctuations such as switching surges and rapid changes in load demand. Perhaps most importantly, rotational inertia minimises changes to the grid frequency and slows down the frequency dynamics of the system, allowing more time to react to fault events and maintain the correct frequency, a vital requirement for stable operation of the grid (21). Power plants are a reliable source of power generation as they operate all day, every day of the year as long as they are supplied with enough fuel to drive their prime movers. They typically have enough generation capacity to allow for one or more generators to be taken offline for routine maintenance or checks whilst the plant continues to supply the grid, as a result, failure of a fossil fuel or nuclear power plant is a relatively rare occurrence.

Concerns over carbon dioxide emissions from traditional fossil fuel power plants has reduced their desirability as a primary power source. In response to a worldwide push towards lower emission energy generation technologies and in light of current and upcoming emissions regulations, the use of renewable energy (RE) sources such as wind and solar PV has increased dramatically. Wind farms, tidal generators and other

such RE installations still utilise generators, typically induction generators, to produce electrical power, though the power generating capacity of a single RE plant is significantly lower than that of a traditional power plant. Ultimately, more RE plants are required to fill in the generation capacity gap that would normally be filled by a single fossil/nuclear power plant, which increases the proportion of distributed power generator to centralised power generation.

A greater proportion of distributed power generation connected to the grid presents a problem to existing grid architecture and the generation equipment connected to it as the stability of the system is effectively reduced. Many forms of RE generation rely on a fluctuating source of energy to supply power, be it wind, tidal currents or solar. Unlike centralised power plants, RE plants are less predictable as they cannot generate maximum power at all times. Until energy storage technology becomes cost effective enough to fill in the gaps between energy source fluctuations, RE plants must either be supplemented with additional diesel generators (which undermines the environmental benefit of the plant) or operated below their full rate power output to improve reliability (at the cost of efficiency).

Another issue that affects the stability of RE systems is the low inertia of the generating plant as a whole. As mentioned previously, the high inertia of the large synchronous generators in a traditional power plant enables a wide range of fast load changes to occur without impacting the stability of the grid. In the case of a wind farm, the generators in the nacelle of each turbine is relatively small and capable of generating up to 2 to 3 MW in the largest of turbines. The total inertia of the system is much smaller than that of a generator in a traditional power plant, reducing its tolerance of electrical

grid faults and transient events. Wind turbine generators effectively increase the speed of frequency dynamics across the system. The fluctuating generating nature of RE systems introduces the following power quality problems to the grid (29).

- Overvoltage during feed-in
- Short and long time voltage fluctuations (including flicker)
- Frequency deviations
- Voltage dips
- Unbalance, the uneven distribution of voltage across each phase.

2.1.5 Low voltage ride through

The low voltage fault ride through (LVRT) capability of generators has become an important consideration when designing electrical networks, this factor determines the length of time that the generator can continue to supply power to the grid at a reduced voltage during disturbances in the system. During a low voltage fault on the grid, connected generators are subjected to a drop in terminal voltage which results in them not being able to convert all of the mechanical power supplied by the prime mover to electrical power. With little power being exported to the grid (no real power during a 100% voltage drop), the excess electrical power contained within the magnetic field and windings is converted into losses (primarily heat) (14). Since the prime mover cannot react with instantaneous deceleration, the mechanical input power remains largely the same as it was before the fault occurred, resulting in rotor acceleration over the fault ride through period.

Historically, generators were simply disconnected from the grid until the fault had cleared and the system returned to normal operating levels, at which point the generator was connected back into the grid at the correct voltage and frequency. This action protects the generator from the large fault currents which result in heating of the windings and insulation and it also avoids the risk of pole slip leading to out of phase synchronisation. Now that the push towards distributed generation has resulted in a larger proportion of power generation coming from smaller generators to larger generators than ever before, the responsibility to maintain a stable grid at the correct voltage and frequency must now be shared by generator operators.

2.1.6 Fault ride through requirements and grid codes

Many electricity grids around the world now require all generators that are connected to it to remain connected over a minimum specified period of time during a low voltage fault. Whilst LVRT functionality has existed in some generators as a feature for some time now, the majority of designs have prioritised power rating. This means that operators installing new generators must check if the machine they are interested in purchasing has fault ride through capability that complies with grid fault ride through requirements.

Fault ride through requirements for a particular grid are specified in grid codes, which are enforced by the transmission system owner (TSO) that operates the grid. Grid codes in Great Britain are drawn up by Ofgem and administered by National Grid, they specify that 275 kV and 400 kV synchronous generators (installed after April 2005) are FRT capable for a 85% voltage drop for at least 140 ms (30).

FRT requirements were first introduced to grid codes in the UK in response to a weakness in wind generation farms where a lack of system inertia and low impedance in the doubly fed induction generators employed in wind turbines would frequently lead to tripping of the system at voltage levels below 90% then nominal level. These events were capable of leading to a cascading loss of generation on the grid as the sudden loss of a number of wind turbines would create a significant voltage disturbance across the grid (31).

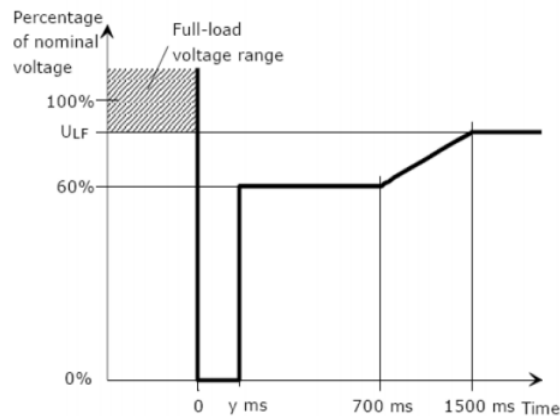


Figure 2.2: Voltage curve during a grid fault (30)

Figure 2.2 shows the length of time that the generator is expected to ride through the fault at a particular voltage level. These voltage curves also specify the recovery behaviour that the generator must meet as a minimum in order to comply with the fault ride through requirement set out in the grid code.

Grid codes differ between different countries. The FRT time for countries in Europe is typically around 150 ms for a 100% voltage drop, varying from country to country depending on the level of renewable energy generation and the needs of the system.

European network codes are to be implemented in the future in order to better coordinate changes to individual grid requirements and build a more robust power supply network for all members connected to it (32).

Where multiple grids are connected to one another, the TSOs of each individual grid agree on standardised requirements for the grid code. Grid code requirements can vary dramatically in some cases as shown in Figure 2.3 and Figure 2.4. For example, Ireland imposes a demanding maximum FRT time of 0.625 s for voltage drops of up to 90%.

Grid code country	During fault		Fault clearance	
	V_{min} [PU]	T_{max} [s]	V_{min} [PU]	T_{max} [s]
Australia	0.0	0.4	0.7	2
Canada	0.0	0.15	0.75	2
Denmark	0.0	0.15	0.6	0.7
Germany	0.0	0.15	0.9	1.5
Ireland	0.15	0.625	0.9	3
New Zealand	0	0.2	0.9	1
Spain	0.0	0.15	0.85	1
UK	0.15	0.14	0.8	1.2
USA (FERC)	0.15	0.625	0.9	3
USA (WECC)	0.0	0.15	0.9	1.5

Figure 2.3: LVRT Requirements of international grid codes (33)

This difference in fault ride through requirements between different grid codes presents a challenge to generator manufacturers. One specific generator designed to comply with one grid code may not comply with another, and so a different design would need to be created for each FRT time requirement to cover the full market for which a single generator design would normally have been acceptable.

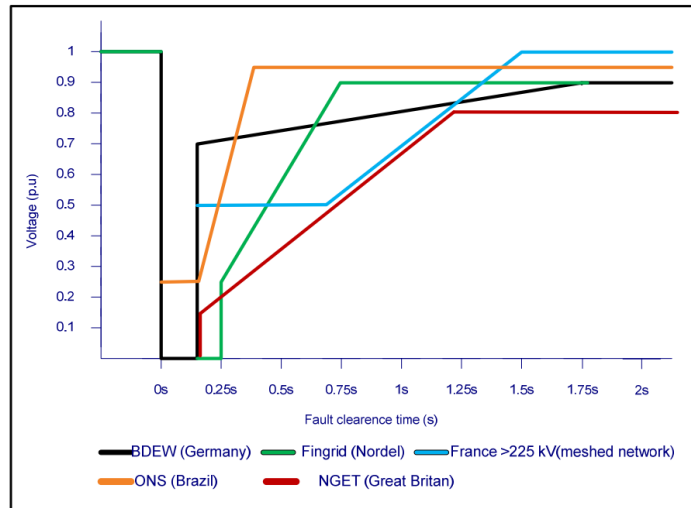


Figure 2.4: Voltage curves for LVRT Requirements of international grid codes (15)

Alternatively, a generator designed to comply with all grid codes around the world would be capable of fault ride through for the maximum time specified and could be sold anywhere. Such a design would however be out competed by designs targeting specific lower FRT time requirements for individual countries or zones given the additional cost required to satisfy the greater FRT (by over sizing the machine for example).

2.1.7 Fault clearing

Following a voltage drop event, when full voltage has been restored to the grid, there is a period of time in which the alternator re-synchronises with the network called the fault clearing time. It is during this time that the alternator may experience pole slip and resulting out of phase synchronisation.

Figure 2.5 details the results for a range of generator parameters during a LVRT test on a 4 MVA machine (14). The top plot shows the terminal voltage falling to zero at $t = 2$

s during a 100% low voltage fault event. The plot directly below it shows the three phase currents in the stator, there is a sudden large increase in current when the terminal voltage drops as the active power is reduced to zero and 100% of the power produced in the machine is now reactive. This is because the flux present in the machine cannot change instantly, so the current increases to maintain the flux at the original level. As the electromagnetic torque falls and the rotor accelerates, the exciter voltage in the machine increases by way of the AVR in an attempt to maintain the stator voltage (terminal voltage).

During the fault clearing time when the grid voltage returns to the normal level (just after $t = 2.1$ s) there is a difference in the voltage of the alternator and the grid voltage. The peak current increases again, by an even greater magnitude than at the beginning of the fault, as the grid attempts to pull the rotor back to the original synchronous speed at 100% of the normal voltage. The load angle of the alternator is at a maximum at the end of the fault by the action of rotor acceleration, hence the increased stator currents when the grid forces a reversal in rotor speed.

During the fault clearing period there is a risk that the increased peak currents on the stator and large rotor torque transients will damage the machine. The peak current here can be up to twice as large as that experienced during a short circuit fault, therefore the fault clearing condition should not be ignored when designing the stator windings and rotor damper bars.

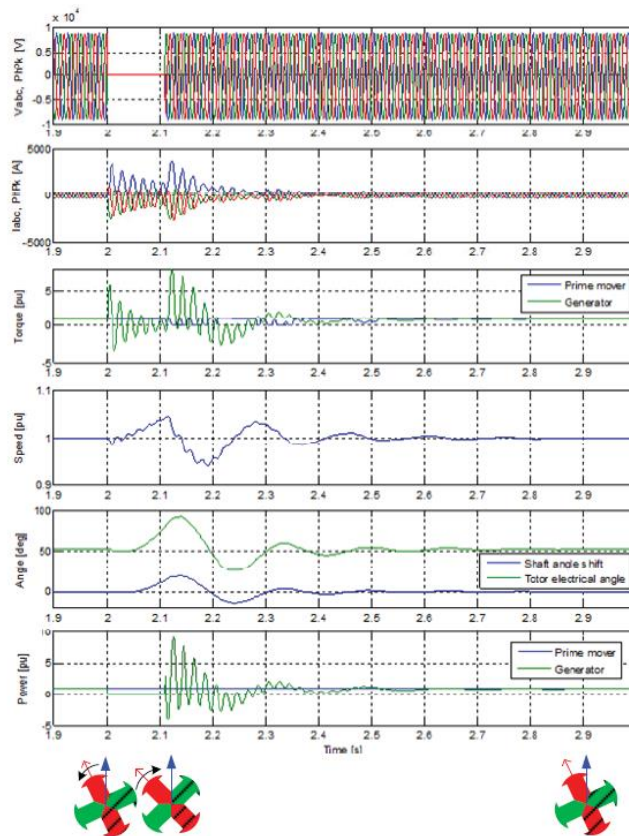


Figure 2.5: Synchronous generator response to a 110 ms low voltage fault (14)

It should be noted that the example here represents a worst-case scenario where the voltage drops by 100% in a single step and recovers in a similar manner. Also, modern diesel engines use advanced feed-forward protection systems to cut off the combustion cycle during a low voltage fault, whereas no such system has been added to this simulation.

Grid codes also specify a fault clearing period with the aim of stabilising all generating equipment on the network as fast as possible as shown in Figure 2.3. For example, the generator should be producing 90% active power to the grid within 0.5 seconds of the grid voltage being restored to pre fault levels.

2.1.8 FRT generator parameters

2.1.8.1 Short circuit ratio

The short circuit ratio is another relevant generator parameter that impacts the physical size, cost and operating characteristics of the machine. It is included for consideration in this review due to the significant impact that SCR has on the transient stability of generators during grid faults.

The short circuit ratio (SCR) of a generator determines the leading reactive capability of the machine and has a direct impact on the static stability. The SCR is defined as; “The ratio of the field current for rated armature voltage on open-circuit to the field current for rated armature current on sustained symmetrical short circuit, both with the machine running at rated speed” (34).

Increasing the SCR requires an increase in ampere-turns in the field windings which in turn requires an increase in the total machine volume and therefore cost. The efficiency of the machine also falls as the field winding losses are increased. SCR is equal to $\frac{1}{X_d}$, where X_d is the reactance in the direct axis. The direct axis reactance should be minimised to increase the length of time that the machine can ride through a fault without becoming unstable, so increasing the SCR effectively improves the dynamic stability of the machine during voltage dips in the power system. A larger torque is also achieved with a greater SCR, and the load angle is decreased (35).

2.1.8.2 SCR and transient reactance

Following a fault on the network when the pre-existing voltage is restored, the generator enters the fault recovery period. Another time period, the critical clearing time (CCT) is given by the grid codes that determines minimum amount of time that the machine can ride through a fault. The CCT of the generator is increased in machines with a larger SCR but other factors, particularly the transient reactance of the machine have the greatest impact on CCT. If the CCT of a machine is lower than the fault time, then loss of synchronism can occur as the maximum allowable time for fault clearing has been passed and the fault is still in effect. The CCT is significantly increased as the transient reactance is reduced. The transient reactance is dominant in determining the time required for fault clearing.

2.1.8.3 Sub-transient reactance

As well as reducing the synchronous reactance and increasing the inertia constant, Narayanan et al. (22) suggests that reducing the sub-transient reactance, X''_d , also improves the transient stability of the alternator during LVRT. The sub-transient reactance of an alternator comes into effect when large currents are induced in the damper bars / windings on the rotor and the stator windings, such as when an LVRT event occurs. A resulting mutual inductance between the damper and windings in the machine sets up a complex magnetic flux between these components and the rotor body which acts to suddenly reduce the synchronous reactance of the alternator. The impact of this reduction in reactance is visible at the beginning of the LVRT event in shown in Figure 2.5 and Figure 2.6.

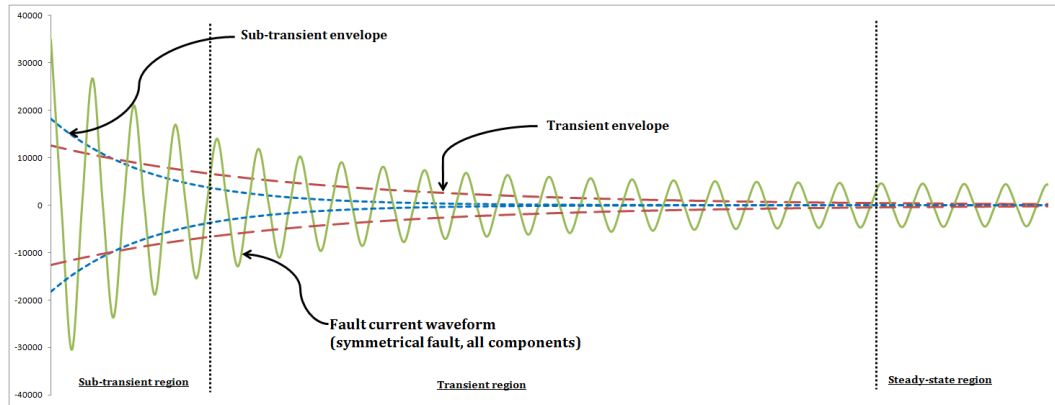


Figure 2.6: Current following a fault event, showing the sub-transient, transient and steady state regions (36)

This effect facilitates the sudden increase in peak current at the beginning of the LVRT event. The region over which the effect of sub-transient reactance dominates the current in the machine is known as the sub-transient envelope.

Though the effect of sub-transient reactance only lasts for the first few cycles, it is directly responsible for the peak current during transient events. A reduction in the sub-transient reactance lowers the maximum peak fault current. The sub-transient reactance is determined by testing and usually given by the alternator manufacturer in datasheets. For example, a Cummins Stamford HC4F industrial alternator has a sub-transient reactance of 0.13 per unit (pu) for a 240V machine (455kVA) (37). As for the transient reactance, the sub-transient reactance can be altered by changing the winding patterns, the depth of the winding slots or the length of the stator core (28).

2.1.8.4 Exciter ceiling voltage

Another design parameter that may be considered during design optimisation for fault ride through is the ceiling voltage. The ceiling voltage is the maximum DC excitation voltage, which ranges around 1.6 to 3 pu (maximum ceiling voltage / rated field voltage). It is called upon during sudden changes in the terminal voltage. The higher the ceiling voltage, the faster the field current can be changed to the required value. Studies have shown that the transient stability improvement offered by increasing the ceiling voltage is limited up to 3 pu, beyond which the CCT does not improve any further.

Increasing the ceiling voltage requires changes to the field winding insulation to deal with the increased maximum voltage. This will reduce the shortest distance between individual windings, the creepage distance, and so additional spacing increases must be made which have a small impact on the rotor diameter (35).

2.1.9 FRT Design considerations for synchronous generators

When designing an alternator to meet LVRT requirements, both the steady state performance and the dynamic transient fault performance should be optimised by altering the design of the engine, alternator and the genset control systems together to control the trade-off between increasing one or the other. The optimised alternator should ideally meet the grid code requirements exactly in order to maximise performance (rated power, cost etc.), the following considerations are made by Cummins Generator Technologies.

2.1.9.1 Design for compliance

Design for compliance is governed by the grid codes, the performance targets here are fixed, though as previously stated, different grid codes exist around the world. So it is up to the manufacturer to decide how wide a range of grid codes they can satisfy whilst keeping the design cost effective.

- The static grid codes regulate steady state performance of generating equipment connected to the grid, frequency, voltage, and power factor (PF) are all specified in the codes. Generating equipment connected to the grid must be able to operate within the specified range of variation for these factors. For example, in the UK the grid typically includes a fluctuation in supply frequency of around $\pm 1\%$ as controlled by National Grid, broadly speaking, grid codes specify that alternators should be designed to cope with frequency variations of up to around $\pm 5\%$. Alternators should also be capable of operating within the specified power factor range to correct the total power factor on the grid, 0.8 lagging to 0.9 leading. A $\pm 10\%$ voltage variation is also required, so connected generating equipment must be capable of operating at additional excitation and thus elevated temperature for extended periods of time (design for higher stator currents) (38).
- Dynamic grid codes regulate the transient performance of the alternator. Fault ride through time (typically up to 250 ms), fault clearing time / recovery time, active and reactive power output are all specified in the grid codes. For example, the grid codes state that the generator must operate with maximum reactive

current without exceeding the transient rating of the unit (the allowable increased current over the rated value for short periods of time) to maintain the terminal voltage (29). The prime mover will be accelerating the rotor of the generator and high currents are induced in the dampers to compensate.

2.1.9.2 Design for robustness

Direct modifications to the physical and electrical design of the alternator such as the reduction in steady state load angle via a reduction of synchronous reactance are important to maintain the stability of the machine during LVRT events which ensures grid code compliance. Other design modifications and additions to the alternator circuits and mechanical structure are typically required to protect the machine from damage during large voltage transients so that the design meets requirements for robustness.

2.1.9.3 Electrical damage

Circuit snubbers are commonly used to suppress voltage spikes generated by the inductance in a circuit when electrical or mechanical switches are opened (39). In a resistor-capacitor (RC) snubber, a path is provided across the switch which allows energy to be dissipated in a resistor placed in series with a capacitor. The resistor is sized according to the circuit inductance in order to provide sufficient damping to minimise the amplitude of voltage spikes. The capacitor is implemented so that resistor is only connected during fast voltage spikes thus the resistor does not present a constant energy loss as heat during normal operation.

As described in the patent for a rectifier snubber circuit (40), such a device is placed between the diodes of the rectifier and the field windings of the main rotor in a synchronous generator. Commutation of the diode bridge results in transient voltage spikes at the DC output terminals of the rectifier which in turn can damage the diodes themselves. Load transients such as sudden loss or reduction in load during an LVRT event also cause voltage spikes in the rectifier. The capacitor resistor snubber circuit reduces the amplitude of the voltage spikes without introducing detrimental losses or harmonic distortion. The snubber circuit can be tuned to help protect the rotor circuits during a 100% voltage drop scenario.

2.1.9.4 Mechanical and thermal damage, stator windings and bracing

The stator windings are subjected to large electromagnetic forces caused by current transients during FRT events (current increases dramatically during LVRT events). The induced electromagnetic forces cause the windings in the alternator to vibrate at twice the grid frequency which can damage the thermal insulation that separates the individual winding strands from each other and the neighbouring phase windings (41). The physical dimensions of the windings must be designed carefully to avoid resonance to avoid the worst-case scenario for insulation breakdown and direct damage to the windings. Winding resonance can lead to fatigue cracking of the windings, particularly where bar copper strands are used, and components connected to the windings such as the phase leads and their mountings on the alternator (42). At the same time, changing the winding design impacts the reactance of the machine so the design for compliance requirement must be considered in parallel with any changes to be made to meet the

robustness requirement. The end winding bracing system can be designed to damp the vibrations of the windings and minimise displacement, however if the mass and length of the windings result in a resonant frequency close to twice the power frequency, the bracing will make little difference in preventing resonance frequency matching during a fault (43). Thermal damage arising from high winding currents is also a potential problem during fault ride through, insulation breakdown between the windings can occur if high temperatures are sustained over a relatively long period of time. Though the fault ride through event may only last a few hundred milliseconds, the temperature rise over this period may be large enough to result in significantly elevated insulation temperatures for many cycles to come.

2.1.9.5 Damper bars

Damper bars are a series of solid copper elements that are positioned just beneath the surface of the rotor in the pole faces that lie along the length of the rotor as shown in Figure 2.7.

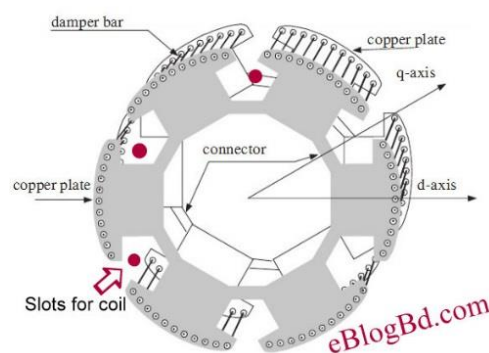


Figure 2.7: Damper bar placement in a salient pole rotor (44)

The damper bars in a synchronous generator serve several purposes relating to the stability and robustness of the machine. Most notably, they produce a damping torque to counteract oscillation from shock transient events such as short circuits, they also help to balance the terminal voltage during unbalance phase loading conditions and suppress harmonics in the voltage waveform (45).

Current flow is induced in the damper bars in a similar fashion to the cage rotor of an induction machine, the resulting magnetic field around the bars interacts with the stator magnetic field and so sudden changes in rotor acceleration are prevented, with a resulting current being induced in the damper bars. During fault ride through, excessive displacement between the rotor angular velocity relative to the magnetic field rotation speed of the stator leads to high current flow through the damper bars and elevated temperatures as a result. Expansion of the damper bars places stress on the rotor iron structure and the bars themselves which can lead to fatigue cracking (41).

2.1.9.6 Rotor shaft

In a genset, the shaft that the rotor is attached to is coupled to the prime mover. The rotor, shaft, couplings and diesel engine must be designed to withstand fast torque transients in order to prevent mechanical failure of the genset. Out of phase synchronisation following a fault ride through event can produce torque spikes large enough to deform or crack the shaft and couplings. Figure 2.8 below shows an extreme case of such damage to the keyway on the shaft and coupling where the key has been torn out of the slot during an out of phase synchronisation event.

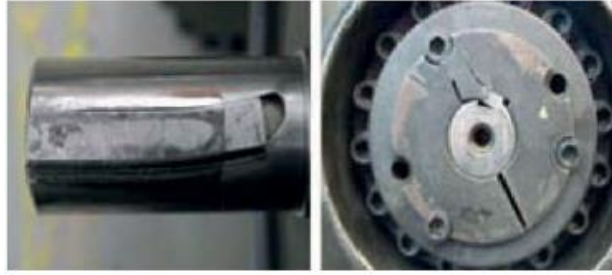


Figure 2.8: Damage to rotor shaft key following an out of phase synchronisation event

(22)

If the engine inertia is too small or too great relative to the alternator inertia, severe torque transients are capable of damaging the engine itself (41). The worst-case scenario of damage to rotor, shaft and engine during crash resynchronisation must be avoided and so it is critical that the shaft design is robust. The couplings in modern generator sets are designed to be flexible enough to protect against severe fast torque transients. A two-bearing alternator coupled to a diesel engine with a flexible coupling is an appropriate choice for a grid code compliant generator set; single bearing machines that are directly coupled subject the engine to potentially destructive loads during under-voltage transients.

2.1.9.7 Genset control

The genset control system plays an important role in protecting both the engine and the alternator from damage during faults. In the case of a low voltage ride through event, the control system can reduce the fuel flow to the engine to minimise acceleration of the rotor and prevent de-synchronisation. The engine control unit must be able to respond to a measured acceleration on the shaft fast enough.

2.1.10 Design practices for LVRT

Designing the generator to maintain a low steady state load angle is the best way to maintain static stability (22). This condition can be achieved by altering the reactance X_d and X_q . X_d represents the synchronous reactance (X_s) on the direct axis of the rotor, and X_q represents the synchronous reactance on the quadrature axis.

A reduction in the steady state load angle effectively (angular displacement between the stator field axis and rotor field axis) increases the available angular displacement before pole slip occurs during LVRT, therefore increasing the possible ride through time. Reducing the synchronous reactance of the machine allows for a reduction in the steady state load angle. Reducing the reactance on the direct axis (main reactance) in particular has the greatest impact on load angle reduction.

Raising the inertia constant (h) of the rotor also reduces the acceleration that occurs during fault ride through. Though doing so would require increasing the size of the generator and adding mass to the rotor, which contradicts the design principles of standby generators which aim to be compact (high power density) and light (22). It would however be possible to add a significant inertia to the rotor in the form of a flywheel which would result in reduced angular acceleration at a relatively low cost.

2.1.10.1 Reactance and load angle

The synchronous reactance (X_s) is composed of a reactance representing the armature reaction and the leakage reactance of the machine. Both components are indicated individually in the terminal voltage equation below (46) ;

$$\vec{V} = \vec{e} - j\vec{I}_A X - j\vec{I}_A X_A - \vec{I}_A R_A \quad (2.1)$$

Where;

$j\vec{I}_A X$ = Voltage drop due to armature reactance

$\vec{I}_A R_A$ = Voltage drop due to winding resistance

$j\vec{I}_A X_A$ = Voltage drop due to leakage reactance

\vec{V} = Terminal voltage

\vec{e} = Internally generated electromotive force (EMF)

Combining both the leakage reactance and the armature reactance into a synchronous reactance X_s as described in (46);

$$\vec{e} = \vec{V} - \vec{I}_A R_A - j\vec{I}_A X_S \quad (2.2)$$

The total internally generated EMF (e) is composed of the EMF induced in the stator windings e_{exc} and the armature reaction e_{AR} EMF that opposes it:

$$e = e_{exc} + e_{AR} \quad (2.3)$$

And,

$$e_{AR} = -j\vec{I}_A X_S \quad (2.4)$$

Therefore, by reducing the reactance responsible for armature reaction (and the leakage reactance for the total synchronous reactance) the internally generated EMF is increased. As indicated by the synchronous generator phasor diagram in Figure 2.9, a decrease in the proportion of armature reaction EMF to the total EMF results in a

decrease in the load angle when the EMF is constant. Similarly, the same reaction occurs when the terminal voltage is fixed and the total EMF increases.

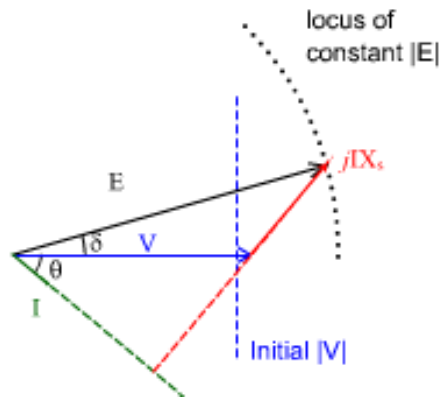


Figure 2.9: Synchronous generator phasor diagram (47)

2.1.10.2 Reducing synchronous reactance

The synchronous reactance of the machine is dependent on the physical characteristics of the design. Both the leakage reactance and the armature reaction reactance are represented as inductive reactances. Inductive reactance can be calculated using the following equation:

$$X_L = 2\pi fl \quad (2.5)$$

Where,

f = Supply frequency (Hz)

l = Length of the machine (m)

Since the supply frequency is fixed by the grid in a synchronous generator, this leaves the inductance as the only variable quantity. In the case of leakage reactance, the slot permeance and the end coil permeance determines how much self-linked flux passes around the machine and does not contribute to the total magnetic field between the

stator and the rotor. Decreasing these permeances requires material changes (to decrease permeability μ) or dimensional changes to reduce the surface area over which the flux can pass and increase the length of material that flux will pass through.

Also, reducing the inductance of the windings to reduce the synchronous reactance ultimately reduces the steady state stability of the system itself (electrical time constant reduces, $t_a = \frac{L}{R}$). And to achieve a reduced inductance, the machine would need to run at lower armature currents or smaller diameter coils would need to be installed which in turn would reduce the electrical power generating capacity of the machine (which would then have to be de-rated).

Reducing the synchronous reactance directly requires some sacrifice in machine performance such as efficiency or rated power. Additionally, a likely increase in manufacturing, material costs or both will follow such alterations to the machine (22).

The equations and explanation of synchronous reactance help to explain the role played by the synchronous reactance of the machine, and how reducing the synchronous reactance can ultimately reduce the peak short circuit current at the cost of derating the machine. The synchronous reactance is considered in section 5.3.4 to explain the impact of increasing the internal resistance of the generator on short circuit current and is further referenced in section 6.2, 7.2.2 and 8 as the typical method of reducing peak fault currents.

2.2 Rotor dynamics

The study of rotor dynamics involves the determination of the dynamic behaviour of rotating structures that are designed to transfer power such as motor, generator and turbine rotors. Rotors typically consist of a horizontal cylindrical shaft that is supported by bearings such that it is free to rotate. In the case of a generator rotor assembly, the shaft supports multiple components that rotate with the shaft and enable the machine to convert mechanical power to electrical power. The synchronous generators of interest in this study have rotors that carry three vital components, a main rotor core, an exciter and a fan.

Rotating assemblies, like their static counterparts, have dynamic properties owing to their geometry, material, support and component interface conditions that dictate the physical response of the structure to external sources of excitation such as a sudden impact applied at a particular point or rapid acceleration of one or more components within the structure. The dynamic behaviour of rotors is however made more complex by a variety of factors that alter how the structure responds to applied excitation; gyroscopic effects, non-linear and direction sensitive bearing support properties, un-symmetric stiffness, non-proportional damping, frequency-dependant effects (48) and rotor mass imbalance which leads to the whirl effect are commonly attributed to significant differences between the dynamic response of static rotor and a rotor rotating at a particular speed. Such phenomena are explored in this review alongside the underlying theory of vibration in electrical machines and rotor-dynamic behaviours particular to synchronous generator rotors.

In the scope of this project it is vital to understand the rotor-dynamic behaviour of the synchronous generator rotor in order to correctly understand how the machine responds to electromagnetic faults in terms of the stresses and displacements that occur across the rotor.

2.2.1 Vibration in electrical machines

One of the main concerns when designing rotors is vibration. Vibration of both the rotating and static components of the machine can lead to significant structural damage and ultimately failure of the assembly.

There are multiple potential causes of vibration in diesel engine generator sets that exist due to a variety of case-by-case factors such as manufacturing defects, environmental noise, faulty or incorrectly specified vibration mounting and wearing/damage. Transverse and torsional vibrations can occur due to the following:

- Unbalance of rotating components (coupling, rotor components etc.)
- Misalignment of shafts between the engine and the generator.
- Cylinder misfiring.
- Torque pulsations in the combustion cycle
- Sudden or repeated changes to electromagnetic torque caused by line harmonics, short circuits, and line faults (voltage drop, frequency swing) (49).

There are two types of vibration of interest when considering the dynamics of a rotor system; forced harmonic vibrations like those excited by the torque pulsations consist

of a sinusoidal oscillating motion at a set frequency and magnitude over an extended period of time equal to that of the applied force.

Transient vibrations are typically associated with non-periodic sudden shock or impact loading cases where an external force is applied over a very short period of time and then removed causing the structure to vibrate at the forcing frequency and magnitude for a brief moment before continuing to vibrate freely with a decaying magnitude (the rate of decay being determined by the amount of damping present in the structure). The applied force may also be suddenly applied and then sustained over a longer period of time, say several seconds, such a condition can be observed in a generator when the electrical load is suddenly increased or decreased causing the mechanical torque to suddenly change and oscillate about the new torque level until it settles at a steady state.

Vibration of the generator is ultimately unavoidable, although additional damping can be introduced to the system to reduce vibration, as long as the magnitude of vibration is within acceptable limits the machine is safe. If the maximum vibratory stress limit of the rotor is exceeded for an extended period of time then it will be operating above the fatigue limit or endurance strength of the rotor material (usually of the shaft). Every time vibrations (either transient or harmonic) pass this safe operating limit, the material is effectively weakened. Failure will eventually occur over several hundreds to thousands of cycles if the vibration magnitude continues to pass within the high cycle fatigue band, just above the fatigue limit. Alternatively, if the magnitude of vibration is very high, such as in the case of resonance or an extreme transient event it may lead to low cycle fatigue, fatigue failure with just a few cycles of extreme vibration required to destroy the rotor.

2.2.2 Transverse vibrations of rotors

All rotors have a small amount of mass unbalance due to variations in the material structure and geometry of rotor components that inevitably occur during manufacturing. This unbalance displaces the mass axis from alignment with the bearing axis (50) and this is responsible for creating vibration in the rotor at a frequency equal to the speed of rotation as every revolution is equal to one full cycle of the resulting centrifugal force around the circumference of the rotor. As a result, the action of rotation alone is capable of exciting the natural frequencies of the rotor and bearing assembly. These natural frequencies are known as whirling natural frequencies due to the orbital nature of the rotating bending mode shape that the rotor shaft takes during resonance.

An interference or Campbell diagram is commonly used to plot the natural frequencies of each mode versus the speed of rotation (RPM) of the rotor. Where the line representing the speed of rotation crosses one of the natural frequency lines is designated as a critical speed. At a critical speed, the action of rotation of the system is directly exciting the corresponding mode of vibration resulting in resonance. Note that the whirl natural frequencies are not equal to the bending natural frequencies of the stationary shaft although the corresponding mode shapes are effectively the same.

The bending modes appear in pairs, the mode with decreasing natural frequency is the backwards whirl condition (anti-synchronous whirl condition), and the mode with increasing frequency has the same mode shape but reversed as it travels with forwards whirl (synchronous whirl condition). When the structure undergoes forward whirl or

backward whirl, the natural frequency changes with the speed of rotation of the structure. The forwards whirl modes increase in natural frequency as the speed of rotation is increased due to the gyroscopic effect adding negative kinetic energy to the system. This effectively increases the stiffness of the rotor, an effect known as the gyroscopic stiffening effect. Conversely, the backward whirl modes decrease in frequency as the speed of rotation is increased. In this case the gyroscopic effect adds positive kinetic energy to the system resulting in the gyroscopic softening effect (51). For some components, the natural frequency in the forward whirl condition is strongly influenced by an additional factor known as the stress stiffening effect. The blades of a fan experience an effectively increased stiffness when subjected to centrifugal forces when rotating at high speed. These forces act to resist the bending, tilting or twist occurring during vibration. For components geometries with no large, relatively flexible radial extrusions such as the shaft and the rotor core, the stress stiffening effect makes little difference to the modal natural frequencies of the system.

The direction of rotation of the component in backwards whirl is opposite to the direction of rotation of the component. Thus, the centrifugal forces are reversed and act inwards towards the axis of rotation. The drop in natural frequencies is further increased when spin-softening effects are included (52). Figure 2.10 shows the additive and subtractive nature of spin softening and stress stiffening on the natural frequencies of lateral whirling modes of a rotor.

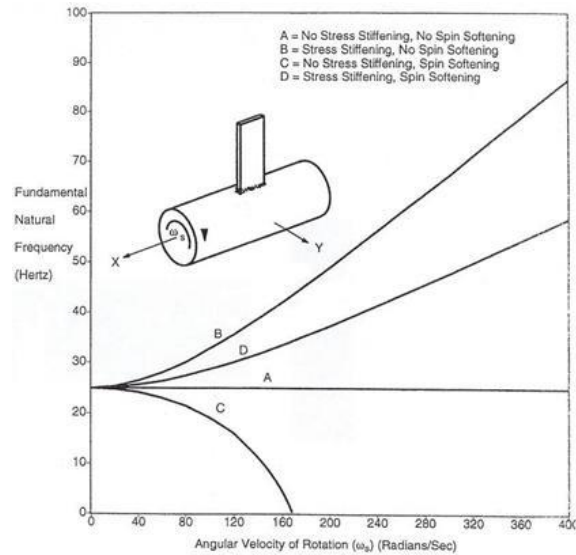


Figure 2.10: Effects of stress stiffening and spin softening (53)

Rao (52) modelled a twin spool rotor with 3D elements to demonstrate the gyroscopic, stress stiffening and spin softening effects. Rao also discusses the advantages of a solid 3D model over traditional beam models in accounting for these effects on a rotor, in particular, the ability of the solid model to take into account the true geometry of rotor components thus automatically accounting for the stress stiffening and spin softening effects.

Torsional and axial modes are unaffected by gyroscopic effects and appear as horizontal lines on a Campbell diagram. The primary focus of rotor design from a rotor-dynamics perspective is to avoid designing a rotor which has a critical speed close to the operating speed of the machine.

2.2.3 Cylindrical and conical mode shapes

The mode shapes of a rotor shaft are greatly influenced by the stiffness of the supporting bearings. A rotor supported by relatively ‘soft’ or low stiffness bearings experiences little bending during rotation, instead displacing entirely in a rigid shape away from the axis of rotation. Such rotors are known as rigid rotors and their first modes are near identical to those of an unsupported rotor. As the rotor is rotating it follows a circular path which traces out the shape of a cylinder, cylindrical modes are not affected by gyroscopic effects (54). If the bearing stiffness is increased to the point that the rotor is almost fully constrained from moving in the radial direction at the bearings then it is considered to be a flexible rotor. This is due to the lateral modes only taking bending shapes (free-body motion modes are now ~ 0 Hz). Due to these constraints, rotation of the shaft takes up a conical shape near the bearings (bending displacement is equal to 0 at the bearing and increases towards the rotor). The bending of the shaft causes the attached components to experience a rocking motion which gives rise to the gyroscopic forces that stiffen or soften the rotor at the component location. Mode shapes that contain conical rotating displacements are susceptible to gyroscopic effects.

2.2.4 Torsional vibration of rotors

The generator rotors of interest in this study operate at speeds much lower than their first critical speed and so, given the rotor is balanced to a satisfactory degree during manufacture, excitation of transverse modes due to whirling is not normally encountered under typical operating conditions. Electrical faults, manufacturing faults and assembly faults such as excessive unbalanced mass due to poor machining, loose

or ill-fitting rotor components, bad shaft alignment with coupled drive shafts and damage (loss of material) are some of the potential causes of shaft whirling when it does occur in an otherwise correctly engineered design. The theory of whirling and resulting transverse vibrations is still a vital consideration when attempting to create an accurate dynamic model of a rotor for validation purposes despite if the real machine is set up and operated with no fault occurrences.

Also of significant concern, though sometimes overlooked due to its imperceptible nature, is torsional vibration. Both the engine and the grid supply can induce torsional vibrations in the generator not only under obvious fault conditions but also throughout the normal steady state operating range of the generator set system. Any internal combustion engine will always produce some level of torsional vibration due to the staggered input of force from each cylinder expansion stroke. This torsional vibration is largely reduced by flywheels and torque pulsation dampers attached to the free end of the crankshaft and coupled with the shaft between the generator and the engine. As the generator is coupled to the diesel engine, there is also always some level of vibration occurring within the generator at any point during steady operation at any fixed rotational speed. The rotor can be designed to keep such inertia forces within safe limits, for example the design can be altered to shift its torsional natural frequencies away from anticipated torsional vibration frequencies from the piston strokes. What cannot be easily predicted are transient shock torsional loads that may arise due to line faults (such as a low voltage event). Such torsional loads may be several orders of magnitude larger than the steady state operating electromagnetic torque of the generator.

As previously shown in Figure 2.5, the electromagnetic torque fluctuates and decreases as the line voltage suddenly drops to 0 V in a pattern of lightly damped free vibration. Although only existing for a few milliseconds, each cycle of this torsional vibration can easily reach peak torques greater than the fatigue limit of the shaft steel. In extreme cases, failure of the shaft, keyways or even the stator to housing mounts could occur over a single fault event, typically at the point the voltage is restored, and the rotor is reconnected out of phase with the supply resulting in de-synchronisation.

2.2.5 Free vibration

The simplest vibrating system that may be considered is that of an un-damped, single degree of freedom oscillator. Such a system is constrained to a single degree of freedom (SDOF) so that the mass may only move in a single direction, once the system is disturbed by an applied force from its equilibrium position it can vibrate freely and return to its equilibrium position without the intervention of external forces.

For a linear free torsional SDOF system, the general equation of motion (derived from Newton's laws of motion) is:

$$I\ddot{\theta} + k_T\theta = 0 \quad (2.6)$$

The force exerted by the mass ($I\ddot{\theta}$) on the spring is equal and opposite to the force ($k_T\theta$) applied by the spring on the mass where;

θ = Angular displacement (rad)

$\ddot{\theta}$ = Angular acceleration (rad.s⁻²)

I = Mass moment of inertia about the axis of rotation (kg.m²)

k_T = torsional stiffness (N.m.rad⁻¹)

$$k_T = \frac{GJ}{l} = \frac{T}{\theta} \quad (2.7)$$

Where;

G = Shear modulus (Pa)

l = Length of uniform shaft (m)

J = Second moment of area about the axis of rotation (m⁴)

T = torque applied in twisting the shaft (N.m)

θ = angular displacement of the shaft (rad)

Equation 2.7 is used in section 5.1.2 to calculate the torsional stiffness of the generator rotor and later in section 7.1 to calculate the diameter of the equivalent shaft sections in the 3DFE models of the motor and diesel engines.

For a solid cylinder J is calculated as;

$$J = \frac{\pi D^4}{32} \quad (2.8)$$

D = Diameter of cylinder

The equation of motion for a single degree of freedom torsional model is;

$$I\ddot{\theta} + C\dot{\theta} + k_T\theta = T \quad (2.9)$$

Where,

T = Torque (N.m)

C = Damping factor

In its simplest form without damping and with no external applied torque the equation reduces to:

$$I\ddot{\theta} + k_T\theta = 0 \quad (2.10)$$

The general solution is obtained:

$$\theta = C_1 \sin \omega t \cdot \sqrt{\frac{k_T}{I}} + C_2 \cos \omega t \cdot \sqrt{\frac{k_T}{I}} \quad (2.11)$$

Applying initial conditions of $t = 0$, $\theta = \theta_0$ and $\dot{\theta} = 0$ produces the solution;

$$\theta = \theta_0 \cos \omega t \cdot \sqrt{\frac{k_T}{I}} \quad (2.12)$$

The reciprocal of the time period is equal to the torsional natural frequency of the system:

$$f_n = \frac{1}{2} \pi \cdot \sqrt{\frac{k_T}{I}} \quad (2.13)$$

Equation 2.13 is used in section 7.1.1 and 7.1.3 to obtain the natural frequencies of the 1D torsional models of the motor and diesel engine driven generator sets. The natural frequencies are compared with those obtained from the 3DFE equivalent shaft models to further validate the 3D models. The use of the equation is shown directly in appendix B and C.

2.2.6 Multi-inertia model and forced vibration

For determining the response of real structures with multiple inertias and shaft sections, it is possible to develop an analytical model which splits the structure into a series of nodes and interconnecting elastic elements.

In a multi-inertia system, the equations of motion must take into account the effect of displacement of neighbouring inertias on one another and therefore the torque acting in the interconnecting beam sections at any moment in time. The equations of motion for a multi-inertia torsional model such as that represented in Figure 2.11 (55) is as follows:

$$J_1 \ddot{\theta}_1 + C_1(\dot{\theta}_1 - \dot{\theta}_2) + k_{T1}(\theta_1 - \theta_2) = T_0 = \sin \omega t \quad (2.14)$$

$$J_2 \ddot{\theta}_2 + C_2(\dot{\theta}_2 - \dot{\theta}_3) - C_1(\dot{\theta}_1 - \dot{\theta}_2) + k_{T2}(\theta_2 - \theta_3) - k_{T1}(\theta_1 - \theta_2) = 0 \quad (2.15)$$

$$J_3 \ddot{\theta}_3 + C_3(\dot{\theta}_3 - \dot{\theta}_4) - C_2(\dot{\theta}_2 - \dot{\theta}_3) + k_{T3}(\theta_3 - \theta_4) - k_{T2}(\theta_2 - \theta_3) = 0 \quad (2.16)$$

$$J_4 \ddot{\theta}_4 + C_4(\dot{\theta}_4 - \dot{\theta}_5) - C_3(\dot{\theta}_3 - \dot{\theta}_4) + k_{T4}(\theta_4 - \theta_5) - k_{T3}(\theta_3 - \theta_4) = 0 \quad (2.17)$$

$$J_5 \ddot{\theta}_5 - C_4(\dot{\theta}_4 - \dot{\theta}_5) - k_{T4}(\theta_4 - \theta_5) = 0 \quad (2.18)$$

Where:

J = Torsional mass moment of inertia (kg.m^2)

The equations of motion shown in Equation 2.15 to Equation 2.18 are expanded upon and used in section 7.1.1 and 7.1.3 to obtain the natural frequencies of the 1D torsional models of the motor and diesel engine driven generator sets. The equation of motion is used to determine the position and value of the elements within the torsional stiffness matrix $[\mathbf{K}]$.

The applied torque provides the forcing function in this case, a sinusoidal torque $T_0 \sin \omega t$ is applied at the end inertia of the torsional model.

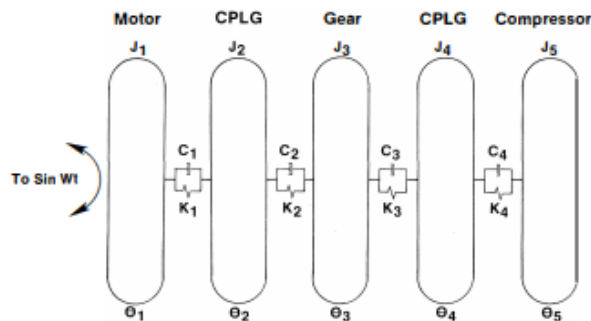


Figure 2.11: Multi-mass torsional model (55)

2.2.7 Modal analysis and testing of rotors

The frequency response functions (FRF) obtained from a modal test may be compared with those from the modal analysis of the model as demonstrated in such examples by (11) and (5). Following the comparison of FRF, particularly in the case of 3D solid FE models, there is usually some difference determined between the two. Given that the modal testing was completed correctly (enough measurement points taken, minimal influence of supports or attached measurement equipment etc.), the FRFs obtained represent the real rotor and can be used as the target that the modal analysis FRFs are compared against.

2.2.8 Model updating

Modal analysis results almost always differ from the modal test results by some degree. For a model of a simple static rotor such as a uniform beam with axisymmetric cylindrical masses attached, the margin of error is typically very small (< 1 Hz). More complex rotor geometries often have large errors ranging from tens to hundreds of Hz with an ever-increasing difference between test and analysis results for each mode. Higher frequency modes are more difficult to match. The rotor designer is normally only ever interested in the first few lateral bending modes and the first torsional mode and high frequency harmonics are rarely of any interest for practical analysis. This is true of the generator rotor analysed in this project as, due to its relatively high stiffness, the machine operates at rotational speeds well below the first bending mode natural frequency of the full rotor structure.

It is important to remember that the machine may also be subjected to transient or harmonic loads at higher frequencies which may be capable of exciting higher order rotor modes. All possible loading conditions including those caused by faults should be considered to determine whether the dynamic properties of the model are accurate enough for second, third and so on orders of modes. If for example the designer was certain the rotor would never experience any loading condition other than normal operating loads, then provided that the modes of interest are validated by modal test results the model is acceptable, even if higher order modes differ significantly.

When the modes of interest are significantly different from the modal test FRFs, the likely causes can be narrowed down to the material properties (Poisson's ratio, Young's modulus, density, shear modulus) model geometry and the boundary conditions for the rotor (bearing stiffness, damping). These parameters control the inertia, stiffness, and damping present in the model. The material properties often vary between the stated and real values, particularly density which can vary between identical components due to differences in the internal structure of the material. The imperfect distribution of mass throughout any material (pockets of higher or lower than average density material) also adds to the unbalance effect inherent in all rotors. The designer cannot account for what exactly the change in unbalance force will be for a rotor chosen at random and can only consider an error factor to be added to the final dynamic results.

Non-isotropic materials have different stiffness properties when loaded in different directions, as a result the natural frequencies are also direction sensitive. For example, an orthotropic material may have the same Young's modulus and shear modulus in the axial direction as an equivalent isotropic material leading to no change in modal results

for a mode with a corresponding shape deforming in the z direction only (such as an axial mode). But if the material has different stiffness properties in the x and y direction then the other modes which deform in these directions will have very different dynamic properties.

The model geometry can be created to perfectly match the true geometry of the rotor, but there are still some assumptions being made when doing so. The rotor being used for validating modal testing is manufactured within specific tolerances, it is unlikely that any 3D solid model will match up exactly to the real dimensions of any rotor in practise although the error will only be very small and have a minimal impact on the dynamic properties of the model. Edge rounds and chamfers should be used wherever possible to avoid miscalculation of material stress in the model for later transient analyses, the real rotor is manufactured with these features at most edges and can be modelled directly from technical drawings. Areas of high stress concentrations such as in the rotor core to shaft keyways and key must not have abrupt changes in the orientation of neighbouring face elements and so edge rounds and finer meshing are recommended.

Another point of interest to consider before moving on is the interface conditions between the shaft of the rotor and the attached rotor components. The rotor components of generators of this size are attached to the shaft with a press fit (rotor core and exciter core) using a hydraulic press or by heat shrinking (fan hub). The interference between the surfaces acts as a pre-load holding the component onto the shaft, the magnitude of pre-load should be great enough to withstand normal operating torque and over torque associated with fault events. As long as the holding torque is not exceeded and

component does not slip on the shaft, the interference fit can be considered as a perfectly bonded contact between two surfaces and has no impact on the natural frequencies of the structure. That is to say that there is no reduced stiffness across the contact area.

This behaviour assumes that a relatively large interference exists, which in the case of this rotor is true; as a general rule the interference of a press fit should be around 0.001" per inch of shaft diameter as a minimum (56). Existing experimental work by Marscher et al (57) on interference fits concludes that for even the lightest degree of interference press fit set out in API 684 specifications between a component and a shaft results in the assembly acting as if the component is integral to the shaft (perfectly bonded). Indeed, API 684 suggests that component sleeves generally do not alter the lateral stiffness of the shaft, however the torsional stiffness of the shaft may be affected by the level of interference and the length of shaft that the component covers. After testing a set of different sized sleeves with different levels of interference, the research found that the degree of interference fit has no measurable effect on the torsional natural frequencies of the system (57) although the torsional stiffness does increase slightly as the interference is increased. Similarly, the lateral natural frequency is unaffected by the degree of interference fit once slip is prevented.

This paper considers that the surface finish of the interference surfaces may have some impact on the stiffness and for very light interference fits, this may impact the natural frequency. Chen (12) obtained the natural frequencies of a hollow rotor and sleeve assembly through modal testing and modal analysis using different interference depths and contact surface friction coefficients. With a very small interference (less than the generally accepted 0.001" per 1" shaft diameter) the lateral natural frequencies are

reduced significantly for surfaces with a greatly reduced friction coefficient. It should be noted that including non-linear contact element analysis in a modal analysis (using interference) greatly increases the computational resources and time required to solve the problem. Defining the contact behaviour correctly requires some model correction against modal results obtained from experimental testing in any case, on the scale of a fully detailed geometry 3D solid model the inclusion of this behaviour cannot be justified.

There are also a range of assumptions that are made in the finite element calculations that, without adjustment, can lead to wildly inaccurate and inexplicable modal results. In order to correct the dynamic properties of a rotor model, the analyst must alter some of the model parameters in a process commonly known as model updating. In its simplest form, and depending on whether the analyst needs a complete set of accurate dynamic properties, a model can be updated by directly modifying one or more parameters such as the mass of a component until the natural frequency of a particular mode matches that obtained from modal experimental test results. A range of different mathematical model updating techniques exist, one such technique utilises a frequency criterion or a modal assurance criterion (MAC) to compare the mode shape results from analytical modal analysis with the experimental modal test results. For example, Kloutsey et al (58) uses an iterative updating method to update a model of a 6-pole synchronous rotor in a turbine generator unit which originally calculates the FRFs of the structure with estimated stand-in values for mass and moment of inertia.

2.3 Dynamic modelling of rotors

2.3.1 Finite element approach

The most popular methods of dynamic analysis are based on finite element (FE) calculations. Finite element analysis (FEA) utilises two dimensional or three dimensions models that are divided into smaller elements to form a network of nodes at which time dependant displacement and force results are calculated and combined in large scale matrix calculations such as the forced response calculation. The technique is particularly useful for analysing complex geometries with multiple components and connection interfaces and is capable of reproducing realistic displacement and stress response in the model for complex loading conditions. FEA can be used to predict the behaviour of a design and identify where improvements need to be made to achieve an optimal design solution (59).

It is important to consider the fact that real rotors (especially when all rotor components are accounted for) are usually not axisymmetric, owing to geometric features on the shaft such as keyways and bladed extrusions on the fan, the finite element calculation contains asymmetric elements (dissimilar moments of area, unsymmetrical stiffness). Prior to the modern development of FEA, the only models that could be developed for dynamic analysis of asymmetric rotors were one-dimensional beam models based on the theory around the Jeffcott rotor (single inertia disks centralised on a shafts) (3). One-dimensional models suffer from a number of disadvantages when compared to the higher order models that can be calculated using modern FEA techniques, resulting from the fact that real rotors are not one-dimensional. Discretising a real rotor into a one-dimensional model is also a complex process which only becomes more

challenging for assemblies of sub-components such as rotor core of a generator. The effect of stiffening for mounted components must be accounted for using equivalent stiffness elements and centrifugal effects for sub-component assemblies is not account for (3).

In recent years 3D solid models have become more popular with the availability of continuously developed finite element software such as ANSYS and vastly increased computing resources. 3D solid models of asymmetric rotors overcome the disadvantages of 1-D beam models with the main drawback of increased calculation time. Gyroscopic effects and centrifugal effects of spin softening and stress stiffening are included in the FE calculations within ANSYS for 3D solid geometries (3). These effects can significantly impact the transverse mode natural frequencies and whirl behaviour of rotors during rotation and must be included in all dynamic analyses if the analyses is to accurately represent the real machine.

For a 3D solid model constructed in ANSYS, directional stiffness and damping can be defined at the points of bearing location with a 3-D spring-damper element known as 'COMBIN14' as shown in Figure 2.12. For example, Ma et al. (4) utilises COMBIN14 elements to represent the bearing connection between rotor and housing of an industrial turbo engine.

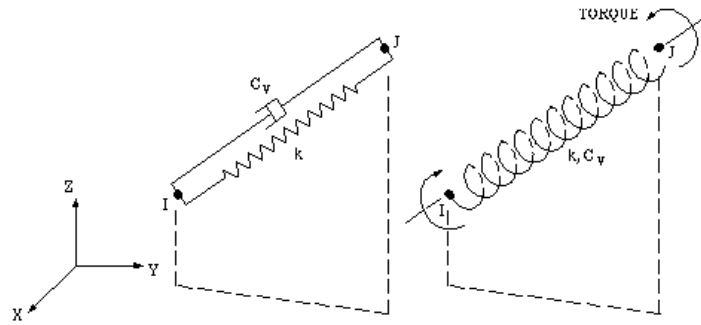


Figure 2.12: Combin14 spring-damper (60)

ANSYS also contains a pre-built 2-D bearing element, COMBI214 (Figure 2.13) for modelling bearings in rotor-dynamic analyses.

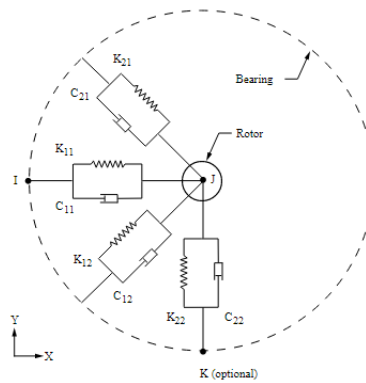


Figure 2.13: COMBI214 2-D spring-damper bearing (61)

This element only applies bearing stiffness and damping properties in the xy plane (perpendicular to the axis of rotation, z). Much of the current research in the field of rotor dynamics is focused on simplifying large order rotor dynamic models by developing model reduction techniques, the primary objective being to improve model efficiency and reduce calculation times. This is of particular interest in modelling turbines due to the excessively large number of degrees of freedom associated with the numerous complex blade geometries. As discussed in the literature review by Wagner

et al. (48), the current model reduction techniques are typically case specific and lack evidence of suitability in practical applications beyond the model they were developed for (which is often a very simple case such as a Jeffcott rotor).

2.3.2 Finite elements

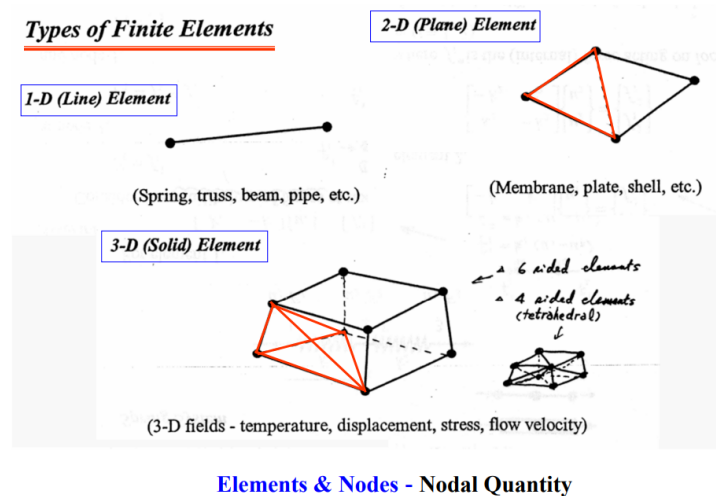


Figure 2.14: Types of finite elements (59)

The line elements used in FEA of rotors and shafts represent the length of shaft between components (such as the rotor core) that are located at the node points. One-dimensional line elements can be used to construct a simple torsional or lateral model of a rotor with the inertia of each component represented at the nodes and the interconnecting lines representing the lateral or torsional stiffness between the components.

Two-dimensional plane elements contain multiple line elements and three-dimensional solid elements contain multiple plane elements. A single solid element contains a greater number of nodal degrees of freedom and thus requires additional rows/columns

within the stiffness and displacement matrices as add additional calculations are required for each node. The three different element dimensions are shown in Figure 2.14.

2.3.3 Stiffness matrix

The element stiffness matrix is composed of all the nodal stiffness elements combined. For calculations of torsional deflection.

$$T = k_T \cdot \theta \quad (2.19)$$

For a single element, the resulting torque due to displacement in one direction;

$$T_1 = k_T(\theta_1 - \theta_2) \quad (2.20)$$

$$T_2 = k_T(\theta_2 - \theta_1) \quad (2.21)$$

$$\begin{bmatrix} T_1 \\ T_2 \end{bmatrix} = \begin{bmatrix} k_T & -k_T \\ -k_T & k_T \end{bmatrix} \begin{Bmatrix} \theta_1 \\ \theta_2 \end{Bmatrix} \quad (2.22)$$

The torsional element stiffness matrix for a single element is;

$$k_{Te} = \begin{bmatrix} k_T & -k_T \\ -k_T & k_T \end{bmatrix} \quad (2.23)$$

Equation 2.22 is used in section 7.1.1 and 7.1.3 to obtain the natural frequencies of the 1D torsional models of the motor and diesel engine driven generator sets. The torsional element stiffness matrix is used construct torsional stiffness matrix $[\mathbf{K}]$.

2.3.4 1D Finite element calculation for torsional modal analysis (un-damped)

The stiffness matrix is also utilised in the finite element calculation of both torsional and lateral modal frequencies and shapes. For an analysis of the torsional modes, the

multi-inertia model shown in Figure 2.15 below is to illustrate the use of element stiffness and inertia matrices in torsional modal analysis.

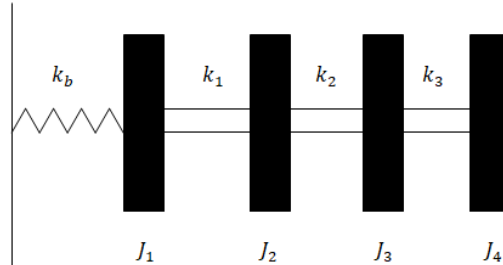


Figure 2.15: Rotor with four masses attached to a shaft.

The general equation of motion for a torsional response in matrix form (undamped) is as follows (62):

$$[\mathbf{M}]\{\ddot{\theta}\} + [\mathbf{K}]\{\theta\} = 0 \quad (2.24)$$

Where,

$[\mathbf{M}]$ = Global mass matrix

$[\mathbf{K}]$ = Global stiffness matrix

$$\{\theta\} = \{\boldsymbol{\theta}\}e^{i\omega t} \quad (2.25)$$

Where,

$\{\boldsymbol{\theta}\}$ = Amplitude of $\{\theta\}$

ω^2 = natural frequency

The natural frequencies and mode shapes (derived from the displacement vector) are found by solving the eigenvalue equation obtained by substituting (2.25) into (2.24)

$$([\mathbf{K}] - \omega^2[\mathbf{M}])\{\boldsymbol{\theta}\} = 0 \quad (2.26)$$

In the case of a torsional system, the mass matrix is assembled using the inertia of nodal components J about the rotating axis. In matrix form the global mass matrix becomes:

$$[\mathbf{J}] = \begin{bmatrix} J_1 & 0 & 0 & 0 \\ 0 & J_2 & 0 & 0 \\ 0 & 0 & J_3 & 0 \\ 0 & 0 & 0 & J_4 \end{bmatrix} \quad (2.27)$$

The torsional stiffness element matrix for Figure 2.15 is:

$$[\mathbf{K}] = \begin{bmatrix} k_{tb} + k_{t1} & -k_{t1} & 0 & 0 \\ -k_{t1} & k_{t1} + k_{t2} & -k_{t2} & 0 \\ 0 & -k_{t2} & k_{t2} + k_{t3} & -k_{t3} \\ 0 & 0 & -k_{t3} & k_{t3} \end{bmatrix} \quad (2.28)$$

The angular displacement matrix for Figure 2.15 is:

$$\{\boldsymbol{\theta}\} = \begin{Bmatrix} \theta_1 \\ \theta_2 \\ \theta_3 \\ \theta_4 \end{Bmatrix} \quad (2.29)$$

The mass and stiffness matrix are combined in the characteristic equation of the dynamic system (2.26):

$$\begin{bmatrix} k_{tb} + k_{t1} - J_1\omega^2 & -k_{t1} & 0 & 0 \\ -k_{t1} & k_{t1} + k_{t2} - J_2\omega^2 & -k_{t2} & 0 \\ 0 & -k_{t2} & k_{t2} + k_{t3} - J_3\omega^2 & -k_{t3} \\ 0 & 0 & -k_{t3} & k_{t3} - J_4\omega^2 \end{bmatrix} \begin{Bmatrix} \theta_1 \\ \theta_2 \\ \theta_3 \\ \theta_4 \end{Bmatrix} = 0 \quad (2.30)$$

Determinants are calculated and the resulting equations expanded and solved to find the eigenvalues and the eigenvectors, the natural frequencies and mode shapes respectively. The 1D finite element approach is a fast and accurate method of determining the modal characteristics of simple geometries, and to some extent, the more complex non-uniform geometries of real rotors. Equation 2.29 is used in section 7.1.1 and 7.1.3 to obtain the natural frequencies of the 1D torsional models of the motor and diesel engine driven generator sets. The Matlab scripts in Appendix B and C are formed from this equation.

With high detail 1D models it is possible to include the influence that the inertias have on shaft stiffness, even non-solid components such as laminated rotors may be accounted for using branched models such as those described in (7). The stiffness of non-uniform, stepped shafts can also be accounted by calculating the equivalent shaft section stiffness although non-axisymmetric features such as keyways are typically ignored.

2.4 Rotor structural characteristics and modelling challenges

The approach used to create the finite element model of the generator rotor is based on minimising any geometry simplifications and maintaining as much of the original geometry detail as possible in order to both accurately model the true mass distribution across each component and to allow for the following study of the resulting stresses across the rotor structure directly from the rotordynamic model. Additional details that contribute little to the overall dynamic behaviour of the rotor such as the plastic/ceramic winding supports or wiring from the exciter do not have to be included in the geometry and can instead be combined into the masses of the surrounding major components through adjustments to their material density. The 3D geometry of all the generator rotor components is shown below in Figure 2.16.



Figure 2.16: Generator rotor components.

The disadvantage of this approach is that of increased element density and additional complexity in the arrangement of elements (particularly where the geometry is asymmetric) which somewhat obscures the finite element calculations, making it difficult to trace the source of errors in the dynamic results. The 3D FE model relies on a generated mesh as opposed to specified points with mass and inertia and interconnecting spring and beam elements. Care and attention must be made when considering contacts where two meshes meet, incorrect assignment of contact

properties (particularly on rounded surfaces and where small gaps exist) can lead to wildly incorrect analysis results.

In the first analytical model, the masses of each component and their mass moment of inertia about the z-axis are known and obtained from the torsional drawing of the rotor. Bearing masses are also known as they are obtained from manufacturer specifications. The material densities for each of the components is then adjusted in order to match the mass of their real counterparts. This method is utilised to adjust the masses and inertias of the laminated core and exciter and also the windings that attach to them. Only the mass and inertia of the fully assembled components are known, however, the exciter and the main core contain subcomponents such as windings and support bars which are composed of different materials. The total mass of each component must be correctly divided between its subcomponents in order to match the inertia of the component to its real value.

2.4.1 Main rotor core

The main rotor core is composed of a stack of electrical steel sheets known as laminations, each sheet is separated by a thin layer of insulating resin which bonds the sheets together and has the ultimate effect of preventing electromagnetic eddy currents (63) that add to the rotor losses and result in rotor heating. The windings are composed of a number of individual copper strands which are coated in epoxy resin to provide stiffness and support to the bundle and to insulate the individual strands from one another. The weight of the copper used in the exciter is known and the coating thickness of epoxy around each strand is also known alongside the diameter of individual copper

strands. This knowledge, combined with measurements of the thickness and height of the winding bundles, it is possible to calculate the volume fractions of epoxy and copper within the windings and therefore the mass of the epoxy to be added to the copper mass to obtain the total mass of the windings.

With the mass of the windings calculated, the density of the material can be adjusted appropriately so that the mass of the modelled windings is also correct. The geometry of the windings will vary slightly between machines and the geometry used in the model is not identical to the real windings due to resin not sitting flush with the copper strands at the surface of the windings. A simplification to the winding geometry has been made here to greatly reduce the mesh cell count at minimal cost to the accuracy of the following analyses, the windings are simply represented as blocks. The density applied to the model of the windings should be close to the calculated density for the real windings but matching the mass of the structure correctly is most important and takes priority. Any difference in density indicates error in the geometry of the modelled windings which will manifest as a small error in the mass moments of inertia for the core as a whole. The structure of the windings match the classical description of a composite material, with strands or fibres of one material surrounded by a matrix material, epoxy resin in this case. The rule of mixtures can be applied to calculate the directional stiffness properties of the material.

The main rotor core also includes two other major subcomponents, the damper cage (with damper laminations) and the support bars. These components are composed of aluminium alloy and mild steel respectively. The known material properties for these subcomponents can be input directly, since they are modelled using true dimensions

from engineering drawings, their mass is known to be correct. The mass of the windings, support bars and damper cage are subtracted from the total mass of the main core to obtain the mass of the lamination stack and therefore the density of the lamination and insulation composite material. The mass of the remaining materials attached to the rotor core (wires from the exciter, plastic/ceramic winding supports overspill of resins etc.) is negligible and is ultimately combined with the lamination stack mass.

2.4.2 Exciter

The exciter is constructed in a similar manner to the main core, a stack of laminations forms the exciter core which is insulated with the same materials used in the main core. The exciter also has windings attached to the core that are positioned around the circumference of the exciter core, but the exciter core has several slots in which the windings sit, similar to the stators in the machine. The exciter windings are composed of smaller gauge copper wires which are supported with epoxy resin which also bonds the windings to the inside of the core slots. The end windings are somewhat more challenging to model as the copper wires coming out from the slots separate away from their bundles and are only held together by small quantities of resin, if any at all.

Modelling the exciter windings as they appear on the rotor is not a realistic option (since it would require modelling of individual wires) and so the windings are again modelled as simple blocks with the outer dimensions of the windings measured from the machine as closely as possible. Since the presence of these windings does impart some additional stiffness to the exciter core (empty slots are more flexible) it is still important to ensure

the stiffness properties of the composite are as accurate as possible. The end windings are again not modelled here.

2.4.3 Shaft and shaft features

The shaft carries all of the rotor components and couples to the prime mover to provide mechanical torque to the generator. The shaft contains keyways cut into its surface under the main core, exciter core and at the drive end. A key is positioned in each keyway to support the connected component under torsional loading. Note that the shaft geometry is stepped, the diameter of the shaft varies across its length. The diameter and length of the shaft greatly influences the torsional stiffness of the generator rotor, thus the dimensions of the model must be carefully checked against the general assembly drawings. Bearings are pressed onto the shaft at the non-drive end and drive end on which the entire rotor is supported.

2.4.4 Fan

The fan is composed of a number of thin aluminium blades which direct air flow through the air gap between the rotor core and the stator core when the structure rotates. The fan is the most challenging component to model given the complexity of the blade geometry.

2.4.5 Material properties of laminated cores

A model with correct masses and inertias is not enough to fully describe the rotor dynamic properties of the rotor. The elastic properties (Young's modulus, E , shear modulus, G and Poisson's ratio, ν) of the materials involved must also be correct as this determines the stiffness behaviour through all interconnected elements of the mesh. The natural frequencies of each group of modes; axial, transverse and torsional, is determined primarily by a corresponding stiffness that is most influential in the direction of displacement for a particular mode shape. For example, the torsional frequencies of the rotor are determined by its torsional stiffness. Axial, torsional and transverse stiffness are in turn is determined by the elastic properties of the materials involved and are therefore sensitive to any changes to E , G and ν .

As for all mode shapes, the section of a structure with the lowest relative stiffness determines the natural frequencies of the entire system. The torsional stiffness of the shaft between each rotor disk determines the resulting calculated eigenvalues. The stiffness contribution from the inertia disks is ignored and not included in the stiffness matrix as these disks have a relatively high torsional stiffness. The torsional stiffness k_t (Nm^2/rad) is calculated as per Equation 2.7.

The stiffness contributions of the rotor components on the real rotor cannot be ignored, this is particularly true for the main core. The core covers a large portion of the length of the shaft and, as it is tightly pressed on to the shaft, it adds to the stiffness of the shaft. (7) Indeed the laminated core contributes significantly less stiffness to the assembly in the axial direction (determined by E_{zz}) and in the yz and xz directions

(determined by G_{yz} , G_{xz}) than a solid core. Assuming the rotor core to be a solid single steel forging would therefore result in a rotor modal that is significantly stiffer than the real rotor is, the modal solutions for such a modal are incorrect, most noticeable is the significantly higher natural frequencies.

Not only the modes of the shaft are of interest in analysing the rotor response to fast transient load conditions, but the modes of the components themselves must also be understood. Whilst resonance of the exciter core for example may impart relatively small deflections on the shaft or other rotor components compared to resonance of a transverse mode of the shaft, such a situation presents a source of potential fatigue damage to both itself and the section of shaft to which it connects. The presence of masses near the radial extremes of the cores in the form of the aforementioned subcomponents also adds to the situation.

The laminated cores are difficult to model directly as a 3D object with several layers of different materials and their interconnecting boundaries. Whilst this is possible, modal analysis results on such as structure would yield inaccurate results unless detailed pre-stress conditions were prescribed and backed up with experimental results on a stack of laminations, the analysis resource requirements are greatly increased in any case. A more direction solution is to use solid, single piece geometries and assign them a material with equivalent non-isotropic elastic properties for E_z , G_{xz} and G_{yz} .

2.4.6 Electromagnetic finite element modelling

Various software packages exist that can simulate the induction of electromagnetic currents and fields in electrical machines. One such package is ANSYS Maxwell, this software can simulate the electromagnetic behaviour of electrical machines using both 2D and 3D finite element models. The transient magnetic solver in the software computes the instantaneous magnetic fields in each element of the machine geometry at defined time steps. The 2D transient magnetic solver uses Equation 2.31 as defined in the ANSYS Maxwell help documentation (64) to calculate the time dependant magnetic and electrical fields.

$$\nabla \times v \nabla \times A = J_s - \sigma \frac{\partial A}{\partial t} - \sigma \nabla V + \nabla \times H_c \quad (2.31)$$

Where;

v = reluctivity (H^{-1})

A = Magnetic vector potential (Wb/m)

J_s = Current source density (A/m^2)

σ = Conductivity (S/m)

H_c = Coercivity of permanent magnet (A/m)

V = Electrical potential (V)

$\nabla \times$ = curl operator

ANSYS Maxwell models can be directly linked to the Simplorer software module that is built into it. Simplorer provides a block based graphical modelling interface that is similar to the more well-known Simulink software found within MATLAB. Simplorer can be used to build models of complex electro-mechanical systems such as diesel engine synchronous generators by coupling external solvers such as the 2D transient

magnetic solver in Maxwell to electrical circuits and mechanical components drawn in Simplorer.

Chapter 3 Generator modelling and dynamic validation

This chapter explores the creation and validation of a mechanical generator rotor model and the generator set models that it is a part of. This process begins with the generation of a three-dimensional finite element (3DFE) model of the generator rotor which includes all sub-components such as the rotor windings. The elastic properties of the rotor are then updated using a parametric based modal analysis technique to match the lateral and torsional modes of the model to experimental results gathered from a roving hammer impact test performed on the generator rotor.

In later sections, the torsional stiffness of the generator rotor is calculated and used in two different generator set models. The first generator set includes an electric motor that is utilised in the short circuit experiments detailed in Chapter 5. The second model sees the generator attached to a diesel engine with a flexible coupling. The 3D FE model is then used again for transient stress analysis of low voltage ride through faults in Chapters 8 and 9.

3.1 Construction of 3DFE rotor model

A detailed model of the UC22F generator rotor shown in Figure 3.1 is created using SpaceClaim, the editor is launched directly from within ANSYS workbench to eliminate the need to manually import from external saved models. An additional model of a UC22G rotor is created that is almost identical to the UC22F rotor aside from its extended core and shaft. Component dimensions and mass properties are obtained

directly from design and manufacturing drawings which were verified with manual measurements taken from the test rotors.

Table 3.1: Mass properties and dimensions of the UC22F and UC22G generator rotors

Properties	Rotor	
	G Core	F Core
Core Mass (kg)	79.08	64.47
Exciter Mass (kg)	8.49	8.49
Fan Mass (kg)	1.94	1.94
Shaft Mass (kg)	23.42	21.97
Core Inertia (kgm^2)	0.575	0.470
Exciter Inertia (kgm^2)	0.051	0.051
Fan Inertia (kgm^2)	0.023	0.023
Shaft Inertia (kgm^2)	0.014	0.013
Core Length (mm)	300	240
Shaft Length (mm)	828	783

The rotor assembly consists of the rotor shaft, fan, main core, exciter core, shaft keys and bearings. The main core supports a number of additional subcomponents, support bars, damper cage and windings, the exciter core also supports its own set of windings.

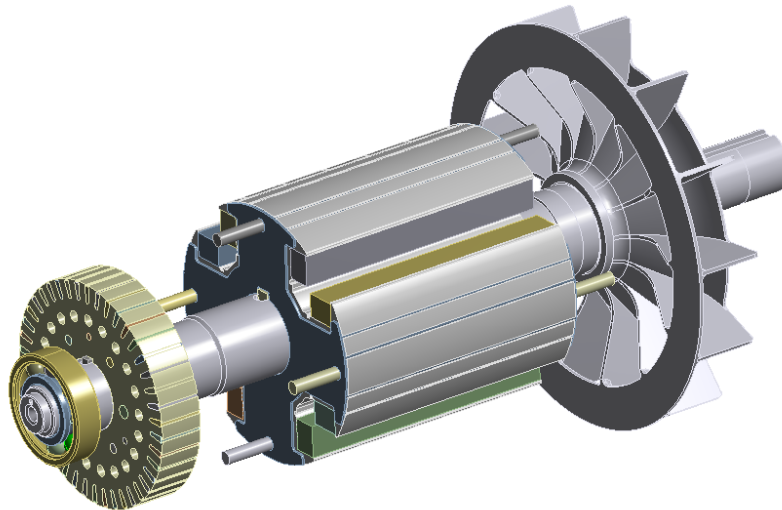


Figure 3.1: UC22F Rotor geometry, view from the non-drive end

The rotor shaft geometry includes three keyways cut into its surface, one across the length covered by the main core, another positioned under the exciter core and a coupling keyway at the drive end of the shaft. The exciter core and main core have corresponding keyways cut into their inside surfaces within which the keys are seated. Small, light components that add to the complexity of the model but have no significant impact on the modal frequencies of interest are not modelled. Such components include the wiring between the exciter rotor commutator and the main core and winding support sections. The mass and inertia of these components are still taken into account as they are added to that of nearby major rotor components. The UC22 rotor can also have a permanent magnet generator attached to the non-drive end of the shaft, this is not present during experimental testing and is therefore not included in the model. The stator and machine housing geometries are also not included in this model.

The main core and exciter core windings are modelled as solid blocks rather than groups of individual copper strands in order to reduce the cell count of the model mesh. The main core and exciter core are modelled as single solid pieces rather than being formed

from individual laminations. The elastic properties of these components are set to be orthotropic in nature during the modal analysis stage in order to take into account the differences in directional stiffness that a laminated structure possesses.

The aluminium fan which attaches to the shaft at the drive end is modelled in full detail. Equivalent lumped mass inertia and simplified geometries do not capture the true torsional response of the fan as discussed in the following modal analysis section

3.2 Modal analysis setup

The modal analysis solver in ANSYS workbench is selected to perform the following analyses. The rotor geometry is imported to the modal analysis module and the solver settings are adjusted in order to correctly calculate the modal frequencies and mode shapes of the 3DFE rotors. The main objective of performing modal analysis on the generator rotor is to obtain a set of modal frequencies and shapes for the model that match the experimentally obtained results. Since the UC22F rotor was to be used for short circuit testing in this project and was also required for several other ongoing projects in the lab, modal test results could only be obtained with the fan and exciter still attached to the shaft. A spare UC22G rotor was identified that had sustained light damage to its end laminations and was no longer fit for use. The fan, exciter and bearings were removed from this rotor so that modal results could be obtained for the shaft and core assembly only. The modes from the disassembled UC22G rotor are then used to determine the elastic properties of the laminated rotor core. The UC22F model is then updated with the validated elastic properties of the core and the final modal results for the fully assembled rotor are obtained.

3.2.1 Rotor mesh

The meshing process involves splitting the geometry of the generator rotor into individual cells to prepare for finite element analysis. The maximum size of the cells must be small enough to adequately capture the detail of the source geometry without unnecessarily increasing the memory resources and processing time required. For the purpose of modal analysis, the quality of the mesh does not significantly impact the results of the analysis provided that detailed geometry features are retained such as the fan blades. For transient analysis purposes the mesh density must be increased, particularly on small features, corner and edges such as around the keyways. The initial parametric modal analysis that is performed to determine the approximate elastic properties of the rotor core requires the completion of a large number of modal analyses before the selection of possible elastic combinations can be narrowed down for further analysis. Larger sized cells are defined on free component surfaces that are sufficiently far away from detailed features. The default mesh size is set to 10 mm max, which makes up the majority of the volume of the rotor core and shaft.

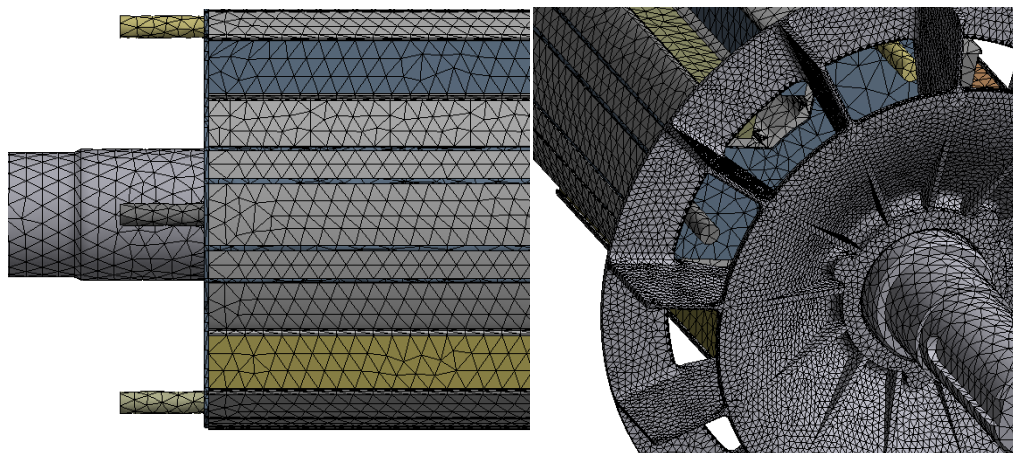


Figure 3.2: Initial meshing on the rotor core and fan of the UC22F rotor

The mesh for the fan has a maximum cell size of 4 mm in order to capture the detail of the fan blades. The damper cage and support bars use a maximum mesh size of 8 mm. All mesh elements use the tetrahedron shape setting. The selected mesh shown in Figure 3.2 is also used in the modal analysis.

Surface contact mesh matching is defined at the contact faces between connected components, for example between the inner fan face and the shaft. This ensures that the cells on each contact face are perfectly aligned with one another. This is important in order to maintain solver stability and correctly translate the relative displacement for each mode across the assembled components.

3.2.2 Boundary conditions

In the initial modal analysis, the rotor is freely supported. The bearings are still present in the model but are not fixed to any ground reference. The freely supported boundary condition is selected to eliminate the need to model the supports and negate their influence upon the modal results. This practise is commonly applied in the modal analysis of many different structures as it makes the validation and modal testing procedure easier to set up and more accurate by isolating the structure of interest from the influence of surrounding supporting structures that would add to the complexity of the analysis.

3.2.3 Contact settings

Various contact settings between components may be selected to represent a wide range of assembly conditions. These contact settings can greatly alter the results of a modal analysis and must be chosen carefully if the user intends to simulate complex contact behaviour. Interlocking and high friction surfaces along with high contact pressure and pre-stressed contacts can be used to increase the relative stiffness of the assembly but the contact stiffness will be lower than that of the material of the neighbouring components. Interference pressure has the greatest impact on contact stiffness and existing studies on shaft mounted, pressed components even a low contact pressure/interference between components can result in a reduction in modal frequencies. Beyond a certain pressing pressure/interference depth, increased contact pressure has little effect on the modal frequencies.

In the case of the generator rotor it is safe to determine that the contact pressure between the shaft mounted components and the shaft is great enough to provide near or maximum contact stiffness. Since the elastic properties of the laminated core are adjusted to match the modal results of the analytical model with the experimental rotor, any reduction in stiffness that could be attributed to the component contact stiffness will be covered by an additional reduction in elastic values (E_{zz} , G_{yz} , G_{zy} etc.).

The bonded multi point constraint (MPC) contact type is selected for all components in the modal analysis. This is a perfect bond contact, which is to say that the contacting surface elements do not move relative to one another. This greatly reduces simulation time when compare to frictional, pre-stressed interference contacts and removes any

additional uncertainty in the modal results that would otherwise be very difficult to solve via the intended parametric updating method.

3.2.4 Known elastic material properties

The material properties for all 'solid' (non-laminated or stranded) components are obtained from component datasheets. The shaft, support bars, shaft keys and bearings are all based on EN8 carbon steel with isotropic elasticity properties, a Young's modulus of 200 GPa and a shear modulus of 76.9 GPa at 20°C. The fan and damper cage are composed of aluminium alloy with isotropic elasticity properties of 71 GPa Young's modulus and 26.7 GPa shear modulus at 20°C. The elastic properties of the remaining components of the main core, exciter core and rotor windings is determined in the following sections.

3.2.5 Windings

The windings are composed of a number of solid copper strands contained within a resin matrix. The material properties for this stranded composite material can be simply calculated using the rule of mixtures. 82.16% of the winding volume is composed of copper and $E_{\text{copper}} = 1.3e^{11}$ Pa. 17.84% of the windings are composed of polyester-amide varnish, which insulates individual laminations. The calculated values for Young's modulus in the axial and transverse directions respectively are: $E_{zz} = 1.07e^{11}$ Pa and $E_{yy} = E_{xx} = 2.54e^{10}$ Pa. As the windings are wrapped around part of the salient poles of the core, they affect the stiffness of the core. The additional lateral and torsional stiffness that is contributed by the windings cannot be ignored when selecting the correct elastic

properties. The presence of the windings ultimately reduces the value of E_{zz} for the laminated core.

Note that the windings are perfectly bonded to the core in this case (MPC bonded contacts) which contributes additional stiffness to the structure. This will artificially increase the modal frequencies of the rotor slightly. In the physical rotor, the real windings are held in place under winding tension which results in a relatively low contact pressure against the core and so the surface and winding is not a true fixed constraint. Since a low stiffness contact will introduce additional modes to the analysis, full bonded contacts are used to reduce the total number of output modes thus reducing the simulation time. The directional stiffness properties of the rotor core are altered until the analytical modes match the experimental modes as described in the following section. As a result, the small error associated with using fully bonded contacts between the windings and the core will be corrected as the stiffness properties are reduced slightly to compensate for the difference in modal frequencies.

3.2.6 Updating material properties

As one would expect, all modes of a solid steel core model have a significantly higher resonance frequency than those obtained from a laminated structure. Without adding equivalent stiffness terms to the stiffness matrix for individual elements in the model, it is possible to alter the elastic properties of the components within a reasonable range to tune the frequencies of the modes in the model to match those obtained from the modal analysis.

Since the main rotor core and exciter core are composed of stacked laminations, the elastic behaviour of the core can be considered orthotropic in nature. The modal properties of such laminated components depend on a range of factors such as the stacking factor S_f , clamping pressure applied in stack assembly and the elastic properties of bonding/insulating “varnish” between laminations (applied for the rotors under consideration here). These factors ultimately determine the elastic properties of the laminated stack. Where z is the axial direction along which the laminations are stacked; E_{zz} , G_{yz} and G_{xz} are the primary elastic variables that differ from their solid isotropic equivalent.

The core stiffness is significantly lower in the axial direction z , along the axis of rotation of the rotor and in shear planes xy and yz . The elastic parameters E_{zz} , G_{yz} and G_{xz} are therefore lowered for the orthotropic material properties of the laminated core. Additionally, a small reduction occurs in the remaining directions which act out of the axial planes. G_{xy} , E_{xx} and E_{yy} are obtained by multiplying the isotropic value of E and G for the steel by the stacking factor S_f .

$$E_{xx} = E \cdot S_f \quad (3.1)$$

$$E_{yy} = E \cdot S_f \quad (3.2)$$

$$G_{xy} = G \cdot S_f \quad (3.3)$$

$$S_f = \frac{n_L \cdot t_L}{l} \quad (3.4)$$

Where;

n_L = number of laminations (steel sheets)

t_L = lamination thickness (m)

l = total physical length of rotor stack (m)

In this case, the stacking factor for the rotors of interest is equal to 0.95 ($n_L = 356$, $l = 0.3$, $t_L = 8e^{-4}$ m). The isotropic value for E is $2e^{11}$ Pa and G is $7.69e^{10}$ Pa so it follows; $E_{xx} = E_{yy} = 1.9e^{11}$ Pa and $G_{xy} = 7.31e^{10}$ Pa.

3.2.7 ANSYS parametric modal analysis

In this section the solver runs a modal analysis for the free-free supported generator rotor and the resulting mode shapes and modal frequencies are obtained. It is important to isolate the main core from the secondary rotor components to narrow down the selection of elastic properties in the following parametric analysis. To achieve this, a slightly larger UC22G core rotor was disassembled so that only the core and shaft remained. A modal test was performed on the rotor to validate a modal analysis which utilises a modified version of the UC22F rotor geometry and the same modal solver setup as outline for the UC22F rotor. The G core rotor is almost identical to UC22F model aside from having a slightly longer core at 300 mm and some shaft features are shifted up the shaft slightly to accommodate for this.

A parametric modal analysis is performed on the UC22G core rotor in which the selected modal parameters, E_{zz} , G_{yz} and G_{xz} are altered and the resonant frequencies are calculated for each parameter combination. A total of 753 different combinations are simulated, a portion of which are narrowed down from the closest matching frequencies. The combination that produces the closest fit between the modal and the experimental results is selected as the initial approximate laminated core material. A similar parametric modal analysis is then performed for the UC22F rotor. With the fan and exciter present, the number of modes within the frequency range of interest increases dramatically. This is taken into account in the selection of the solver settings.

Thusly, the number of elastic combinations is reduced to a smaller selection that yields closely matching results as identified by the analysis on the UC22G rotor.

3.3 Experimental testing and modal analysis results

3.3.1 Rig setup and instrumentation

In preparation for the modal impact testing, the F and G core rotors are suspended off the ground. Given the mass and physical dimensions of the rotor, lifting slings are used to suspend it safely, as shown in Figure 3.3, whilst allowing for accurate modal measurements in the horizontal direction (x) to be obtained. The slings are positioned on the shaft at each end of the core, as close to the core as possible in order to minimize the influence of the supports on the measured frequency response functions. It should be noted that the rotor must not be supported by the ends of the shaft, early testing revealed that the lateral modes were greatly affected by the end supported configuration. A roving hammer test is performed with a single accelerometer positioned in the horizontal direction at the drive end of the shaft. Thirteen impact points are evenly spaced apart as shown in Figure 3.4, and additional four impact points along the rotor core are recorded to obtain torsional modes. The accelerometer is magnetised with a thin coating of wax applied to the contact surface to ensure a stable connection to the rotor and minimise interference from vibration of the accelerometer itself. Both steel and aluminium hammer heads are tested with the former providing greater vibration energy (resulting in smooth high magnitude frequency response peaks) at lower frequencies and the latter for high frequencies. In these tests, frequencies above ~2500 Hz produce a response of insufficient magnitude (dB) to be used as reliable indicators of modes.



Figure 3.3: Suspended F Core Rotor. Accelerometer positioned for torsional mode acquisition from the core

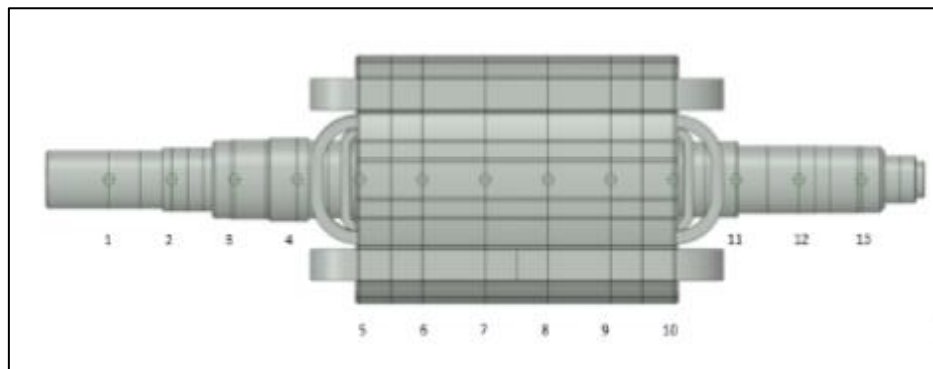


Figure 3.4: Modal test impact locations

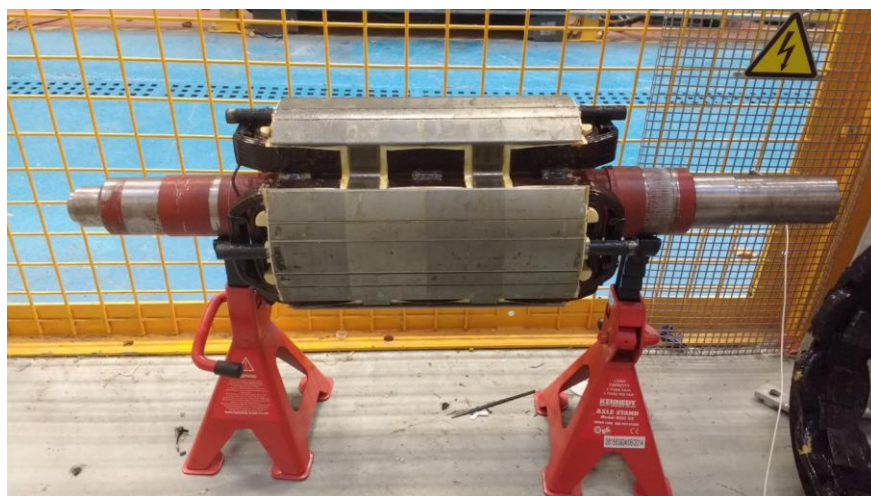


Figure 3.5: Dismantled UC22G rotor (bears, fan and exciter removed)

The modal frequencies are obtained using the peak picking method on the frequency response function plots produced by the frequency analyser. The mode shapes are obtained from the imaginary plot of frequency response function for each impact location. The torsional modes are obtained by placing accelerometers on the main core windings in both the vertical and horizontal directions (x and y) and then generating a frequency response function waveform from averaged results of impacts on the edges of the core poles.

3.3.2 Modal test and modal analysis results

The modal test results for the UC22G rotor identified four significant modes (significant modes are identified by relatively large displacements on the imaginary FRF plot obtained from the frequency analyser). These plots are displayed in Appendix A. Comparisons between the analytical and experimental modal results for the UC22F rotor are shown in Figure 3.6 and Figure 3.7.

From the analytical modal results list of sixty modes, those with frequencies that closely match the experimental modal frequencies are identified and the relative displacements in the horizontal (y axis here) direction, normal to the keyways in the shaft, are obtained for comparison with the corresponding experimentally obtained mode shapes. The same thirteen points along the rotor are studied in the lateral displacement direction and four points along the main core in the direction of rotation (around z axis using cylindrical co-ordinates system).

Table 3.2: Solid G core rotor modal analysis frequencies vs. modal test frequencies

Mode Shape	Solid core 3DFE modal frequency (Hz)	Modal test frequency (Hz)	Error (%)
First lateral (M1)	774.0	715.6	8.16
Second lateral (M2)	1111.4	1017.2	9.26
Third lateral (M3)	2685.3	2311.0	16.19
First Torsional (T1)	2885.0	1506.3	91.53

Table 3.2 shows the experimentally obtained frequencies of the first four modes of the dismantled G core rotor. Additionally, the same modes identified from modal analysis of the G core rotor with solid material properties indicates the error in modal frequencies when the elastic properties of the core remain at $E = 2e^{11}$ Pa and $G = 7.69e^{10}$ Pa. The most significant observation to be made from a comparison between the modal test results and modal analysis results (solid core) is that the first analytical torsional mode is almost twice the frequency of that from the test.

3.3.3 Influence of elastic variables on modes

All three lateral modes are influenced by the axial stiffness of the laminated core. Some key results from the parametric analysis are plotted in Figure 3.6. This indicates the relative sensitivity of each mode to changes in E_{zz} . The first and third lateral modes are

particularly sensitive to changes in E_{zz} . The first torsional mode T1 is independent of E_{zz} .

The lateral modes are also highly sensitive to the selected shear modulus of the laminated core. Figure 3.7 plots the error associated with each mode frequency at different values of G_{xz} and G_{yz} . The torsional mode is very sensitive to changes in the shear modulus. Note that the error here is an absolute value.

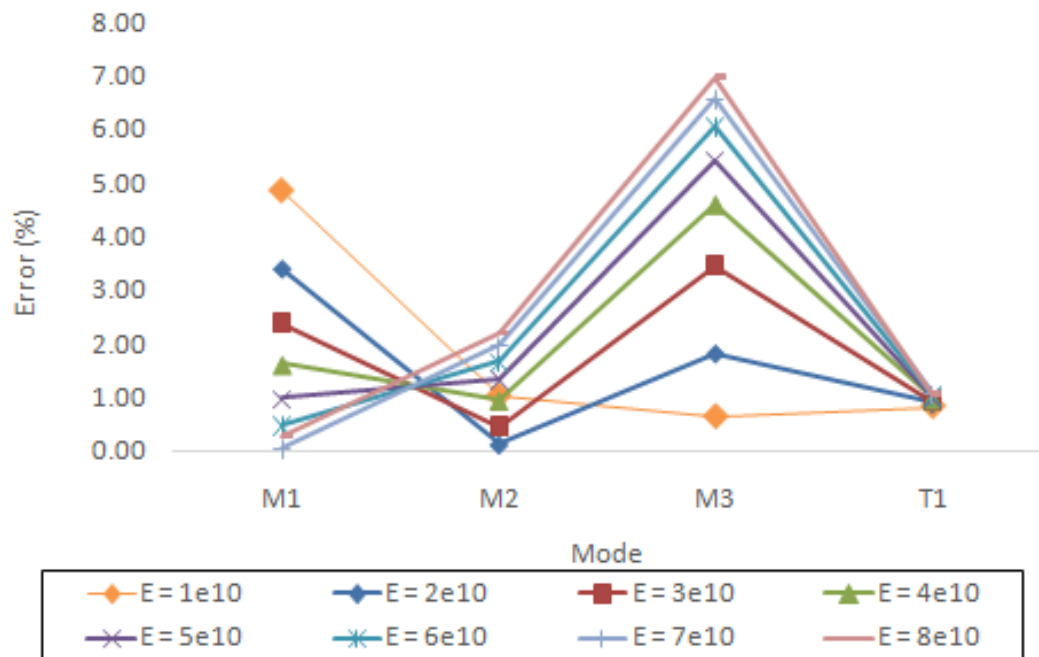


Figure 3.6: G core parametric variation of E_{zz} with constant $G_{xz}/G_{yz} = 1.6 \times 10^{10}$ Pa

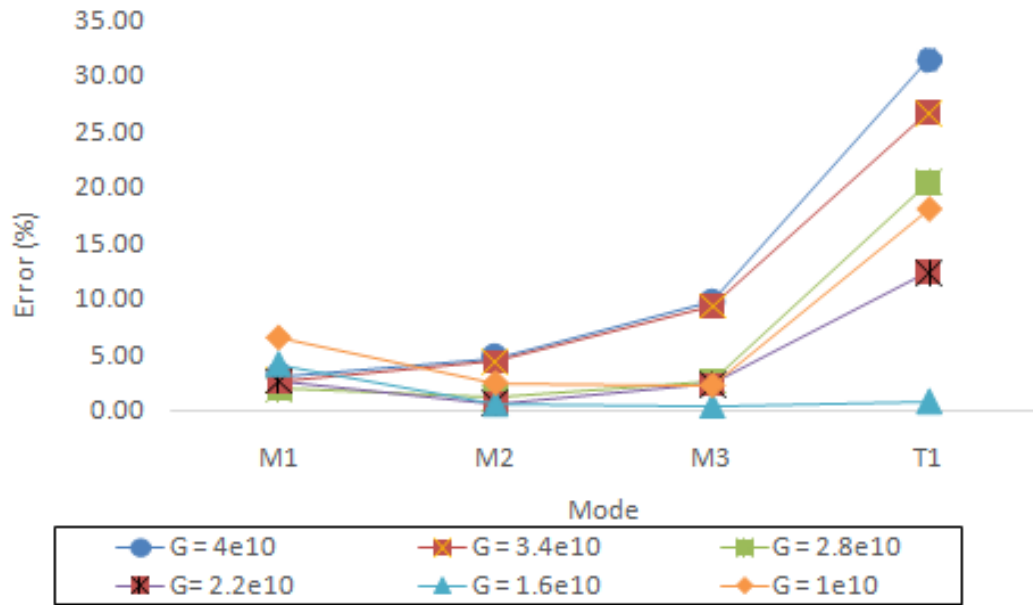


Figure 3.7: G core parametric variation of G_{xz}/G_{yz} with constant $E_{zz} = 1.4e^{10}$ Pa

3.3.4 Observations for UC22F modes

With the addition of the fan to the rotor, a greater number of significant resonance modes becomes apparent in both experimental and analytical results. Most of these modes can be attributed to the fan blades which possess a great number of degrees of freedom. The same also applies for the rotor core end windings and the exciter end windings. If left in the rotor geometry when the modal analysis is performed, these components add hundreds of additional modes to the analysis results which greatly increases simulation time. The displacement of such modes is far too small to be detected with the experimental setup used here, therefore the mass and inertia of both end windings is added to the neighbouring winding blocks under the core poles and in the exciter core slots. Both the UC22F and UC22G geometries have their end windings removed for the modal analyses.

Displacement of the major fan modes cannot be ignored however; the significant torsional modes in particular are largely influenced by fan blade deflection patterns. Three-dimensional representation of the torsional modes for the UC22F rotor are shown in Figure 3.11.

3.3.5 Selection of elastic properties for parametric analysis

From the parametric analysis results, the potential combinations of E_{zz} and G_{yz}/G_{xz} were narrowed down to the following shown in Table 3.3 and Table 3.4. Figures 3.8 to 3.10 show comparisons between the experimentally obtained torsional and lateral mode shapes for both the G and F core rotors.

Table 3.3: Final elastic property combinations for the UC22G rotor

Mode	Young's Modulus E_{zz} (Pa)	Shear Modulus G_{yz}/G_{xz} (Pa)	FE Model Frequency (Hz)	Experimentally obtained frequency (Hz)	Error (%)	Mean error (%)
M1	1.4e10	1.56e10	680.8	715.6	4.86	1.48
M2	1.4e10	1.56e10	1007.7	1017.2	0.93	
M3	1.4e10	1.56e10	2312.8	2311.0	0.08	
T1	1.4e10	1.56e10	1506.8	1506.3	0.03	
M1	7e10	1.56e10	710.5	715.6	0.71	2.42
M2	7e10	1.56e10	1035	1017.2	1.75	
M3	7e10	1.56e10	2462.9	2311.0	6.57	
T1	7e10	1.56e10	1515.9	1506.3	0.64	

Table 3.4: Final elastic property combinations for the UC22F rotor

Mode	Young's Modulus E_{zz} (Pa)	Shear Modulus G_{yz}/G_{xz} (Pa)	FE Model Frequency (Hz)	Experimentally obtained frequency (Hz)	Error (%)	Mean error (%)
T1	1.5e11	1.56E+10	460.19	479.70	4.07	1.30
M1	1.5e11	1.56E+10	502.73	503.10	0.074	
T2	1.5e11	1.56E+10	723.12	729.70	0.90	
M2	1.5e11	1.56E+10	752.13	768.80	2.17	
M3	1.5e11	1.56E+10	927.94	920.30	0.83	
M4	1.5e11	1.56E+10	1725.96	1727.00	0.06	
T3	1.5e11	1.56E+10	2166.54	2178.00	0.53	
M5	1.5e11	1.56E+10	2253.37	2214.00	1.78	
T1	1E+10	1.56E+10	460.16	479.70	4.07	2.01
M1	1E+10	1.56E+10	477.70	503.10	5.05	
T2	1E+10	1.56E+10	722.76	729.70	0.95	
M2	1E+10	1.56E+10	744.99	768.80	3.09	
M3	1E+10	1.56E+10	904.62	920.30	1.70	
M4	1E+10	1.56E+10	1720.94	1727.00	0.35	
T3	1E+10	1.56E+10	2164.54	2178.00	0.62	
M5	1E+10	1.56E+10	2218.53	2214.00	0.20	

3.3.6 Mode shapes

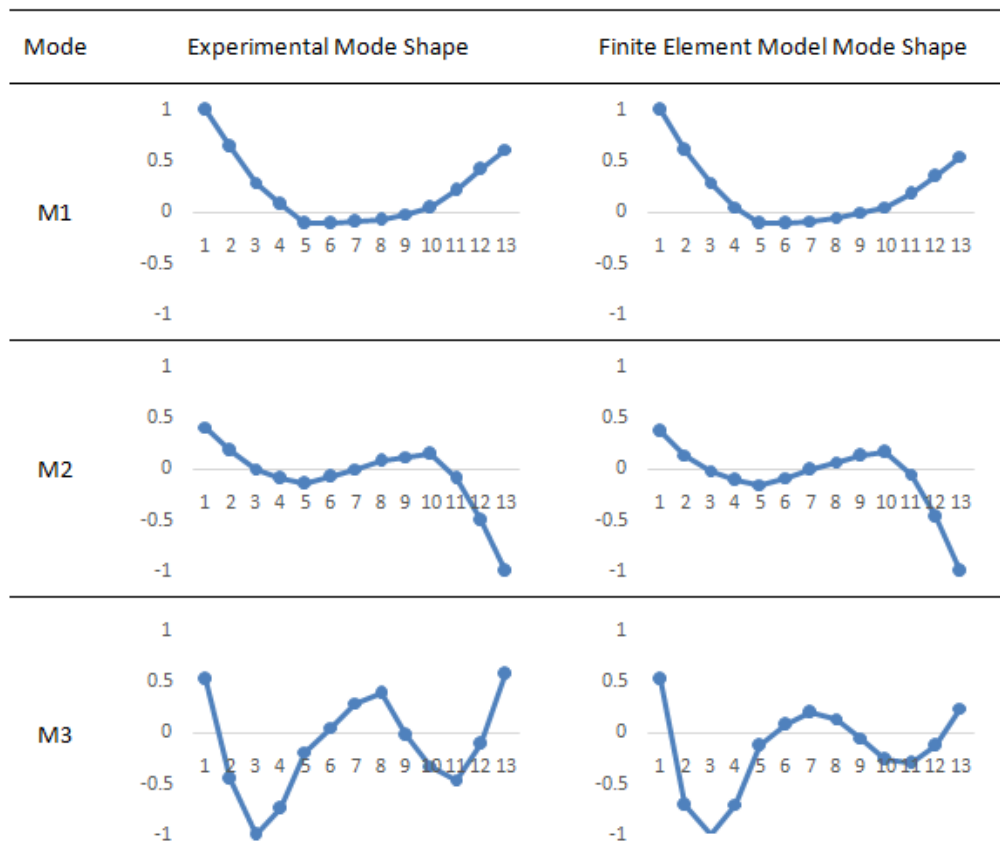


Figure 3.8: Lateral mode shapes of the G core rotor

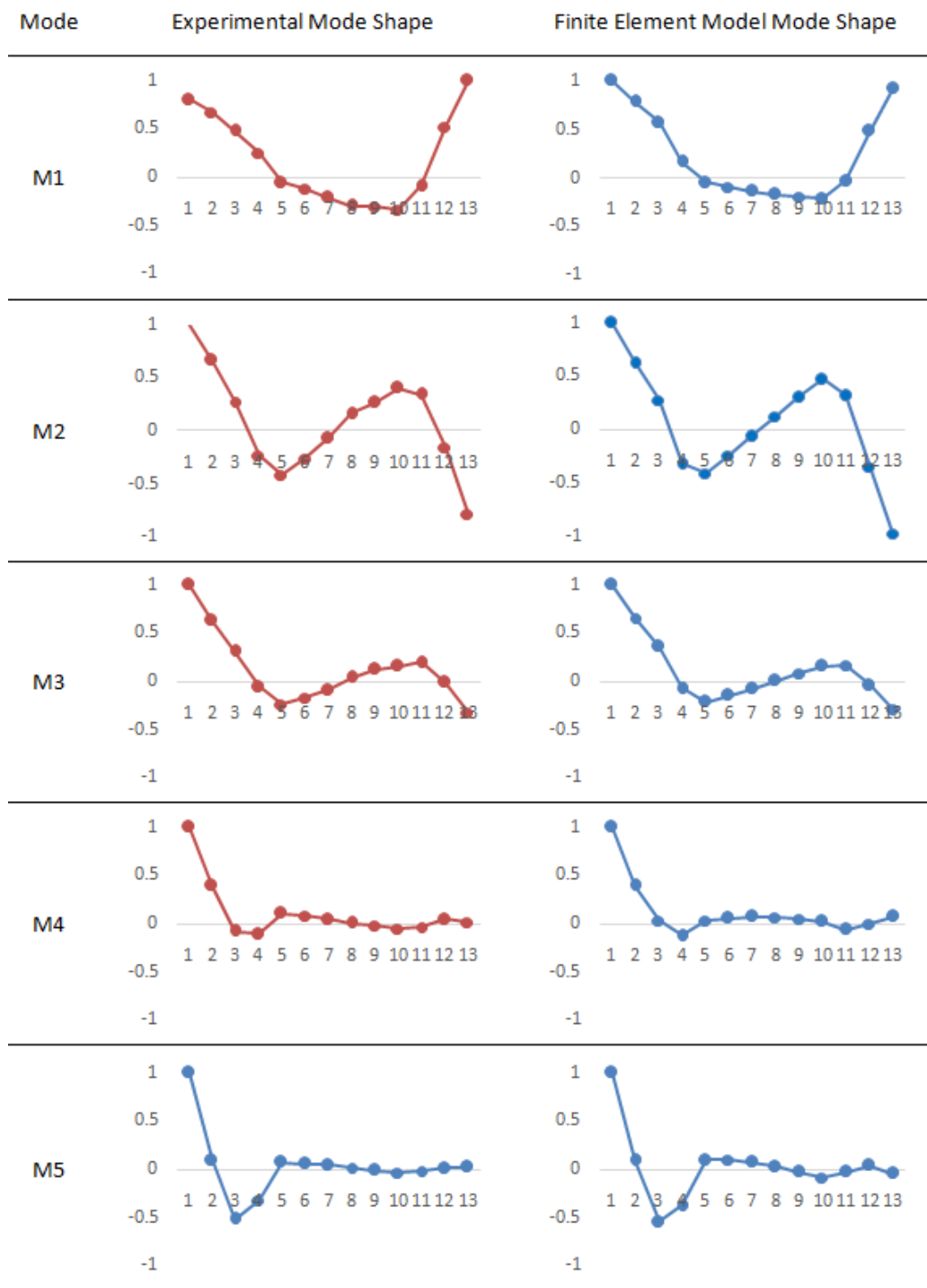


Figure 3.9: Lateral mode shapes of the F core rotor

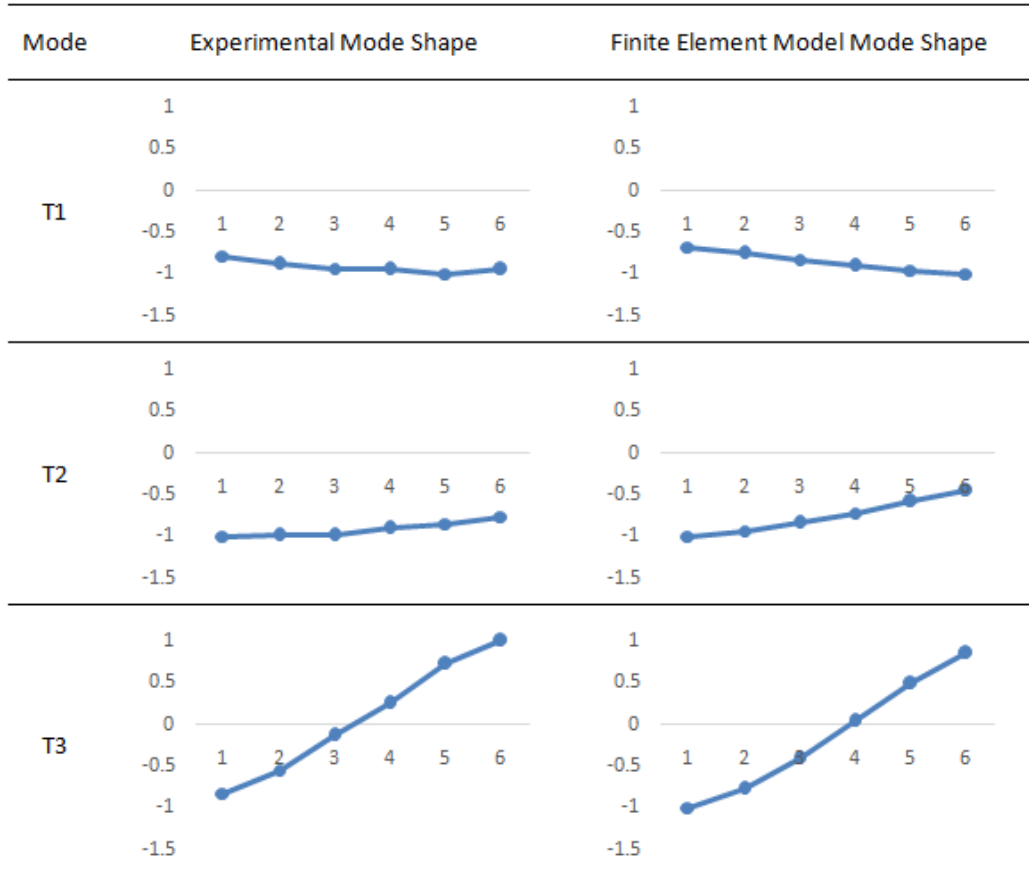


Figure 3.10: Torsional mode shapes of the F core rotor

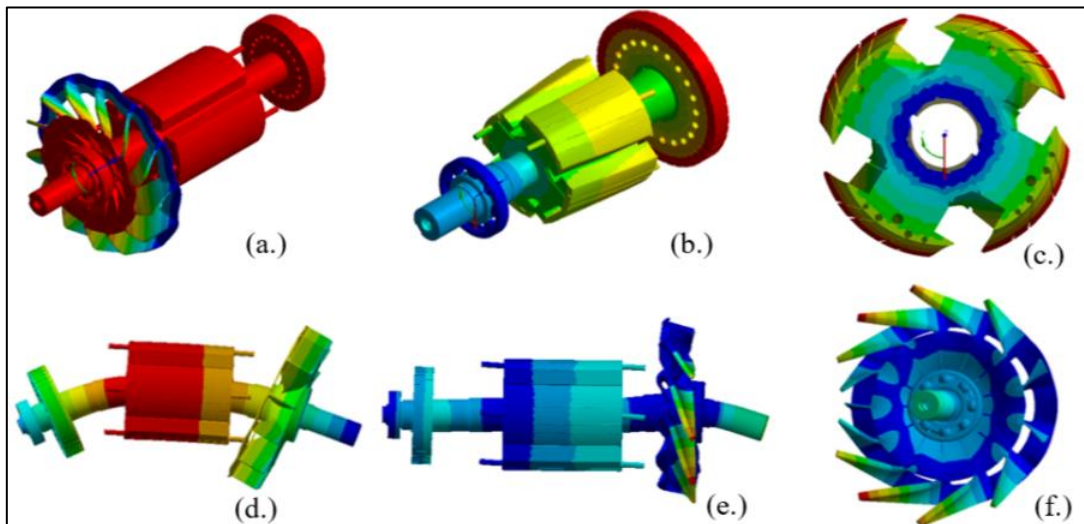


Figure 3.11: Exaggerated deflections of torsional and lateral rotor modes: (a) first torsional mode, (b) first torsional mode with the fan hidden, (c) axial view of the rotor

core in the first torsional mode, (d) first lateral mode, (e) fifth lateral mode, (f) axial view of the fan in the fifth lateral mode

As shown in Figure 3.6 and 3.7, the torsional modes of the rotor are sensitive to only the shear modulus, therefore the correct torsional resonance can be determined by parametric analysis with G_{yz} and G_{xz} as the sole variables. The target frequency of 1506.3 Hz is obtained when G_{yz} and G_{xz} are set to a value of $1.56e^{10}$ Pa.

This narrows the selection to values of E_{zz} that produce the lowest error for the three lateral modes. In this case, there exists no combination of modal parameters that produces exactly zero error between all the measured and analytically obtained modes simultaneously owing to both modelling simplifications and experimental limitations such as imperfect free-free suspension. The combination of elastic values that produces the lowest combined error for all modes is found to be $E_{zz} = 1.4e^{10}$ Pa and $G_{yz}, G_{xz} = 1.56e^{10}$ Pa.

Table 3.3 displays the modal analysis results for the G rotor with $E_{zz} = 1.4e^{10}$ Pa and $7e^{10}$ Pa. The general trend to observe here is that values of E_{zz} above or below $1.4e^{10}$ Pa produce a greater total error for this rotor. Once again, the selected shear modulus holds true for any combination of E_{zz} . In the case of the F core rotor, the combination of elastic values that produces the lowest combined error for all modes for the final modal is as follows. $E_{zz} = 7e^{10}$ Pa and $G_{yz} / G_{xz} = 1.56e^{10}$ Pa. The results for the final selection are shown in Table 3.4. Any value for E_{zz} greater or less than $7e^{10}$ Pa results in a higher total error. Note that the elastic properties of the exciter core affect the modal frequencies and shapes included here by a small margin. A separate parametric analysis

was conducted with a range of exciter elastic properties to fine tune the results further. The selected elastic properties of the exciter are as follows; $E_{zz} = 8e^{10}$ Pa and $G_{yz} / G_{xz} = 4e^{10}$ Pa. An additional observation made on the modal properties of the exciter core is that all the measured modes are significantly more sensitive to E_{zz} than to G_{yz} / G_{xz} .

3.3.7 Discussion of results

The laminated structure of the core reduces the axial modulus E_{zz} stiffness to just 7% of its fully solid equivalent and the shear modulus is reduced to 20% of the solid value. The shorter F core rotor model has a much larger value of E_{zz} than the G core rotor, whilst the shear modulus remains the same. The parametric modal analysis results for both rotors appears to suggest that the value of E_{zz} can be altered by a significant amount without great effect on the combined error for all lateral modes. The error associated with individual modal frequencies can be quite large however. The first bending mode of the G core rotor has an error of 4.86% whilst the other three modes remain below 1%. Increasing the value of E_{zz} will result in a decrease in the error for the first bending mode but will also increase the error for the other modes. Should both values of G_{yz} / G_{xz} and E_{zz} be selected incorrectly then the resulting error may be very great. Since at least the shear modulus is fixed first there is room for error in the selected value for Young's modulus.

3.3.8 Chapter 3 summary

This section covers the creation of a 3DFE generator rotor model for the purpose of obtaining the stiffness properties via modal analysis.

The steps taken in this chapter are as follows:

- Two 3D models of generator rotors are built, one for the UC22G rotor which was stripped down to the core and shaft assembly, and the other for the fully assembled UC22F rotor.
- The models are imported to the ANSYS modal solver and the mesh cell size is determined via a simple sensitivity analysis (modal frequencies versus cell size). Surface contact mesh matching is used to align the elements between subcomponents in the assembly.
- The material properties of the subcomponents are assigned, and the unknown elastic properties of the windings are determined using the rule of mixtures. The elastic properties of the rotor core are estimated by multiplying the directional elastic properties by the lamination stacking factor.
- The experimental modal frequencies and shapes are obtained for both rotors by performing a suspended rotor modal impact test.
- Modal analysis is performed on the UC22G rotor to obtain the initial modal frequencies and shapes. A parametric modal analysis is performed to obtain the closest fit for the first four modes by simulating with a wide range of possible combinations of E_{zz} , G_{yz}/G_{xz} . The values of shear modulus G_{yz}/G_{xz} are fixed at $1.56e^{10}$ Pa. This analysis is performed first on the UC22G rotor to narrow down the value of G as doing so on the UC22F alone would be difficult due to the influence of the fan and exciter.
- The shear modulus of $1.56e^{10}$ Pa is applied to the UC22F rotor core and another parametric analysis is performed to obtain the equivalent axial young's modulus E_{zz} .

The key points from this chapter as follows:

- The elastic properties of the UC22F rotor core are reduced to $E_{zz} = 1.5e^{11}$ and $G_{yz}/G_{xz} = 1.56e^{10}$ Pa. The shear modulus is found to be the most dominant factor in determining the modes of the generator rotors.
- The parametric mode matching technique applied here achieves a mean error of 1.3% between the first eight experimentally obtained modal frequencies and a close match between the mode shapes.

The work completed here is used in the following chapters are as follows:

- With the elastic properties of the UC22F rotor validated in this chapter, the model is used in Chapter 5, section 5.1.2 to obtain the torsional stiffness k_T of the rotor by using Equation 2.7 to calculate k_T for the shaft sections between the exciter and core, core and fan, and fan to the end of the rotor shaft. The torsional stiffness properties are displayed in Table 5.1. These results are used to construct the 1D torsional model of the generator set as part of the multi-physics model developed in Chapter 5. The modified value of shear modulus is included in the calculation of k_T for the core section which ensures accuracy in the rotor angular position during LVRT simulations (as the electromagnetic air gap torque is applied directly to this element of the 1D torsional model).
- The UC22F rotor geometry is also used in the following chapter when it is included in the electromagnetic model as part of a 2D slice through the generator.

3.3.9 Chapter 3 contributions to the literature

The parametric analysis technique is used to tune the elastic properties of the laminated rotor core until the analytically obtained frequencies and shapes match their experimentally obtained counterparts. A similar method is applied in the literature (see section 1.3.3) where the modal analysis is performed in a reverse sense using 3DFE analysis but is expanded upon here by:

- Using a parametric approach applied with ANSYS workbench to compute many combinations between the elastic properties E and G to narrow down the modal results that are closest to the experimental results for a number of modes (8) simultaneously.
- Performing the analysis on not only the rotor core / shaft assembly, but also the fully assembled synchronous generator rotor, including the windings, fan and exciter.

The resulting dynamic model of the rotor achieves a mean error between the first 8 modes that were obtained in the modal test of 1.3%, proving that the method can be highly accurate over a wide frequency band.

Chapter 4 Electromagnetic modelling and transient short circuit testing

4.1 Model construction and features

A transient electromagnetic model of the UC22F generator is built using ANSYS Maxwell to simulate the magnetic field and currents induced in the stator during short circuit and low voltage fault events. The model is based on a two-dimensional slice through the rotor and stator of the machine, but the true core length of 240 mm is taken into account in the simulation settings in order to simulate the full volume of the machine and obtain the equivalent electromagnetic field interactions between the rotor and stator for the full length of the rotor core. The simulations can be set up with multiple, two dimensional slices positioned through the rotor core at equal lengths, each displaced at a constant angle from the previous slice in order to simulate the skewing that is present in the real rotor core. Skewing effectively stabilises the electromagnetic air gap torque, however the additional simulation runs required significantly adds to the simulation time. Note that the skewing option is not enabled in later LVRT simulations, thus the electromagnetic torque results contain a small increase in magnitude of oscillations.

4.1.1 Geometry setup

The UC22F rotor has four salient poles with field windings wrapped around the top of each pole. Each block of field windings contains 84 copper conductors and on each pole one winding block has negative polarity current and the other has positive polarity current to represent the flow of DC current around the windings. The damper bars and support bars are also present within the ends of each pole, placed in the same position

as in the 3DFE model. The rotor is mounted on the shaft with both keys are included as part of the shaft for simplicity. Note that the actual rotor is assembled with only one key as the shaft of the UC22F only has one keyway for the main rotor core despite the core possessing two keyways.

The generator stator contains 48 slots that each contain double layered copper windings. Twelve conductors run through each slot in total, half of these belong to one of the phase branches and the other half to another. The minimum distance between the rotor and stator across the air gap is 1.1 mm. The air gap size is minimised in generator design in order to reduce electromagnetic losses by minimising the distance over which the electromagnetic field extends between stator and rotor (65). Note that an excessively small air gap thickness can result in reduced thermal efficiency and can also increase the chance of contact between the rotor and stator. This can arise due to unbalanced magnetic pull, mechanical imbalance, severe vibration and so on. The complete 2D geometry of the generator used in the electromagnetic model is shown below in Figure 4.1.

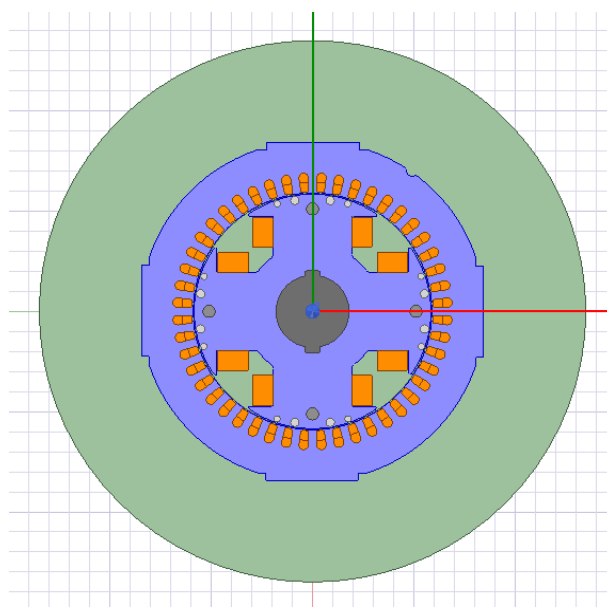


Figure 4.1: Maxwell model of 2D slice through UC22F rotor

4.1.2 Stator field

Figure 4.2 below shows the two stator winding branches of each phase. The phase order progresses as U, V, W, therefore the stator field rotates in the anti-clockwise direction as shown in Figure 4.3 with all three phases highlighted.

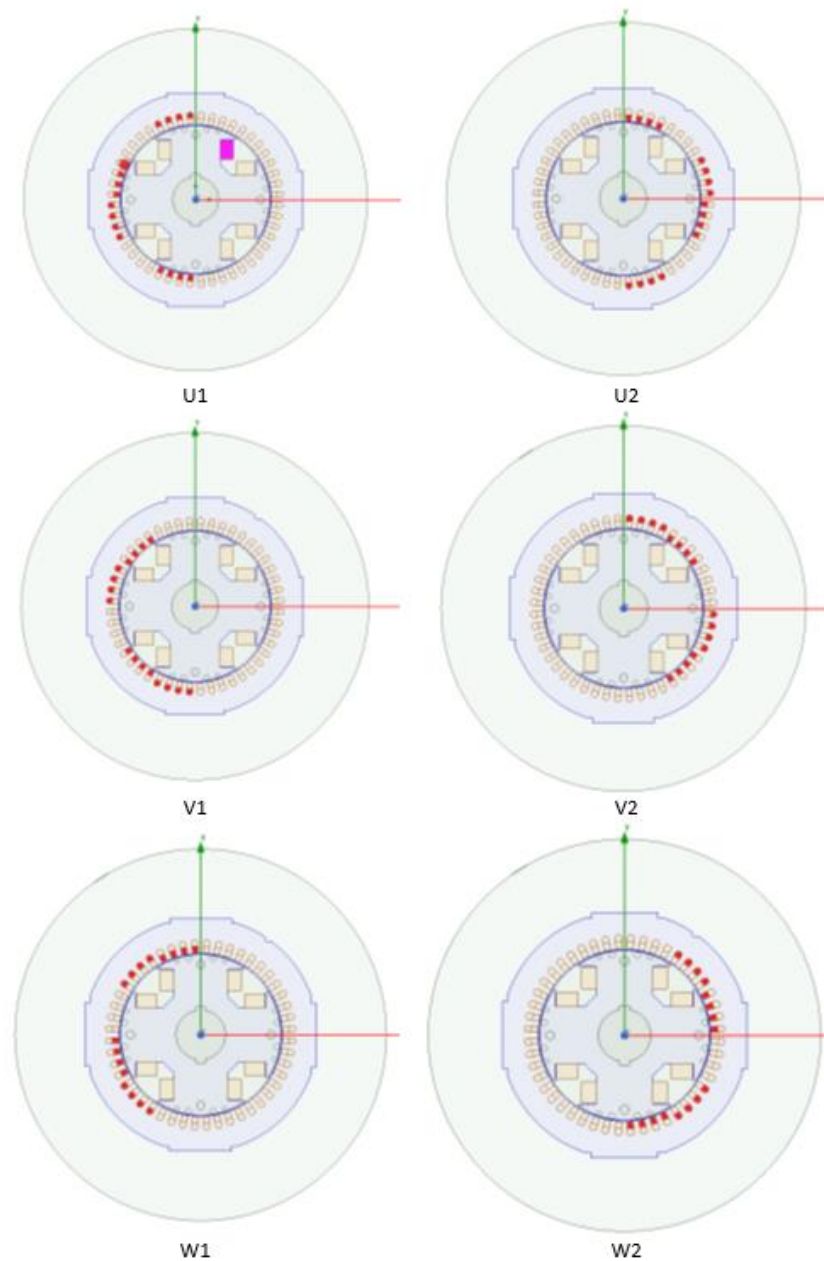


Figure 4.2: UC22F Stator Windings

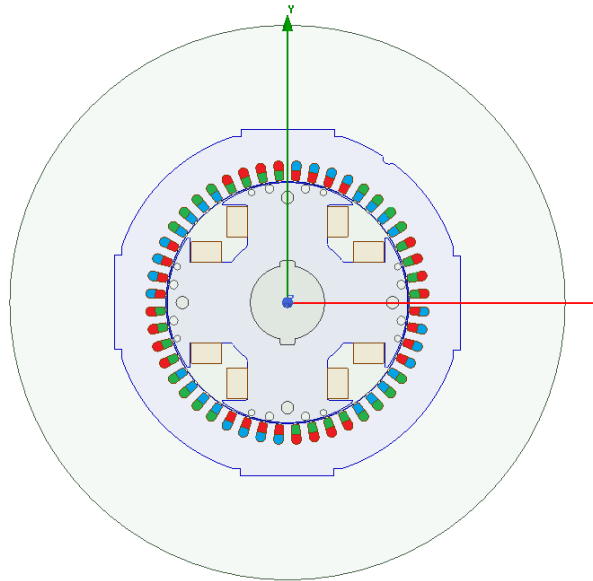


Figure 4.3: All stator phases, U = red, V = blue, W = green.

4.1.3 Electrical materials

The material properties of the stator windings, rotor windings, rotor core, stator core and air gap all determine the electromagnetic performance of the generator. The selected material properties are as follows. The rotor and stator cores are composed of electrical steel with a bulk conductivity of $2e^5$ siemens/m. The relative permeability, μ , is determined by the BH curve shown in Figure 4.4 (change in magnetic flux density, B with change in magnetic field, H). In addition, a standard core loss model for electrical steel is selected for the material.

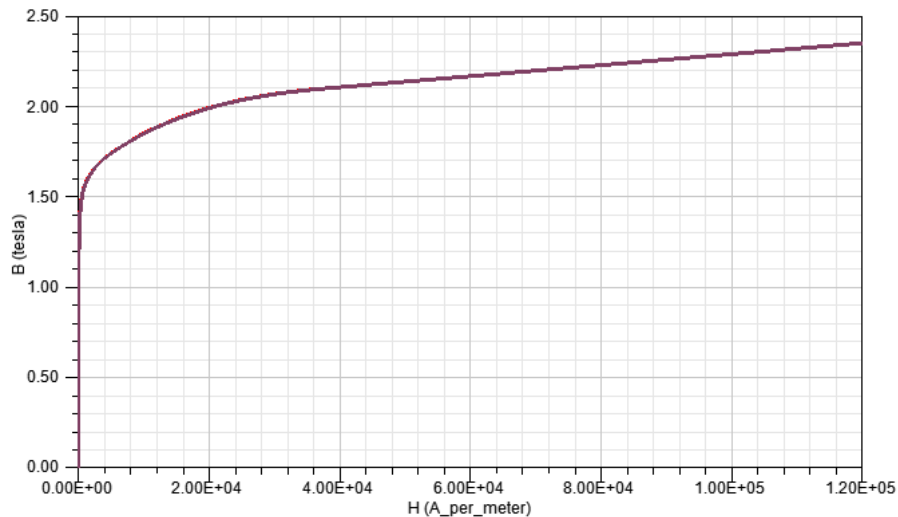


Figure 4.4: B-H curve for stator and rotor core electrical steel

The copper in the rotor and stator windings has a bulk conductivity value of $5.8e^7$ S/m and relative permeability of 0.99. The aluminium that composes the damper bars has a bulk conductivity of $3.8e^7$ S/m and relative permeability of 1. The air gap between the rotor and the stator and the boundary surrounding the outer circumference of the stator is set to the 'vacuum' material. Electromagnetic fields can still extend through these layers but no electrical current is induced in them since they contain no material (other than air in reality). The bulk conductivity is set to 0 S/m and relative permeability is 1. Note that the elastic properties of the materials can also be defined here but these are left at default values (including the rotor core) as torsional displacements are to be calculated in the connected Simplorer model.

4.1.4 Simulation setup and adjustable variables

The rotor windings carry an adjustable field current which may be set at a constant value equal to that required to induce a given stator voltage. Alternatively, the field current variable could be connected to a control circuit representing the AVR

(automatic voltage regulation) for the generator. In this arrangement, the field current is automatically adjusted by the control loop to regulate terminal voltage.

The simulation setup also includes control over the mechanical aspects of the generator. Firstly, the initial rotor angle is specified, this determines the power factor of the machine. Generators, including those in the UC range, typically operate at a lagging power factor of 0.8, however the test generator runs at unity power factor since it is connected to a resistive load bank. To achieve this, the rotor is aligned exactly with the rotating electromagnetic field of the stator (64 degrees rotation counter clockwise) which is identified by knowledge of the winding order and positioning the rotor under the first group of energised windings. The winding current and voltage traces are compared to ensure that they are in phase and unity power factor is achieved.

All rotor components are added to a motion setup which allows the rotor to rotate freely at either a constant rotational speed or rotational speed determined by the mechanical input to the model. Mechanical transient effects may be accounted for by selecting the rotational speed of the rotor, rotor inertia, rotational damping and load torque (from the prime mover). These settings are useful for simulating the electromechanical behaviour of the generator rotor alone, however such a model cannot be extended for multi-inertia assemblies like the full generator set and thus is overridden in the Simplorer model.

The generator is rated to produce power at a frequency of 50 Hz, as the machine has a four-pole rotor, the synchronous rotational speed for normal operation is 1500 RPM or 157 rad/s as calculated by Equation 4.1 below;

$$N = \frac{120f}{p} \quad (4.1)$$

Where;

N = Synchronous speed (RPM)

f = Electrical frequency (Hz)

p = Number of poles

The solver settings are chosen carefully to obtain accurate results. This is particularly important during simulation of fast transients as in the case of short circuit testing. For the initial steady state tests a relatively long step time of 0.8 ms is selected, this allows for tests to be completed quickly and still obtain accurate results. Parametric analysis performed to obtain the correct rotor angle and field currents also utilised this time step. For transient short circuit tests the time step was initially reduced to 0.2 ms, but it was later determined that a step of 0.05 ms was required to provide a high enough resolution to capture the full current and voltage traces. This time step was chosen following a sensitivity analysis where the peak short circuit current and electromagnetic torque was compared for different time steps. Time steps smaller than 0.05 ms continued to increase the simulation time but did not significantly affect the peak current/torque. In addition, increasing the number of cells in the mesh by reducing the cell size in the automatically generated mesh made no significant difference to the current/torque results. Note that thermal effects and windage (air friction) is not included in the following electromagnetic simulations of the rotor.

4.1.5 Circuit setup for steady state simulations

The three phase windings that connect from the stator terminals through the stator are split into two branches, these branches can be connected in either parallel or series depending on the required operating voltage for the machine.

The circuit builder in ANSYS Maxwell is used to connect the windings to the terminals of the machine. Figure 4.5 below shows a simple example circuit in which the generator is connected to a resistive load. The test machine is set for 380 V operation and the generator windings are connected in the series star configuration. The windings are represented as inductance elements in the circuit model, these elements link directly back to the copper winding components in the stator of the 2D slice model. The neutral line between the load and the generator is included alongside a common ground for the three phases. The branch resistance of 0.0325Ω is correct for the UC22F generator.

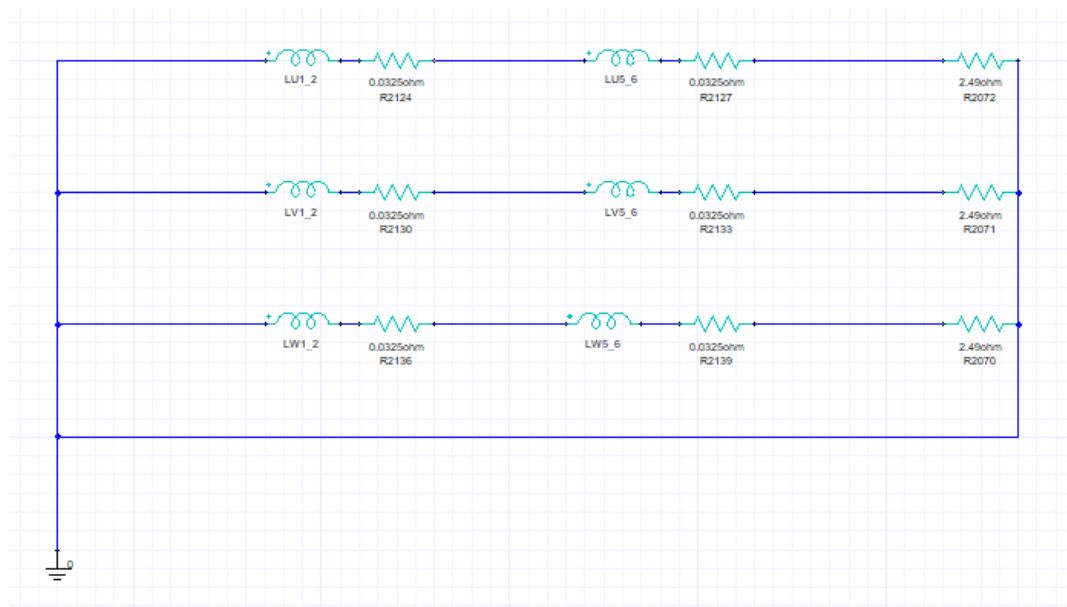


Figure 4.5: Simple resistive load connected circuit diagram for UC22F model

In the case of a grid connected simulation, the load resistances on each phase can be replaced with voltage sources to represent a connection to an inflexible grid supply (inflexible as the grid voltage/current/frequency is not affected by the generator, as would be the case for a single small generator connected to a large power network with many other larger power generation sources). The voltage sources for each phase are set with a peak voltage of 311 V (220 V RMS for each phase), phases V and W are phase shifted 120° and 240° respectively from phase U.

4.2 Experimental setup

The test generator set shown in Figure 4.6 is used for validation of the electromechanical model. The rig consists of the 72.5 kVA UC22F synchronous generator coupled to a Brook Crompton Parkinson electric motor. The machines are coupled together through a torque transducer and both machines and the transducer are fastened to the test bed with bolts to prevent any movement during testing. During short circuit testing, the high magnitude transient torque produced has the potential to displace the machines from the test bed should they not be fixed down adequately. Immediately following the short circuit the generator visibly shakes due to this sudden change in torque.



Figure 4.6: UC22F generator and electric motor test rig prepared for steady state and three phase short circuit experimental tests

The three phases from the generator terminals are connected to an adjustable load bank which is remotely operated to allow for selection of various loads. From the same terminal connections, each phase is also connected to a remotely operated contactor which in turn is connected to a copper bar. A push button located outside the test cell is connected to the contactor. When pressed, the contactor shorts the three phases together and when released, the short circuit is removed. During the short circuit tests, the current in the fault lines is measured via current clamps placed around each of the three phase lines that are connected to an oscilloscope. An additional measurement for voltage in the U phase line is also recorded by the oscilloscope.

The torque transducer utilises strain measurements from a rotor that is hard coupled (bolted and clamped) between the generator and motor coupling sections to measure the applied torque from both machines and the rotational speed of the rotors. The unit is rated for 1 kNm peak torque, but is capable of measuring up to 2 kNm, any torque applied above this value will result in a flat peak in the measured torque. The transducer

is connected to a laptop outside the test cell to monitor speed and torque measurements during the test.

For the short circuit tests, the generator voltage is automatically regulated by the AVR. This is set for 220 V RMS for full voltage operation and the voltage input from the winding terminals is placed between the two branches of each phase to obtain half voltage operation for the 110 V tests. For the steady state tests, the generator voltage is controlled with a DC supply connected directly to the generator rotor circuit via slip rings. This is so in order to verify the rotor current or field current for use in the electromagnetic model.

Motor speed is controlled through a Eurotherm variable speed drive, also positioned outside of the test cell (speed controlled loop), which actively seeks to maintain the rotor speed of 1500 RPM or 157 rad/s.

4.2.1 Operation and test procedure

The generator is first ran up to speed with no load set on the load bank, once up to speed the rig is left to run at steady state for around ten minutes until the test cell reaches a steady temperature. Once the correct steady state voltage and current is verified using the oscilloscope readout, the steady state results are recorded by saving the transducer output on the laptop (Figure 4.7) and the current/voltage results on the oscilloscope. The same process is repeated for the three-phase short circuit tests but the contactor is activated and released with the push button once steady state is achieved and results are saved immediately following the short circuit. The contactor is released as soon as

possible to prevent the generator from being subjected to sustained short circuit currents for longer than necessary. Maintaining a sustained short circuit would also damage the contactor and in the worst case scenario, fuse the contactor closed. An emergency stop button for the test cell is positioned nearby to shut off power to the area in the event of an electrical or mechanical failure. The half voltage (110 V RMS) short circuit tests were performed first to estimate the potential current and torque in the generator at full voltage. The measured torque was found to be well below the specified limit torque of the transducer of 2 kNm, enabling the following full voltage tests.

4.2.2 Results from the electromagnetic model: steady state simulation and validation

For full load and no-load steady state operating conditions the generator is expected to produce power under the following conditions (per phase) as shown in Table 4.1 below. The corresponding field current required to produce these results and the load resistance per phase to achieve the target load is also shown. The field current must be confirmed in order to obtain the correct steady state current, voltage, torque and load. Note that for no load operation, the load resistance for each phase is increased to a very large value to simulate zero power drawn from the circuit by the load.

Table 4.1: Target simulation results for steady state operating conditions of the generator for full and half voltage operation (power factor 1).

Test Number	Power Factor	Terminal Voltage (V) (RMS)	Load (% of 58 kW)	Terminal Current (A) (RMS)	Speed (rad/s)	Field Current (A)	Load Resistance (Ω)	Torque (Nm)
1	1	110	100	43	157	13.0	2.5	100
2	1	110	0	0	157	4.0	1e ⁶	0
3	1	220	100	88	157	29.7	2.3	364
4	1	220	0	0	157	13.0	1e ⁶	0

The simple resistive load bank connected circuit shown in Figure 4.5 is used to check that the desired steady state conditions are reached under the given parameter values. The load resistance per phase is calculated with the knowledge of power exported and the target voltage/current.

With the load set correctly, electromagnetic simulations are performed for full voltage and half voltage cases under full load and steady state conditions. Half voltage steady state tests are carried out in order to set the generator up for short circuit testing by checking the stability of the setup (no arcing, damage to the rig, contactor and measurement equipment etc.) and ensure that fault current and torque magnitude is not excessively high before full voltage testing is performed. The following Figures show the experimentally obtained steady state rotor speed, rotor torque (Figure 4.7), current and voltage (Figure 4.8 and Figure 4.12) plots for full voltage and half voltage operation at full load. Steady state simulation results for current and voltage are also shown for comparison in Figure 4.9 to Figure 4.11 and Figure 4.13 to Figure 4.15.

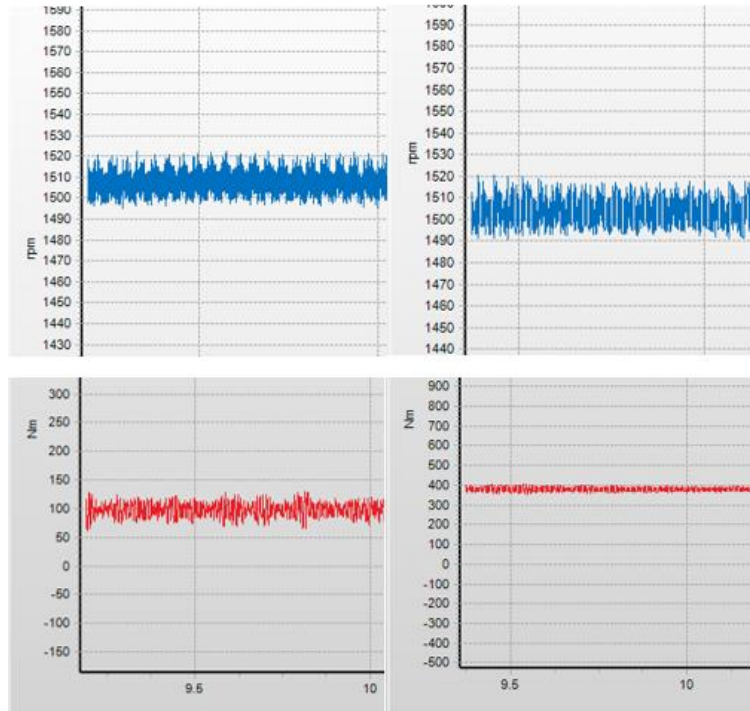


Figure 4.7: Experimental results for half voltage (left) and full voltage (right) operation. Rotor speed and rotor torque at full load

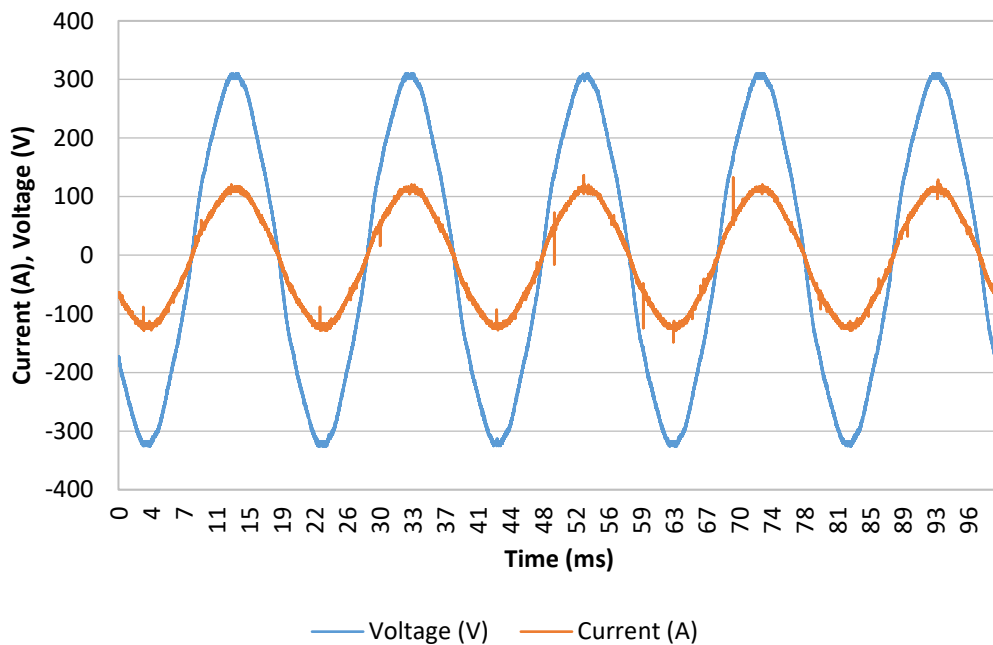


Figure 4.8: Experimental results for full voltage operation. Terminal current and voltage for U phase (power factor 1, full load)

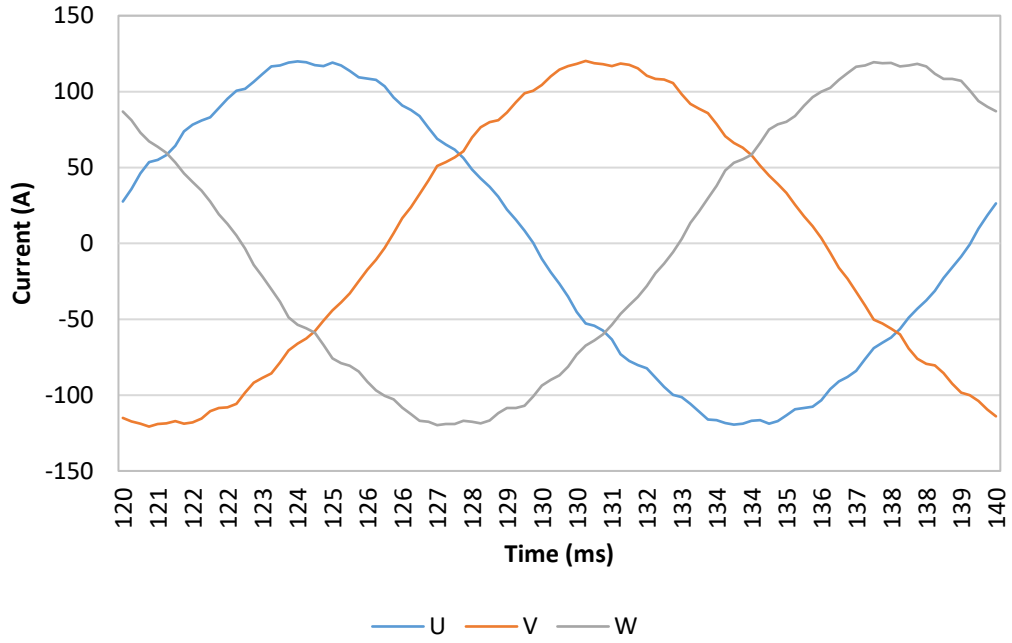


Figure 4.9: Steady state, full voltage simulation results. Terminal current (PF = 1, full load)

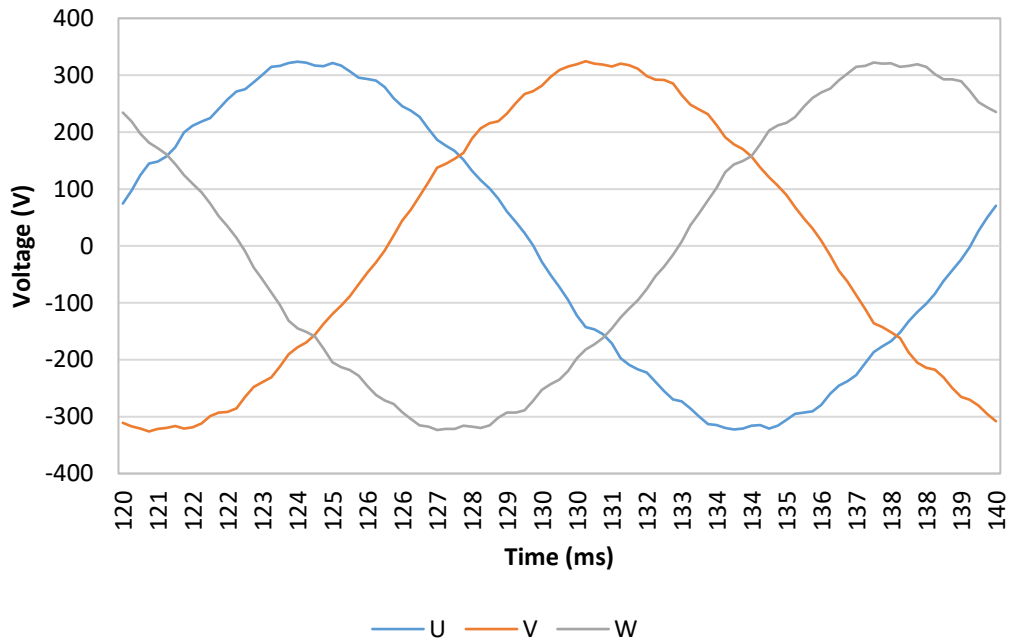


Figure 4.10: Steady state, full voltage simulation results. Terminal voltage (PF = 1, full load)

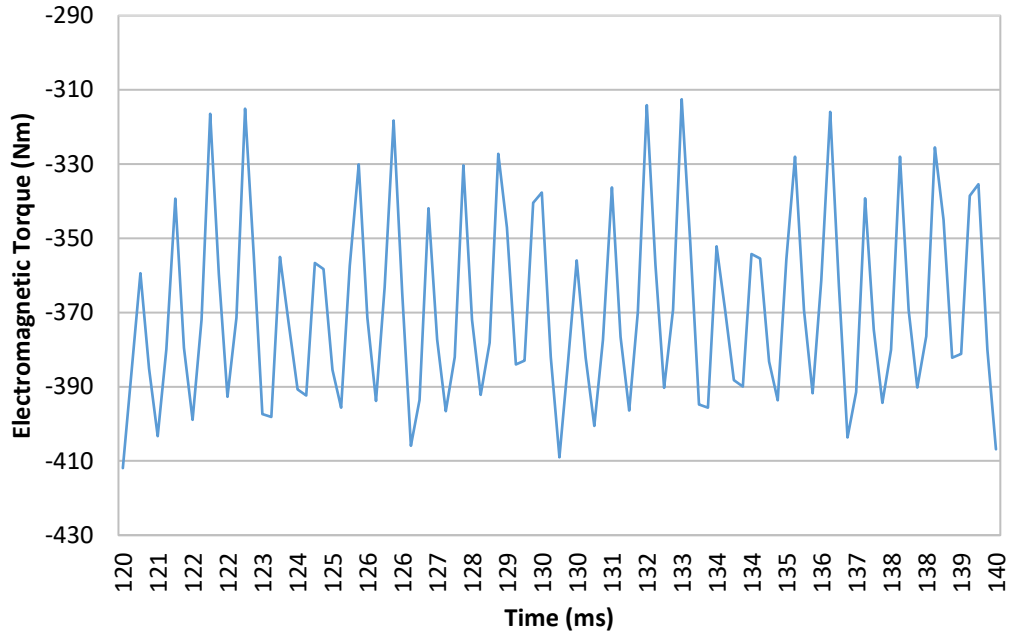


Figure 4.11: Steady state, full voltage simulation results. Electromagnetic torque (PF = 1, full load)

The terminal current is measured at 120 A peak (three-phase current of 147 A), and the voltage is 311 V peak (380 V three-phase voltage). The power produced is calculated as per Equation 4.2:

$$P = V \cdot A \cdot PF \quad (4.2)$$

Where;

P = Power delivered by three-phase machine (kW)

V = Three-phase voltage (V)

A = Three-phase current (A)

PF = Power factor

In the experimental test here the power output was 2 kW lower than the full rated load of 58 kW. Field current was 27.7 A, 2 A lower than the 29.7 A field required for full load.

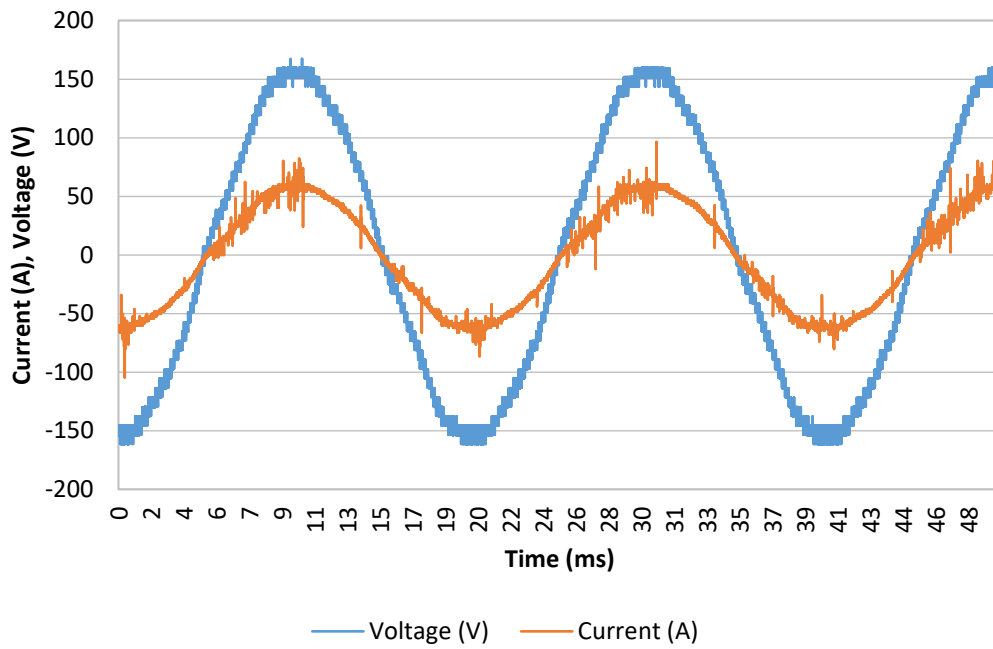


Figure 4.12: Steady state, half voltage experimental results. Terminal current and voltage for U phase (PF = 1, full load)

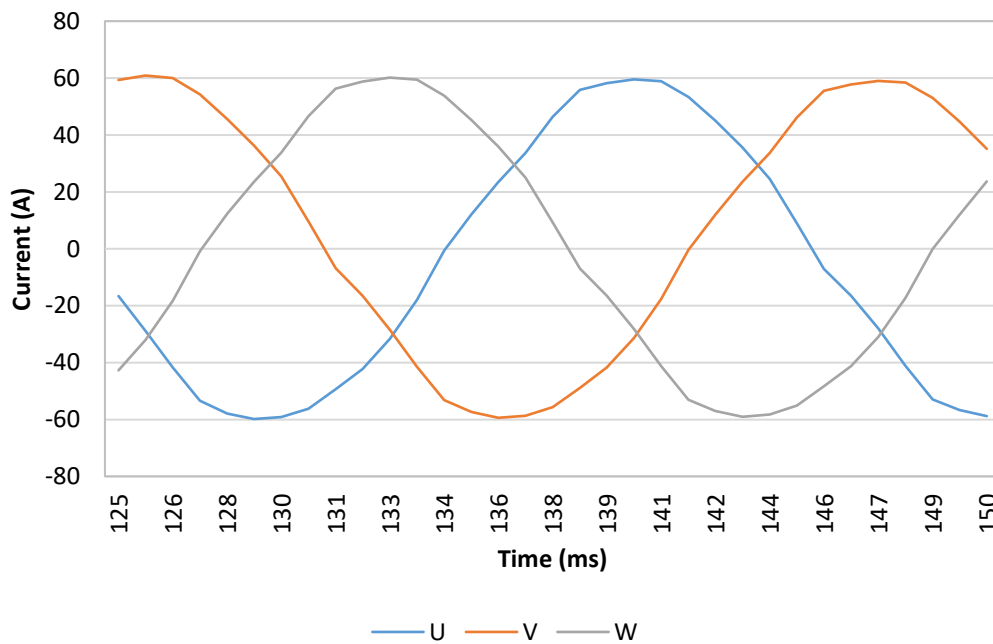


Figure 4.13: Steady state, half voltage simulation results. Terminal current (PF = 1, full load)

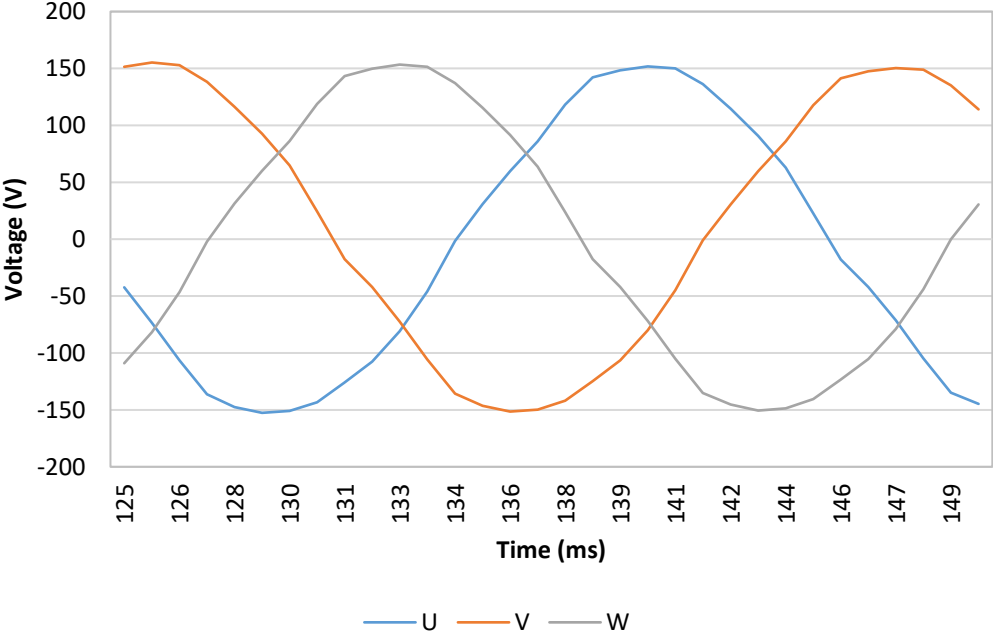


Figure 4.14: Steady state, half voltage simulation results. Terminal voltage (PF = 1, full load)

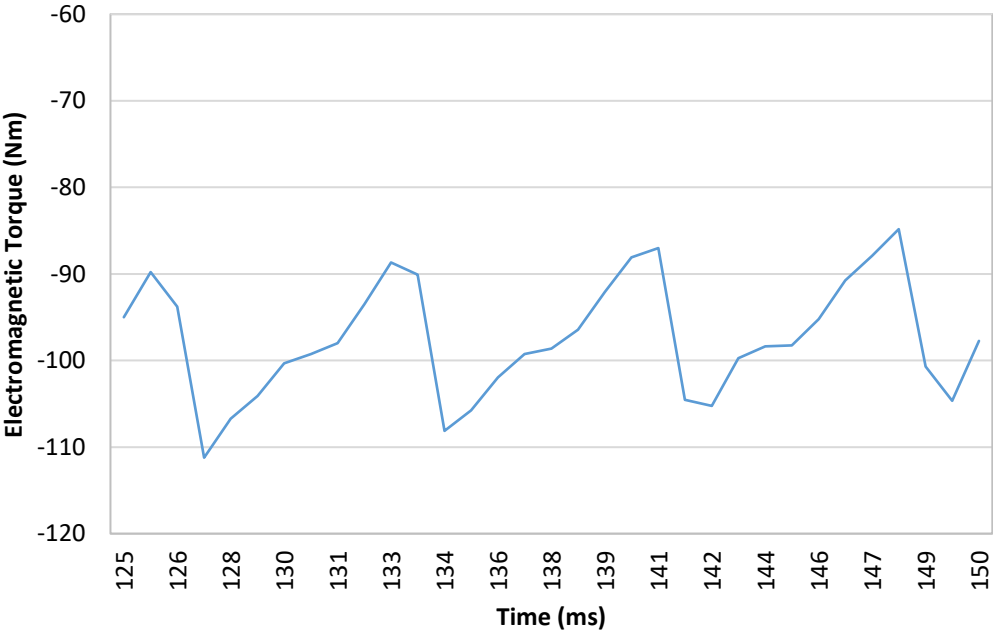


Figure 4.15: Steady state, half voltage simulation results. Electromagnetic torque (PF = 1, full load)

The average electromagnetic torque produced by the generator for the full voltage test is 364 Nm and the average torque for the half voltage test is 100 Nm. Both machines rotate at a constant 1500 RPM or 157 rad/s during the steady state tests.

The Maxwell model results closely match the experimentally obtained results for both full voltage and half voltage operation at steady state. The steady state validation of the model is concluded with similar results.

4.2.3 Chapter 4 summary

The steps taken in this chapter are as follows:

- The 2D geometry of a slice through the generator is created and imported into the ANSYS Maxwell electromagnetic solver (steady state). The windings of each phase are arranged into groups and the electrical material properties are selected. The rotor speed is set to a constant 1500 RPM (157 rad/s) and the time step is set to 0.05 ms following a short sensitivity analysis for steady state current / voltage versus time step.
- The three phases of the stator are connected to a circuit which contains resistive load elements for each phase.
- Steady state current, voltage and torque results are obtained from an experimental test performed on the UC22F generator which is connected to a

load bank that is set to provide the full rated load of the generator. The results are obtained for tests performed at 100% and 50% of the rated terminal voltage of the generator. In the following chapter, the three-phase short circuit tests is first performed at half voltage for safety purposes.

- The electro-magnetic model is simulated under the same steady state conditions at full and half voltage and the current, voltage and torque results are compared to validate the model.

The key point from this chapter is as follows:

- The electro-magnetic model of the UC22F generator is capable of accurately reproducing the steady state operating conditions of the real machine and be used for further transient analysis.

The work completed here is used in the following chapters are as follows:

- The steady state tests are performed to ensure that the electro-magnetic model produces the correct current and voltage for the applied input torque and rotor field current. With the model validated under steady state conditions, it is further used in Chapter 5 where it is coupled to the 1D torsional model of the motor and three-phase short circuit testing is performed.

Chapter 5 Multi-physics modelling

5.1 Model construction and simulation setup

As mentioned previously, the transient mechanical simulation in Maxwell is too limited to reproduce the full torsional behaviour of the generator set. In this section, an ANSYS Simplorer module is used to couple the electromagnetic Maxwell model to a one-dimensional torsional mechanical model of the generator set. The multi-physics model developed here is used to determine the mechanical response to electrical short circuit and low voltage faults. Simulation results from the generator/motor set are used to validate the electromagnetic rotor model and inform the assembly of the generator/diesel engine set model. Short circuit and low voltage faults are then simulated in the diesel engine genset model.

The key parameters of interest from these simulations include rotor angular speed, shaft torque (measured at the transducer), angular acceleration and rotor angle (between the rotor and rotating magnetic field of the stator). The degree of rotor angle shift during the fault ultimately determines if the rotor slips or not during the fault clearing phase and also determines the magnitude of transient torque during this period.

5.1.1 Co-simulation

In order to import the Maxwell model into the Simplorer model, the co-simulation transient link option is checked in Maxwell under design settings > advanced product coupling. The Simplorer model uses the electromagnetic setup from the source Maxwell model, any changes required for the electrical construction of the machine are

done by opening the connected Maxwell model. The same solver settings are applied in Simplorer as for the Maxwell model (shared time step settings and simulation time). As mentioned in section 4.1.4, a time step of 0.05 ms was selected based on a sensitivity analysis and the mesh size remained unchanged from automatically generated mesh. Note that the magnetic transient solver does not use adaptive mesh refinement, therefore a suitable initial mesh size must be defined prior to solving.

A general overview of the co-simulation arrangement for a synchronous generator set driven by a prime mover and connected to an electrical load is shown in Figure 5.1 below. In all multi-physics simulations from this chapter onwards, the Simplorer model includes the main subsystems in Figure 5.1. The 3-phase short circuit sub-system is active only for short circuit simulations. The full Simplorer model for the diesel engine driven generator set can be found in Appendix E.

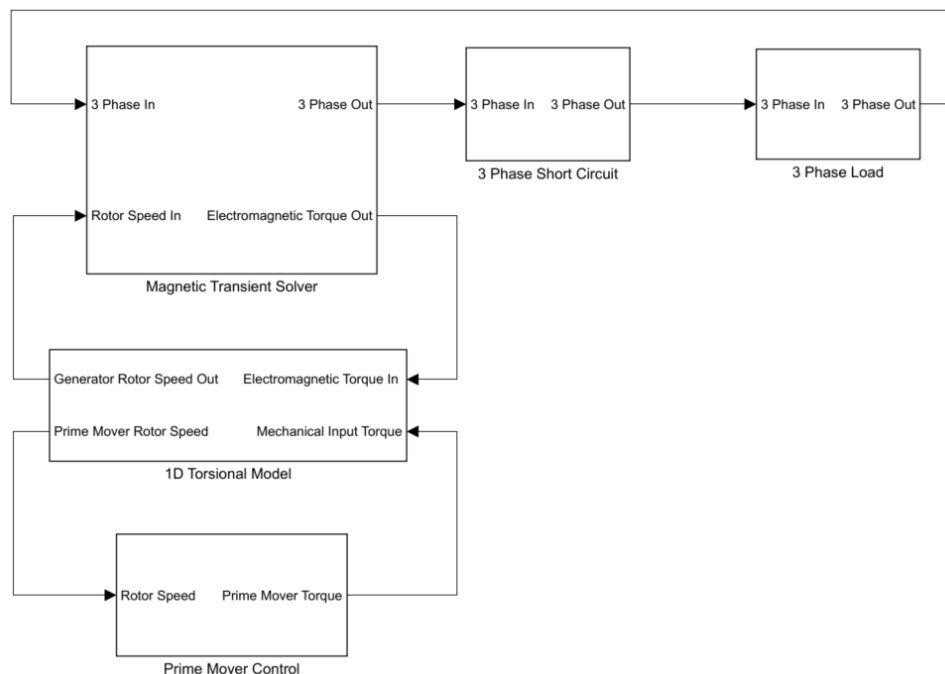


Figure 5.1: Block diagram for general co-simulation setup of the synchronous generator set.

The input and outputs of the magnetic transient solver block are linked directly to the Maxwell model of the generator defined in Chapter 4. The three phase branches of the generator terminals (U, V and W phases) are connected to the load sub-system through the short circuit sub-system. The load sub-system takes the form of either a resistive load for the short circuit simulations or a rigid voltage source in the case of the LVRT simulations. The short circuit sub-system contains time-controlled switches for each phase which are engaged to short all three phases together.

The 1D torsional model sub-system contains all the inertia and torsional stiffness elements for either the motor driven genset or the diesel engine driven genset. The magnetic transient solver block takes a speed input from generator rotor inertia element in the torsional model sub-system, and it outputs an electromagnetic torque signal to the torsional model which acts as the load torque for the generator rotor inertia.

The mechanical torque supplied by the prime mover is controlled by the prime mover control sub-system. This sub-system contains a PI control loop which compares the speed of the prime mover with the target speed of 157 rad/s and outputs a corrective torque to the prime mover inertia element. In the case of the electric motor, the torque is applied to the rotor core inertia and in the case of the diesel engine, the torque is split between six cylinder inertia elements. For this generator, the required torque is 364 Nm for 220V at full load, 100 Nm for 110 V at full load and 0 Nm for both cases at no load.

5.1.2 1D torsional mechanical model

The equivalent torsional stiffness of the generator rotor core is calculated from deflection results for a given torque applied in a static structural analysis of the 3DFE model. The stiffness of the shaft and coupling sections is calculated using Equation 2.27. Torsional stiffness and mass properties of the model are listed in Table 5.1. The stiffness and inertias of the diesel engine generator set are also calculated here for use later in the LVRT transient simulations.

Note that the inertia of the shaft under each component is included in the corresponding element inertia. In the motor/generator set the transducer rotor links the coupling sections together and is therefore included in the model. It is also the point in the structure at which the torque and speed is measured and is sensitive to the torsional stiffness of the coupling and the transducer rotor itself. The engine/generator set model contains the individual inertia elements for each piston on the crankshaft and the other engine train components to accurately obtain the torsional modes and correctly simulate the dynamic response of the system. The engine generator set is also linked by a coupling hub that has a significantly larger torsional stiffness than the transducer coupling used in the motor generator set.

Table 5.1: Mechanical properties of the motor/generator test genset

	Preceding Torsional Stiffness (Nm/rad)	Inertia (kgm ²)
NDE Bearing	0	0.0001
Exciter	537000	0.0511
Shaft 1	2890000	0.0026

Main Core	1200000	0.4720
Shaft 2	4420000	0.0021
Fan	3020000	0.0280
DE Bearing	8130000	0.0013
Shaft 3	3890000	0.0009
Coupling 1	559000	0.0087
Transducer	1165000	0.0045
Coupling 2	1165000	0.0687
Coupling 3	1176000	0.0397
Motor (lumped)	2000000	1.2000

Table 5.2: Mechanical properties of the diesel engine/generator genset

	Preceding Torsional Stiffness (Nm/rad)	Inertia (kgm ²)
NDE Bearing	0	0.0001
Exciter	537000	0.0511
Shaft 1	2890000	0.0026
Main Core	1200000	0.4720
Shaft 2	4420000	0.0021
Fan	3020000	0.0280
DE Bearing	8130000	0.0013
Shaft 3	3890000	0.0009
Coupling Hub	2011330	0.0671
Flywheel	2011330	1.2000
Gear	5106922	0.0101
Cylinder 6	1751267.5	0.0397
Cylinder 5	1175044	0.0275
Cylinder 4	1175044	0.0379

Cylinder 3	1175044	0.0379
Cylinder 2	1175044	0.0262
Cylinder 1	1175044	0.0389
CNGear	1852954	0.0030
Damper Hub	2689043	0.0547
Inertia Ring	90388	0.1243

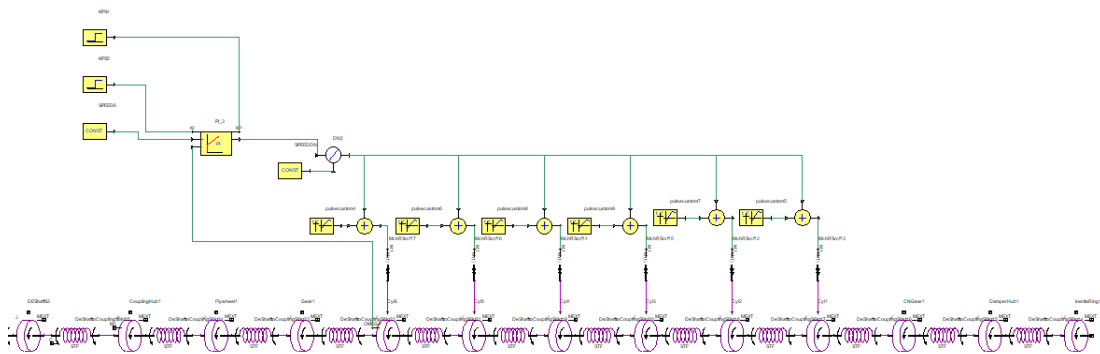


Figure 5.2: Torsional model of the diesel engine/generator set

The stiffness and inertia properties of the engine model are obtained from data sheets for the diesel engine. The diesel engine driven generator set model contains the same inertia and stiffness elements that form the generator up to the end of the generator shaft. Moving left to right in Figure 5.2; the mechanical components of the engine start with the coupling hub attached to the generator shaft, and end with the inertia ring at the non-drive end of the engine. Each of the six in-line cylinders are driven by a steady state torque source based on the torque produced during their firing cycle. The resulting average torque applied to the engine is 364 Nm. The engine driven generator model is only used in full voltage LVRT simulations; thus, the cylinder torque is set to produce an average 364 Nm only. The firing cycle follows that for a six cylinder in-line diesel

engine 1-6, 2-5, 3-4. The torque output of the engine at steady state, full load is shown in Figure 5.3.

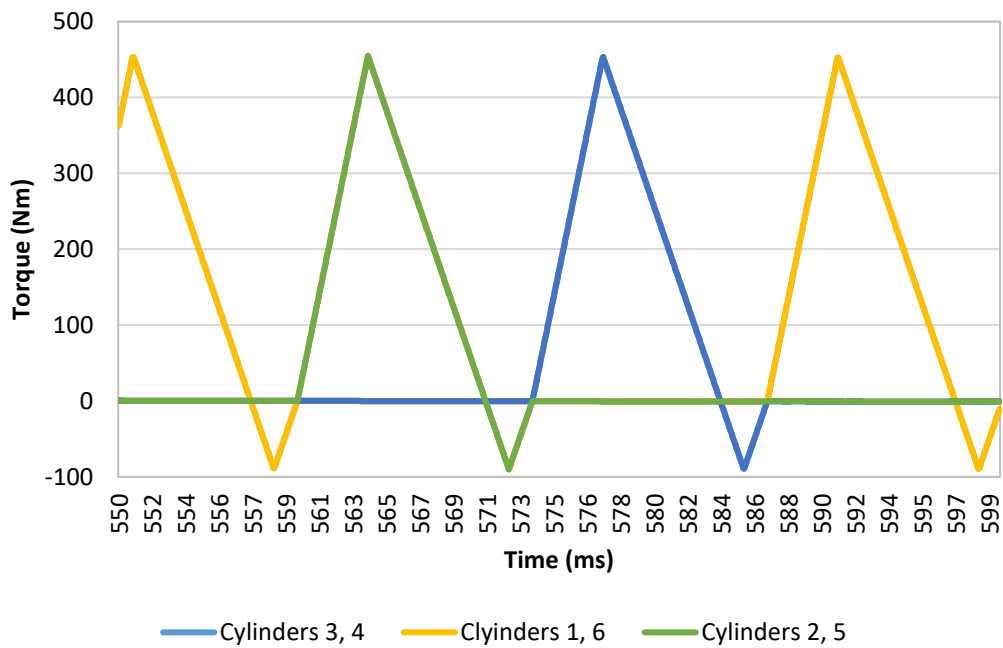


Figure 5.3: Steady state combined engine torque

5.1.3 Three-phase short circuit co-simulation setup

The phase lines from the magnetic transient sub-system are connected to a resistive load in the three-phase load sub-system and the three-phase short circuit sub-system is active. Current and voltage in the short circuit fault lines and across the load are measured through the voltmeter and ammeter elements in the circuit. The fault lines in the short circuit sub-system possess a resistance of 1Ω owing to the presence of the contactor and shorting bar connected to it. The resistance was adjusted to this value to correct the fault current measured in each phase. Once enough time has passed for the simulation to reach steady state, the short circuit subsystem is engaged. The torsional model sub-system contains the motor driven genset in this set-up.

5.2 Short circuit experimental test and simulation results

In the experimental three-phase short circuit tests, all three phase terminals are connected to the contactor short circuit lines. The first test is carried out at no load and half the target stator voltage and the second at full load and half stator voltage. The AVR is then connected in series to maintain the stator voltage at the target voltage, 220 V. A no-load test and a full load test is then performed at 220 V. Each test is performed three times to ensure the results are repeatable and one set of results is selected for each test. Transducer torque, transducer speed and terminal current measurements are captured simultaneously after the contactor short is removed.

Simulations for each of these short circuit tests are also performed using the motor driven generator set model. The current, speed and torque results from these models are compared directly with the experimental results. The field current in the generator model is manually adjusted for all three-phase short circuit simulations and until the peak current in the simulation closely matches the peak experimental current.

The speed and torque results for the analytical model are obtained from the inertia in the respective 1D model that represents the torque transducer between the two machines.

5.2.1 Half voltage (110 V RMS), full load three-phase short circuit

Figures 5.4 to 5.7 show the experimentally and analytically obtained stator current, transducer torque and transducer speed at no load and half the rated target stator voltage.

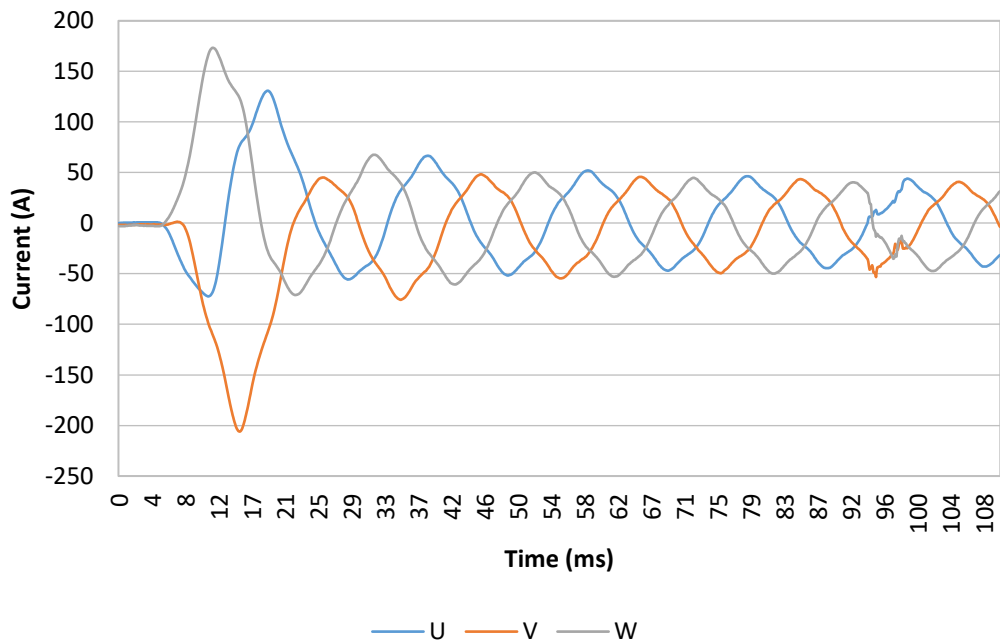


Figure 5.4: Experimental full load 110V 3-phase short circuit terminal current

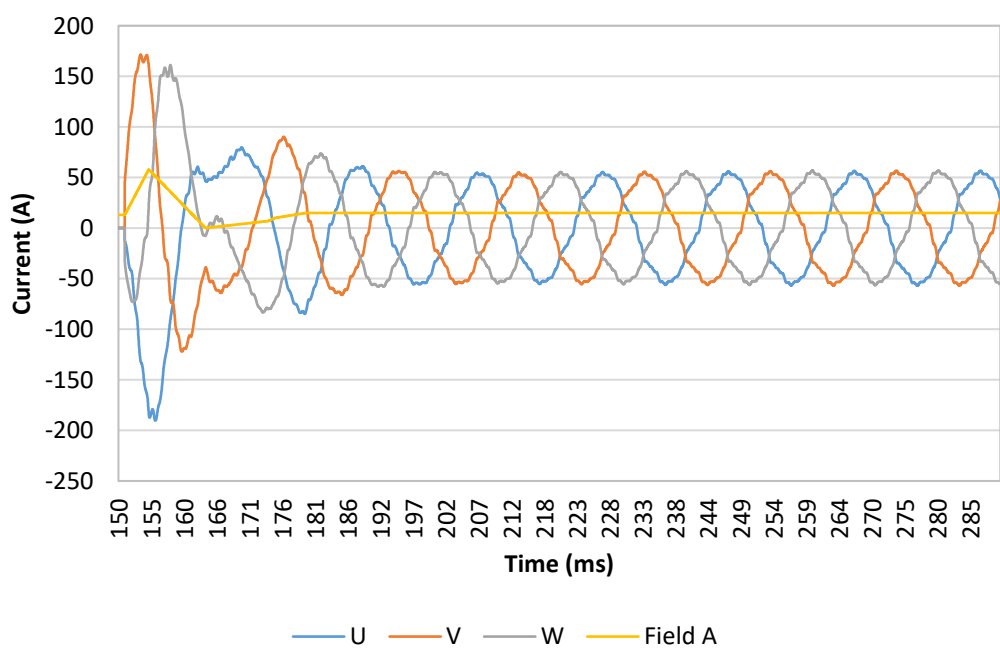


Figure 5.5: Simulation full load 110V 3-phase short circuit terminal current

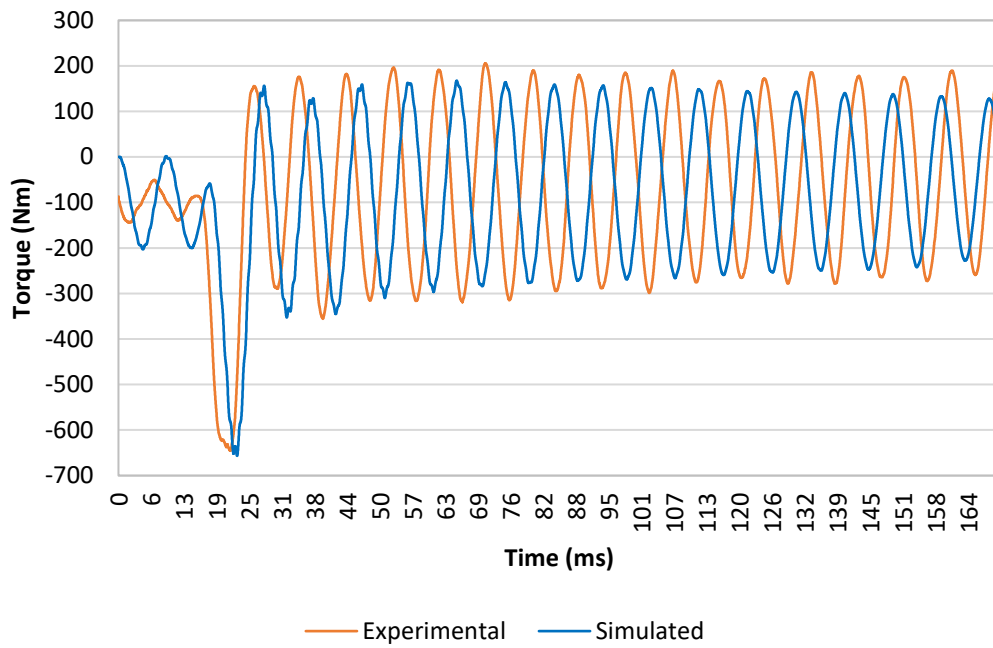


Figure 5.6: Simulation full load 110V 3-phase short circuit transducer torque versus experimental transducer torque

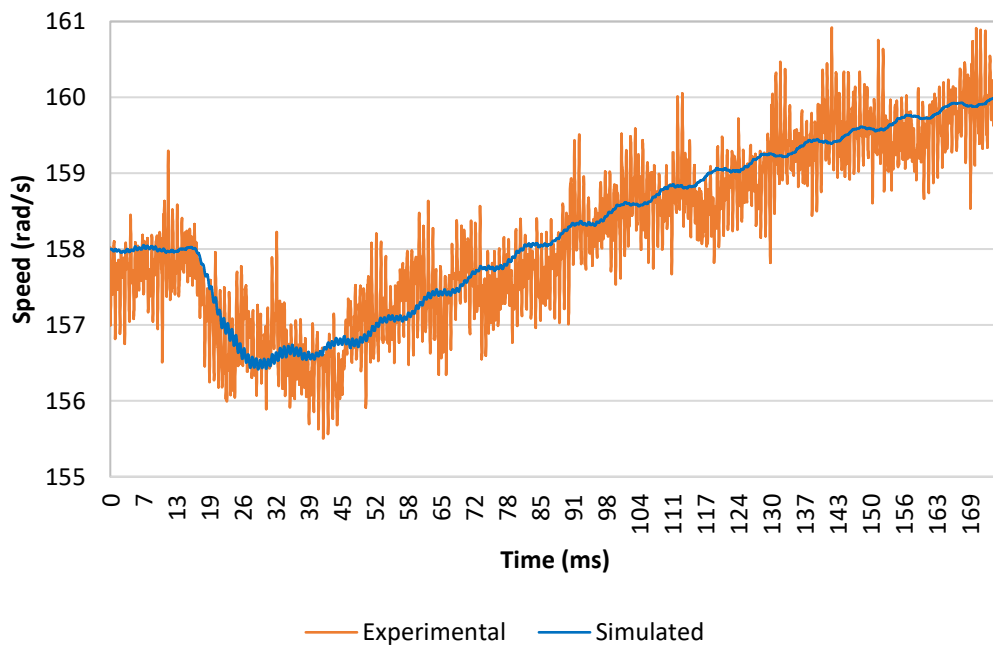


Figure 5.7: Simulation full load 110V 3-phase short circuit transducer speed versus experimental transducer speed

The results follow the expected trend for short circuit faults. The rotor speed drops immediately following the beginning of the short circuit within the sub transient period of elevated short circuit current. The fault current during the sub-transient period reaches a peak magnitude of 200 A, resulting in an increase in electromagnetic torque across the air gap. The peak torque measured at the transducer is increased from its steady state value of 100 Nm to 640 Nm and the amplitude of the following torsional oscillations are sustained at an average 200 Nm. Note that in the other two test runs, the peak torque reaches 700 Nm and 660 Nm. This variation in peak torque is produced as a result of the phase position of stator current at the point of short circuit initiation.

The angular speed drops by 1.8 rad/s over 30 ms, followed by a period of acceleration to 2 rad/s above steady state speed over the simulated time period. The average measured torque during this period of acceleration is lower than the steady state torque. This, combined with increased torque applied by the motor as the speed control responds to the drop in speed, produces a net positive acceleration for the generator set.

5.2.2 Half voltage (110V RMS), no load three-phase short circuit

Figure 5.8 to Figure 5.11 show the current, torque and angular speed results for the generator operating under no load conditions at half the rated voltage.

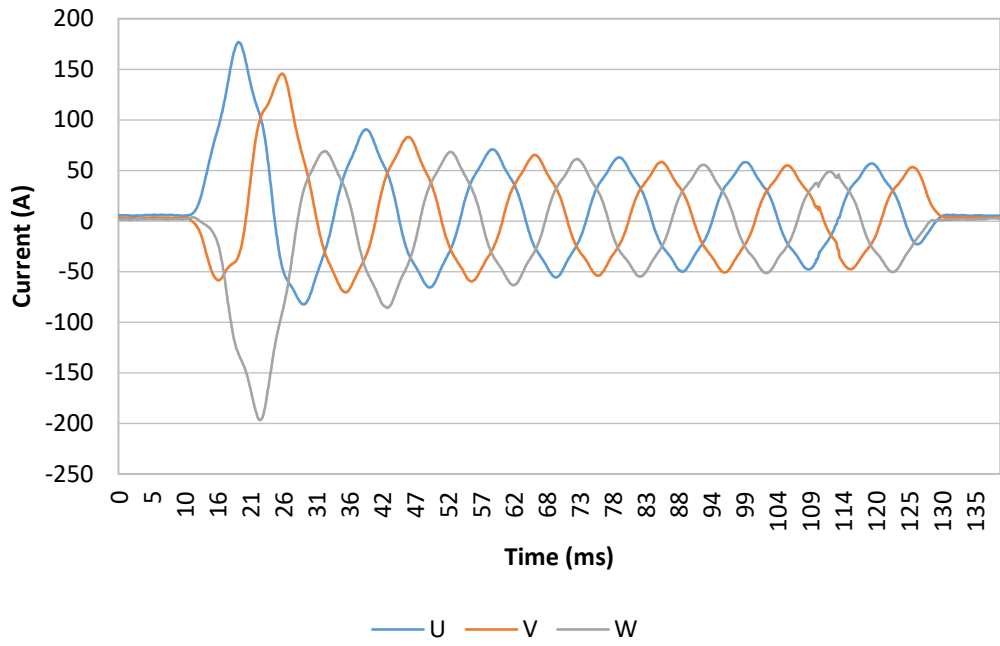


Figure 5.8: Experimental no load 110V 3-phase short circuit terminal current

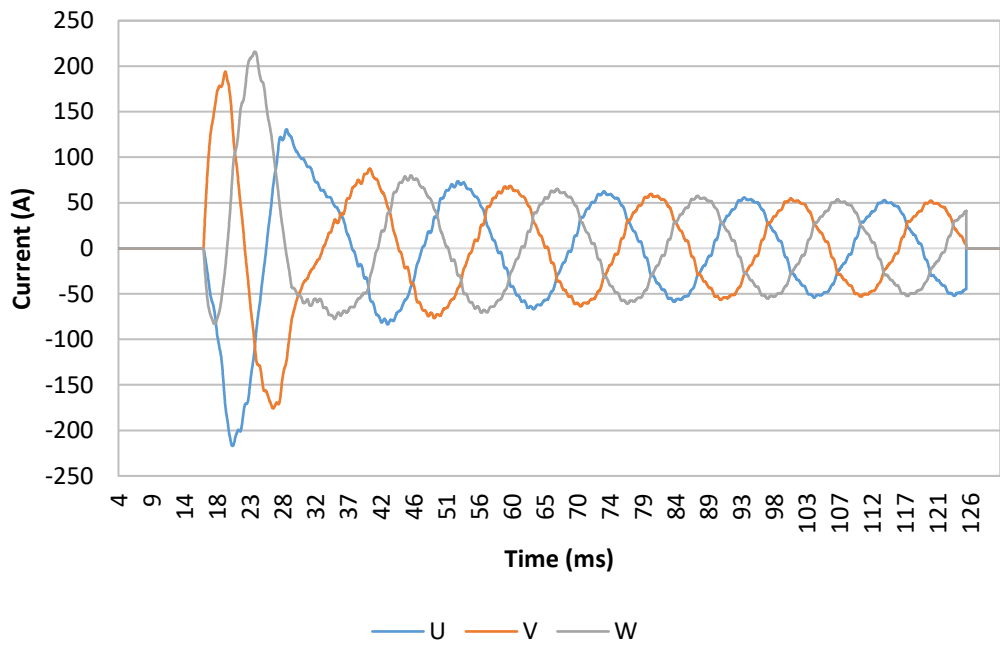


Figure 5.9: Simulation no load 110V 3-phase short circuit terminal current

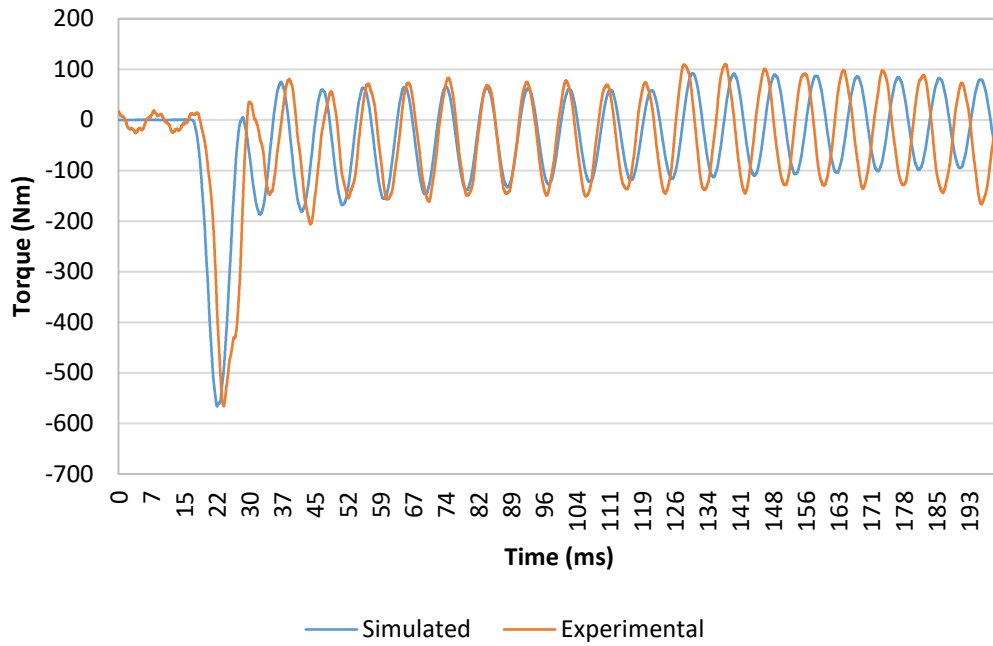


Figure 5.10: Simulation no load 110 V 3-phase short circuit transducer torque versus experimental transducer torque

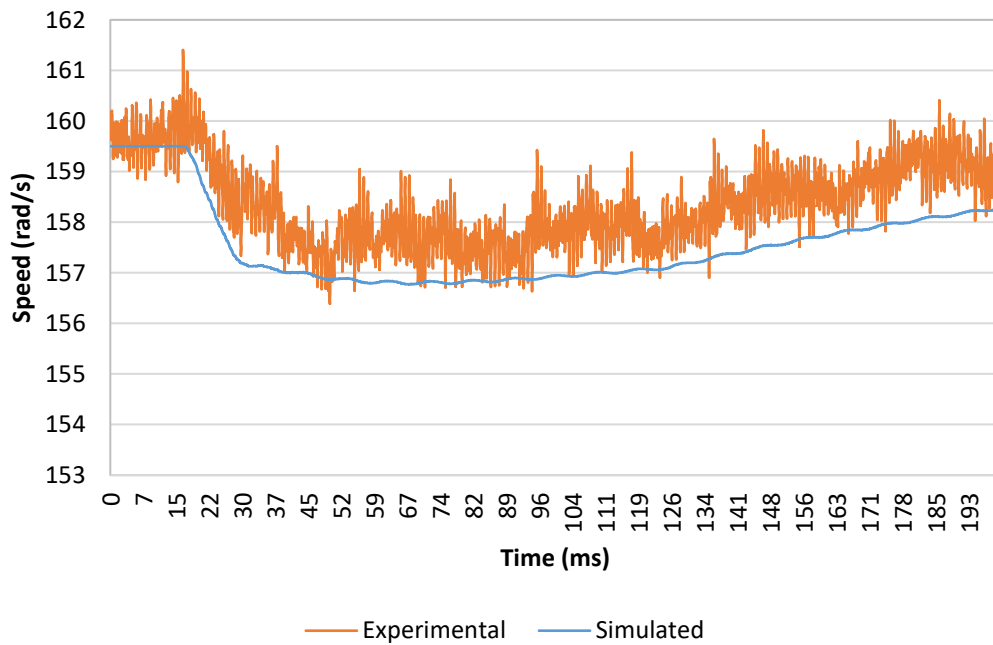


Figure 5.11: Simulation no load 110 V 3-phase short circuit transducer speed versus experimental transducer speed

The measured no-load fault current shown in Figure 5.8 above peaks at 200 A, the same amplitude as for the full-load test. However, the sustained short circuit current drops to 50 A as the field current remains at around 4 A compared to 13 A in the full load test.

In this test the steady state speed was slightly higher than the target speed, at 159 rad/s. The rotor acceleration during the short circuit at no-load is significantly lower over the same time period when compared to the full-load case as a result of the motor torque being only around 20 Nm. This is enough to sustain the 4 A field current and 110 V terminal voltage but not enough to sustain any generator output load. The torque measured at the transducer peaks at 555 Nm and the sustained torsional oscillation falls to 100 Nm, half the amplitude of that in the full-load test. Note that in this test the steady state speed was slightly larger than the target speed, at 159 rad/s. The difference in the intended speed makes no significant difference to the results, especially during no-load operation.

5.2.3 Full voltage (220 V RMS), full load three-phase short circuit

A three-phase short circuit test was carried out on the machine to obtain the fault current, coupling torque (measured at the torque transducer) and coupling speed when operating at full load. These results are provided in Figure 5.12 to Figure 5.15. They provide a direct comparison between the experimental results and the results from a simulation of the same fault using the multi-physics model of the motor driven generator set.

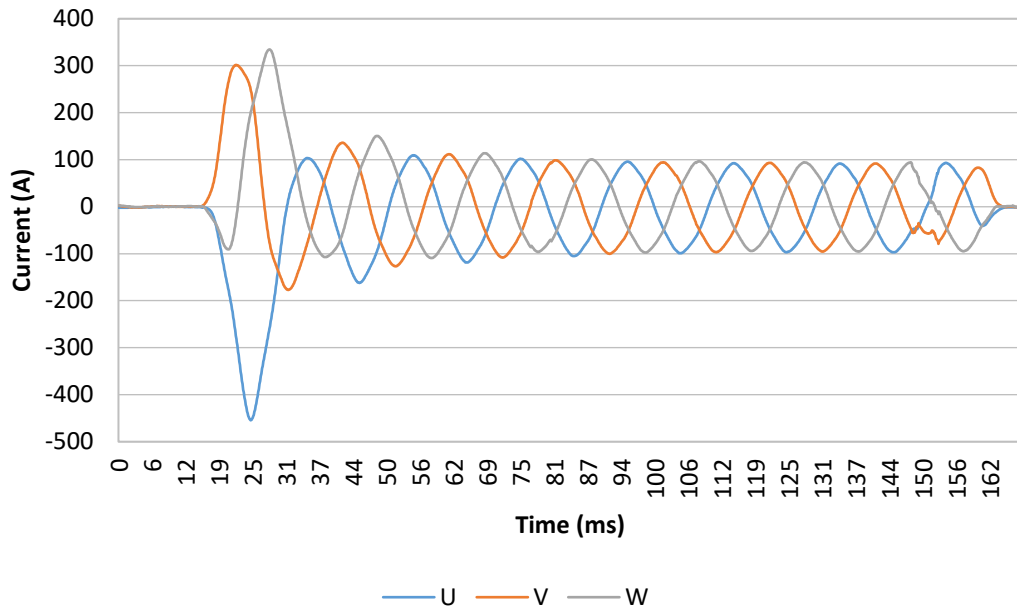


Figure 5.12: Experimental full load 220 V 3-phase short circuit stator current

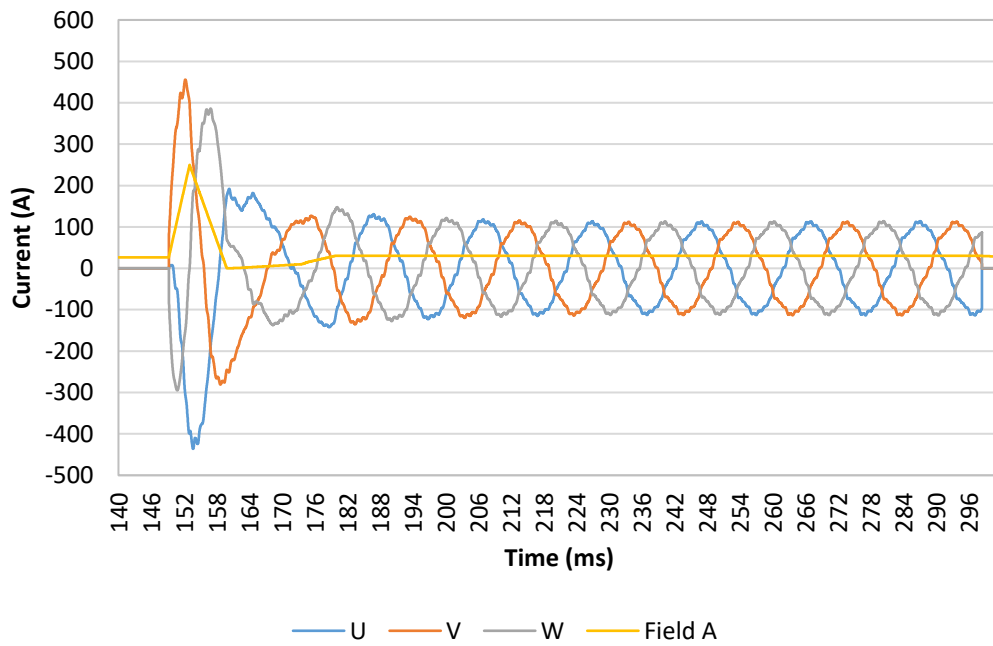


Figure 5.13: Simulation of full load 220 V 3-phase short circuit stator current

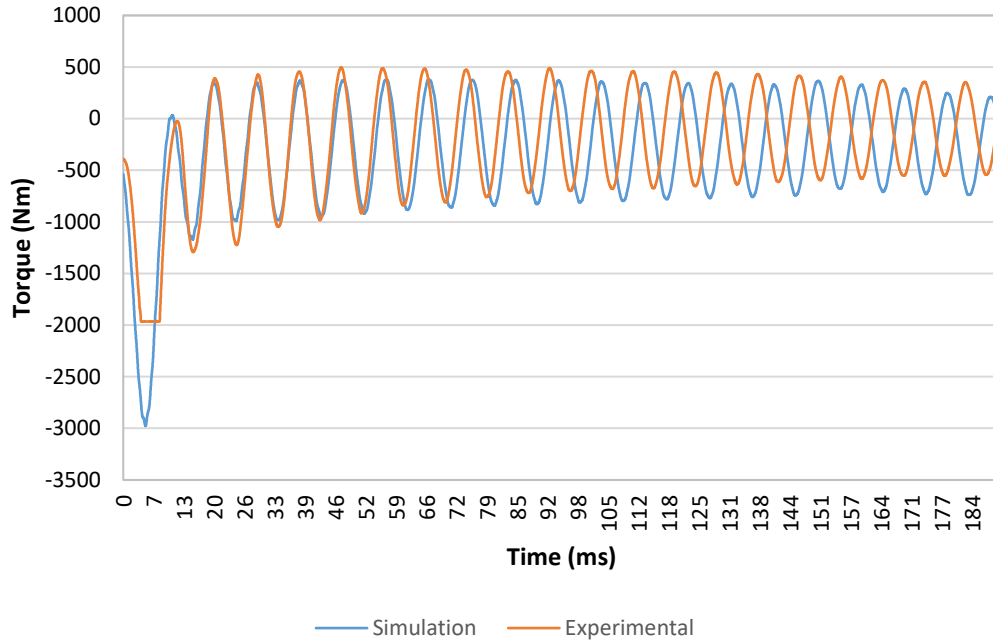


Figure 5.14: Simulation of full load 220 V 3-phase short circuit transducer torque versus experimental transducer torque (scaled)

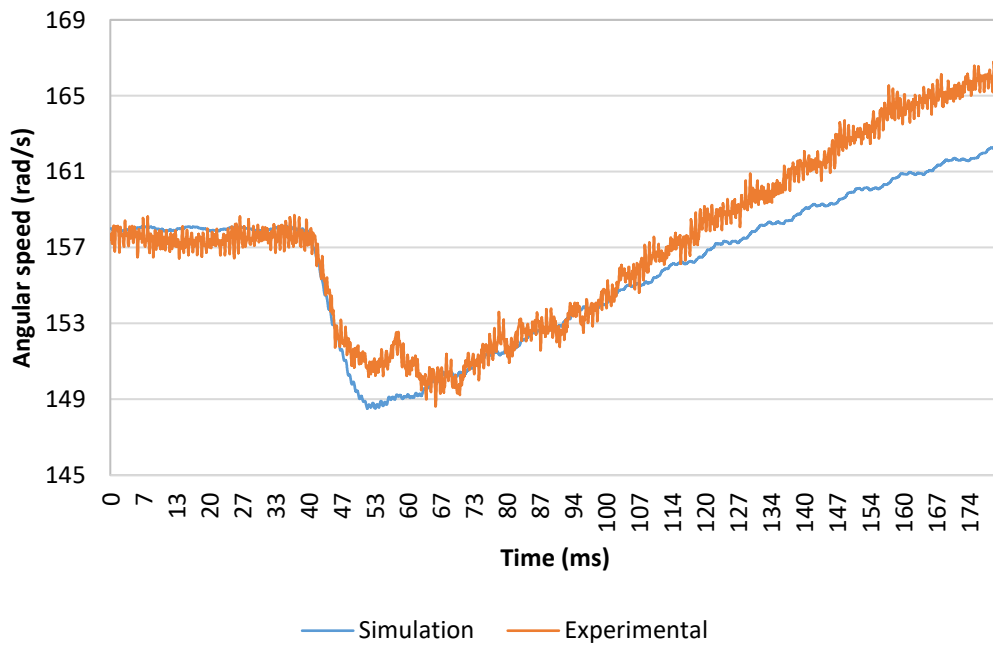


Figure 5.15: Simulation full load 220 V 3-phase short circuit transducer speed versus experimental transducer speed (scaled)

This model closely matches the performance of the real synchronous generator, particularly during the sub-transient period in the transducer torque results. Note that the peak torque is trimmed due to the 2 kNm measurement limit of the torque transducer but the gradient of the of the curve prior to and following this limit is similar that of the simulated curve, suggesting a similar peak is achieved by the model. The model used in this simulation is developed further in Chapter 6 to prepare for the simulation of LVRT faults

5.2.4 Full voltage (220 V RMS), no load three-phase short circuit

The previous simulation is repeated with the generator operating under no-load conditions to ensure that the model is valid over a range of load conditions, the results are shown in Figure 5.16 to 5.19. The torque and speed results are extended over the FRT period to show the difference between the simulation results and experimental results over the post fault period.

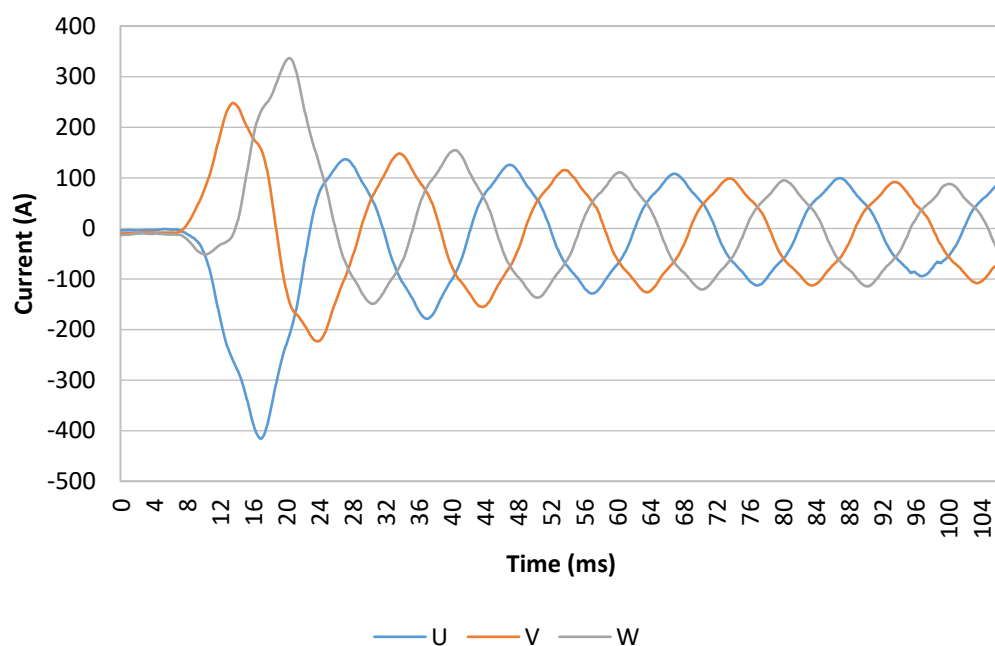


Figure 5.16: Experimental no load 220V 3-phase short circuit stator current

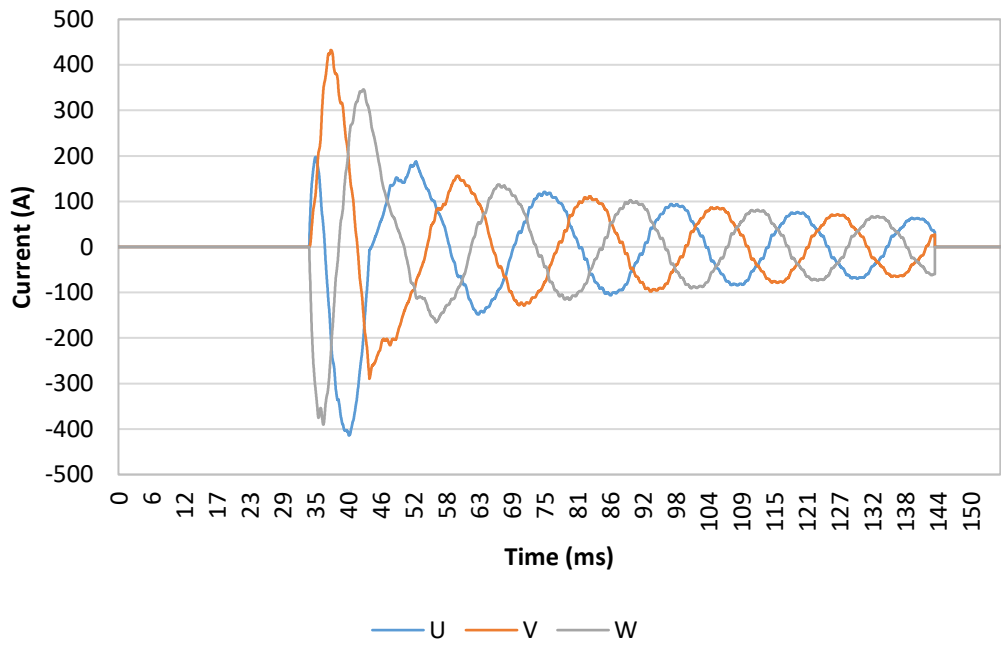


Figure 5.17: Simulation no load 220V 3-phase short circuit stator current

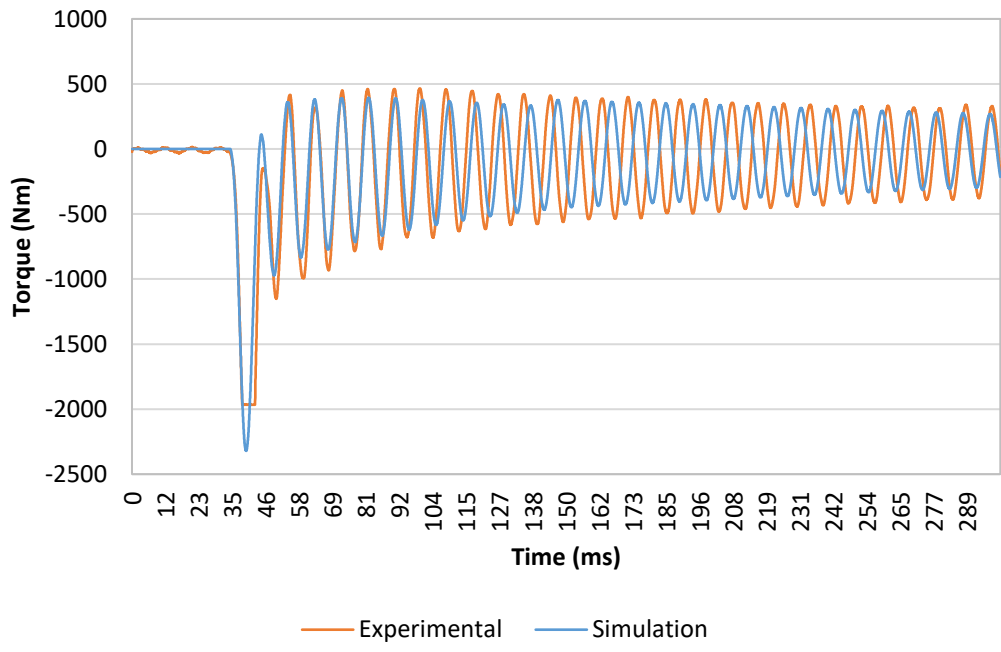


Figure 5.18: Simulation no load 220V 3-phase short circuit transducer torque versus experimental transducer torque

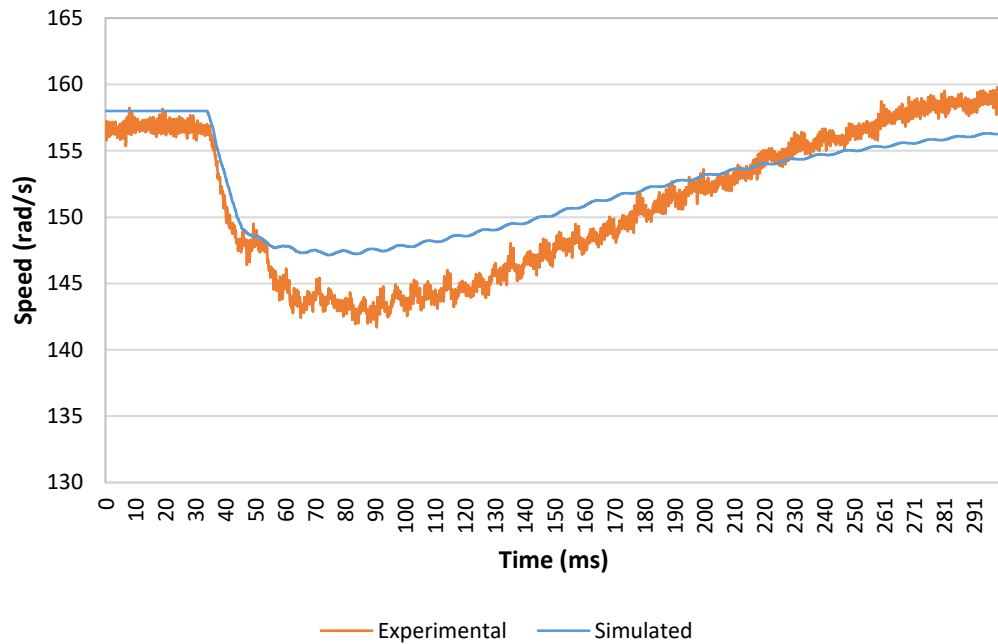


Figure 5.19: Simulation no load 220V 3-phase short circuit transducer speed versus experimental transducer speed

In the no load case, the simulation sustains a slightly lower average torque and maximum speed increase during the short circuit than the experimental results show. The slower rotor speed recovery in the simulation results also causes the decreased frequency of torsional oscillations. An increase in motor torque control gain, alongside an increase in sustained rotor current and three-phase short circuit resistance (to increase short circuit load) could be applied to tweak the simulation results until they perfectly match the experimental results.

The full load case sees a greater peak torque during the short circuit as shown in Figure 5.17, but the minimum speed reached (Figure 5.19) is still lower than in the experimental results. In this case, further improvements to the accuracy of these results could be made by again increasing the motor torque control gain. The sustained short

circuit current is evidently slightly greater than in the experimental test and thus the sustained rotor current should be decreased, or the short circuit resistance can be increased.

In addition, the short circuit is not applied at the exact same phase angle in the simulation as it is in the experiment. Thus, the peak currents of each phase during the sub-transient period do not match those from the experiment. The amplitude of each phase peak is however reasonably close to the experimental results and provided this, the peak electromagnetic torque and thus peak transducer torque are a good match.

5.3 Simpler transient short circuit testing: Influence of variables on results

During the initial attempts to match the simulation results to the experimental results and validate the electromagnetic models, some adjustments were made to the available electromechanical parameters in the Simpler model. The adjustments made provide an insight into the effect of both the mechanical and electrical variables on the speed, current and torque of the generator during three-phase short circuit events. This knowledge is also required when developing improvements to the fault ride through capability of the generator which is covered in more detail in Chapter 8.

5.3.1 Voltage and field current

The first key relationship to note is that between the generator voltage and the peak short circuit current. When the stator/terminal voltage is reduced to half its original

value, the resulting fault currents for a three-phase short circuit are also halved. The peak fault current is also not affected by the electrical load present prior to the short circuit.

Recall that a series star winding connection scheme is utilised for both half voltage and full voltage short circuit tests. Half voltage operation can also be achieved with a parallel star connection, but the severity of fault (current, torque and speed drop) is even greater for such connections (1.5 x peak current for symmetric fault on the decrement curve for the UC22F machine). The choice of winding configuration must therefore also be considered when measuring the performance of the machine during short circuit.

Close attention must be paid to the field current during the short circuit fault, particularly at the beginning of the fault and throughout the sub-transient region. The field current sharply increases at the start of the fault as the energy stored in the main stator field is released. The magnitude and time period of the peak field current significantly affects the peak torque magnitude and the magnitude of all the following torsional oscillation peaks thereafter. If the peak fault current is sustained for even a fraction of a millisecond longer, the resulting sustained electromagnetic torque can significantly increase the magnitude of oscillatory torque and also reduce the angular speed further.

The magnitude of the steady state fault current is dependent on the sustained field current during the fault. AVR systems with an external power supply will aim to restore the target stator voltage during the latter stages of the transient and the steady state time envelope. This typically results in a steady state sustained fault current of around 300%

of the rated current of the machine. AVR systems that are powered directly from the generator stator, as in the case of the AVR used in these experiments, are incapable of maintaining the target 300% rated load fault current. As a result, the fault current drops to a significantly lower magnitude as seen in the experimental results, to around 50 A for 110 V and 100 A for 220 V (66). The AVR did not appear to increase the field current above the value required to maintain its target voltage at steady state. The field current input is therefore maintained at pre-fault levels to match this behaviour following the peak induced field current.

5.3.2 Simulation time step

As previously mentioned, the time step size should be carefully chosen in order to obtain accurate results from the simulation. This is particularly important for transient analyses. In the case of the very fast transients analysed in this model, the transducer torque results are extremely sensitive to the time step, largely due to the complexity of the 1D torsional model. The previous step size of 0.2 ms that was suitable for steady state simulation is not appropriate for fast transient simulation, using such a step size results in artificially damped torsional oscillations. The peak magnitudes of stator current, electromagnetic torque and transducer torque are also significantly reduced when using a relatively long time step. A step size of 0.02 ms is instead selected which is capable of capturing the full range of torsional displacement in the 1D torsional model, additional detail is also added to the fault current and angular velocity results. A slightly longer step size of 0.05 ms is also commonly used throughout the LVRT analysis section due to long simulation time requirements, particularly in the case of extended ride through periods lasting up to 750 ms.

5.3.3 Line resistance and load

The line resistance determines the resistance in the phase connections to the connected load, this may include resistance of power control and transfer equipment in a real power generation system. In a generator the line resistance is typically very small compared to the inductance of the generator, in the case of the test motor driven generator set, the load is purely resistive and connected directly to the generator and so the line resistance is determined entirely by the load. Note that this is true primarily in the case of three-phase short circuits. For single phase and two-phase short circuit faults, some line resistance is still connected to the generator during the fault. Thus, the sustained fault current is affected by the line resistance. The load connected to the machine has little impact on the speed, torque, and fault current during the short circuit fault. However, when the load is reconnected a measurable difference in fault current may be observed.

5.3.4 Fault resistance

The fault resistance, the resistance between the three shorted phases, significantly affects the current, speed and torque results measured during a fault. The synchronous reactance of the generator is partly determined by the L/R ratio in the winding circuit to the connected short circuit, hence the fault resistance partly determines the peak sub-transient fault current and the "damping" or rate of decay of the fault current. Increasing fault resistance reduces the peak fault current, increases the rate of decay of fault current and also reduces noise in the waveform over the first few cycles, but also acts as a resistive load, thus increasing the magnitude of sustained fault current.

The stator winding resistance is relatively small (0.0325Ω per phase branch in series) compared to the fault resistance in these experiments (1Ω). The resistance of the contactor (and copper shorting bar) represents the bulk of the resistance in the three-phase fault circuit. This impedance is significantly larger (almost twice as large) than that of the test machine used by the manufacturer to produce the official short circuit performance information. Hence the short circuit current is reduced in the experimental test results for the motor driven generator set by a factor (2) equivalent to the increase in fault resistance.

5.3.5 Rotor inertia

The inertia (about the axis of rotation z) for each element in the generator set models strongly influences the acceleration of the rotor during fast transients. The generator rotor and prime mover rotor inertias also affects the shaft torque experienced between the two machines. A generator rotor with high inertia will decelerate relatively slowly during the short circuit fault. Adding inertia to a generator set to reduce acceleration during fault ride through as described in Chapter 1 is a possible solution, but the minimum acceleration achievable is limited somewhat by the physical size of the machine. Rotor inertia does not significantly affect the fault current or electromagnetic torque during three-phase short circuit events but it does strongly influence the change in rotor angle during the fault ride through period. For the load bank connected configuration, the shift in rotor angle during a short circuit does not make any difference to the electromagnetic performance of the machine. But for a generator connected to a grid or larger power supply network where rotor synchronisation is vital, the shift in

rotor angle and rotor speed determines the magnitude of the current and torque at the point of reconnection to the grid. Typically, a high inertia system will experience lower rotor angle shift and rotor acceleration during the fault and thus smaller current transients.

5.3.6 Component torsional stiffness

The torsional stiffness determines the relative torsional displacement between inertias in the generator set assembly. The presence of the transducer and its adapter couplings reduces the equivalent coupling stiffness between the generator and motor somewhat (a direct coupling such as that used in a single bearing generator, coupled directly to the engine flywheel has a significantly higher equivalent coupling stiffness). The torsional stiffness of the assembly influences the peak magnitude and frequency of oscillatory torque measured at the transducer, it also affects the rate of decay in the oscillations to a lesser extent in a similar manner to the damping present. Since the torsional stiffness for all components in the test generator set are known, they remain unchanged throughout the three-phase short circuit tests. Note that using incorrect values of torsional stiffness can significantly alter the torsional results. During the early testing stages, a solid rotor core with a greater torsional stiffness than the real core was used in the torsional model. The resulting shaft torque was clearly incorrect when compared with the experimentally obtained torque.

5.3.7 Motor speed control

The speed control system for the electric motor has a significant impact on the speed of the generator set and the torque applied by the electric motor. Neglecting to include the speed control results in an exaggerated deceleration during the fault and a slow recovery back to steady state speed. In reality the motor control increases the applied motor torque when the system speed drops and overshoots the steady state speed during the fault and undershoots during the resynchronisation recovery period. In the Simplorer model, speed control is achieved via a PI control loop. Within the PI block the gain, integral gain and derivative gain values are varied to match the experimentally obtained speed and torque response for the generator/motor set.

5.3.8 Fault start time

As previously mentioned, the time that the fault is started can affect then peak current and torque results for three-phase short circuits. It is vital to ensure that the simulation is running at steady state at the moment the short circuit is applied. If for example the transducer torque or speed does not match that measured in the experiment at this time, the resulting sub-transient peak values will increase or decrease relative to this error.

5.3.9 Chapter summary

This section covers the creation of the multi-physics model of a motor driven generator set by coupling the electromagnetic model constructed in Chapter 4 with a 1D torsional

model of the generator set which is constructed using torsional stiffness data derived from the 3DFE model that is built in Chapter 3.

The steps taken in this chapter are as follows:

- The electromagnetic model is imported into a new Simpler model which contains an electrical circuit which connects the three terminal phases from the generator model to a resistive load and a three-phase circuit breaker.
- The 1D multi-inertia torsional model of the experimental generator set is constructed using torsional stiffness and inertia properties derived from the 3DFE model, test machine and datasheets. A simple PI speed control loop for the motor is included. A similar 1D model is also constructed here for the diesel engine driven generator set which is used following validation of the motor driven generator set. Both mechanical models are connected to a copy of the electromagnetic model to produce two multi-physics models. One of the motor driven genset and one of the engine driven genset.
- Experimental three-phase short circuit tests are performed on the motor driven generator set at both half and full voltage, rated load and no-load. Three-phase short circuit faults are also simulated on the motor driven genset model and the stator/terminal current, rotor speed and rotor torque results are compared. The field current and coupling stiffness properties are fine tuned to ensure a match between the analytical results and experimental results.
- The influence of a range of different variables on the short circuit results is also considered at the end of this chapter for further consideration in the LVRT testing section.

The key points from this chapter are as follows:

- The electromagnetic and mechanical models of the motor driven genset are successfully coupled together using Simplorer to form the first multi-physics model.
- This model produces current, speed and torque results during that closely match those obtained from the experimental three-phase short circuit test under both full and no load. The model is validated for short circuit faults, forming the starting point for the simulation of LVRT faults in Chapter 6.
- The simulation time step (0.05 ms) for further LVRT simulations is decided upon following the comparisons made between experimental and analytical results.

The work completed here is used in the following chapters as follows:

- The multi-physics models of the motor driven genset and the engine driven genset are used in Chapter 6 to simulate 100% voltage drop faults over various FRT periods.
- The models are adjusted for LVRT testing in Chapter 6, (resistive load changed to voltage sources to simulate the grid, flexible coupling added).
- Both engine and motor driven genset models are used in Chapter 7 to validate their equivalent ANSYS 3DFE models (using torque and speed results) which are used for stress analysis.
- The engine driven genset model is used in Chapter 8 when it is modified to improve LVRT performance.

Chapter 6 Low voltage fault testing with the multi-physics generator set model

6.1 LVRT tests with the grid connected model

Following on from the three-phase short circuit testing, the validated Simplorer model of the motor driven generator is altered to be suitable for grid connected simulations. The resistive element is removed and replaced with voltage sources for each phase representing connections to the grid as shown in Figure 6.1. The three-phase voltage is equal to the rated voltage of the machine connected in the series star configuration at 380 V and 50 Hz, the same as for the full voltage three-phase short circuit tests. The voltage is controlled manually using step signals to define the time at which the supply voltage is changed. This enables the simulation of partial and full voltage drop faults, with the latter effectively disconnecting the supply entirely in a similar manner to a three-phase short circuit.

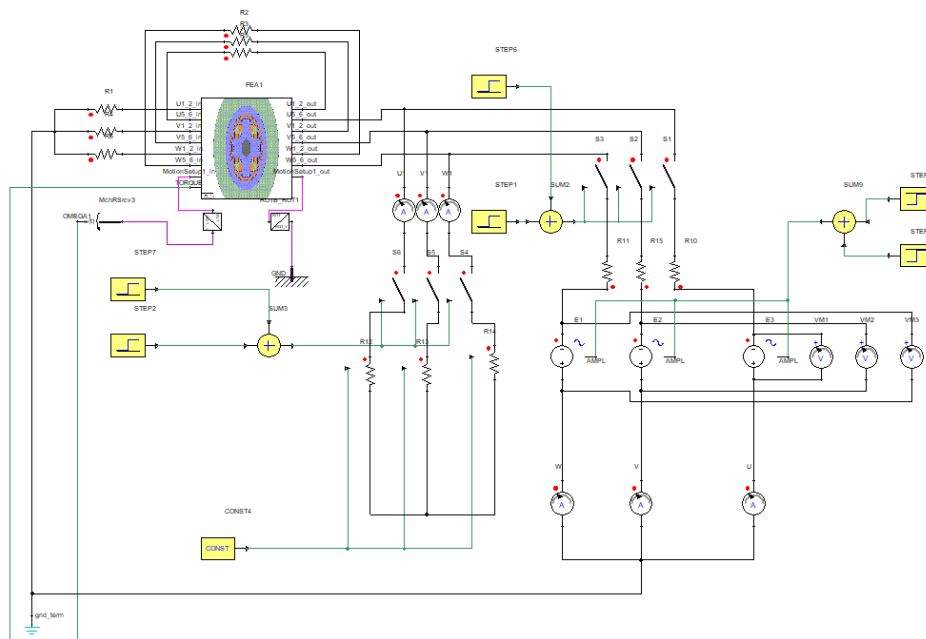


Figure 6.1: Grid connected generator set Simplorer model

The voltage phase is also adjusted to alter the power factor of the machine (changing the initial rotor angle in Maxwell does not affect power angle power factor in a co-simulation model). The first set of tests are performed with the generator operating at a power factor of 1, as it is in the short circuit tests, in order to validate the LVRT simulation against the three-phase short circuit results. For a full 100% voltage drop, the sub-transient current and torque is confirmed to match that obtained from the three-phase short circuit tests. Later in this section, the power factor is reduced to a 0.8 lagging power factor to simulate the conditions under which the real generator produces power when connected to the grid. This is achieved by iteratively shifting the supply voltage phase and observing the power angle between stator voltage and current.

The three-phase short circuit line is still used in this model for some comparative simulations, but the switches remain open for the majority of grid connected LVRT simulations. The resistive elements on the grid connected line here represent the line resistance only (0.1Ω per phase), since the load resistance is replaced with supply voltage sources.

The grid connected circuit is used for LVRT simulations, starting with the motor driven generator model and then progressing on to the diesel engine driven generator model. The diesel engine generator set model builds on the validated electromechanical behaviour established in previous simulations by introducing performance altering adjustments to the model (adding a flexible coupling, then engine related time delays etc.). These adjustments are made in steps to highlight their impact on the LVRT behaviour of the machine and ultimately build a full picture of how a diesel engine generator set behaves during low voltage faults and allowing for certain behaviours

(such as sudden spikes in transient torque) to be traced back to those previous adjustments.

Three different time periods of fault ride through are selected to investigate the behaviour of the machine under low voltage fault conditions, 40 ms, 180 ms and 320 ms. UK grid codes demand that the machine stay connected to the grid for 140 ms for a 100% voltage drop fault, the extended ride through times simulated here demonstrate the danger of allowing the machine to remain connected beyond the requirements of the grid codes.

6.1.1 100% voltage drop: 40 ms fault ride through

The initial low voltage fault ride through test is performed by disconnecting the supply for 40 ms and simulating a 100% voltage drop. As with the full voltage three-phase short circuit test, the field current is increased (~250 A) during the first few milliseconds within the sub-transient envelope of the fault ride through time. The torsional model for the generator driven motor genset is used here with the speed control of the prime mover remaining the same as in the short circuit tests (both normal and integral gain remain the same at 15 and 10 respectively). The fault is initiated 311 ms from the start of the simulation. The simulation results for electromagnetic torque, transducer speed, fault current / line current, transducer torque and motor torque are shown below in Figure 6.2 to Figure 6.7.

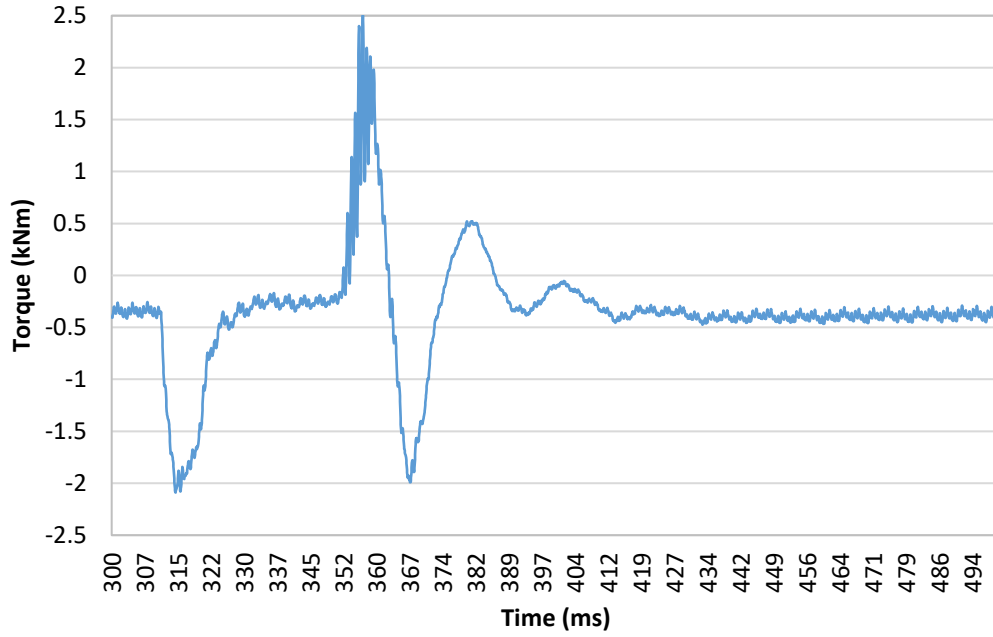


Figure 6.2: 100% voltage drop fault applied to motor driven generator set, PF = 1. Air gap electromagnetic torque for 40 ms FRT.

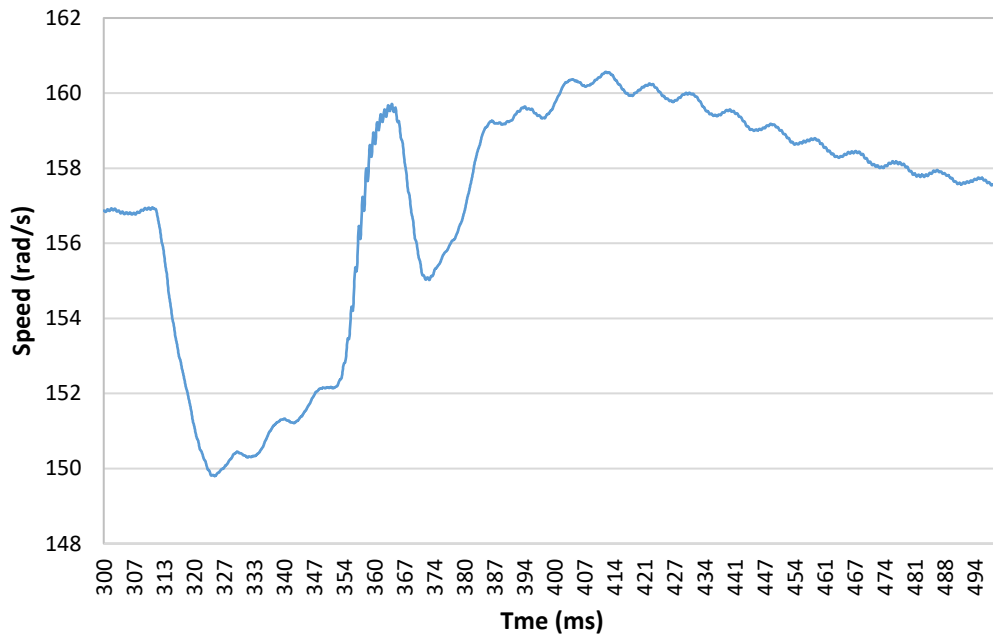


Figure 6.3: 100% voltage drop fault applied to motor driven generator set, PF = 1. Transducer speed for 40 ms FRT.

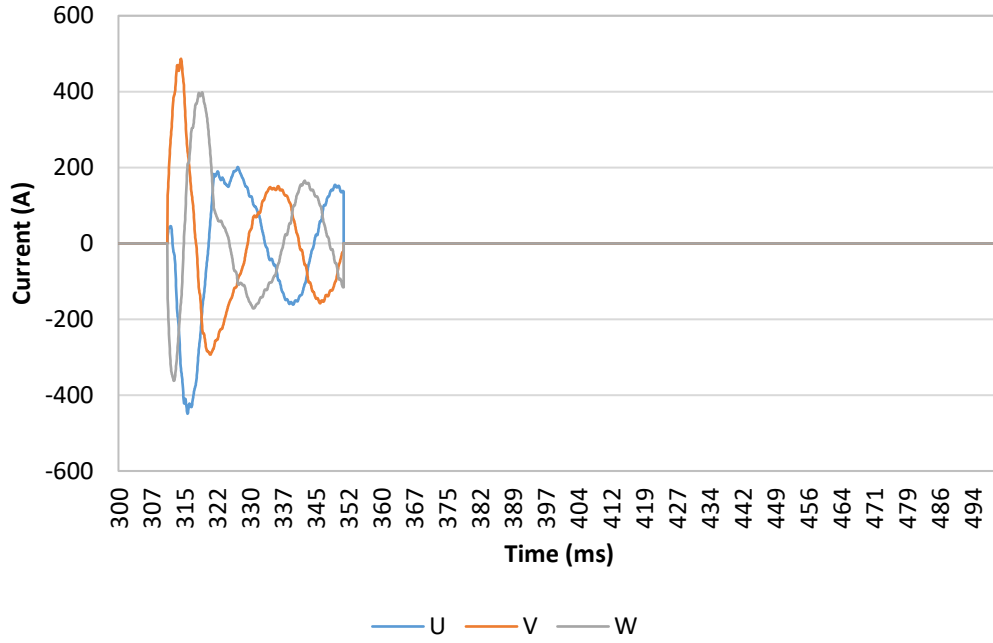


Figure 6.4: 100% voltage drop fault applied to motor driven generator set, PF = 1.

Fault current for 40 ms FRT.

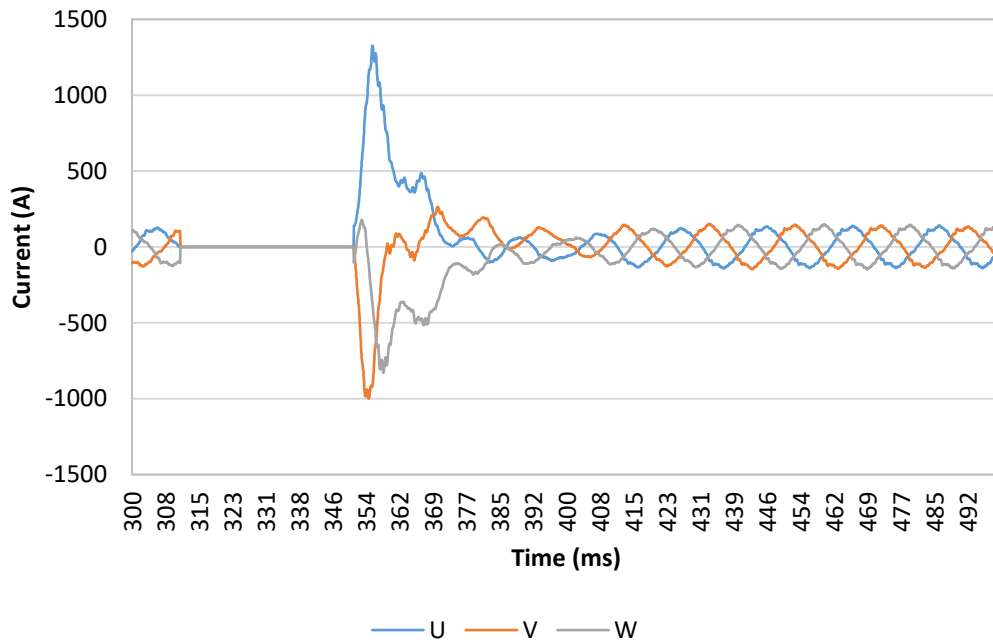


Figure 6.5: 100% voltage drop fault applied to motor driven generator set, PF = 1.

Line current for 40 ms FRT.

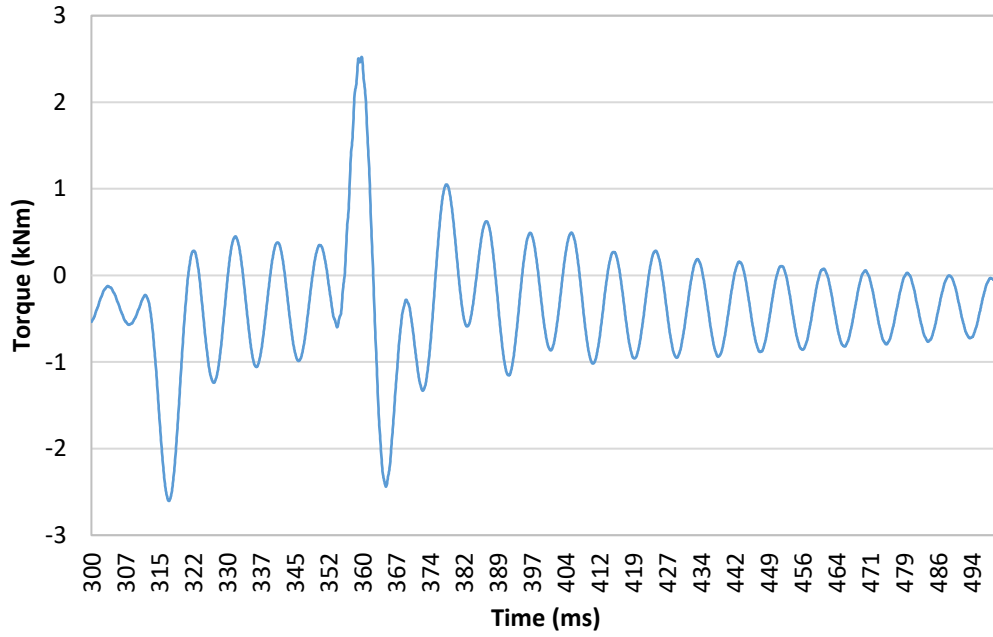


Figure 6.6: 100% voltage drop fault applied to motor driven generator set, PF = 1.

Transducer torque for 40 ms FRT.

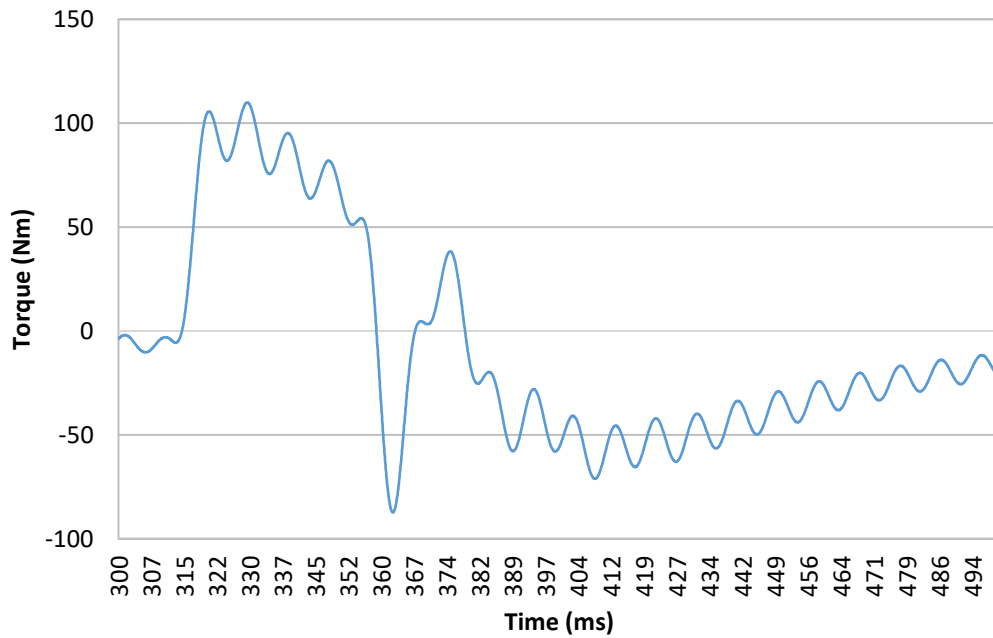


Figure 6.7: 100% voltage drop fault applied to motor driven generator set, PF = 1.

Motor torque control response for 40 ms FRT.

6.1.2 100% voltage drop fault: 180 ms ride through

The ride through period is extended to 180 ms. The fault is initiated at the same time as in the 40 ms test, at 311 ms in order to begin the test under normal steady state conditions. This also ensures that each current line is in phase at the point of grid disconnection (grid voltage dropping to 0 V) and the magnitude of the initial electromagnetic torque peak is exactly the same. Note that the electromagnetic torque oscillates at steady state at 50 Hz, if the phase of currents is shifted at the point of disconnection then the resulting electromagnetic torque will also be altered which adds or subtracts from the peak torque of the initial fault torque peak. This results in a relatively small but still noticeable rotor acceleration or deceleration which ultimately shifts the rotor angle at the point of grid reconnection. This would be unacceptable when studying the impact of rotor angle shift on reconnection torque. An identical simulation start time is used for the 320 ms fault ride through simulation. The simulation results for electromagnetic torque, transducer speed, fault current / line current and transducer torque are shown below in Figure 6.8 to Figure 6.12.

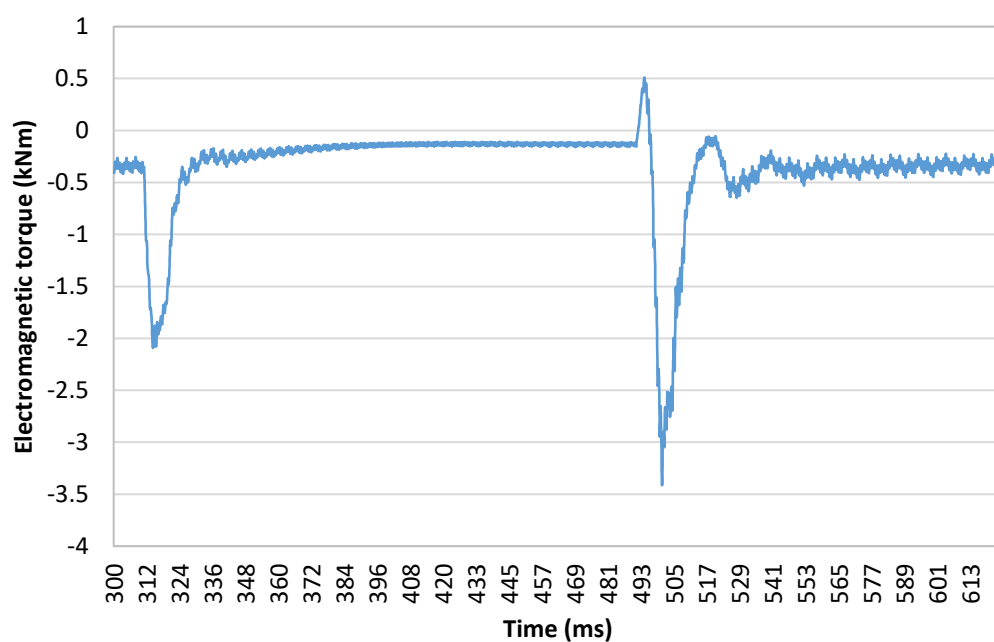


Figure 6.8: 100% voltage drop fault applied to motor driven generator set, PF = 1.

Electromagnetic air gap torque for 180 ms FRT.

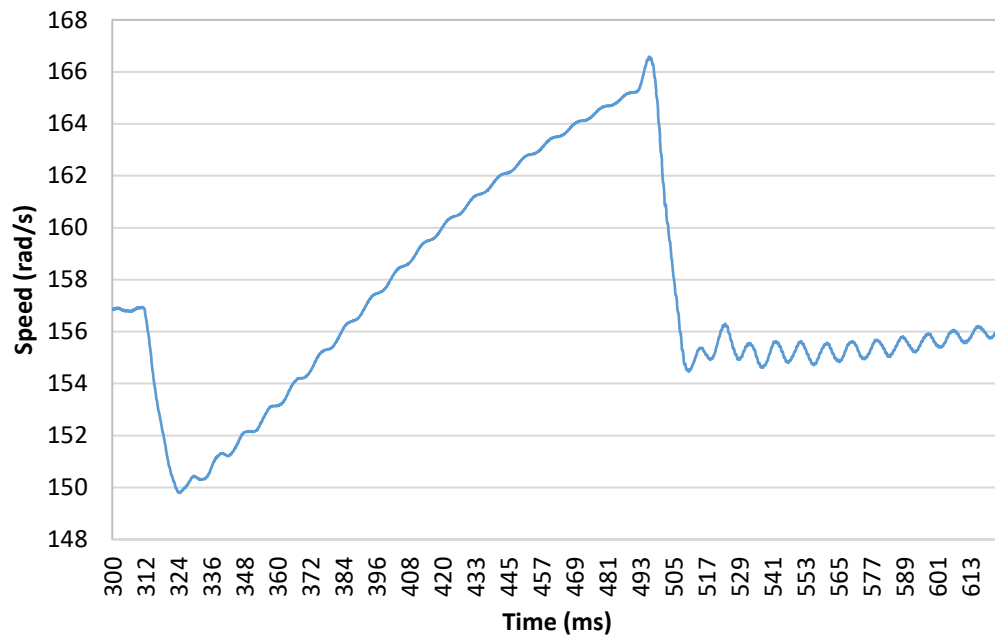


Figure 6.9: 100% voltage drop fault applied to motor driven generator set, PF = 1.

Transducer speed for 180 ms FRT.

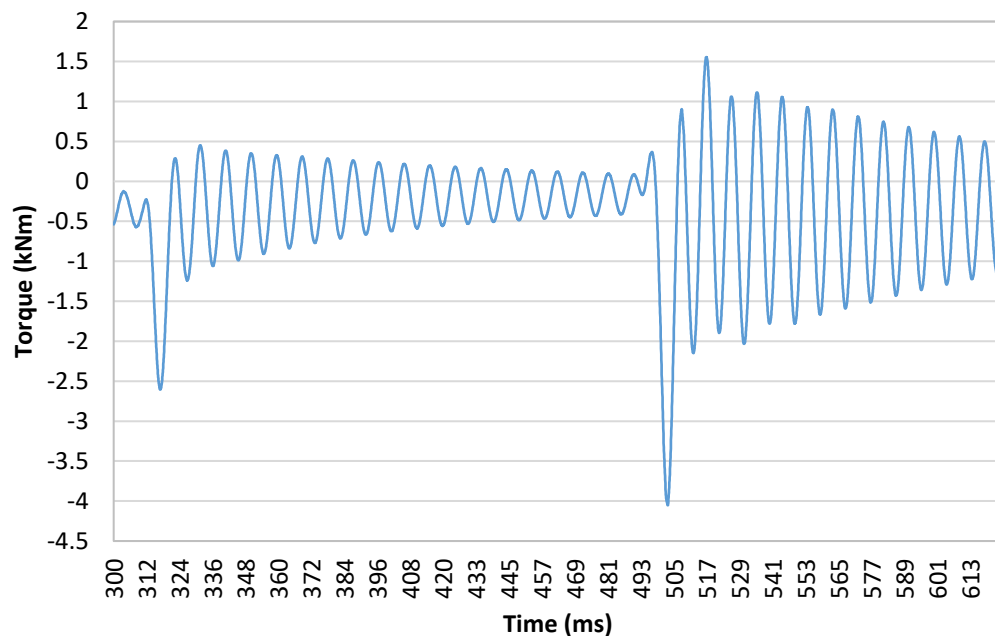


Figure 6.10: 100% voltage drop fault applied to motor driven generator set, PF = 1.

Transducer torque for 180 ms FRT.

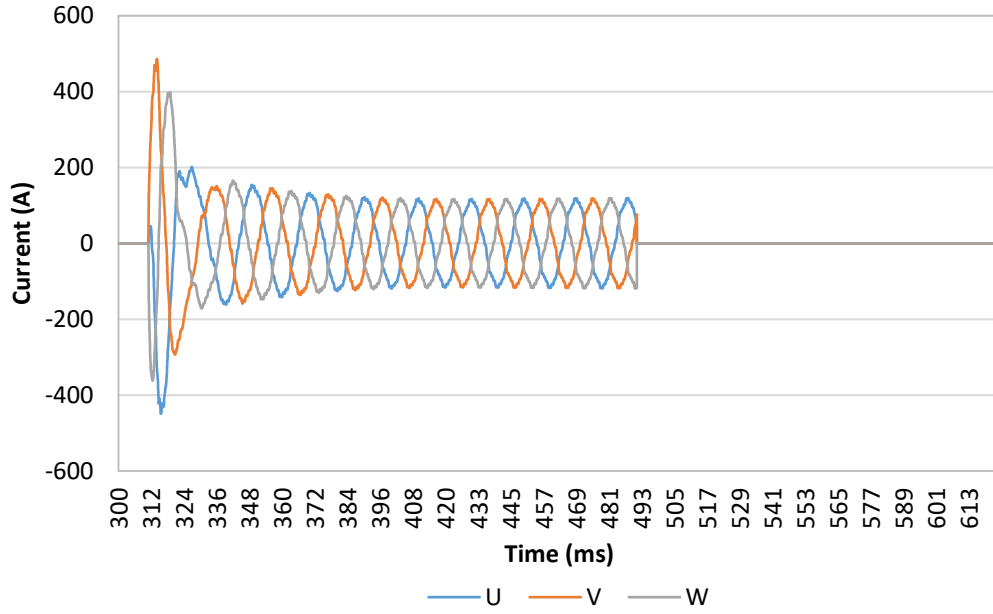


Figure 6.11: 100% voltage drop fault applied to motor driven generator set, PF = 1.

Fault current for 180 ms FRT.

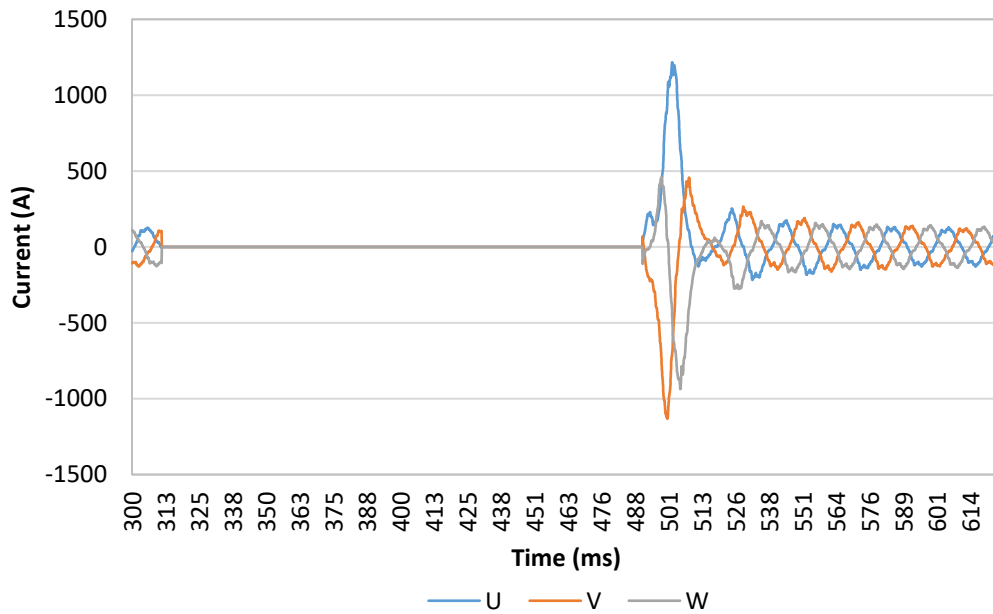


Figure 6.12: 100% voltage drop fault applied to motor driven generator set, PF =

1Line current for 180 ms FRT.

6.1.3 100% voltage drop fault: 320 ms ride through.

Finally, the fault ride through time is extended again to 320 ms. As in the previous analyses the step size is maintained at 0.05 ms. The simulation results for electromagnetic torque, transducer speed, transducer torque, motor torque and fault current / line current are shown below in Figures 6.13 to Figure 6.18.

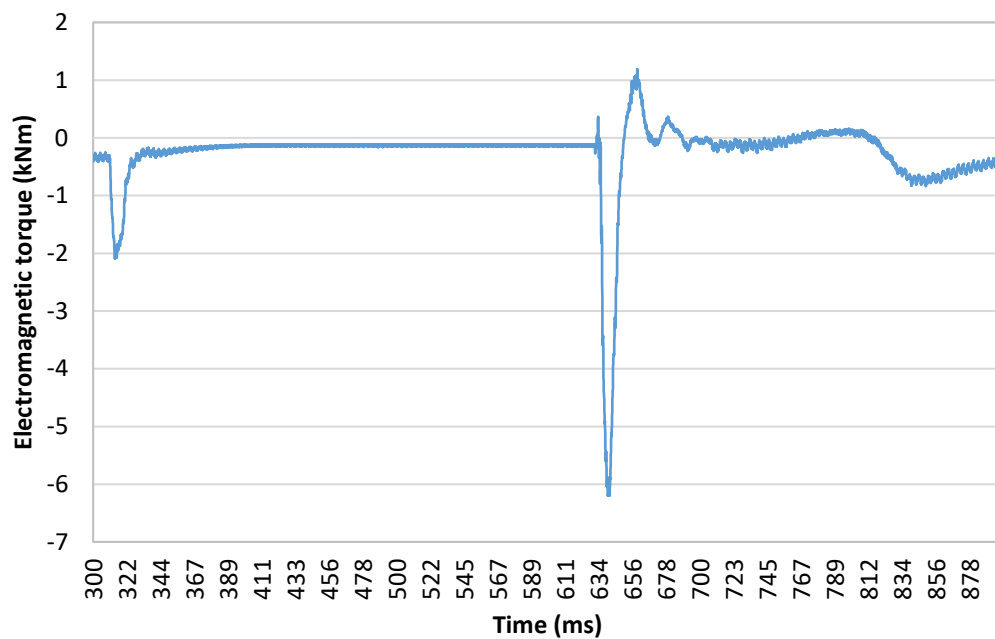


Figure 6.13: 100% voltage drop fault applied to motor driven generator set, PF = 1.

Air gap electromagnetic torque for 320 ms FRT.

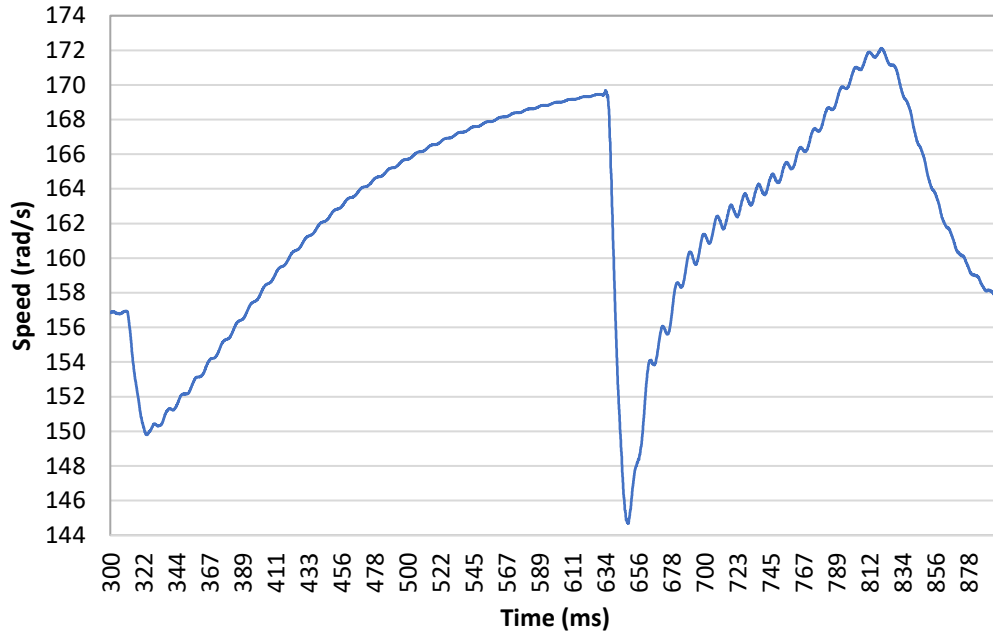


Figure 6.14: 100% voltage drop fault applied to motor driven generator set, PF = 1.

Transducer speed for 320 ms FRT.

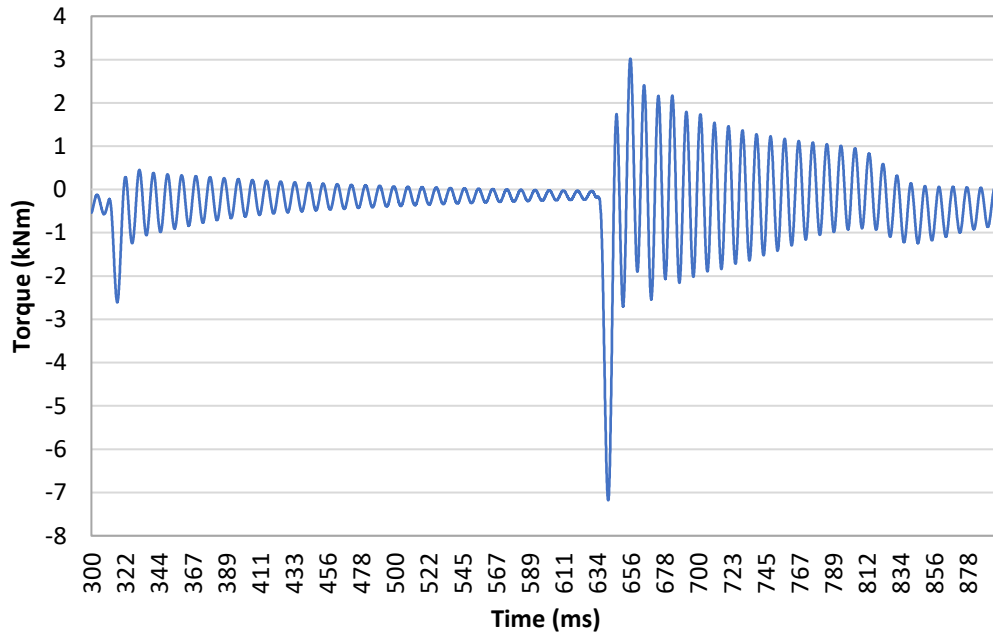


Figure 6.15: 100% voltage drop fault applied to motor driven generator set, PF = 1.

Transducer torque for 320 ms FRT.

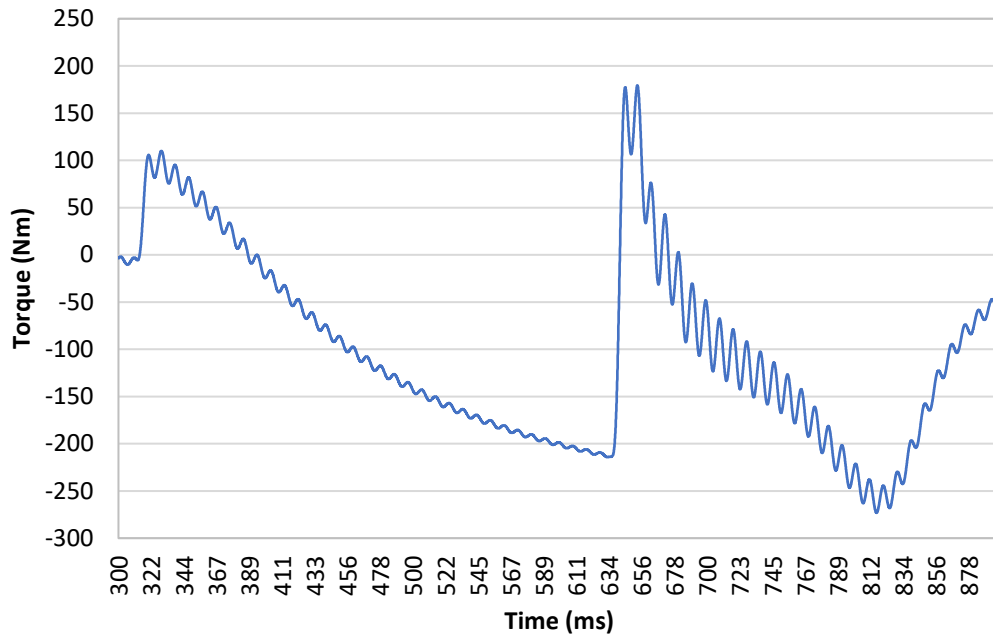


Figure 6.16: 100% voltage drop fault applied to motor driven generator set, PF = 1.

Motor torque control response for 320 ms FRT.

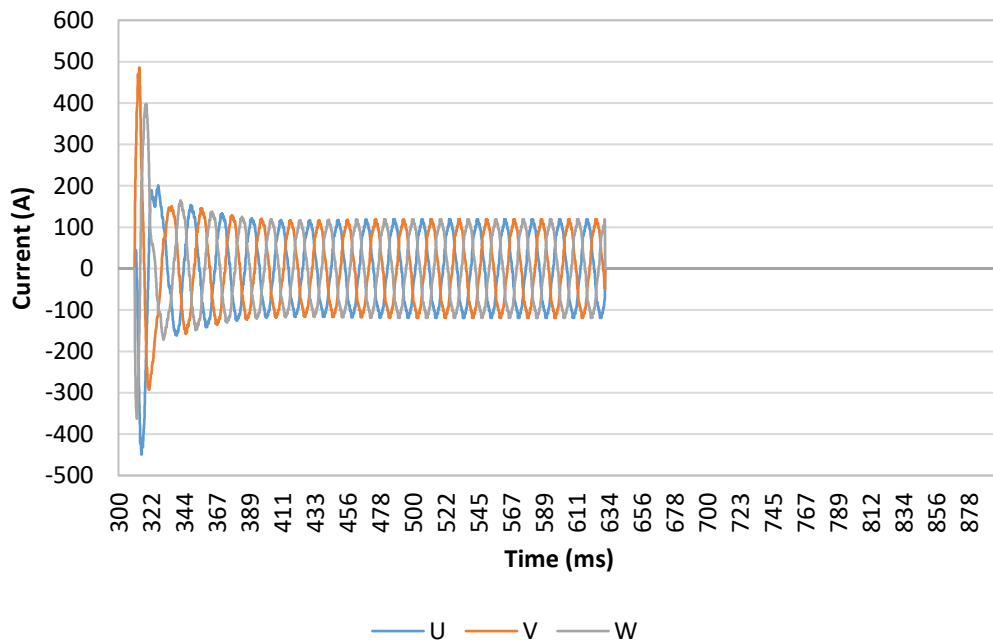


Figure 6.17: 100% voltage drop fault applied to motor driven generator set, PF = 1.

Fault current for 320 ms FRT.

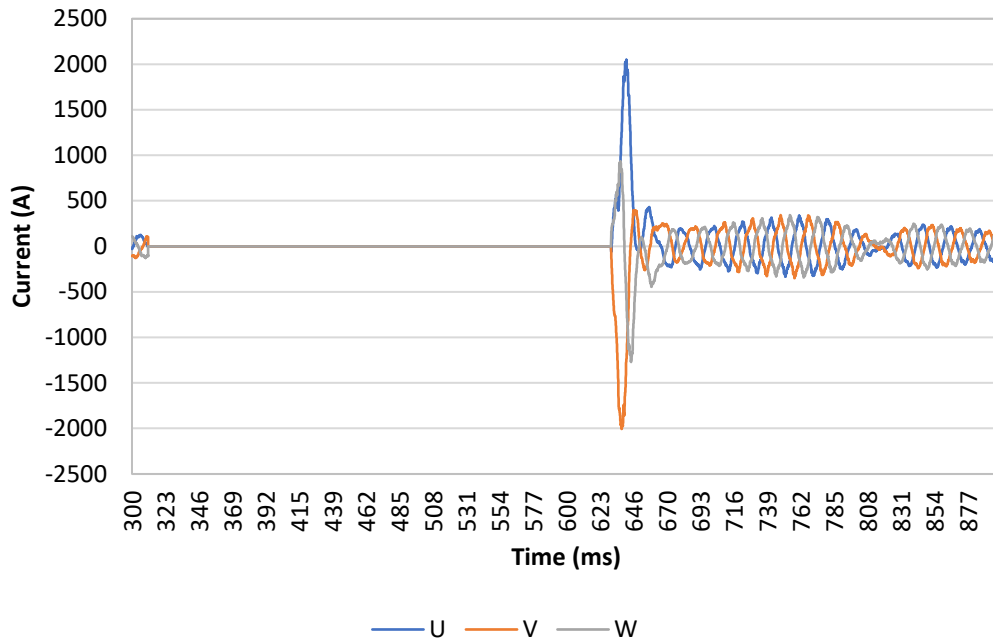


Figure 6.18: 100% voltage drop fault applied to motor driven generator set, PF = 1.

Line current for 320 ms FRT.

6.1.4 Observations and typical fault ride through characteristics

As the voltage drops, the electromagnetic field collapses, generating a high transient current in the stator windings which manifests in the air gap as a sudden increase in electromagnetic torque. The electromagnetic torque acts in the same direction as the steady state air gap torque as would occur with an increase in electrical load. In the case of a 100% voltage drop the fault is effectively identical to a three-phase short circuit provided that the impedance of the short circuit is low enough to produce a transient fault current equal to that following a grid connected low voltage fault. The three-phase short circuit line is still activated here and the fault resistance is kept the same as in the three-phase short circuit tests for the sake of comparison. A case study for a more realistic low voltage ride through is explored in section 6.2 which reduces the fault resistance for an extended fault ride through period.

The initial electromagnetic torque transient is equal in magnitude for all three LVRT tests here as each test begins at the same time after steady state is reached thus rotor angle, shaft torque current and voltage phase are identical in each case prior to initiation of the fault. Again, the magnitude of electromagnetic torque is determined by the magnitude of the fault current during the sub-transient time period. Both the torque and fault current are determined by the field current set in the simulation (which accounts for the change in magnetic field during the fault drop). Also, the rate at which the electromagnetic torque is returned to steady state/pre-fault magnitude is determined by the rate at which the field current falls. The electromagnetic torque peak is also highly sensitive to the impedance of the generator and the circuit that its phase terminals are connected to.

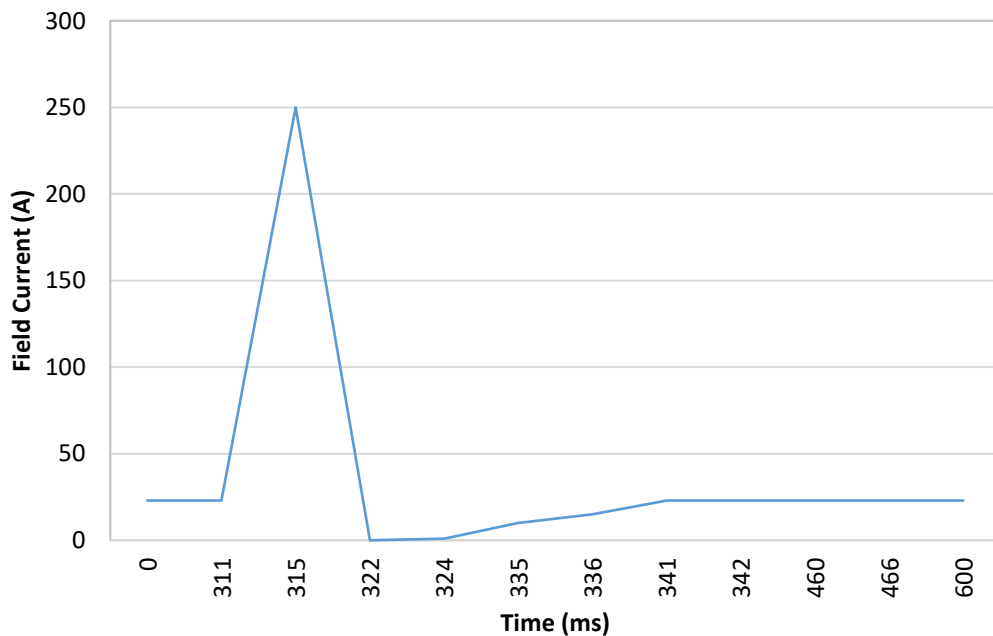


Figure 6.19: Field current input for Maxwell LVRT Simulation (100% voltage drop)

The field current input shown in Figure 6.19 is the same in all three LVRT simulations, and again matches that used for the full voltage, three-phase short circuit tests. Note that the field current here is simplified from a typical field current plot that may be observed from other LVRT simulations which often include some oscillation in the field current following the first peak. Inclusion of the initial field current peak and trough was found to be adequate in this simulation given the close match in torsional oscillation and angular speed between experimental and simulation results. The field current trace is tuned to produce the correct peak sub-transient current and transducer torque (Figure 6.20) for the initial peak following torsional oscillations.

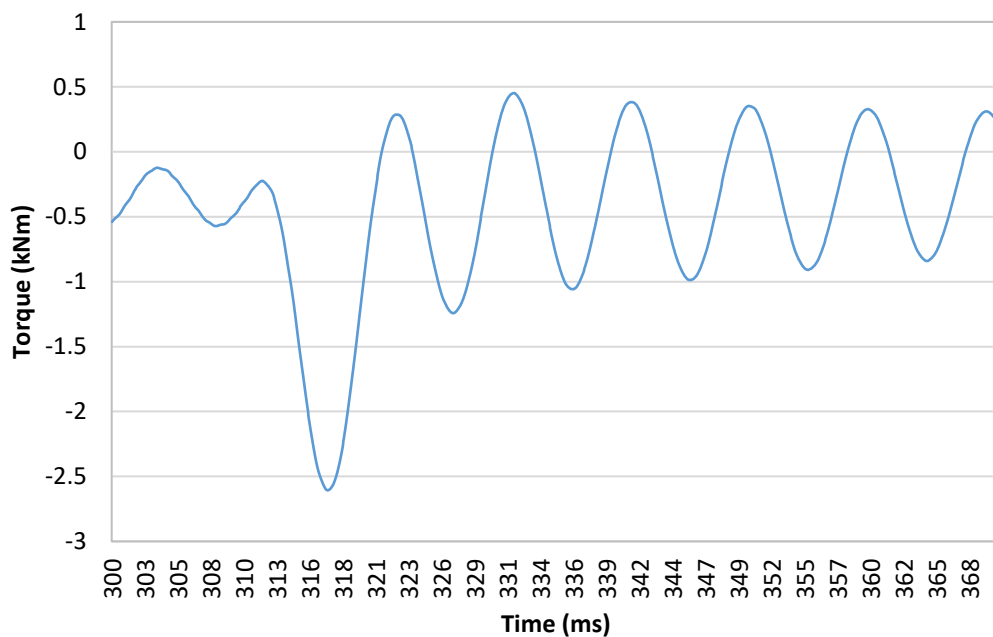


Figure 6.20: Transducer torque immediately following fault initiation.

During the fault ride through period, the motor is still producing torque as it was prior to fault initiation, but it is not constant as the motor torque changes over time as the motor's speed controller reacts to the changes in speed. The rate of torque correction simulated here is relatively fast compared to a simple governor-controlled diesel

engine. However, there is no forward feed control or other special fault mitigation systems in place in this simulation, so the results gathered here represent a baseline of ride through performance. Consequently, the speed control system does not respond fast enough to correct the motor torque at the same rate at which the electromagnetic torque changes to maintain a constant rotational speed. The speed controller manages to increase the motor torque by 100 Nm during the initial electromagnetic torque transient, thus reducing the angular speed drop by a small amount, but still the generator rotor briefly decelerates, lowering the angular speed, in this case to ~ 150 rad/s. Whilst the generator is disconnected from the grid voltage source the electromagnetic torque settles at a new, smaller steady state level, in this case around 150 Nm. Note that the steady state electromagnetic torque during fault ride through is not equal to zero in this case, the generator still maintains a steady stator current in all three phases of ~ 120 A, equivalent to the sustained short circuit fault current. The excess power generated during fault ride results in rapid heating of the stator windings which easily leads to thermal failure over a short period of time. The rotor continues to accelerate throughout the fault ride through period whilst the motor torque is slowly reduced by the speed controller. Rotor acceleration finally falls to zero as the speed overshoot reaches its peak at 320 ms. If the ride through time is extended beyond this time, the rotor speed will begin to drop again as the motor torque continues to fall.

The magnitude of the electromagnetic torque and fault current at the point the grid voltage is restored is determined by the shift in rotor angle with respect to its steady state value. If the grid voltage is restored within the initial speed drop envelope as in the case for the 40ms fault ride through simulation, the angular position of the rotor is shifted by 12.42° back in its cycle from its steady state position as shown in Figure 6.21

and Figure 6.22. The position it would have been in had the rotor continued at 1500 RPM.

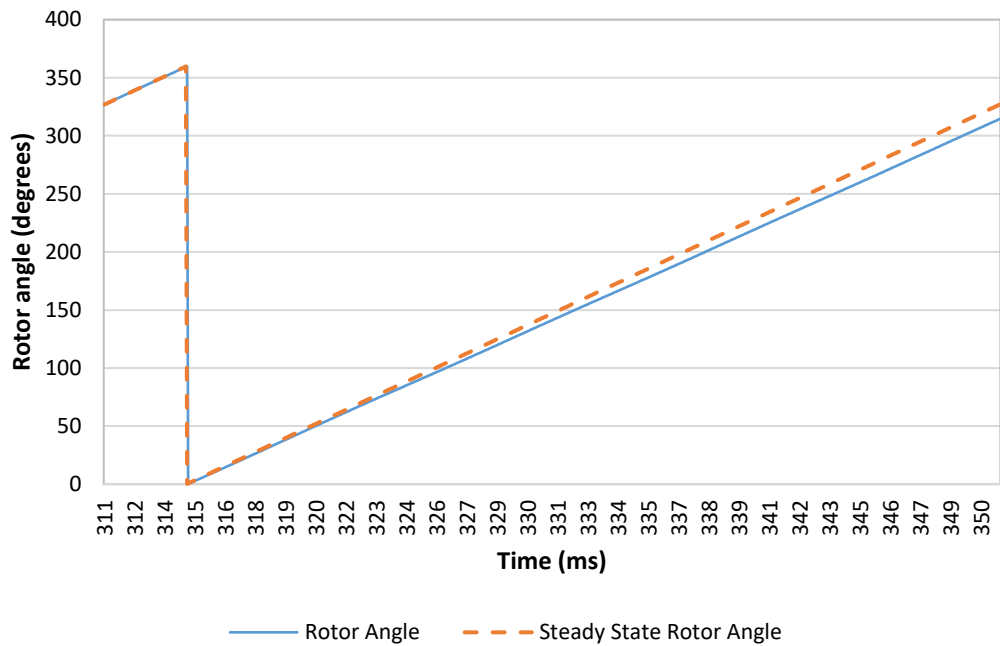


Figure 6.21: Rotor angular position for 40 ms LVRT vs. steady state angular position

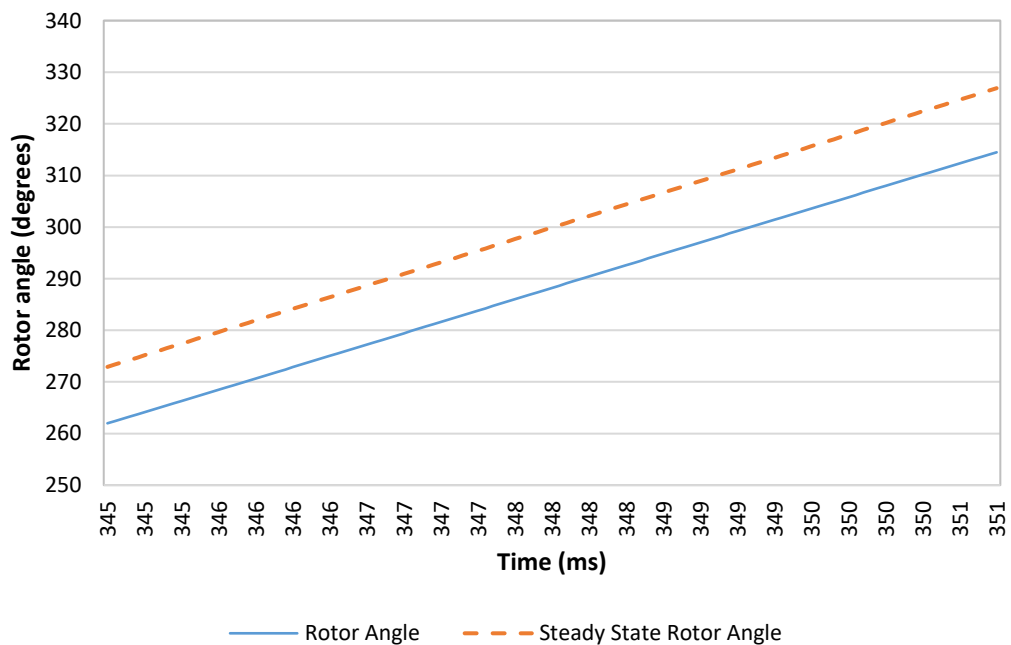


Figure 6.22: Magnified rotor angular position for 40 ms LVRT vs. steady state angular position

The generator produces a positive torque at the moment of reconnection, accelerating in the direction of rotation before the torque is reversed and the rotor speed is rapidly reduced. This initial positive torque peak is reduced as the ride through time is increased, this shows the effect of the grid forcing the generator back into resynchronisation. With the rotor angle shifted back from its steady state position due to rotor deceleration. The grid effectively 'drags' the rotor along during reconnection, forcing the now lagging rotor angle back towards its steady state value which is seen from the rotor perspective as an applied positive torque.

If the grid voltage is restored during the acceleration phase and the rotor speed is overshooting the target speed as in the case for the 180 ms fault ride through simulation, the rotor angle will begin to increase. With an increased shift in rotor angle, the phase of the stator current is ahead of the grid voltage phase (leading factor). The rotor angle will be forced further ahead again, this time producing a lower magnitude positive torque, but a greater negative torque as magnetic field is restored.

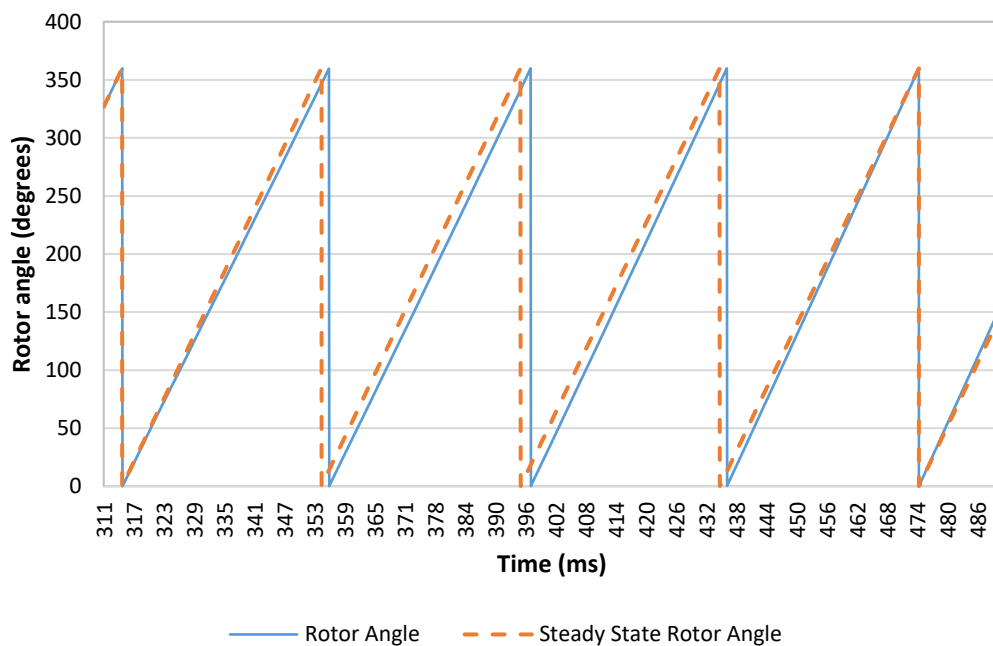


Figure 6.23: Rotor angular position for 180ms LVRT vs. steady state angular position

The rotor angle shift at the point of grid reconnection for the 180 ms LVRT case is obtained from Figure 6.23 as 7.31° and the peak-to-peak electromagnetic torque at this point is 4 kNm, compared to the 4.5 kNm peak to peak value for the 40 ms LVRT case. Note that at 474.6 ms (after the start of the simulation), the rotor angle is almost exactly in synchronism with the steady state angle with a difference of 0.01° . A 163.6 ms LVRT case is simulated to investigate this reconnection condition further. The simulation results for electromagnetic torque, fault current, line current, transducer speed and transducer torque are shown below in Figures 6.24 to Figure 6.28.

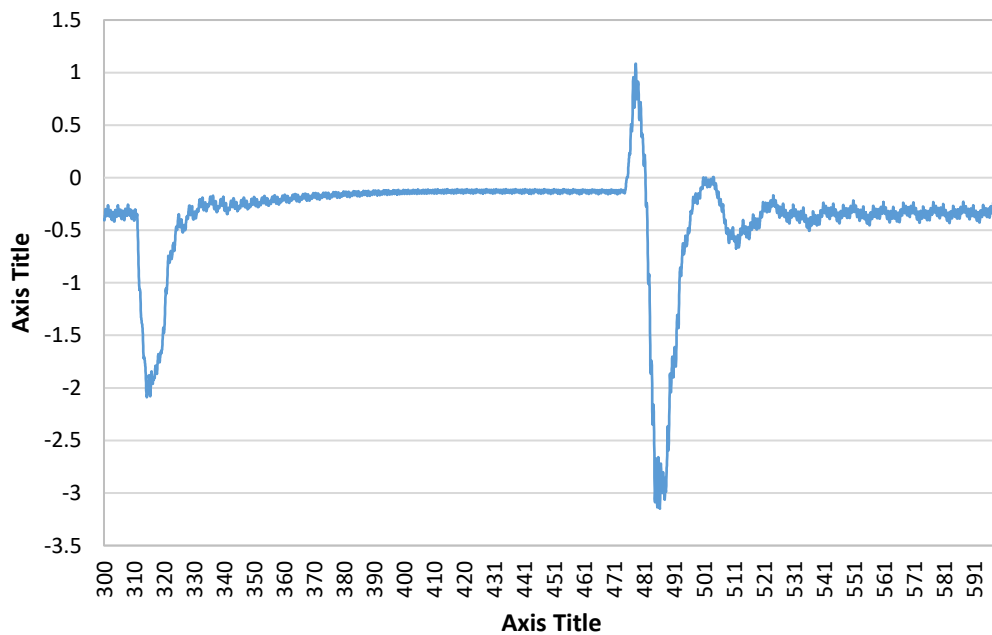


Figure 6.24: 100% voltage drop fault applied to motor driven generator set, PF = 1.

Air gap electromagnetic torque for 163.6 ms FRT.

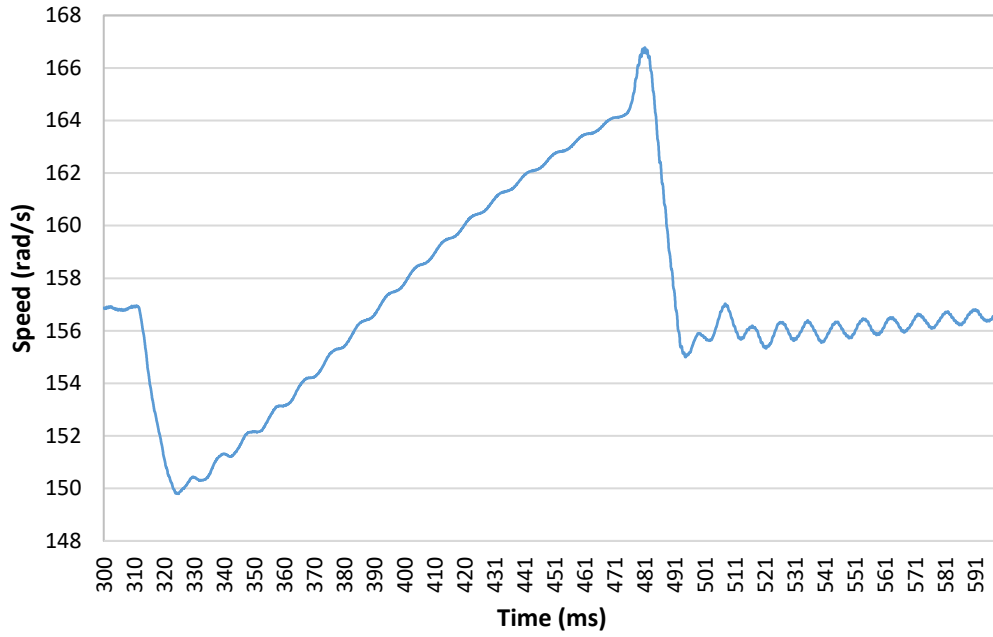


Figure 6.25: 100% voltage drop fault applied to motor driven generator set, PF = 1.

Transducer speed for 163.6 ms FRT.

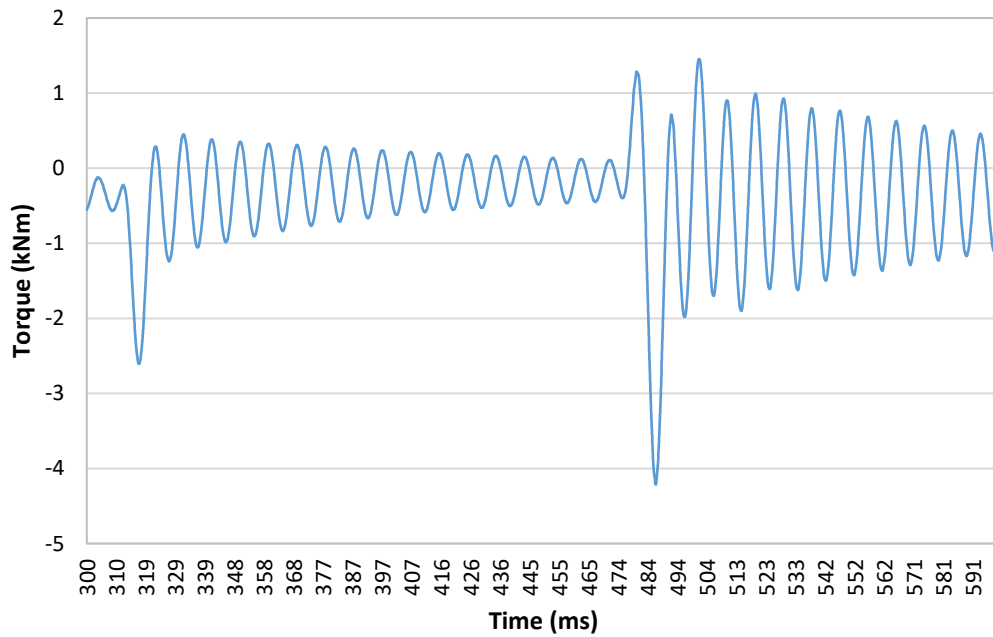


Figure 6.26: 100% voltage drop fault applied to motor driven generator set, PF = 1.

Transducer torque for 163.6 ms FRT.

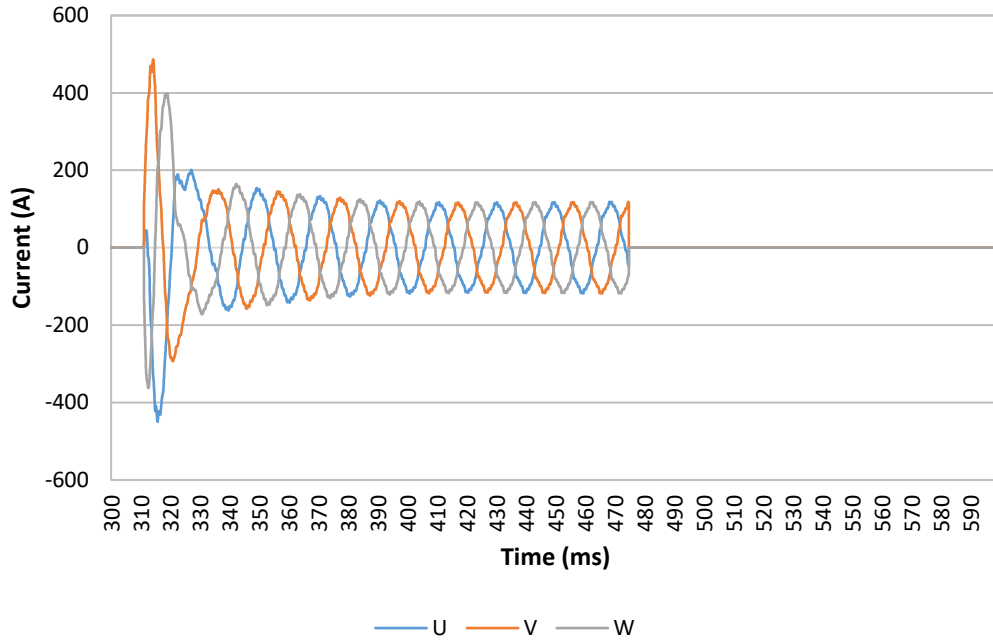


Figure 6.27: 100% voltage drop fault applied to motor driven generator set, PF = 1.

Fault current for 163.6 ms FRT.

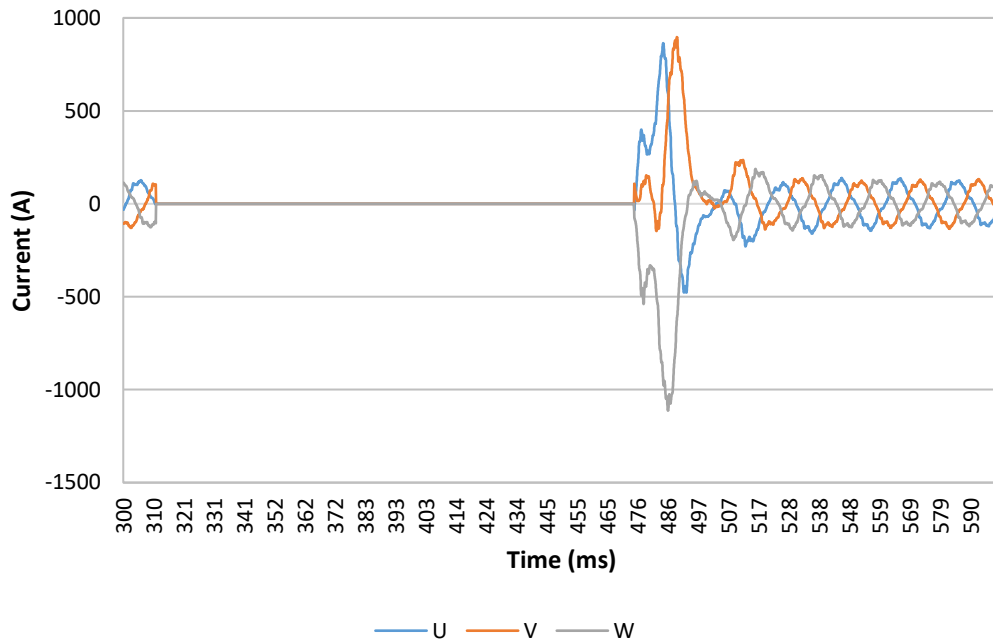


Figure 6.28: 100% voltage drop fault applied to motor driven generator set, PF = 1.

Line current for 163.6 ms FRT.

The peak-to-peak torque at $\sim 0^\circ$ rotor angle shift is 3.85 kNm, producing the lowest theoretical reconnection fault torque possible and this value is indeed lower than that for the other low voltage ride through tests. The reconnection torque is still greater than the disconnection torque for the given circuit resistance here. The 7.3° difference between reconnecting at 163.6 ms and reconnecting at 180 ms results in a reconnection torque difference of 0.15 kNm peak to peak.

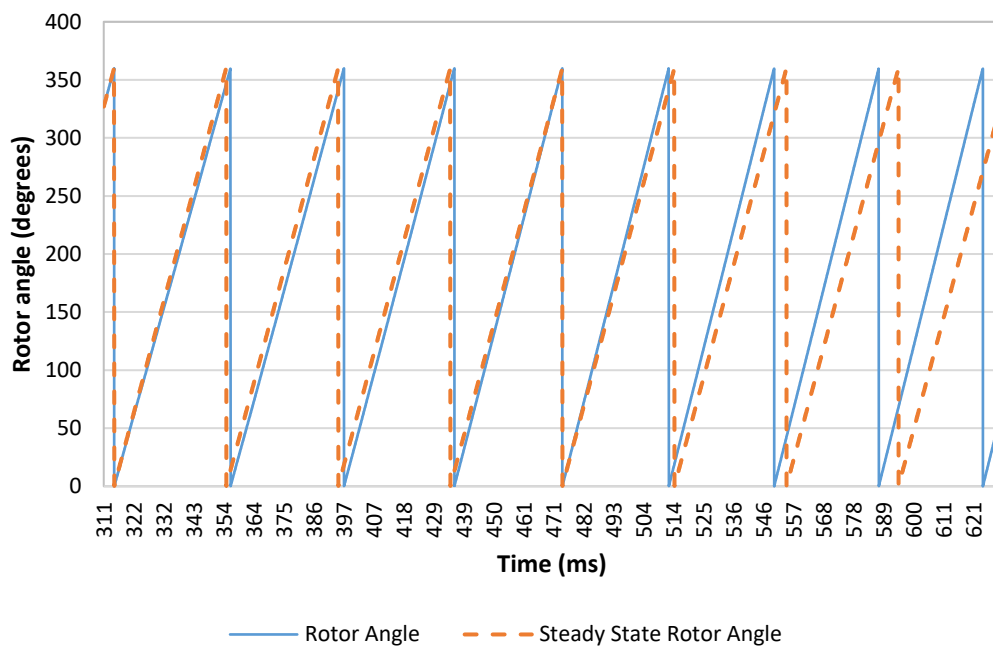


Figure 6.29: Rotor angular position for 320 ms LVRT vs. steady state angular position

For the most extreme case here, a 320 ms LVRT, the rotor angle clearly shifts far ahead of its steady state position as shown in Figure 6.29 above, the final rotor angle difference at the point of reconnection is 93.42° . The resulting peak electromagnetic torque is 6.25 kNm.

An additional observation can be made from the electromagnetic torque following reconnection of to the grid for the 320 ms LVRT simulation. The torque does not return

to steady state value upon reconnection, instead it reconnects at a low value of torque and then increases in positive torque before sharply increasing in negative torque. This behaviour indicates that the rotor angle at the point of reconnection was sufficiently displaced to cause the rotor to 'slip', a reoccurring problem for extended ride through periods.

Table 6.1: Simulation results for LVRT testing of the validated UC22F

motor/generator Simplorer model

FRT (ms)	Peak disconnection electromagnetic torque (kNm)	Peak to peak re-connection electromagnetic torque (kNm)	Peak disconnection stator current U, V, W (A)	Peak re-connection stator current U, V, W (A)
40.0	2.09	4.49	-450.49 486.13 397.89	1326.10 -1001.16 -800.00
180.0	2.09	3.5	-450.49 486.13 397.89	1216.09 -1132.92 -938.36
320.0	2.09	7.50	-450.49 486.13 397.89	2022.84 -2005.92 -1271.74
163.6	2.09	3.84	-450.49 486.13 397.89	-850.00 -1049.20 1183.84

6.2 Effect of Reduced Circuit Resistance on LVRT response

In the previous simulations, the three-phase short circuit resistance matched that in the test machine. In a three-phase short circuit or low voltage fault occurring in the grid, the transient current circulating in the generator is dependent upon the internal resistance of the generator which is significantly lower than the resistance used

previously. In the following simulation, the generator set is subjected to a 140 ms, 100% voltage drop LVRT event, the short circuit line resistance is reduced to 0.01Ω so that the remaining resistance in the stator circuit is largely due to the internal resistance of the windings (0.065Ω per phase).

6.2.1 Minimum grid code: 140 ms FRT

The simulation results of electromagnetic torque, transducer speed, transducer torque, line/fault current, and rotor angle for a 140 ms LVRT fault are shown below in Figure 6.30 to Figure 6.34. The voltage drop occurs at 311 ms.

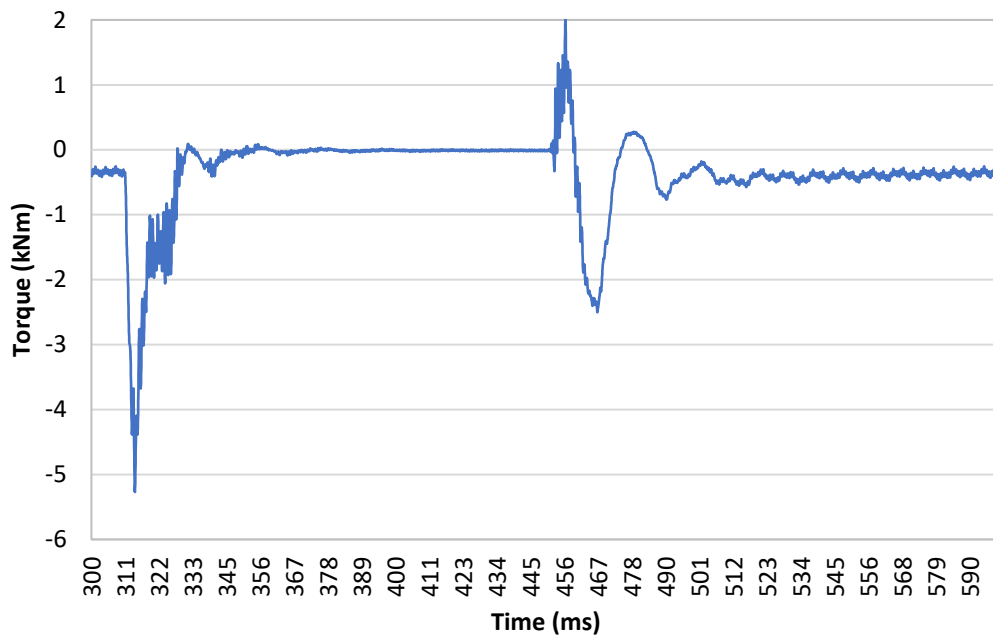


Figure 6.30: 100% voltage drop fault applied to motor driven generator set, PF = 1.

Air gap electromagnetic torque for 140 ms FRT with reduced resistance.

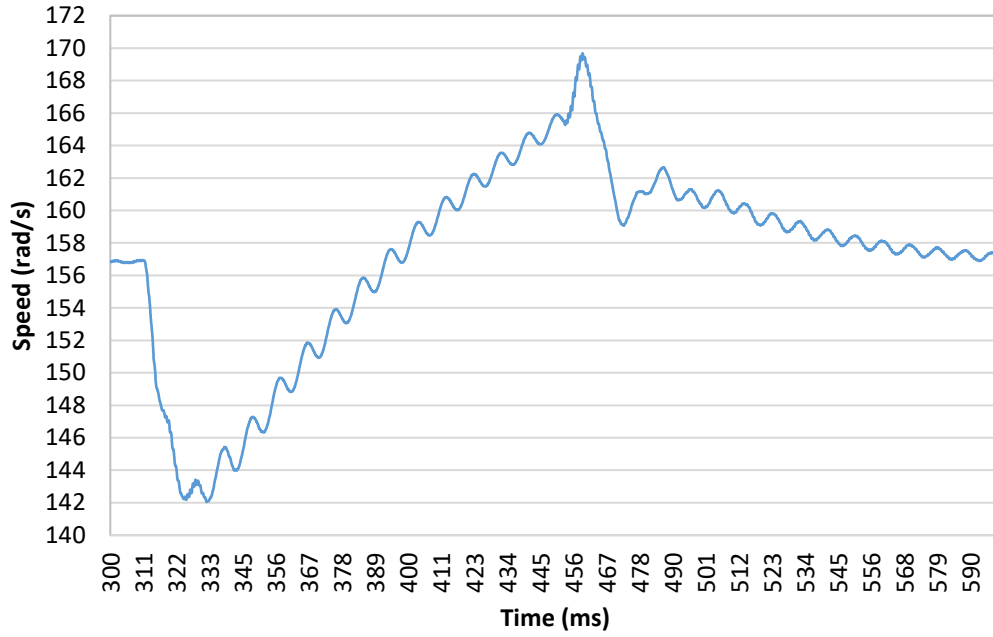


Figure 6.31: 100% voltage drop fault applied to motor driven generator set, PF = 1.

Transducer speed for 140 ms FRT with reduced resistance

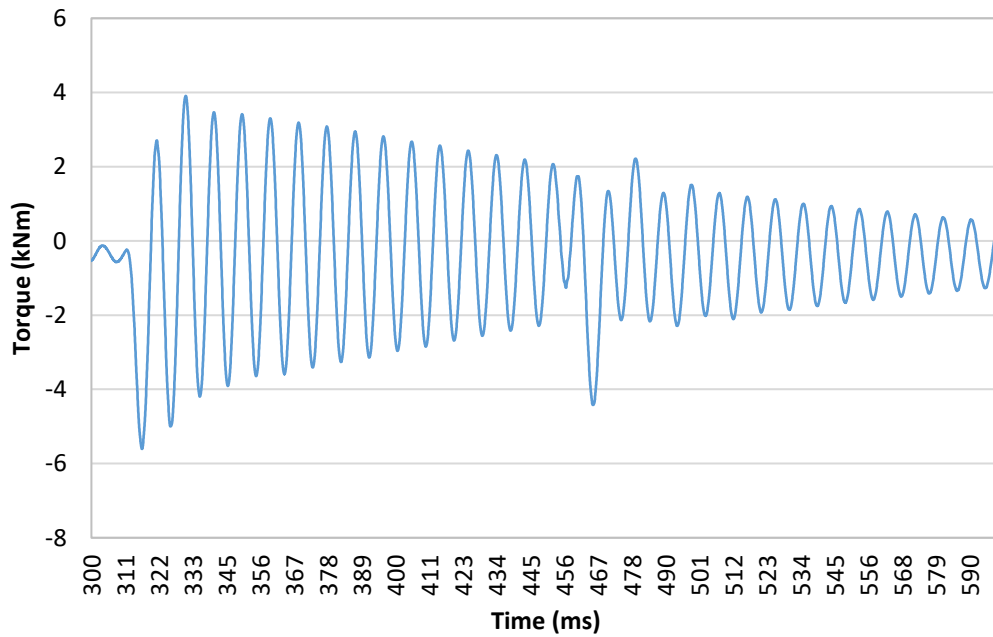


Figure 6.32: 100% voltage drop fault applied to motor driven generator set, PF = 1.

Transducer torque for 140 ms FRT with reduced resistance.

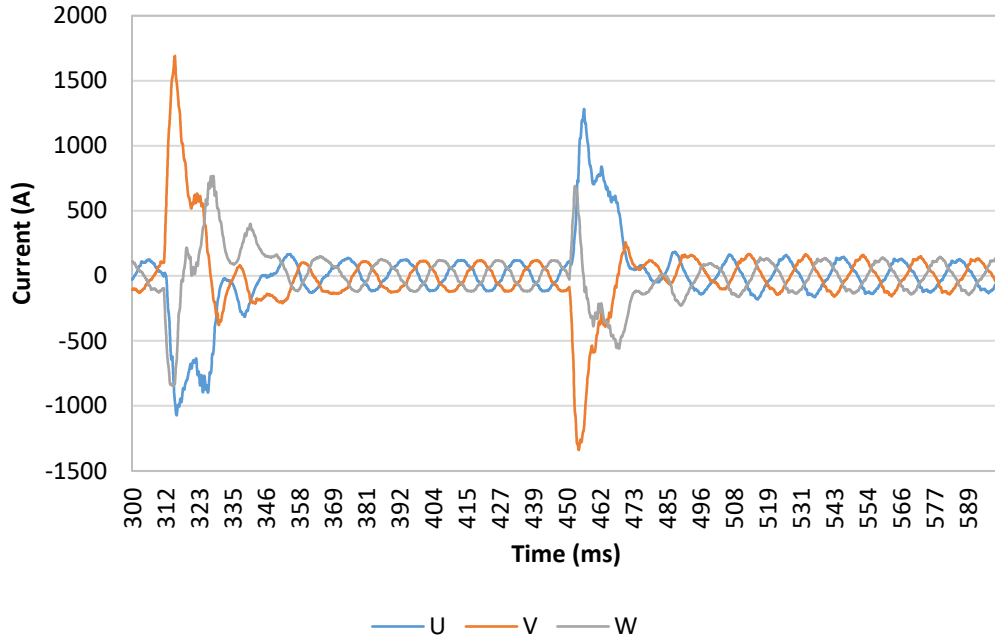


Figure 6.33: 100% voltage drop fault applied to motor driven generator set, PF = 1.

Line / fault Current for 140 ms FRT with reduced resistance.

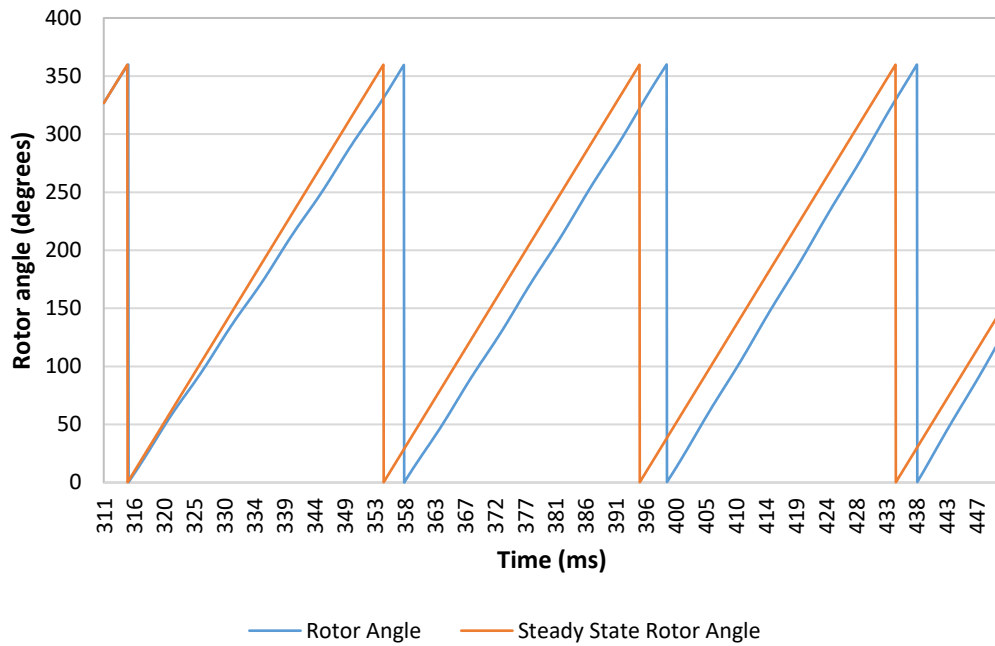


Figure 6.34: 100% voltage drop fault applied to motor driven generator set, PF = 1.

Rotor angle for 140 ms FRT with reduced resistance.

The 140ms, 100% voltage drop simulation represents the minimum required ride through conditions required to meet UK grid codes as shown in Figure 6.35 and on the minimum voltage/time limit curve in Figure 6.36.

Voltage parameters [pu]		Time parameters [seconds]	
U_{ret} :	0	t_{clear} :	0.14 – 0.15 (or 0.14 - 0.25 if system protection and secure operation so require)
U_{clear} :	0.25	t_{rec1} :	$t_{clear} - 0.45$
U_{rec1} :	0.5 – 0.7	t_{rec2} :	$t_{rec1} - 0.7$
U_{rec2} :	0.85 – 0.9	t_{rec3} :	$t_{rec2} - 1.5$

Figure 6.35: UK grid code voltage limits for 'Type D' synchronous machines (67)

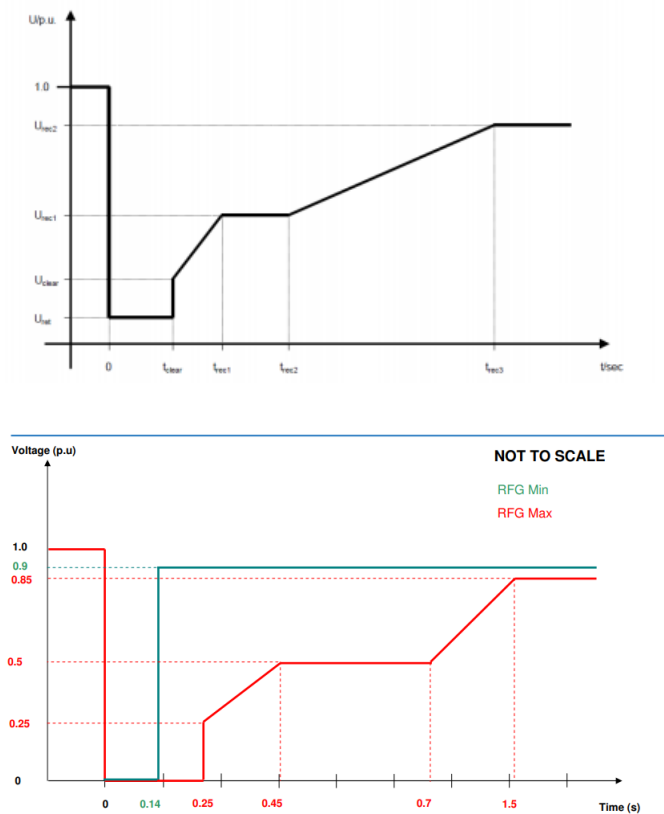


Figure 6.36: Minimum and maximum fault voltage against time curves (68)

The disconnection peak torque is 5.27 kNm and the peak-to-peak reconnection torque is 4.5 kNm (2 kNm positive torque and 2.5 kNm negative torque). Minimum angular speed reached is 142.1 rad/s and maximum angular speed reached is 169.7 rad/s. The rotor angular shift at the point of reconnection is 23.59° lagging the steady state angle.

The terminal current during LVRT is significantly increased here and now better fits the peak three-phase fault current indicated in the sub transient region of the decrement curve supplied by the generator manufacturer (900 A to 1800 A for asymmetrical faults). Note that the voltage is instantaneously restored to 100% at 140 ms, however the grid code requires the machine to be capable of maintaining a sustained voltage drop of 10% for an indefinite period following reconnection. Should the grid voltage be reconnected at 0.9 pu, the reconnection torque will be slightly reduced and the AVR will increase the rotor field current to restore the stator voltage to its target (311 V peak).

Another interesting observation can be made from the measured transducer torque shown in Figure 6.37 which is obtained from a similar simulation but with a 180 ms FRT period. The torsional oscillations during FRT are of a significantly higher magnitude in the low resistance case, and even surpass the peak-to-peak magnitude of the initial torque at the point of disconnection.

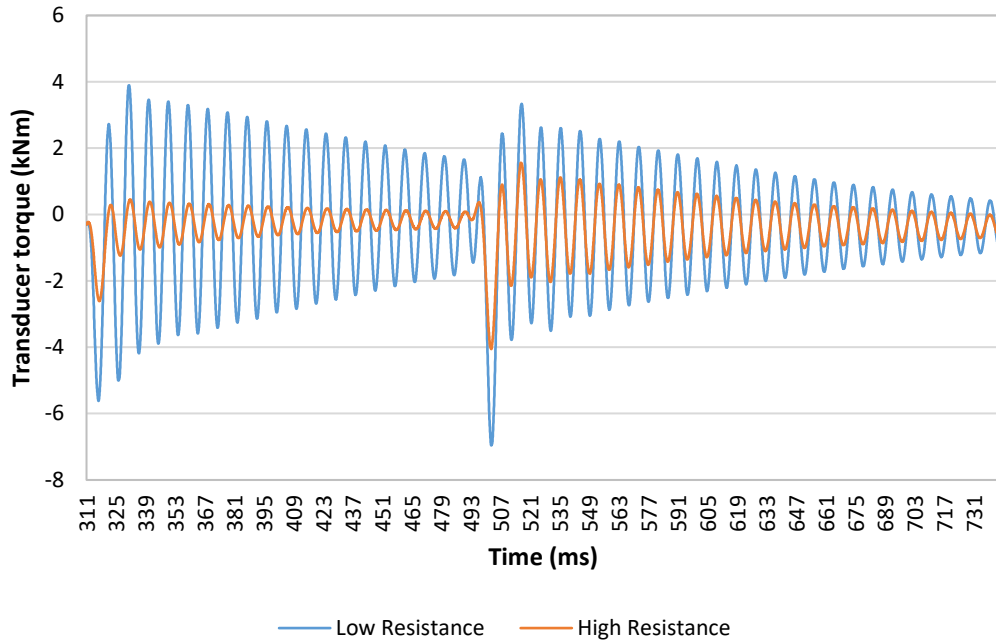


Figure 6.37: Transducer torque comparison for low resistance circuit versus high resistance circuit

The reduction in circuit resistance reduces the stability of the stator current during both the sub transient period and transient period. Steady state current is achieved approximately 90 ms after fault initiation, within this time the frequency of current in each phase line is not constant and slowly shifts from a low frequency towards steady state.

Note that the generator field current spike will need to be dropped by a factor corresponding to the voltage drop (pu) for the partial voltage simulations to correct the disconnection torque. The three-phase short line is not utilised here since partial voltage drop can be simulated by simply reducing the supply voltage at the initiation of fault.

6.3 Case study model

As the worst-case scenario has been measured from the previous analyses, more realistic boundary conditions are applied to the model to obtain results that can be expected from the real machine in service when subjected to low voltage ride through events. Recall that the experimental test possessed a greater impedance in the short circuit line (largely due to the contactor) than in the three phase short circuit tests performed by the manufacturer. The operating conditions for this model are as follows; 0.8 power factor, low resistance circuit, 140 ms ride through time at 100% voltage drop and a stiff coupling between generator and prime mover. This model is split into two variants, one driven by the electric motor as per the previous simulations and the other driven by the diesel engine. The simulation results of electromagnetic torque, transducer speed, transducer torque, and current for a 140 ms LVRT fault on the motor driven case study model are shown below in Figure 6.38 to Figure 6.41.

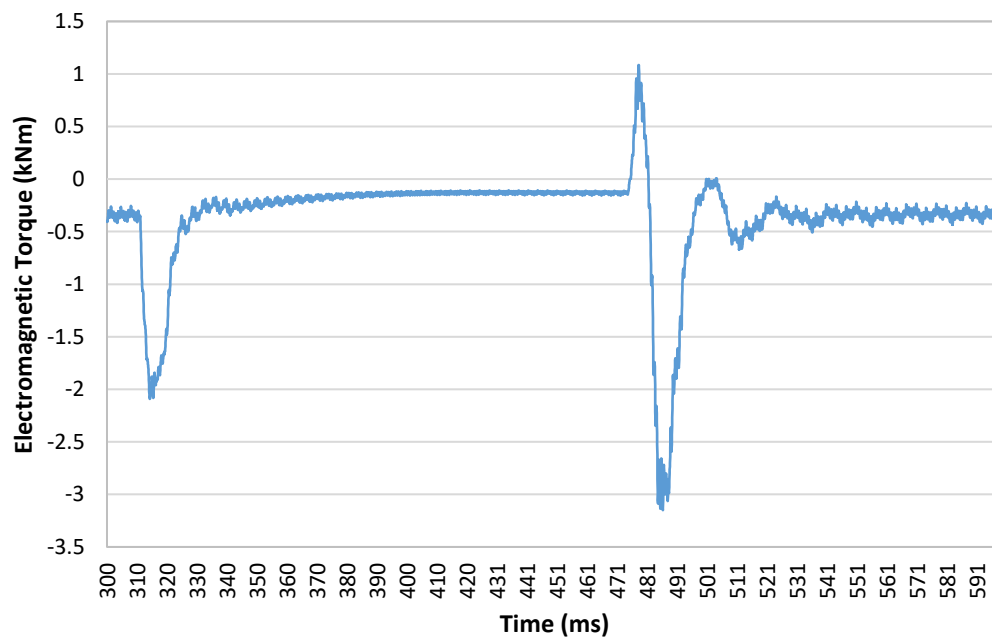


Figure 6.38: 100% voltage drop fault applied to the case study model, PF = 0.8.

Electromagnetic torque for 140 ms FRT.

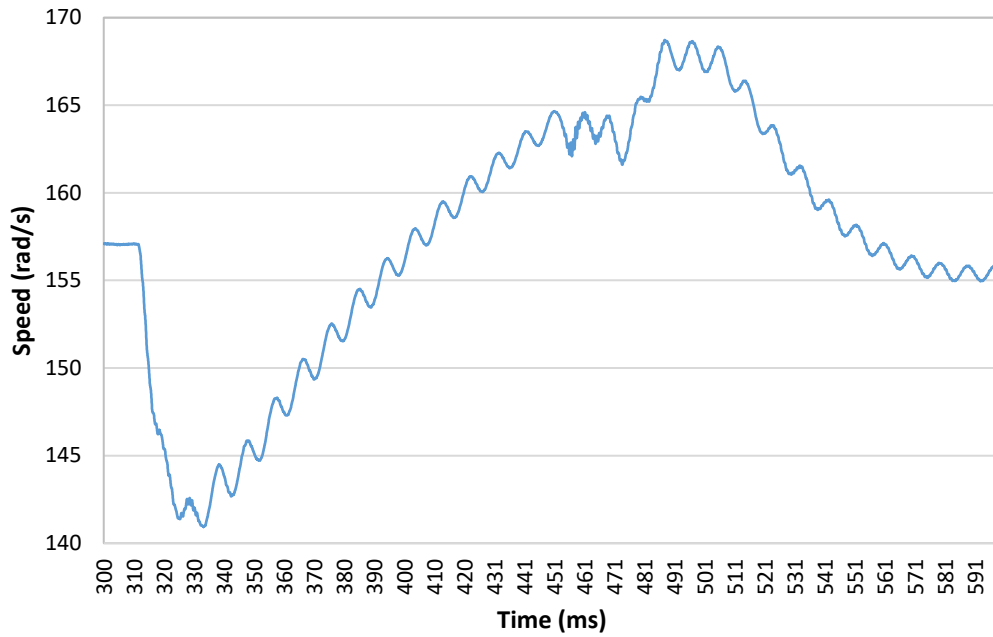


Figure 6.39: 100% voltage drop fault applied to the case study model, PF = 0.8. Speed for 140 ms FRT.

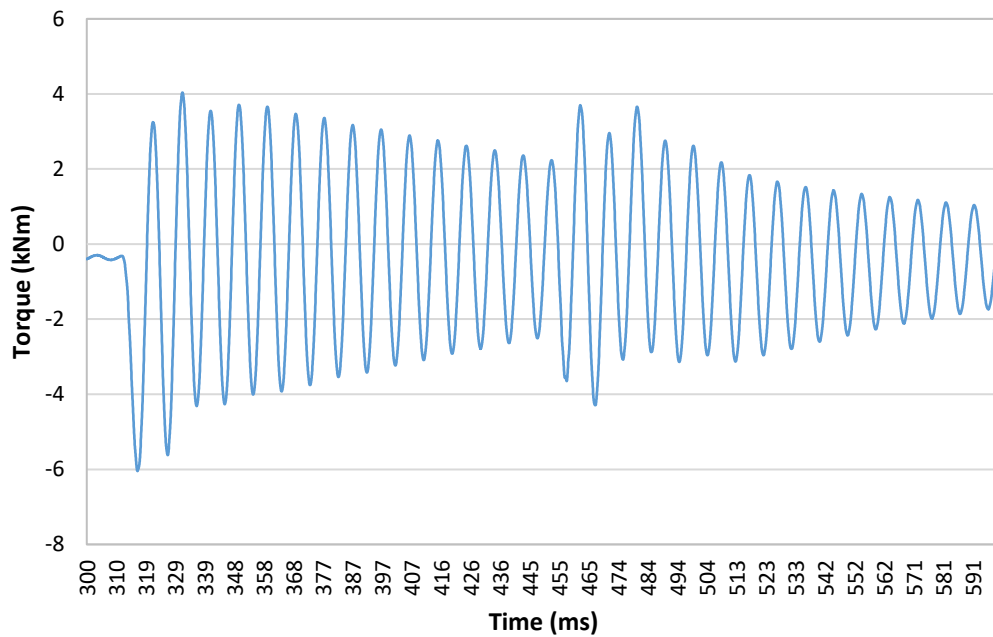


Figure 6.40: 100% voltage drop fault applied to the case study model, PF = 0.8.

Torque for 140 ms FRT.

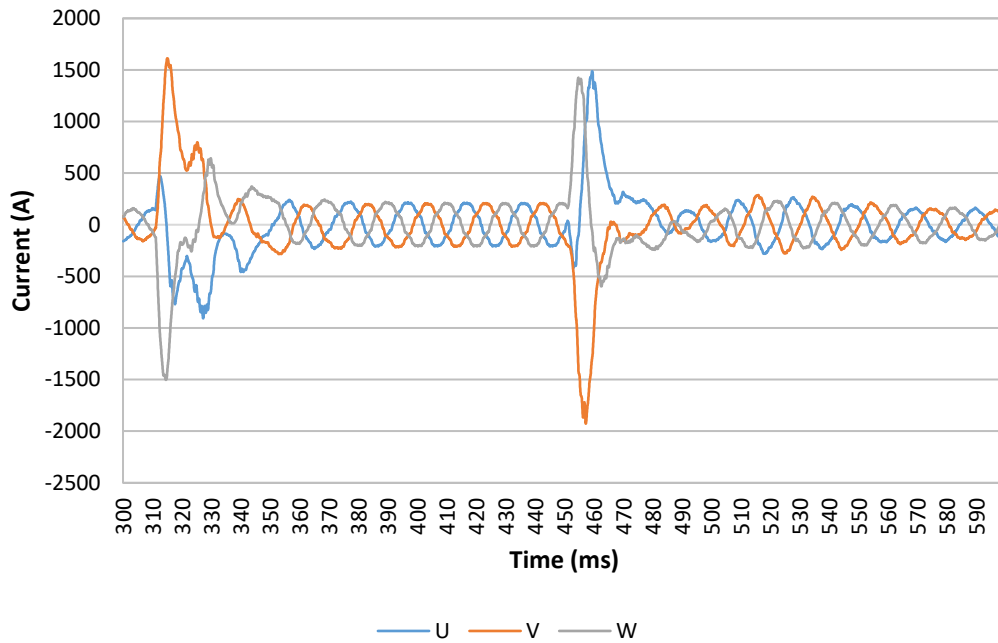


Figure 6.41: 100% voltage drop fault applied to the case study model, PF = 0.8.

Current for 140 ms FRT.

The steady state current for a power factor of 0.8 is 110 A (RMS) and the field current is raised to 41 A accordingly. The steady state torque is again 364 Nm. The initial field current peak at the point of voltage drop remains at 250 A here. The disconnection peak torque is 5.24 kNm and the peak reconnection torque is 1.98 kNm. Minimum angular speed reached is 140.88 rad/s and maximum angular speed reached is 168.7 rad/s. The rotor angular shift at the point of reconnection is 34.18° lagging behind the steady state angle.

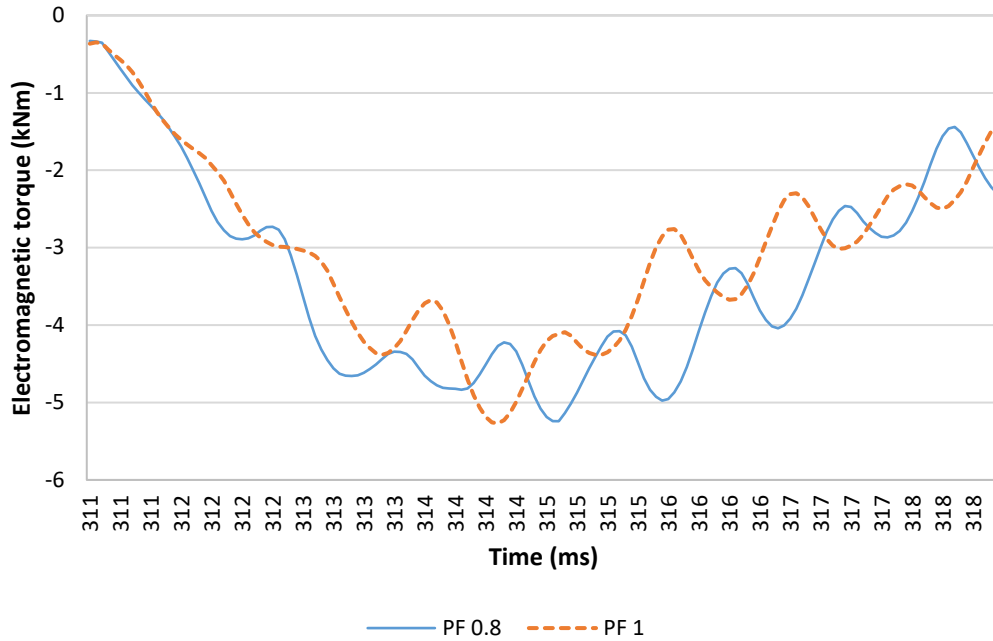


Figure 6.42: Electromagnetic torque following disconnection for 140 ms ride through at power factor 1 and power factor 0.8

Compared to the simulation performed at power factor 1, the disconnection peak torque is 0.03 kNm lower as shown in Figure 6.42. Due to the shift in rotor current phase as a result of the power factor being reduced to 0.8, the sub transient fault current at the point of disconnection is altered. The peak disconnection torque is reduced as a result, but the average torque over the sub-transient period is increased as the elevated negative torque is sustained at a greater magnitude.

The initial rotational speed drop for the 0.8 power factor simulation is therefore increased which leads to the angular position at reconnection lagging further behind. The initial peak reconnection torque is of the same magnitude as in the simulation with a power factor of 1, but acts as negative torque. Since the rotor was already lagging behind the stator current by 2 ms, the rotor angle is 93.38° , the rotor angle for a power factor of 1 is 123.35° .

6.3.1 Symmetric fault simulation: Motor/generator set

In all previous simulations, the field current has been fixed at 250 A, a value used to simulate the correct fault current and disconnection electromagnetic torque in the short circuit models in order to match them to their experimentally obtained values. This is reasonable for producing simulation results for asymmetric fault conditions, but in most cases the machine will produce symmetric fault currents of a lower magnitude.

The peak field current for these simulations has remained unaltered, therefore the peak disconnection fault current for a single phase was over 1500 A as a result, this is the top end possible fault current indicated on the decrement curve graph for the UC22 generator. This is reasonable for a highly asymmetric fault but for a symmetric fault, the peak fault current for this machine ranges between 800 A and 1000 A. In order to simulate the correct symmetric fault conditions the peak field current is reduced to one third of its original value (now 83A). The circuit retains a low phase resistance. The simulation results of electromagnetic torque, transducer speed, transducer torque and line/fault current for a 140 ms LVRT fault on the motor driven case study model are shown below in Figure 6.43 to Figure 6.46.

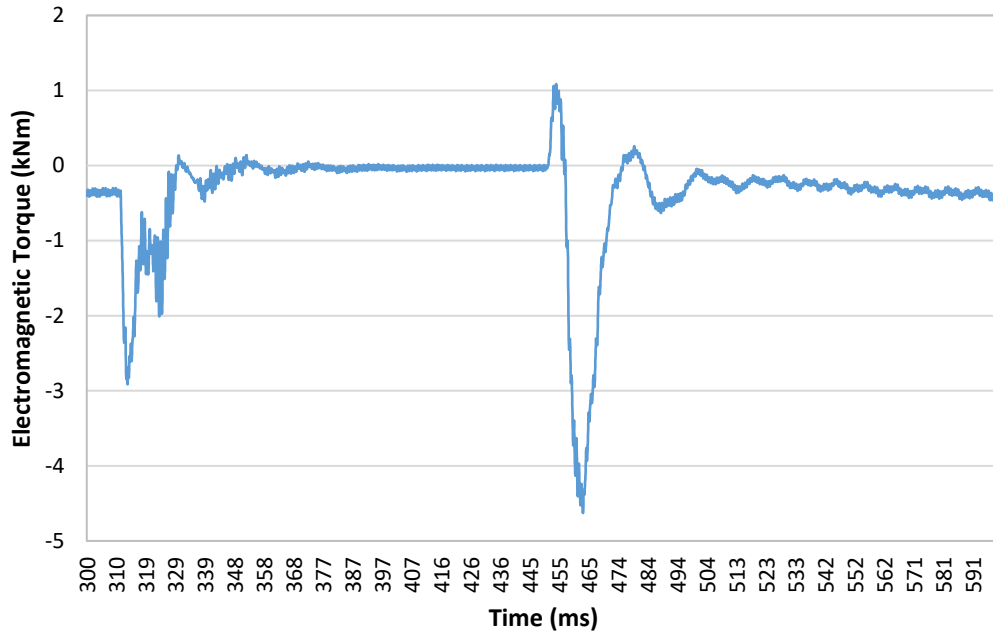


Figure 6.43: 100% voltage drop fault applied to the case study model, PF = 0.8.

Electromagnetic torque for 140 ms FRT. Reduced field.

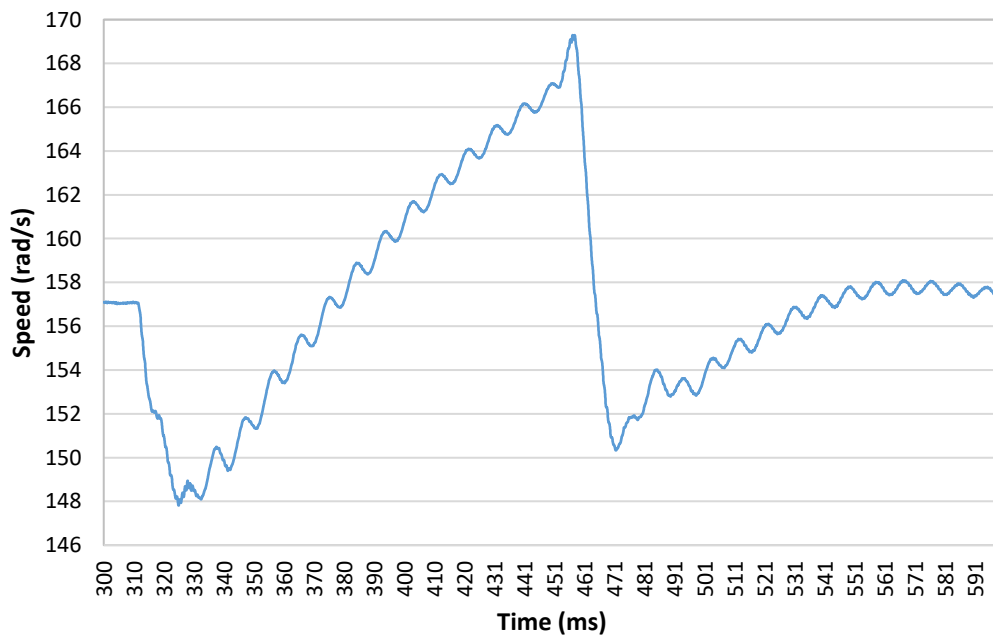


Figure 6.44: 100% voltage drop fault applied to the case study model, PF = 0.8. Speed for 140 ms FRT. Reduced field.

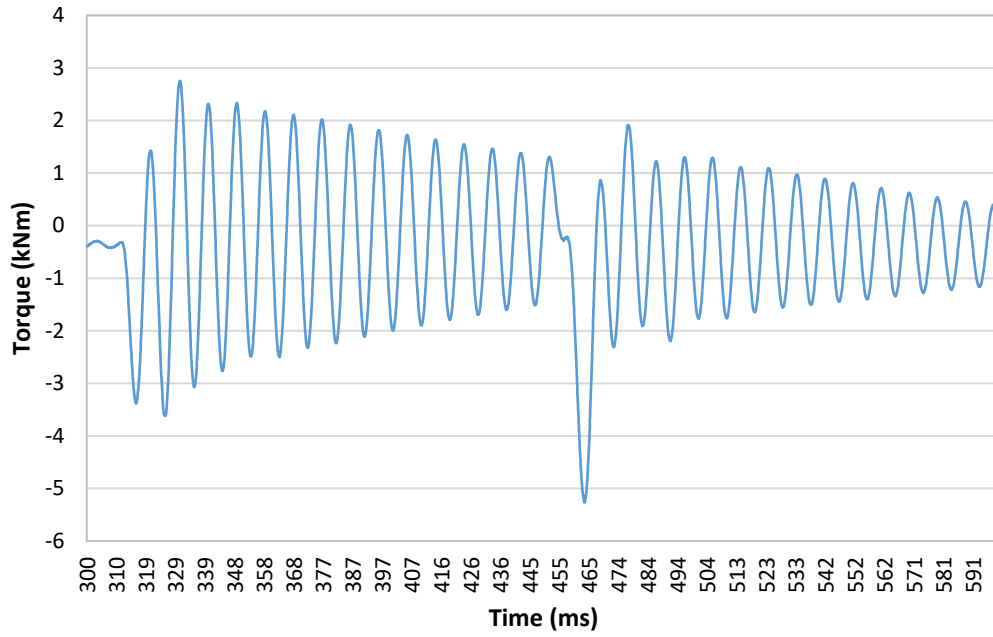


Figure 6.45: 100% voltage drop fault applied to the case study model, PF = 0.8.

Torque for 140 ms FRT. Reduced field.

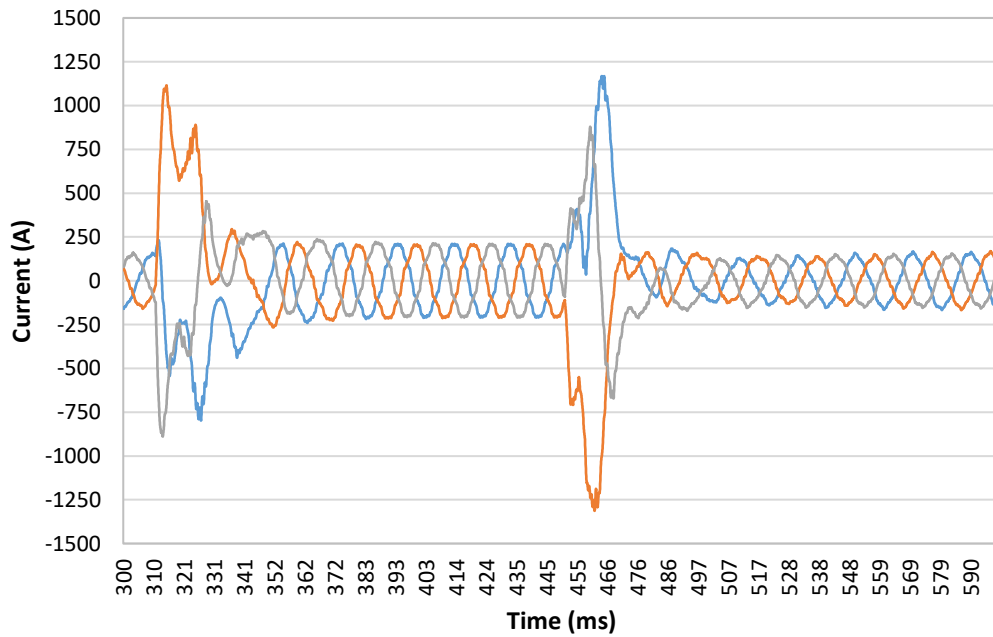


Figure 6.46: 100% voltage drop fault applied to the case study model, PF = 0.8.

Current for 140 ms FRT. Reduced field.

The lower resistance again produces some deformed current waveforms in the sub-transient region, and some asymmetry between the phases still exists but the magnitude of electromagnetic torque nonetheless better fits the expected value for a symmetric fault. The magnitude of peak disconnection electromagnetic torque is significantly reduced when compared to the previous asymmetric fault simulations, now reduced to 2.9 kNm versus 5 kNm. The resulting reduced speed drop shifted the rotor angle further ahead in time at the point of reconnection causing the reconnection torque to be significantly increased.

6.3.2 Symmetric fault simulation: Motor/diesel engine set

The previous simulation is repeated for the diesel engine connected model. The simulation results of electromagnetic torque, transducer speed and transducer torque for a 140 ms LVRT fault on the engine driven case study model are shown below in Figures 6.47 to Figure 6.49.

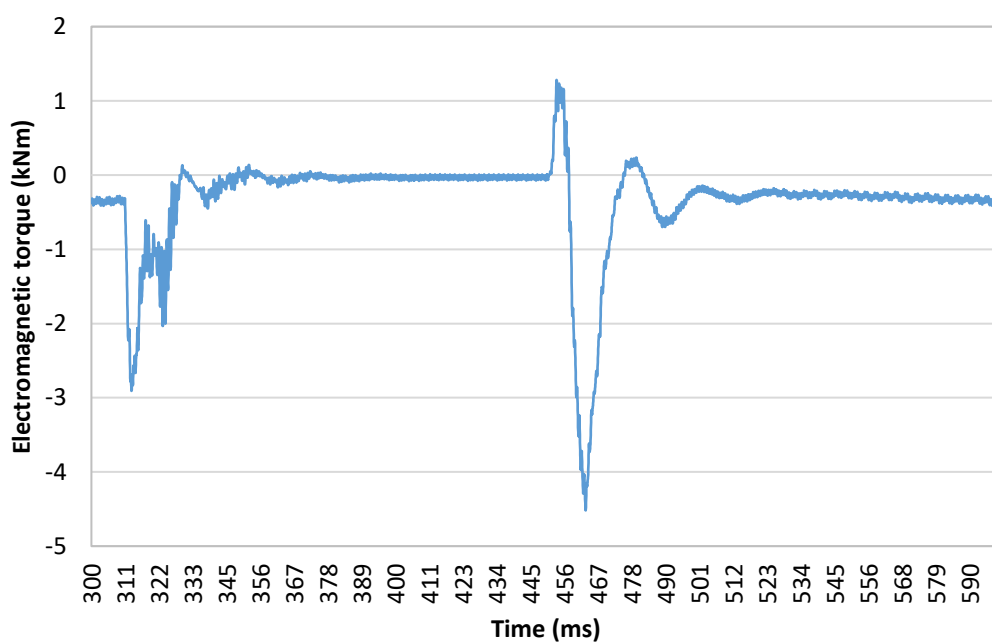


Figure 6.47: 100% voltage drop fault applied engine driven generator set, PF = 0.8.

Air gap electromagnetic torque for 140 ms FRT. Reduced field.

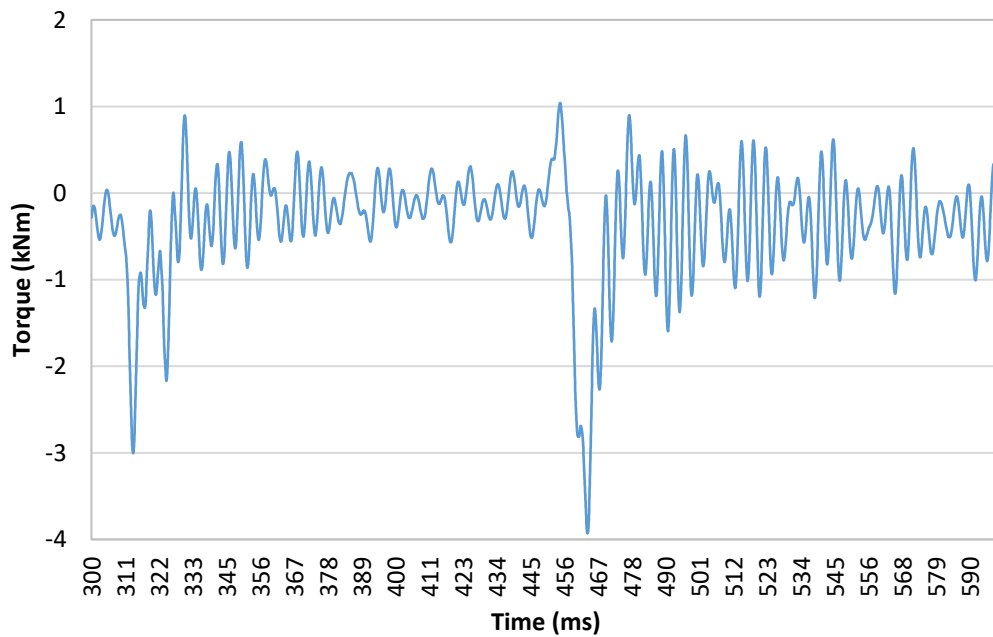


Figure 6.48: 100% voltage drop fault applied engine driven generator set, PF = 0.8.

Transducer torque for 140 ms FRT. Reduced field.

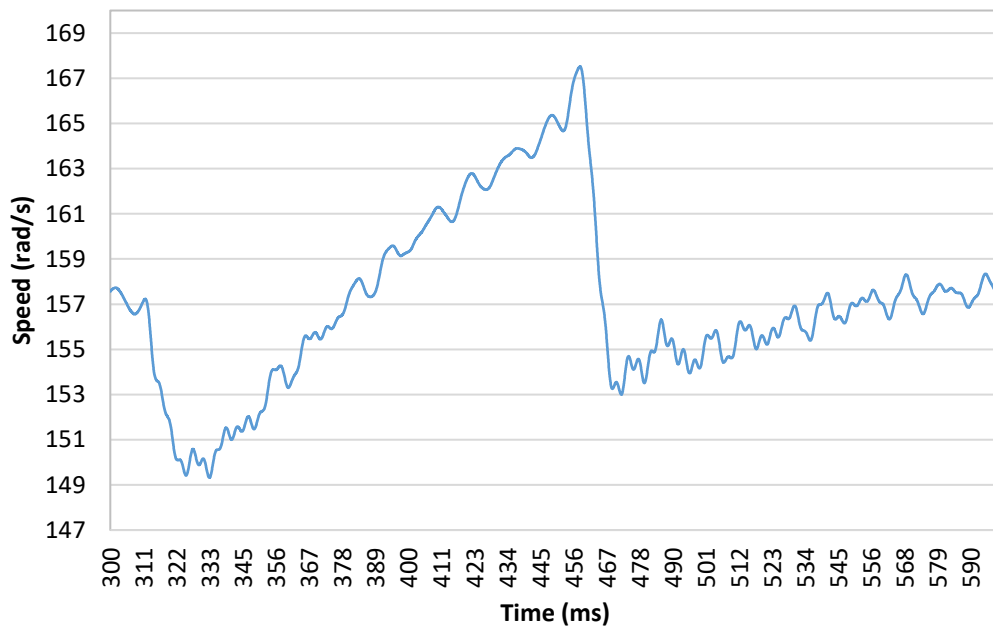


Figure 6.49: 100% voltage drop fault applied engine driven generator set, PF = 0.8.

Transducer speed for 140 ms FRT. Reduced field.

Peak torque at grid disconnection is 2.9 kNm and peak to peak torque at reconnection is 5.8 kNm. Rotational speed drops to 149.3 rad/s and peaks at 167.5 rad/s. The diesel engine genset simulation contains the expanded 1D torsional model of the engine as described in section 5.1.2. The shaft torque is measured at the coupling hub that connects between the generator shaft and the engine flywheel. Although the coupling hub has a greater rotational inertia than the torque transducer used in the motor/generator set and is connected to both machines with a different torsional stiffness it is still positioned similarly to the torque transducer. Hence it is the chosen location from which to compare the torsional oscillations between the two machine arrangements.

The low voltage ride through behaviour of the engine driven generator set is broadly similar to the motor driven generator set given that the response to changes in rotor speed occurs at the same rate for both the engine and the motor. There are some further modifications to be made to the diesel engine generator set in order to distinguish it from the motor driven set and better represent the true engine performance during LVRT. These include:

- Including a flexible coupling in the engine driven generator set.
- Increasing speed response time delays associated with the diesel engine governor and continued combustion following changes in fuel injection.

6.3.3 Flexible coupling

In all simulations performed until this point, the generator to prime mover coupling was a stiff, solid steel component that was perfectly coupled (contact stiffness equal to 100% material stiffness) to both machines. Modern grid connected generator sets will typically utilise a flexible coupling when connected to the grid in order to protect the engine from severe fault torque that arises from electrical faults, incorrect synchronisation and so on. The flexible coupling also impacts the magnitude and frequency of torsion vibrations. It is the most flexible component (for angular displacement) in the assembly so its associated torsional stiffness k_T greatly influences the frequency of the torsional modes for the entire generator set. The flexible coupling influences torsional vibration at any rotational speed (including far away from modal frequencies) which in turn can affect the power quality by altering the magnitude of electrical harmonics. The UC22F generator is most commonly produced with a bolted disk coupling which attaches directly to the flywheel and flywheel housing of the driving diesel engine. In this configuration the machine also contains only a single bearing positioned at the non-drive end and it relies on the drive end bearing of the engine for support.

For the purposes of this analysis the two-bearing configuration is used (this is also more common for larger dedicated prime power generators) with the drive end section of the generator shaft connected to a HTB-GS flywheel to shaft flexible coupling. The real flexible coupling contains a number of rubber blocks to absorb the bulk of severe torsional vibrations and shock loads that arise from short circuit and low voltage events. Since a number of other flexible coupling designs exist that could be selected for use in

grid connected generator sets, a simple approximation of k_T is used over the expected normal operating and maximum fault torque range in order to generalise the coupling dynamics.

The torsional stiffness of the coupling is obtained from datasheets for the HTB-GS flexible coupling (69) as 0.15 MNm/rad (at 30°C) at 25% of nominal torque for the coupling (rated at 4 kNm) at steady state torque with a rotational speed of 1500 RPM. The coupling is selected based on the flywheel size (SAE 18, SM80 rubber), minimum diameter of the coupling (55 mm) and the nominal torque for the generator (364 Nm). Note that in previous simulations the existing torsional stiffness for the flywheel to coupling, and coupling to generator shaft was 2 MNm/rad. At 100% of nominal torque (4 kNm) the value of k_T increases to 549 kNm/rad. With this in mind, the projected increase in torsional stiffness with applied torque follows the curve of nonlinear static torsional stiffness vs. torque as shown in Figure 6.50.

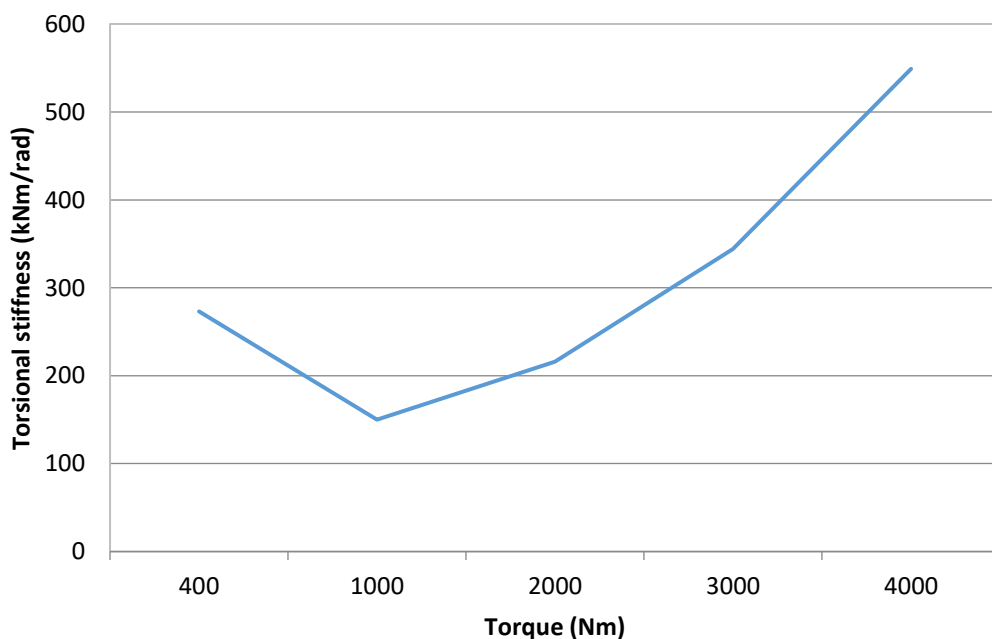


Figure 6.50: Non-linear static torsional stiffness versus applied torque for the flexible coupling.

The reduction in torsional rigidity has foremost significant impact on angular speed throughout the FRT period. The initial speed drop is increased, changing the shift in rotor angle and therefore the amplitude of the reconnection torque.

The presence of a variable stiffness coupling can significantly impact both the disconnection and reconnection peak torque and magnitude of the following torsional oscillation even when the maximum torsional stiffness is equal to that of a coupling with a constant torsional stiffness. In order to explore this behaviour further, the input electromagnetic torque and motor torque is obtained from the existing motor/generator set case study model (140 ms FRT) and input to a separate torsional model of the motor/generator set shown in Figure 6.51 with no connection to the electromagnetic model or speed control loop of the motor.

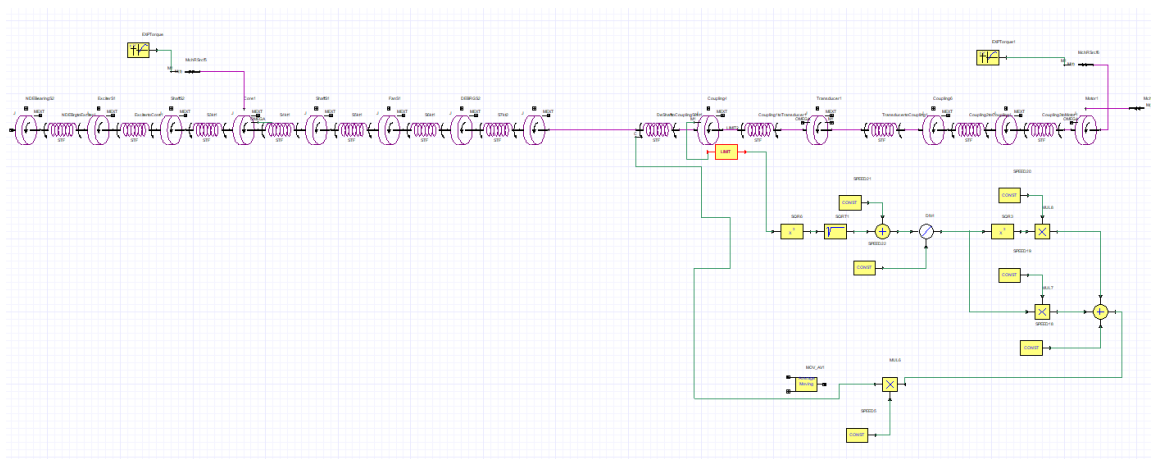


Figure 6.51: Simplorer model for flexible coupling testing on the motor/generator torsional model

This setup allows for greatly reduced simulation time whilst reproducing the torsional behaviour of the system albeit with reduced accuracy of results (1 minute simulation time versus ~12 hours). The torsional stiffness of the flexible coupling spring element is directly controlled by the signal control loop which contains the equation of the curve for coupling stiffness shown in Figure 6.50. The curve represents the torsional stiffness of the flexible coupling under various torsional loads (taken as 10, 25, 50, 75 and 100% of the nominal torque, 4 kNm). The stiffness of the coupling at any point in time during transient loading conditions will vary given a number of factors including preload, temperature and frequency of vibration. The rubber in the coupling possesses non-linear torsional stiffness properties under torsional vibration, thus the torsional stiffness may be greater or smaller than the static stiffness under the same peak load given variations in the aforementioned factors.

6.3.4 Diesel engine generator set with flexible coupling

The same flexible coupling is attached to the diesel engine case study model. An additional viscous damping of 67.8 Nms/rad is provided by the damper hub at the non-drive end of the engine. No additional structural damping is included. The simulation results of electromagnetic torque, transducer speed and transducer torque are in Figure 6.52 to Figure 6.54.

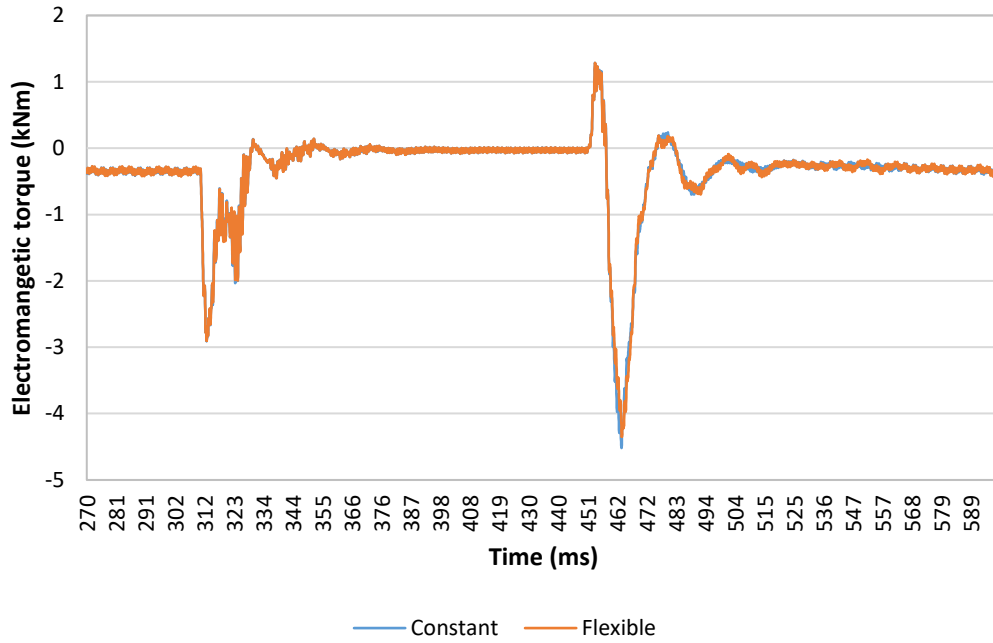


Figure 6.52: Electromagnetic torque in the case study diesel engine generator set versus coupling torque in the same model with the flexible coupling.

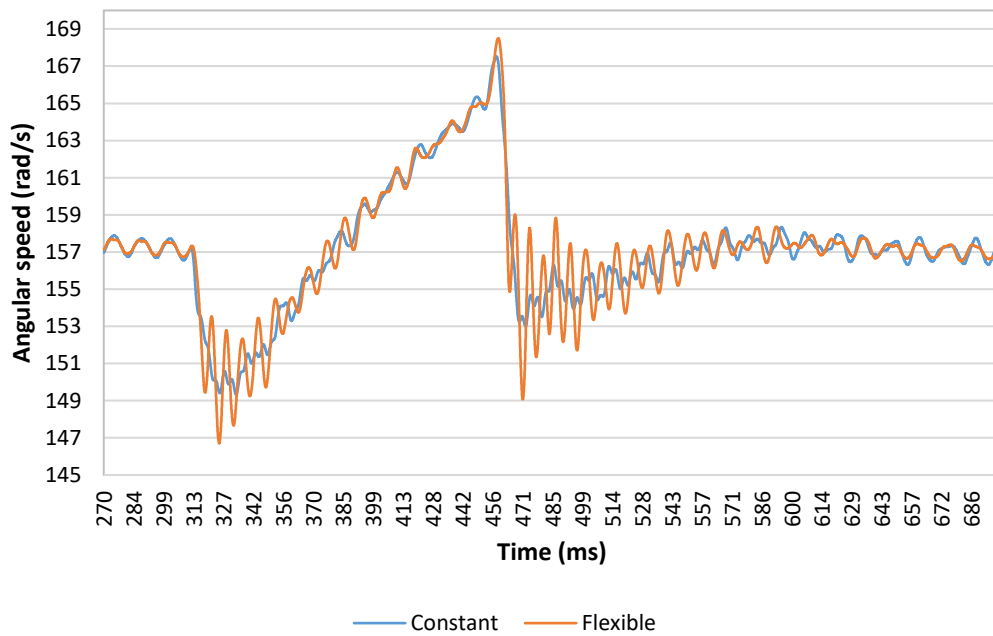


Figure 6.53: Coupling angular speed in the case study diesel engine generator set versus coupling torque in the same model with the flexible coupling.

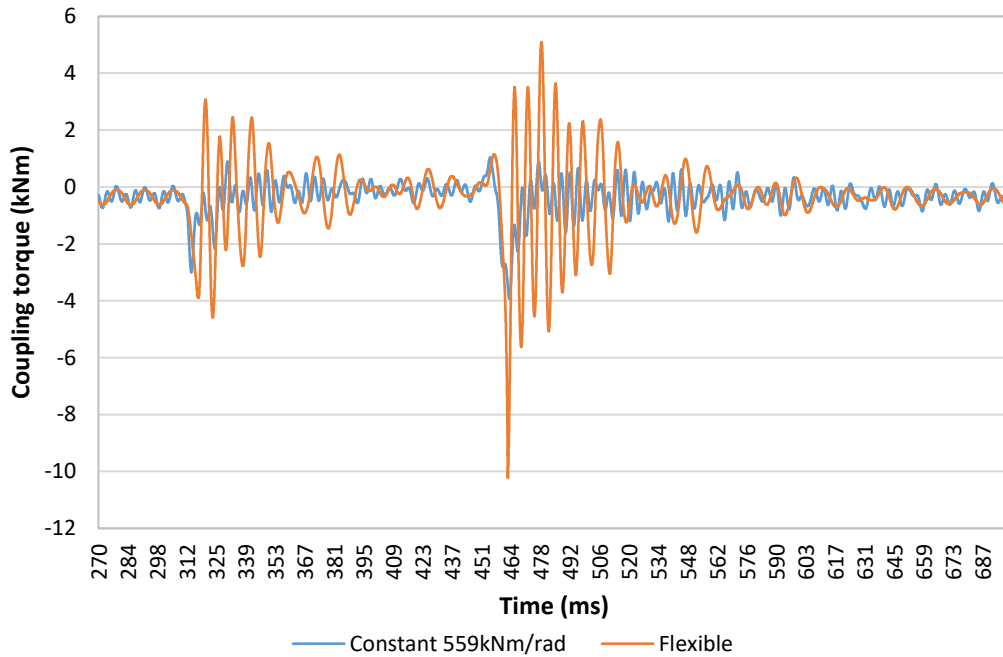


Figure 6.54: Coupling torque in the case study diesel engine generator set versus coupling torque in the same model with the flexible coupling

The engine driven generator set experiences an elevated peak reconnection torque as a result of the flexible coupling arrangement. The coupling stiffness increases to its maximum value of 554 kNm/rad over a period of 12.85 ms. The additional damping offered by the coupling and damper hub significantly reduces torsional vibration in the assembly both at steady state and during fault ride through.

6.3.5 Diesel engine speed correction delay

Since the prime mover response is based on the electric motor used in the short circuit experiments, the rate of speed recovery for the previous simulation is greater than a standard diesel engine can achieve. The diesel engine cannot reduce or increase applied

torque as fast as an electric motor, owing to limitations in fuel flow rate and delays caused by continued combustion. To account for this, the proportional and integral gain values are decreased by 50%. The simulation results of electromagnetic torque, transducer speed, motor torque and transducer torque are shown below in Figure 6.55 to Figure 6.58.

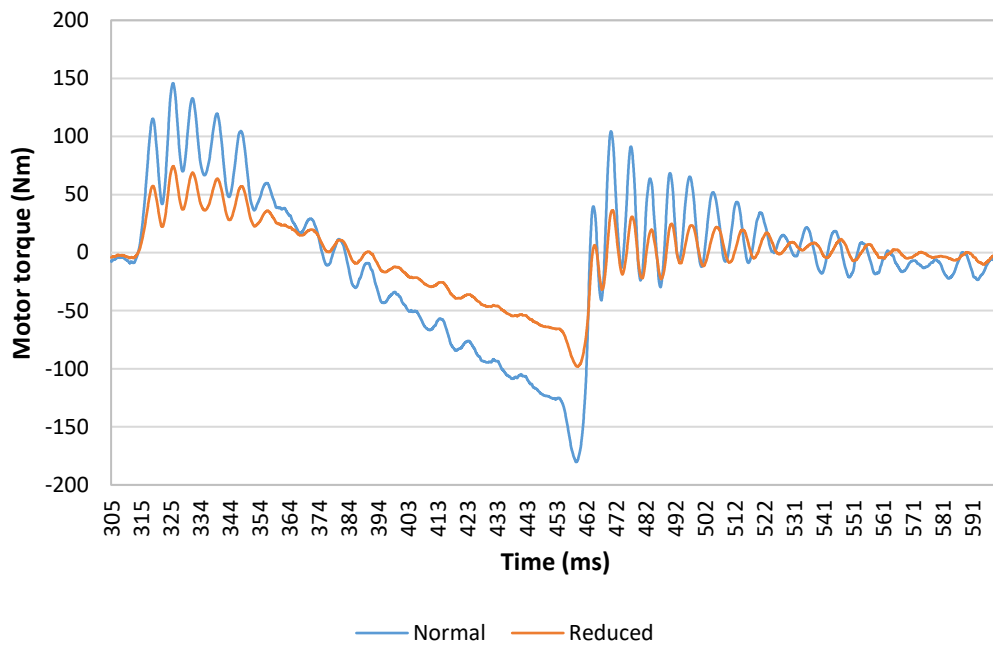


Figure 6.55: Case study simulation of diesel engine genset with reduced speed control gain vs existing speed control response. Motor torque.

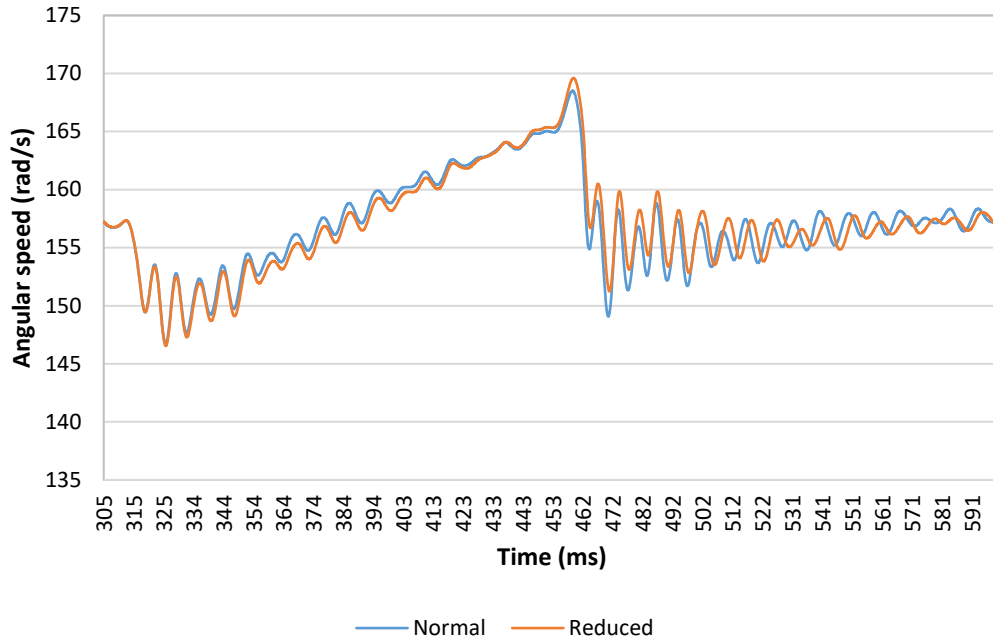


Figure 6.56: Case study simulation of diesel engine genset with reduced speed control gain vs existing speed control response. Angular speed.

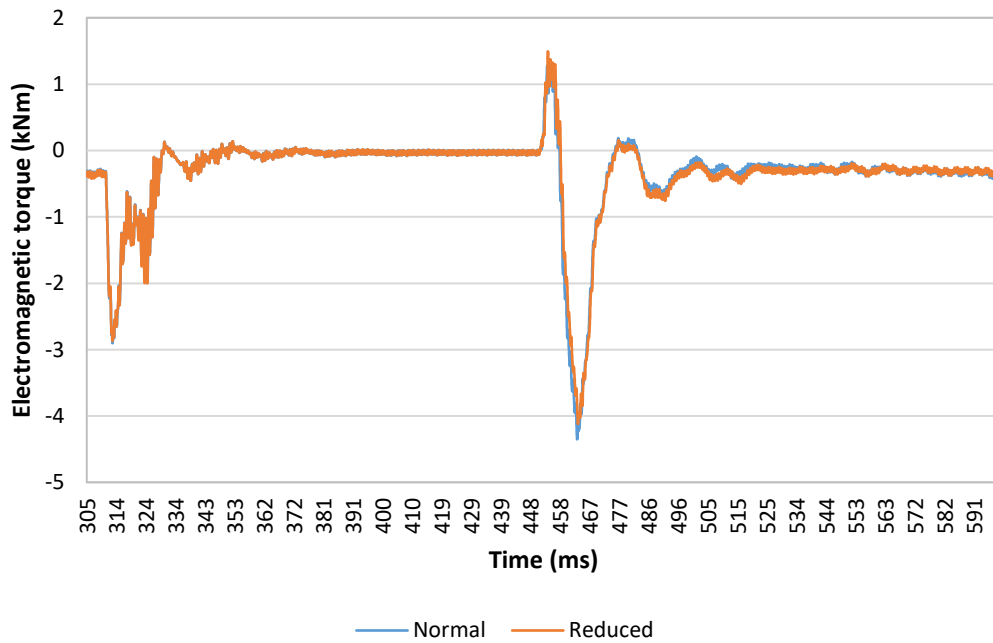


Figure 6.57: Case study simulation of diesel engine genset with reduced speed control gain vs existing speed control response. Electromagnetic torque.

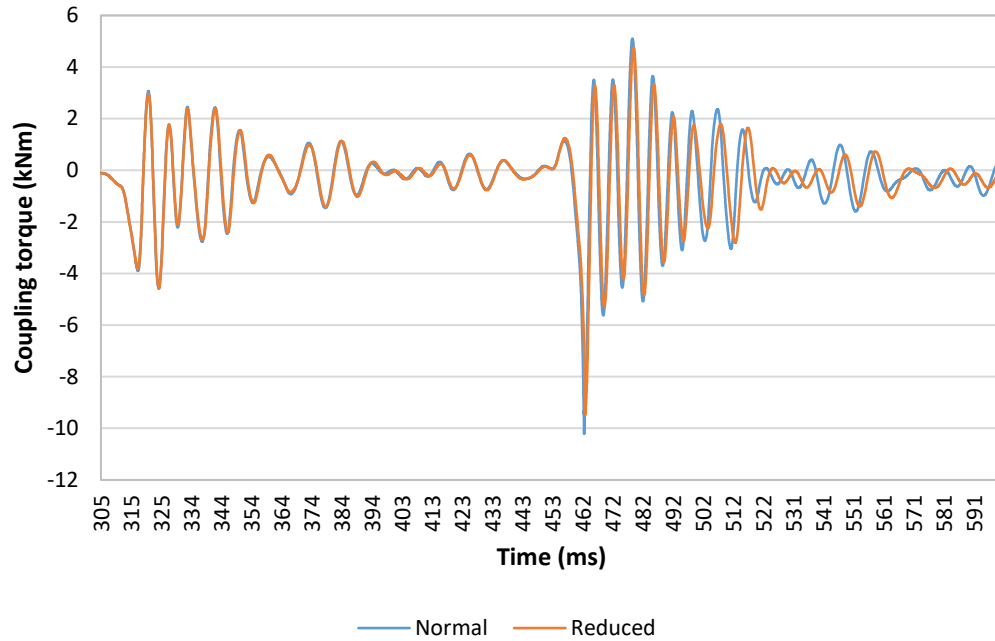


Figure 6.58: Case study simulation of diesel engine genset with reduced speed control gain vs existing speed control response. Coupling torque.

Even with a speed control gain value equal to the electric motor used in the experimental testing, the torque correction provided to the diesel engine is relatively low compared to the fault torque being transferred from the generator. Indeed, reducing the control gain by half does not have a significant effect on the resulting torque and speed measured at the flexible coupling. The peak corrective torque only reaches -180 Nm (producing a total average torque of $364 - 180 = 184$ Nm at the point of disconnection in the case of the existing, normal gain values. The reduced control gain values produce a corrective torque of -97 Nm at the same time. The angular speed at the point of reconnection increases from 168.37 rad/s to 169.59 rad/s with reduced control gain.

6.4 Rotor angle and reconnection electromagnetic torque of the engine generator set model

With all the major factors that can affect the fault ride through behaviour of the generator sets taken into consideration, the complete relationship between fault ride through time and reconnection electromagnetic torque can be obtained as follows. Using the final diesel engine generator set model, the fault ride through time is iteratively increased. The time required for a full rotation depends on the speed of rotation of the rotor which is constantly changing throughout the ride through period. The final diesel engine generator set model is simulated with a 100% voltage drop FRT over a period of 1 second. The resulting shift in rotor angle is recorded in Figure 6.59.

6.4.1 Rotor angle shift

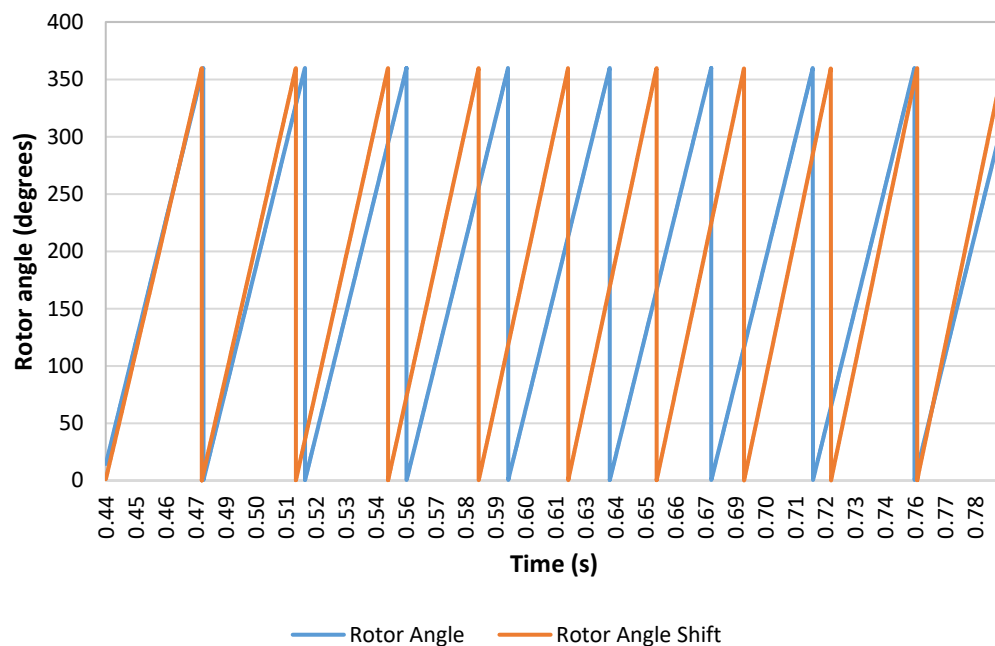


Figure 6.59: Rotor angle vs. steady state angle for final diesel engine generator set

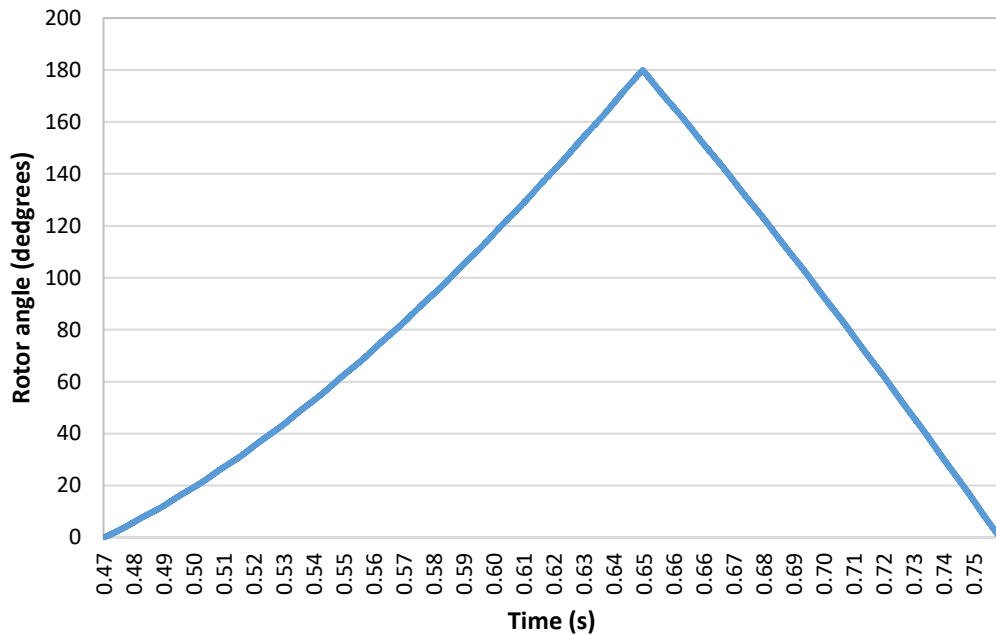


Figure 6.60: Magnitude of rotor angle shift over time (180° maximum shift)

At steady state speed, the rotor makes 25 rotations per second (25 Hz), one rotation takes 40 ms. During this FRT, the rotor rotates several times (peak to peak on rotor angle graph), the shift in rotor angle is $\sim 0^\circ$ at 466 ms when the angular position is 267.67° . The shift in rotor angle returns to 0 degrees at 763.3 ms at a rotor angle of 63.3° , thus the time required for the rotor to shift one full rotation ahead of (ahead in this case as the rotor speed is increasing) the steady state rotor position is 297.3 ms.

Figure 6.60 shows the change in rotor angle shift over time for the final Simplorer engine generator set model during low voltage ride through. Note that past 180° the displacement between the actual rotor position and its steady state position is effectively decreasing due to the rotor approaching synchronism with the steady state position (albeit being one full rotation ahead). In fact, due to the rotor having four poles rather than two, the rotor can return to full synchronism with its steady state position at four

different rotor shift angles, each displaced 90° apart. Figure 6.61 and Figure 6.62 show the electromagnetic torque and angular speed results for a relative angular shift of 90° , which is reached after a period of 261 ms.

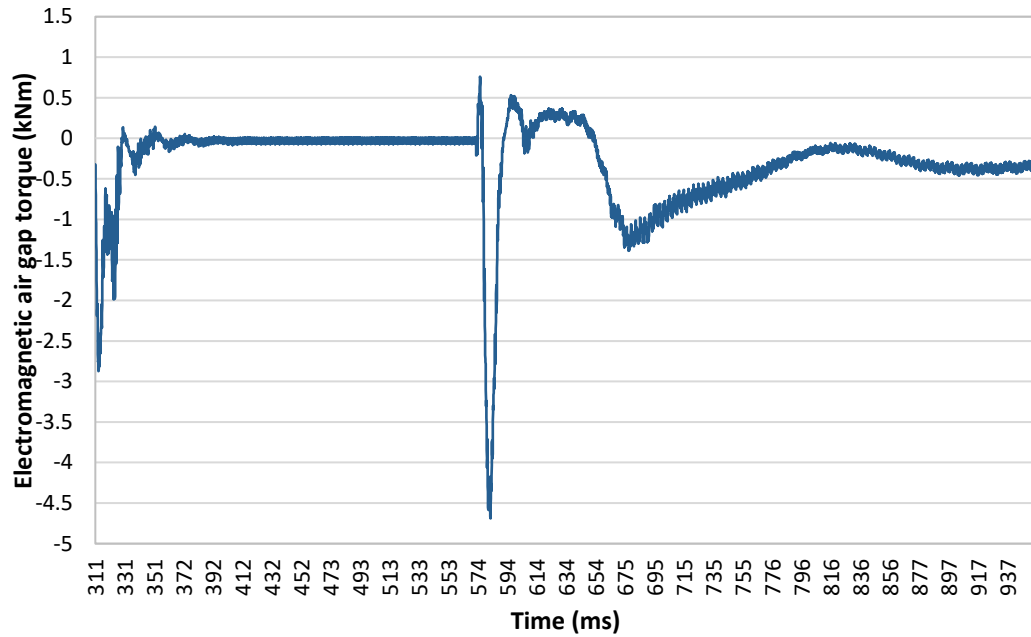


Figure 6.61: Electromagnetic air gap torque for the engine generator set reconnecting at rotor angle shift of 90°

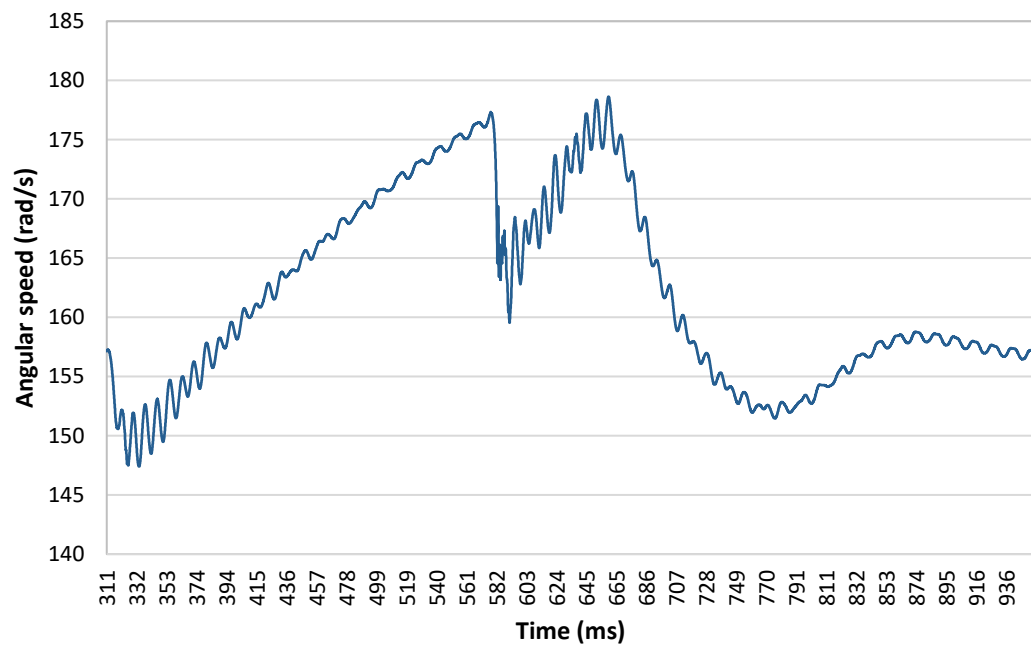


Figure 6.62: Coupling angular speed for the engine generator set reconnecting at rotor angle shift of 90°

The first 90° rotor angle shift occurs at 571.95 ms, when reconnected to the grid at this time, the peak electromagnetic torque is 4.69 kNm. Additionally, note the rotor slip events that occur following reconnection due to the increase in rotor speed over the extended FRT period.

As the machine is operating at a power factor of 0.8, the actual zero point for synchronisation is shifted a few degrees off the rotational coordinate system attached to the rotating electromagnetic field in the stator windings. All rotor angle shift positions calculated here are relative to the rotor reference frame rather than the reference frame for the electromagnetic field.

6.4.2 Relationship between the relative angular position of the rotor and peak electromagnetic torque at the point of grid reconnection

Twenty-five simulations are performed with a value of rotor angle shift of 15° (0.26 radians) between them. The grid is reconnected at each iteration and the following reconnection electromagnetic torque results are recorded in Figure 6.63.

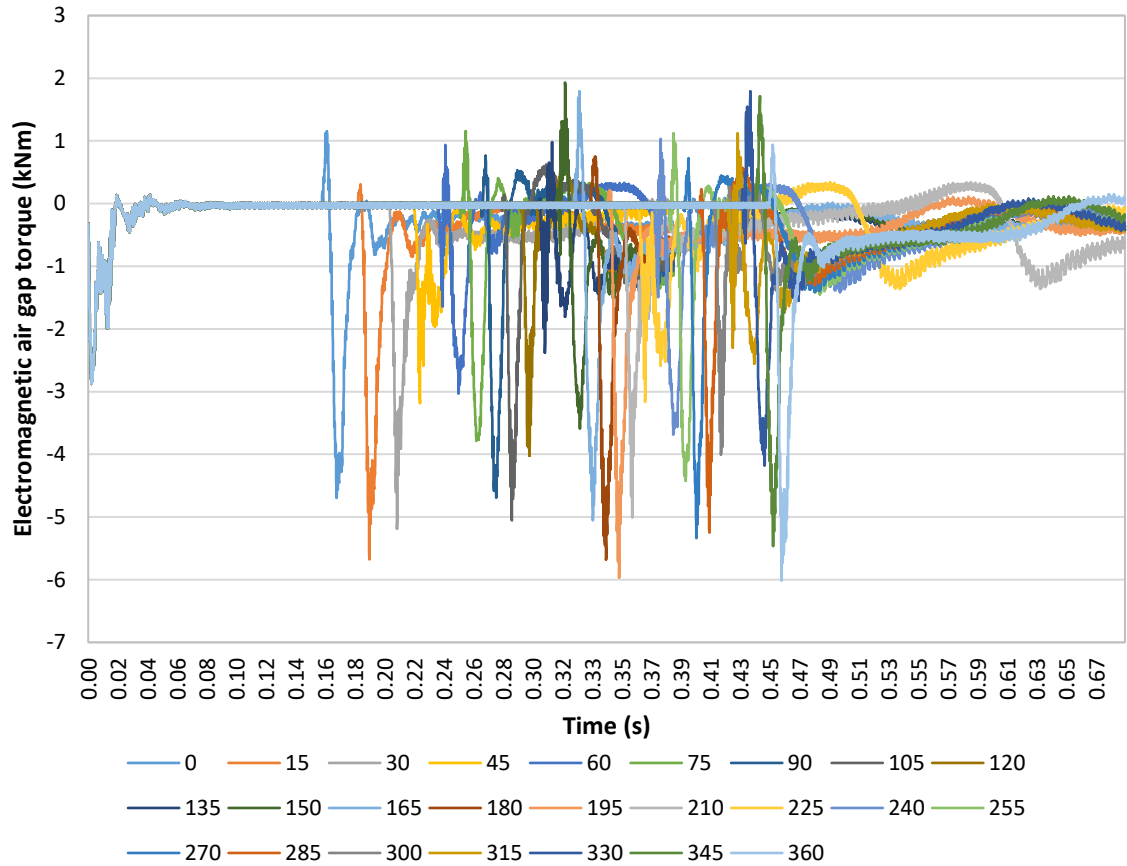


Figure 6.63: Electromagnetic torque for reconnection at various values of rotor angular shift. Peaks appear in order of increasing rotor angle shift.

At zero degrees rotor angle shift (the generator is reconnected when the rotor angle is in synchronism with the rotating stator field) the peak negative electromagnetic torque is -4.7 kNm and the total peak to peak torque is 5.84 kNm. The electromagnetic torque results for each rotor position are shown in Table 6.2.

Table 6.2: Electromagnetic torque for reconnection at various values of rotor angle shift

Rotor angle shift (degrees)	Time of reconnection (ms)	Peak electromagnetic torque (kNm)	Peak to peak torque (kNm)	Time to peak torque (from disconnect) (ms)
0	466.00	-4.70	5.85	10.05
15	489.75	-5.67	5.97	8.10
30	509.80	-5.19	5.19	6.45
45	527.30	-3.19	3.19	4.15
60	543.10	-3.03	3.97	14.05
75	557.90	-3.79	4.94	11.15
90	571.95	-4.69	5.45	10.25
105	585.20	-5.04	5.17	10.80
120	597.90	-4.02	4.64	6.35
135	610.15	-2.38	3.38	4.35
150	622.00	-3.59	5.52	15.75
165	633.60	-5.05	6.84	12.80
180	644.75	-5.68	6.43	10.40
195	655.55	-5.96	6.16	8.30
210	666.05	-5.00	4.77	6.45
225	676.50	-3.16	2.98	4.60
240	686.80	-3.68	4.71	13.00
255	696.85	-4.42	5.53	11.25
270	706.60	-5.33	6.02	8.55
285	716.35	-5.25	5.457	7.40
300	726.05	-3.96	4.17	5.50
315	735.50	-2.29	3.42	3.85
330	744.75	-4.18	5.96	15.75
345	754.10	-5.46	7.13	12.05
360	763.30	-6.02	6.94	8.40

As predicted, the reconnection torque is similar at 0° and 90° rotor angular shift. The reconnection torque is greater at 180° shift given that the rotor is rotating at a higher speed at this moment in time. This behaviour demonstrates that the peak electromagnetic torque depends upon not only the rotor angle at the instant the machine is reconnected to the grid, but also the total angular displacement over the following few milliseconds until the peak reconnection torque is reached.

During the time period (~ 10 ms) in which the peak (sub-transient) electromagnetic torque is produced, the rotor will have displaced by a greater angle, pushing the rotor further out of synchronisation. The resulting electromagnetic torque induced back into the rotor is increased. This behaviour is evidently true for values of rotor angle shift spaced 90° apart but difficult to identify between consecutive shifts in rotor angle such as between 15° and 30° . Additionally, recall that the phase of stator currents at the point of disconnection also affects the peak electromagnetic torque to a small degree.

Another observation is made for the magnitude of peak electromagnetic torque and corresponding shift in rotor angle. The minimum peak torque is produced when the shift in rotor angle is 45° , halfway between two rotor poles where the stator field is weakest and the rotor is positioned as far out of synchronism with the stator field as possible. The peak torque is also achieved in the shortest period of time, 4.15 ms. The following rotor positions of 60° and 75° produce increased electromagnetic torque peaks, though of a lower magnitude compared to their equivalent positions of 15° and 30° . Additionally, the peak to peak torque tends to decrease as the rotor shift angle increases towards the 45° and the peak to peak torque increases as the rotor angle shift progresses further towards 90° .

As shown in Figure 6.63 and Table 6.2, The maximum peak electromagnetic torque occurs at relative angular positions of 15° , 195° and 360° , repeating every 180° and increasing in magnitude as the fault ride through time is extended. The lowest peak electromagnetic torque occurs at relative angular positions of 45° , 135° , 225° and 315° , repeating every 90° . The difference between the minimum peak torque (2.38 kNm) and the maximum peak torque (6.02 kNm) is 3.64 kNm, an increase of 253%.

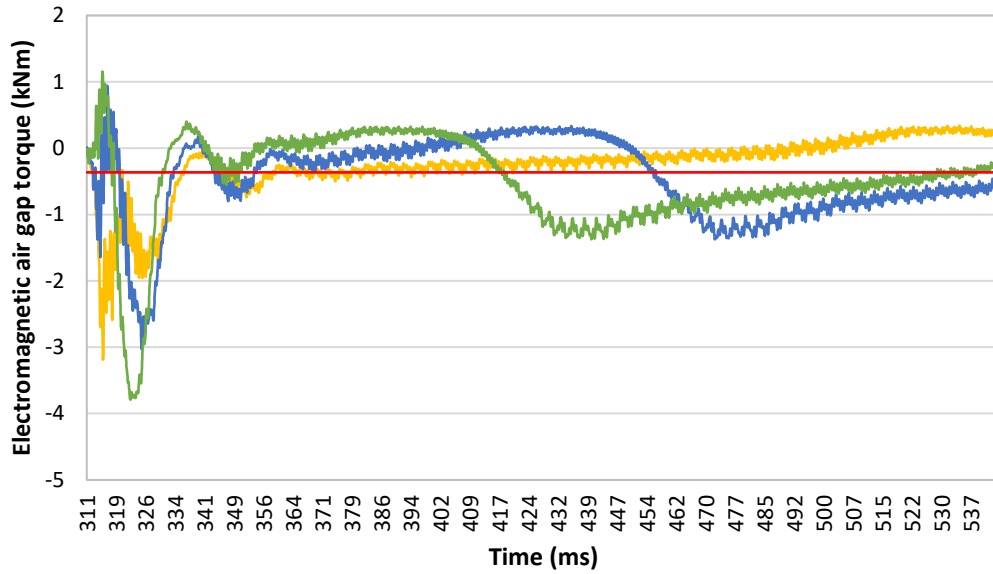
The results of this analysis show just how unpredictable the peak reconnection torque can be for an unprotected synchronous generator. The peak electromagnetic torque is highly sensitive to the relative angular position of the rotor, which can dramatically increase over a period of 20 ms. This observation is particularly important when considering the magnitude of torsional stress that the rotor shafts and couplings are subjected to when such extreme reconnection scenarios occur following LVRT. While the overall FRT performance is typically determined by how long the machine can ride through the fault and whether or not the rotor will be capable of resynchronising with the grid, the magnitude of the electromagnetic torque at the point of grid reconnection is overlooked in the existing body of research. Whilst the magnitude of transient reconnection torque does not significantly affect the post fault performance of the generator, it can make the difference between a safe and an unsafe reconnection event from a mechanical integrity point of view.

This outcome suggests that when analysing the peak stress in the machine couplings and shafts, the peak electromagnetic torque must be obtained for a range of rotor angular positions to correctly determine the maximum possible applied torque.

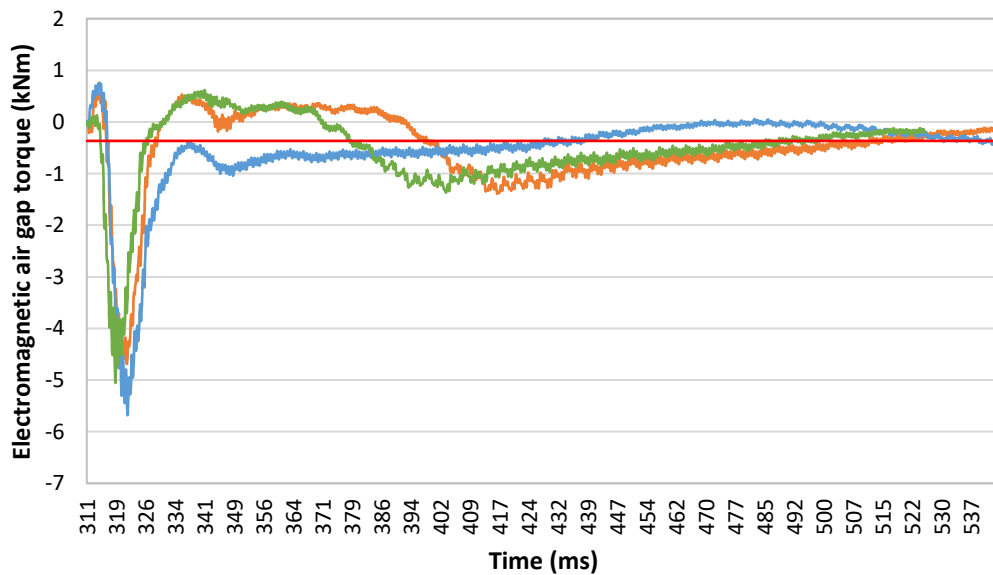
Similarly, for estimating the life of the generator when subjected to several LVRT events it is important to use the relative angular position versus electromagnetic torque data to obtain the number of cycles (in this case LVRT events) to fatigue failure.

6.4.3 Post grid reconnection torque

At any angle of rotor shift at the point of grid reconnection, the rotor experiences a period of increased electromagnetic torque before fully re-synchronising with the grid due to the increase in rotor speed during the fault ride through period as shown in Figure 6.64. After around 45° of rotor shift from its steady state position, rotor de-synchronisation slip events begin to increase in intensity following reconnection. The slip events (as visualised by a second drop or rise in electromagnetic torque following reconnection) following on from this point all have the same magnitude of peak positive and negative torque. As the shift in rotor angle at the point of reconnection is increased, the time before the rotor slip event occurs decreases as the rotor angle approaches 90° shift. As the shift angle is increases further, the slip continues to occur earlier in time until 180° is reached.



— 45 — 60 — 75 — Steady state



— 90 — 180 — 105 — Steady state

Figure 6.64: Electromagnetic torque for reconnection at various values of rotor angle shift over post reconnection time period

At 180° the rotor resynchronises with minimal rotor torque/speed deviation from steady state, the post reconnection electromagnetic torque is almost identical to that of a rotor angular shift of 15° . In conclusion to this observation, the rotor can reconnect in

synchronism with the grid at 180° and rapidly stabilise torque and speed following reconnection. The downside of this is that due to the rotor effectively 'snapping' suddenly back into synchronisation with the grid, the magnitude of sub-synchronous transient electromagnetic torque reaches its maximum value.

The presence of a flexible coupling has little impact (aside from a small decrease attributed to the change in rotor speed) on the reconnection electromagnetic torque of the generator, nor does the relatively small engine/motor torque. The relationship between fault ride through time and peak electromagnetic torque holds for any prime mover or coupling scheme connected to the generator.

6.4.4 Comparison of rotor angular position

Figure 6.65 shows the angular position of generator rotor at a selection of simulated reconnection rotor angle shifts. Note that the rotor is rotating anti-clockwise. Also note that the rotor angle shifts further ahead of the grid synchronised position as time passes.

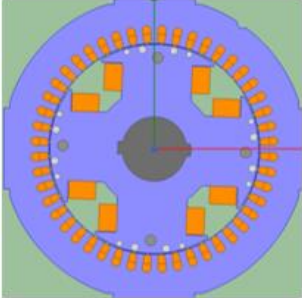
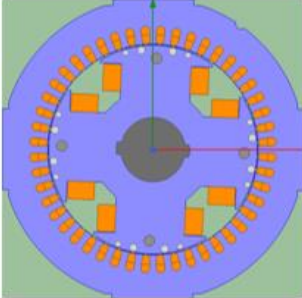
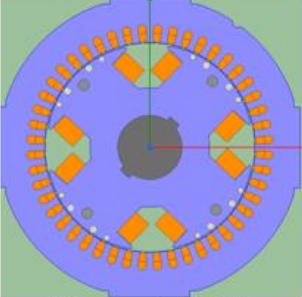
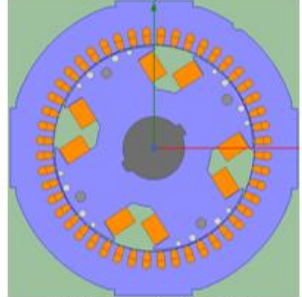
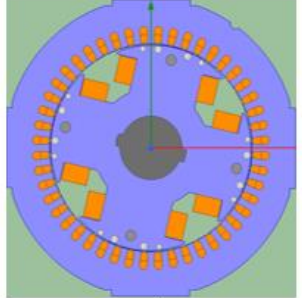
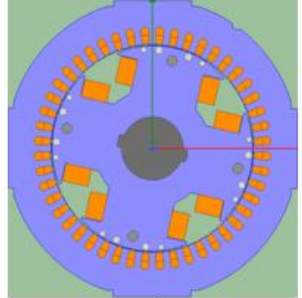
Rotor angle shift (°)	Transient	Steady State
0	 Rotor angle 267.67	 Rotor angle 267.67
15	 Rotor angle 136.45	 Rotor angle 121.42
180	 Rotor angle 76.86	 Rotor angle 256.93

Figure 6.65: Physical shift in rotor angular position at 0°, 15° and 180° shift

6.4.5 Worst-case scenario

The worst-case scenario is defined here as the rotor shift angle at grid reconnection that produces the greatest reconnection torque at the highest maximum rotor speed. From the angular shifts that were simulated, the 360° rotor angle shift results in maximum magnitude electromagnetic torque and maximum rotor angular speed reached prior to grid reconnection. As the rotor speed increases over extended ride through periods, the time required for resynchronisation will continue to increase until the point that the

engine torque is reduced to provide a net negative torque. The peak electromagnetic torque will continue to appear at intervals of 180° , around 15° , 195° , 375° ($/15^\circ$). The second largest electromagnetic torque peaks occur every 90° .

The rotor speed also affects the time required for resynchronisation. Figure 6.66 and Figure 6.67 compare the torque results between a 180° shift in rotor angle and a 360° shift. The initial electromagnetic torque at reconnection is very similar between the two examples since they are spaced 180° apart.

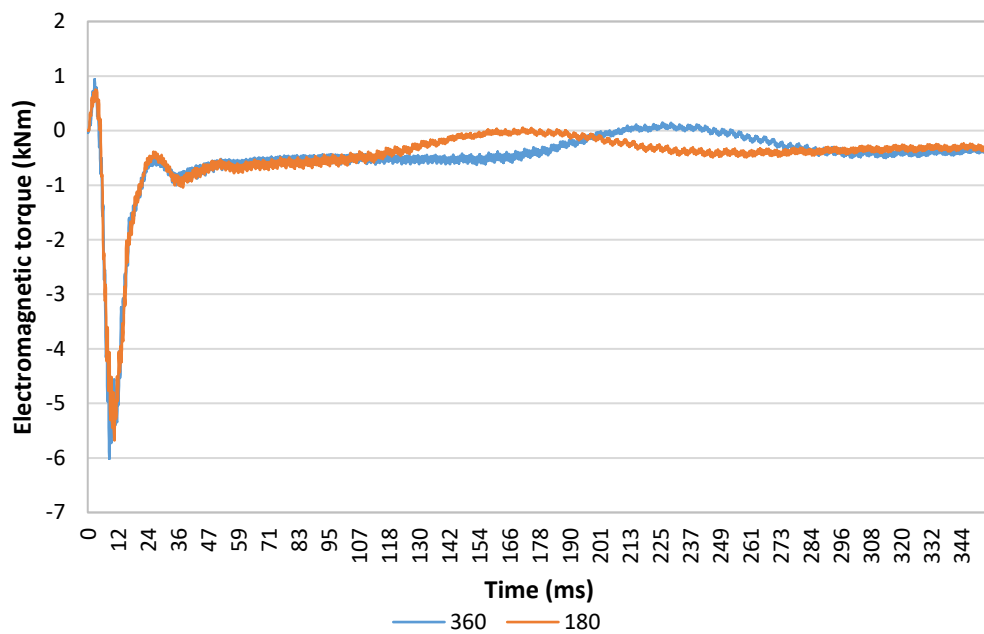


Figure 6.66: Electromagnetic torque for rotor angle shift of 180° and 360° extended

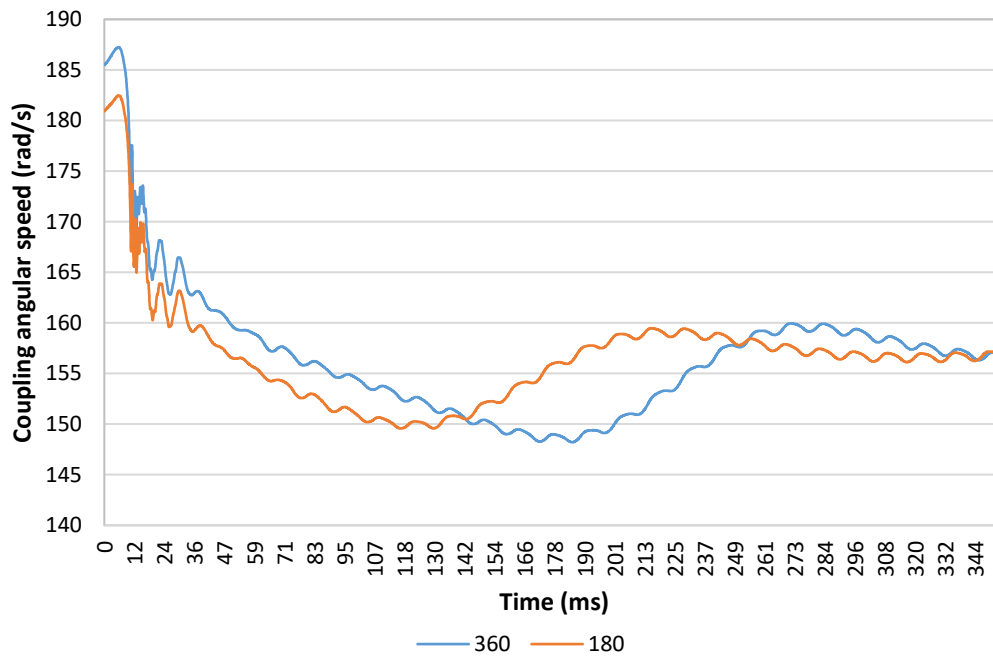


Figure 6.67: Coupling angular speed for rotor angle shift of 180° and 360° extended

Grid reconnection at 180° represents a fault ride through time of 333.8 ms in this case and reconnection at 360° takes 452.3 ms. At the time of disconnection, the 180° rotor shift reached an angular speed of 182.45 rad/s and the 360° shift, 187.23 rad/s. Depending on the rotor inertia and the gain value of the diesel engine speed controller, the difference in pre-reconnection rotor speed between the two angular shift values may be greater if rotor acceleration was increased. Given that these ride through periods are significantly longer than those required by grid codes for a 100% voltage drop, it is unlikely that such an FRT would occur in reality without the generator being tripped. In this case, system stability is restored earlier in time for the shorter fault ride through period.

6.4.6 Chapter 6 summary

This chapter investigates the relationship between low voltage fault ride through faults and the speed, torque and current results of a synchronous generator set. A case study model is developed with the worst-case operating scenario for the diesel driven genset. In this model, the machine is reconnected with the grid (fault cleared) when the relative angular position between the rotor and stator fields results in a maximum peak electromagnetic torque.

The steps taken in this chapter are as follows:

- The three-phase short circuit breaker is removed from the circuit in the Simplorer model and replaced with a three-phase voltage supply to form the grid connected model.
- 40 ms, 180 ms and 320 ms LVRT faults are simulated on the motor driven, grid connected genset and the typical fault ride through characteristics are discussed. It is noticed that the shift in rotor angular position is dramatically altering the peak electromagnetic torque at the point of grid reconnection.
- Additional LVRT simulations are performed to investigate the impact of reducing the circuit resistance and field current peak at the point of grid disconnection and better match the peak current with existing data for the UC22 generator.
- With the generator set model producing predictable LVRT results, a flexible coupling is added to both generator sets to better represent a real coupling configuration for the genset in service.

- 25 LVRT simulations are performed on the engine driven genset where the grid is reconnected in increasing steps of 15° relative angular position between the rotor and the stator field of the generator.
- The angular positions that produce the greatest peak electromagnetic torque at the point of grid reconnection are highlighted.

The key points from this chapter are as follows:

- The Multiphysics genset models are capable of successfully simulating 100% LVRT faults.
- The peak electromagnetic torque at the point of grid connection can be up to 3 times greater than the electromagnetic torque at the point of grid reconnection for this genset.
- Grid reconnection at the point when the relative angular shift is 15° , 195° and 360° produces the highest peak electromagnetic torques of 5.67 kNm, 5.98 and 6.02 kNm. There are also two large torque peaks of 5.04 kNm and 5.96 kNm between these relative angular positions at 105° and 195° . Essentially there are 5 large peak torques that can be produced throughout 360° of rotor angular shift.
- The key observation is that the peak electromagnetic torque and thus the stress in the genset shafts can vary by a wide margin depending on the exact moment the grid is reconnected.

The work completed here is used in the following chapters are as follows:

- The electromagnetic and engine torque results from the case study model with the worst angular position at grid reconnection is used in Chapter 7 to validate the ANSYS 3DFE models of the complete engine and motor driven gensets. And the electromagnetic torque throughout FRT is applied in the transient analysis of the engine driven genset.
- The key observation noted above is utilised in Chapter 8 when the engine driven genset is compared with its modified counterpart. Care is taken to ensure that both machines are reconnected at precisely the same relative angular position so that the beneficial effect of the modifications can be properly quantified. If the modified model was simply reconnected following the same FRT time, the peak electromagnetic torque would be completely different due to the increased inertia and reduction of fault current.

6.4.7 Chapter 6 contributions to the literature

The existing literature on the use of electro-mechanical models for the simulation of LVRT faults in electrical machines detailed in section 1.3.4 is expanded upon in this chapter by:

- Exploring the behaviour of several different LVRT conditions using a dynamically validated, multi-physics model of a synchronous generator set.
- Determining the relationship between the relative angular position of the rotor and the peak electromagnetic torque observed at the point of grid reconnection. The data obtained from the simulations is used to determine the maximum peak electromagnetic fault torque and therefore the most damaging reconnection

scenario. The existing research does not provide an explanation or any example data which shows that the fault torque varies significantly as the relative angle increases. For example, the variation in shaft torque shown in (21) over 110° is constantly increasing whereas in Figure 6.63, two distinct peaks with reduced electromagnetic torque in between are shown.

Chapter 7 Transient torsional analysis

7.1 ANSYS 3DFE genset model

In the next stage of the analysis, the obtained generator and diesel engine torque is applied to a 3D finite element model of the diesel engine generator set. Transient analysis is performed on the genset model to compare the speed and torque traces measured at the coupling with those obtained from the 1D torsional model in Simplorer. The full Simplorer model is further validated, and the results inform the next stage of transient analysis in Chapter 8. But before transient analysis of the 3DFE model can take place, the torsional modes of the model must be validated. The modes are already validated for the generator rotor alone, but the 3DFE will now include the prime mover and coupling elements that are present in the 1D Simplorer torsional model. Simplified 3DFE models of the generator sets are created to bridge the gap between the 1D torsional model and a full detail 3DFE model. This allows for direction comparison of torsional vibration between the 1D models and the final 3DFE models.

These equivalent models consist of 3D cylindrical shafts representing the torsional stiffness between the inertia elements which are represented by point masses. The torsional stiffness of the shaft sections is selected by altering their diameter value and calculating stiffness as per Equation 2.7. The torsional stiffness can also be controlled by altering the shear modulus value and maintaining a constant shaft diameter. Values of torsional stiffness and inertia are equal to that of the 1D models as shown in Tables 5.1 and 5.2.

There are two options available to perform the analysis here. The first option, mode superposition (MSUP), uses the modal analysis data obtained from a separate modal simulation by linking the transient simulation to the modal results. The second option performs a full transient analysis which is capable of updating modal frequencies during the simulation. The first option is faster, however the modal results are fixed throughout the transient analysis (no non-linear behaviour is accounted for) and the solution file size is also substantially larger than that of a full analysis. The full transient analysis takes into account the shift in modal frequencies when non-linear stiffness properties are applied to the materials of the structure as in the case of the flexible coupling. Modal superposition transient analysis also does not support the addition of viscous damping at specified points within the model, only overall adjustments to model damping via damping ratio and numerical damping.

The first simulation of this section is performed to compare the constant stiffness coupling case from the case study results of the motor and diesel engine generator sets with their equivalent stiffness ANSYS 3DFE models. The torsional stiffness of the coupling element is set to a constant 559 kNm/rad by adjustment of material shear modulus to match that used in the Simplorer case study models. Electromagnetic torque for the 140 ms LVRT simulation is applied to the shaft section representing the torsional stiffness between the rotor core and the fan. Motor/engine torque is applied to the edges where the pistons/motor inertia are positioned. The MSUP method is used first in order to establish the correct boundary conditions and simulation settings since results can be obtained quickly and compared with the 1D modal results in order to make adjustments.

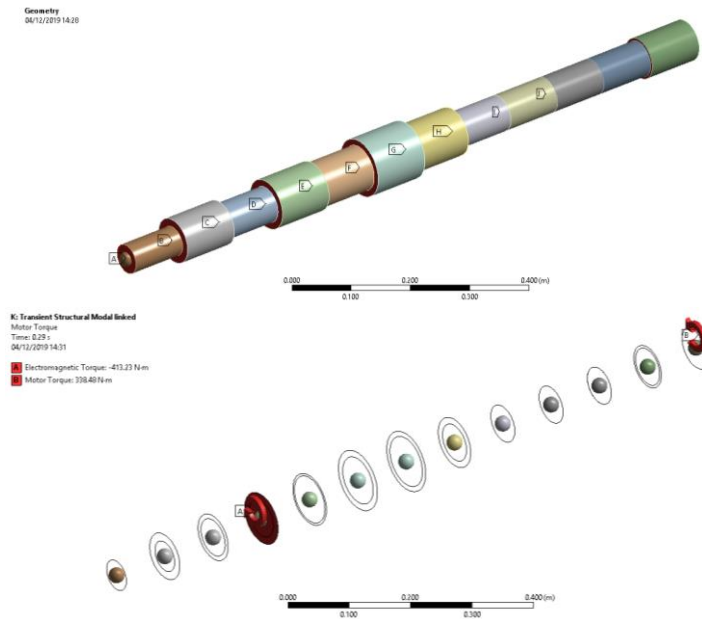


Figure 7.1: Motor/generator set equivalent shaft ANSYS model

7.1.1 Modal superposition method

Firstly, the modal results are checked against the calculated torsional modes for the 1D motor/generator set model with a coupling stiffness of 559 kNm/rad. The free-free torsional natural frequencies for the 1D Simplorer model are calculated using a simple MATLAB script as shown in Appendix B, the first three (non-free body) modes are 107 Hz, 561 Hz and 674 Hz. The ANSYS model is supported by cylindrical joints but they have zero torsional stiffness, thus the model is effectively free of constraints in the rotational (z) direction. The same arrangement is used in transient analysis solver. The first three torsional modes from the ANSYS model are 106.87 Hz, 559.6 Hz and 666.26 Hz. The ANSYS model is validated for further transient analysis.

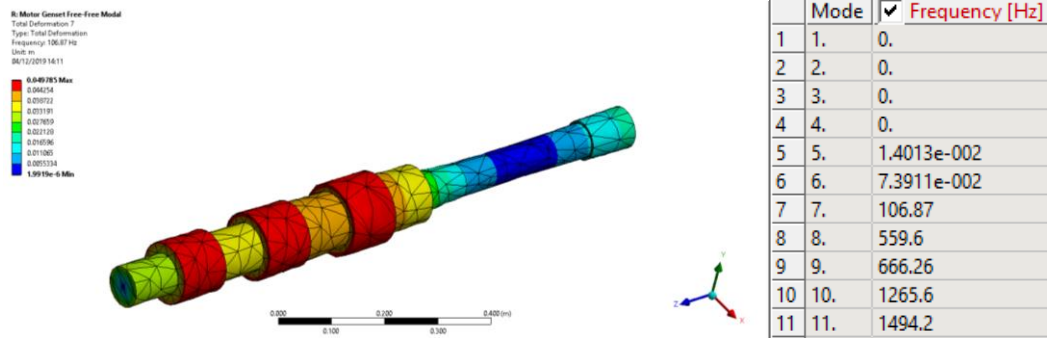


Figure 7.2: Modal analysis results for the 3D equivalent shaft model of the motor/generator set (rotational displacement for 106.87 Hz mode shown)

Angular speed of the coupling element relative to an assigned cylindrical co-ordinate system is obtained in the solution results in m/s. Once converted to rad/s this relative speed is added to the steady state speed of 157 rad/s for direct comparison with the Simplorer model results;

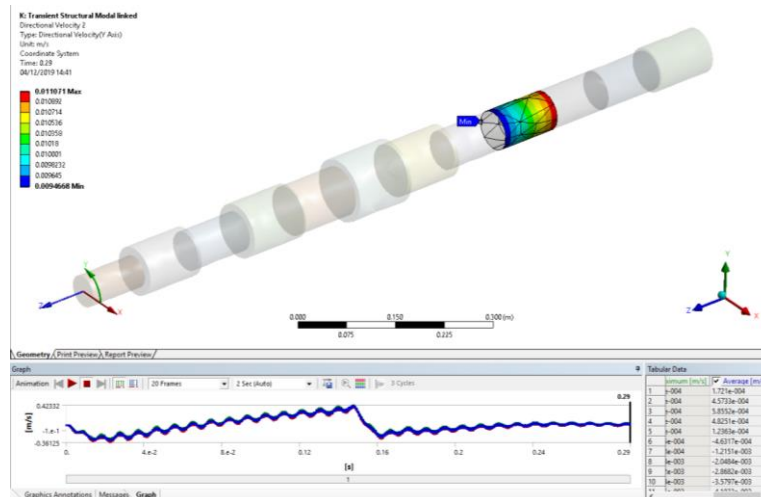


Figure 7.3: Raw directional velocity results for the 3D equivalent shaft model of the motor/generator set. (Results obtained at the end with minimum displacement, in blue, where the coupling inertia is positioned)

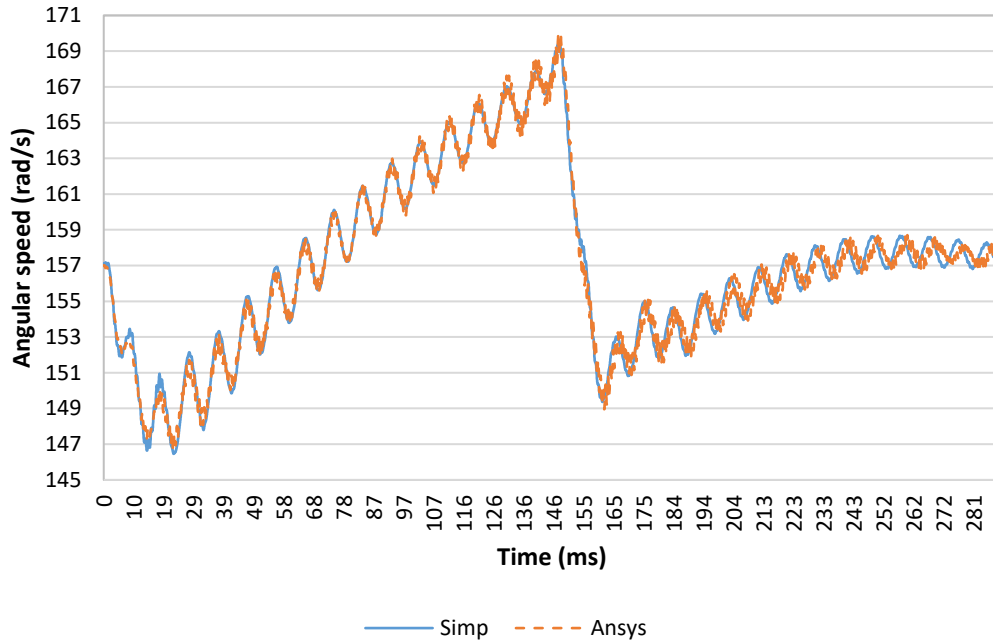


Figure 7.4: Equivalent ANSYS model angular speed vs. Simpler model angular speed

The coupling torque is obtained from a moment reaction probe placed on the equivalent shaft section neighbouring the coupling to generator section.

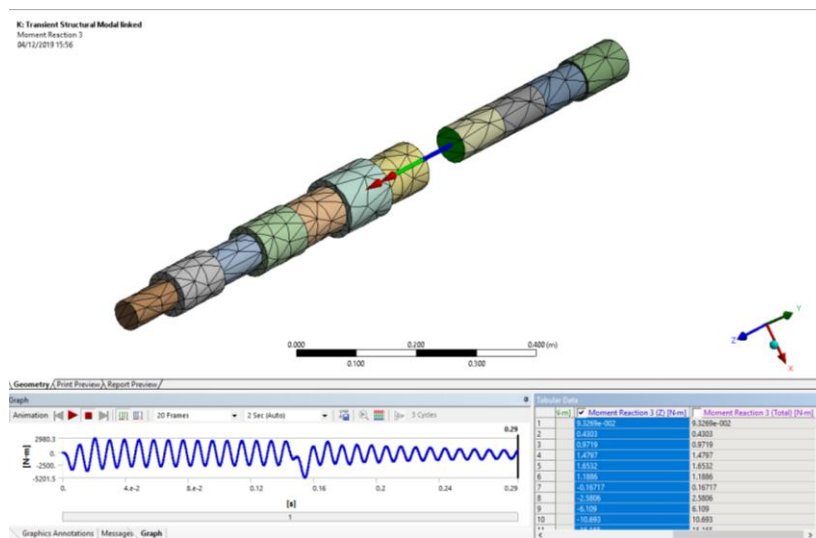


Figure 7.5: View of moment reaction probe results at the motor/generator set coupling

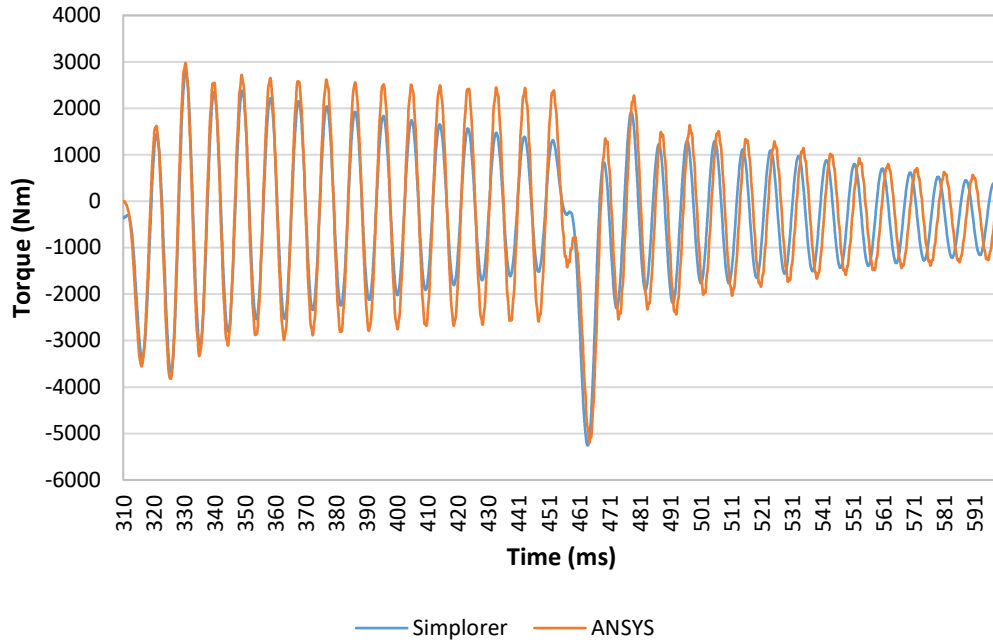


Figure 7.6: Coupling torque for the 1D Simplorer model versus torque for the 3DFE equivalent shaft model. Motor genset

Careful selection of the directional velocity measurement is required here. If measurements are taken from the shaft representing reduced stiffness between the coupling and the generator, the additional torsional flexibility present will increase the magnitude of oscillations in speed and torque. Note that the frequency of torsional vibration decreases more following reconnection for the ANSYS modal than the Simplorer model. Nonetheless, since the frequency of vibration prior to reconnection is the same for both models, the positioning of stiffness elements, point inertias, interface stiffness and both transient and modal analysis settings defined in the ANSYS model are further validated.

7.1.2 Full transient analysis method

As previously mentioned, the full transient analysis method requires a significantly longer simulation time. Since the modal superposition method was validated against the Simplorer results, the same model, constraint and loading arrangement can be applied in the full transient analysis with confidence.

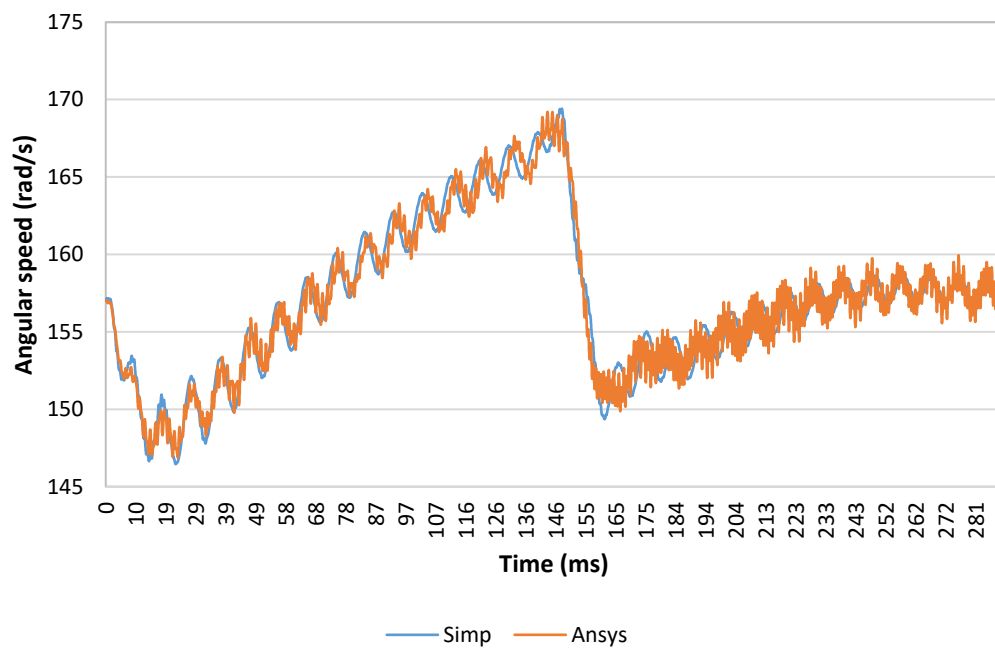


Figure 7.7: Un-damped transducer angular speed results from Simplorer model versus 3DFE equivalent shaft model of the motor genset (311 ms fault start time, zeroed)

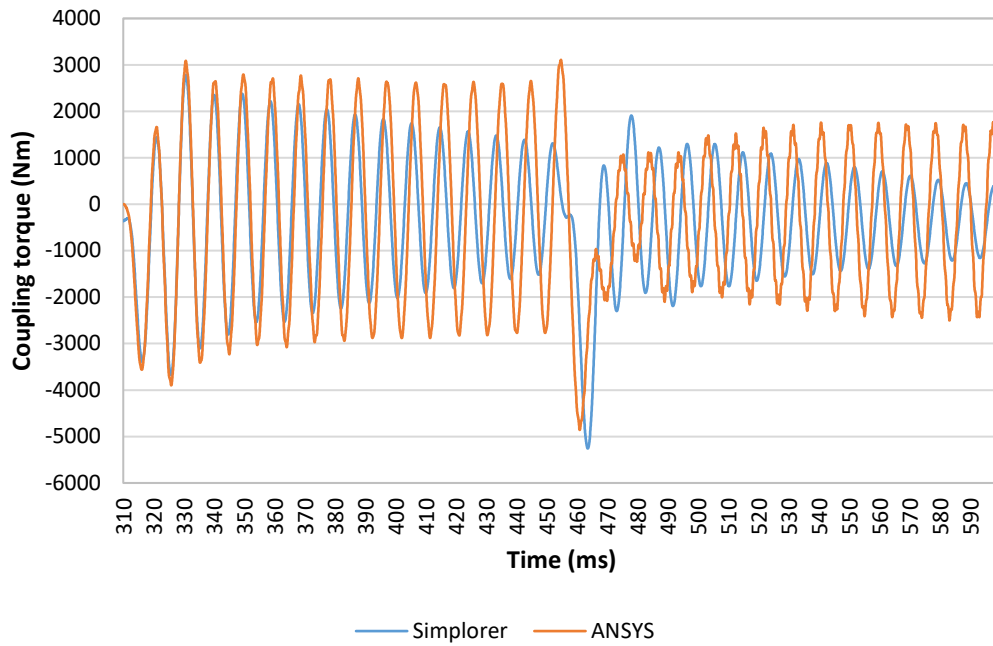


Figure 7.8: Un-damped transducer torque results from Simplorer model versus 3DFE equivalent shaft model of the motor genset

Full transient analysis enables the selection of viscous damping in the coupling to generator equivalent shaft section. As previously added to the Simplorer model, a value of 20Nms/rad is applied to the 3DFE model.

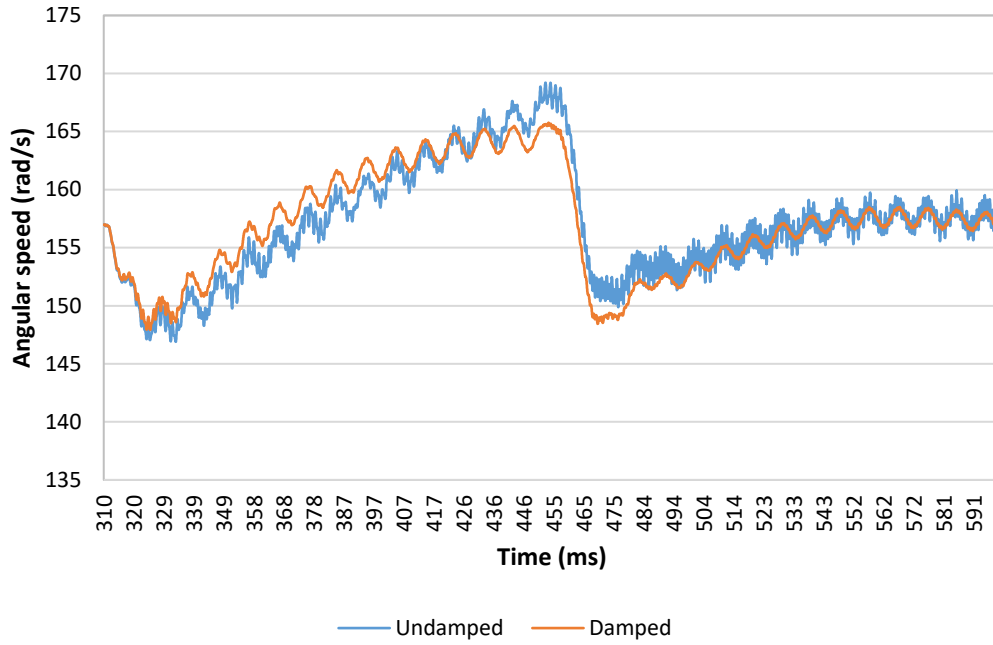


Figure 7.9: 3DFE model angular speed for damped coupling vs. un-damped coupling.

Motor genset

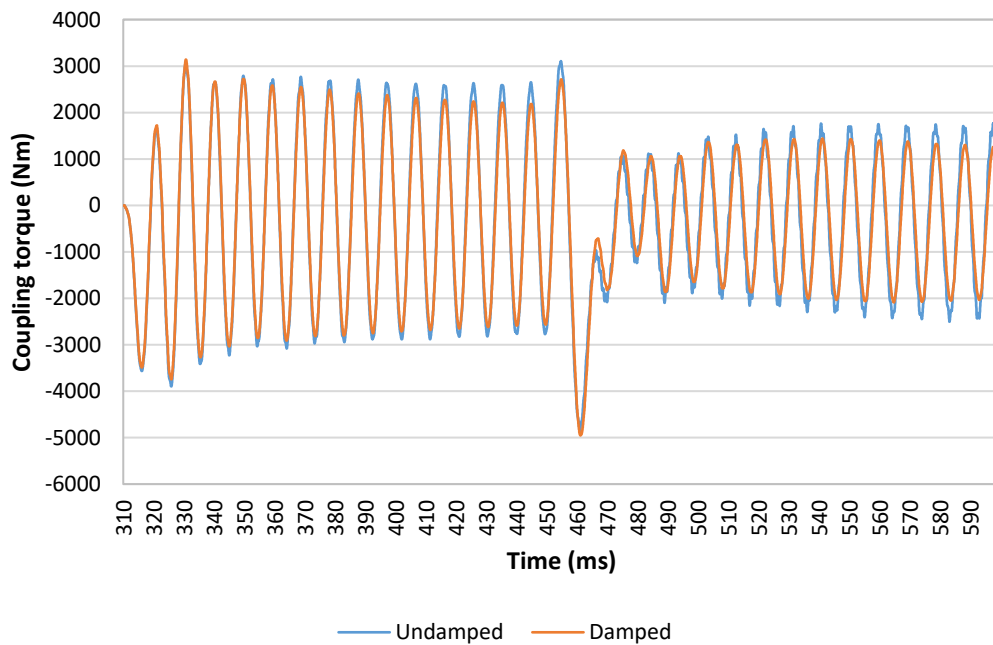


Figure 7.10: ANSYS torque for damped coupling vs. un-damped coupling. Motor

genset

7.1.3 Engine generator set transient analysis

The same simulations are repeated for the diesel engine generator set. The equivalent shafts and inertias in the generator model remain the same as in the previous analyses, but the coupling sections and motor are replaced with those representing the engine and its coupling to the generator. The coupling stiffness between the flywheel and generator coupling is set to its original, constant value of 2.11 MNm/rad and the 50% speed control gain reduction is included. Close attention is paid to the direction of torque applied to each cylinder, ensuring that when a positive torque is applied, the torque acts in an anti-clockwise direction as the electromagnetic torque applied to the generator core acts in a clockwise direction. Torsional damping (viscous) is accounted for by using revolute joints between the damper hub and its neighbouring point inertia. Note that the damping provided by the real coupling is frequency dependant but is simplified to a constant damping value here.

The frequencies of the first four un-damped torsional modes for the equivalent shaft ANSYS model of the engine generator set are as follows, 107.83 Hz, 183.89 Hz, 246.83 Hz and 555.27 Hz. The MATLAB script provided in Appendix C is applied to verify these modes, the calculated torsional modes are 107 Hz, 183 Hz, 246 Hz and 555 Hz.

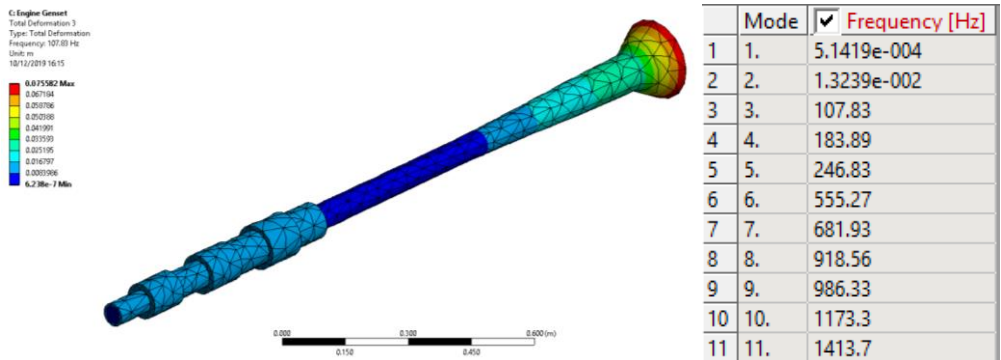


Figure 7.11: Modal results for equivalent shaft model of engine generator set. Original coupling stiffness of 2.11MNm/rad. (107.83Hz mode with large displacement of engine inertia ring shown)

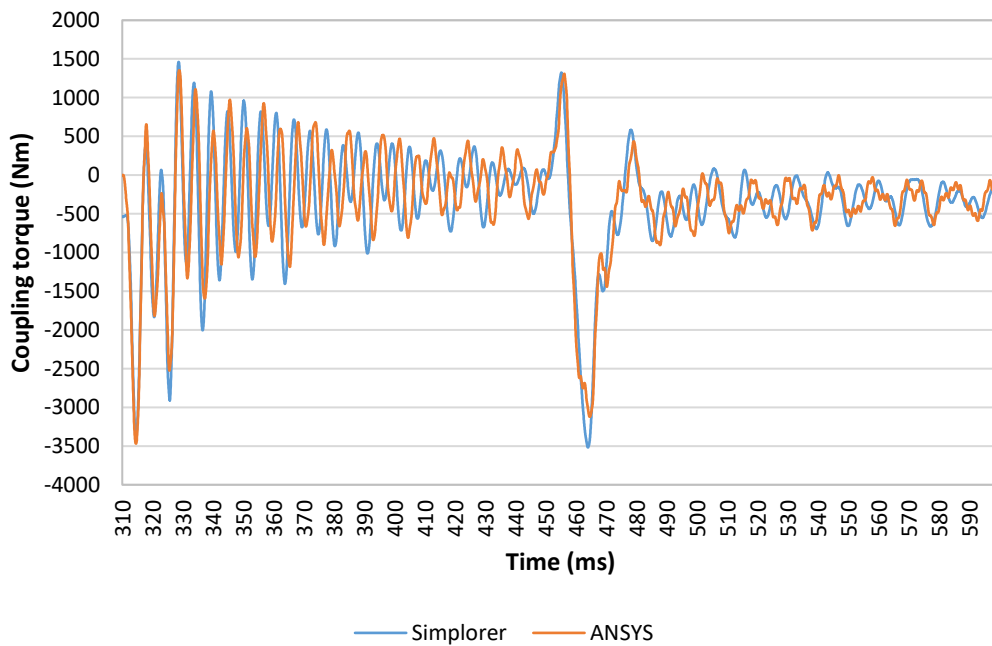


Figure 7.12: Coupling torque results from Simplerer model versus 3DFE equivalent shaft model of the motor genset

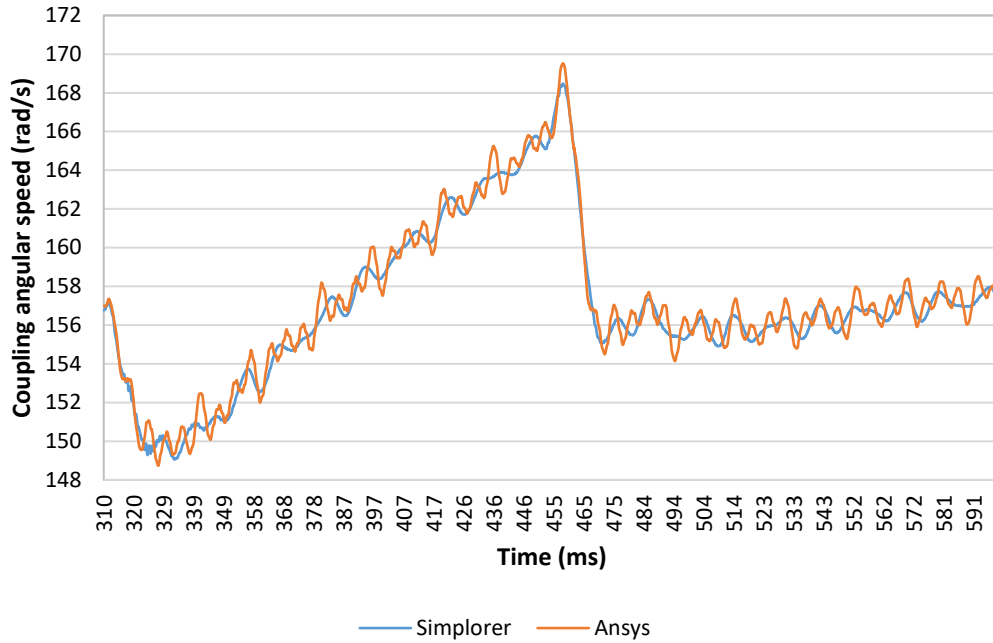


Figure 7.13: Coupling angular speed results from Simplorer model versus 3DFE equivalent shaft model of the motor genset

7.1.4 Flexible coupling model

In order to analyse the transient response of the models with the flexible coupling included, the material properties of the coupling element in the 3D model must be altered to account for non-linear torsional stiffness. The torsional stiffness for the flexible coupling section is applied by using a custom material definition that includes a shear modulus versus time curve which simulates coupling stiffness results equivalent to those obtained from the Simplorer model. Note that the coupling material properties can also be set to shear modulus vs. applied torque as calculated in the Simplorer model, however this sacrifices any control over the rate of change of coupling stiffness.

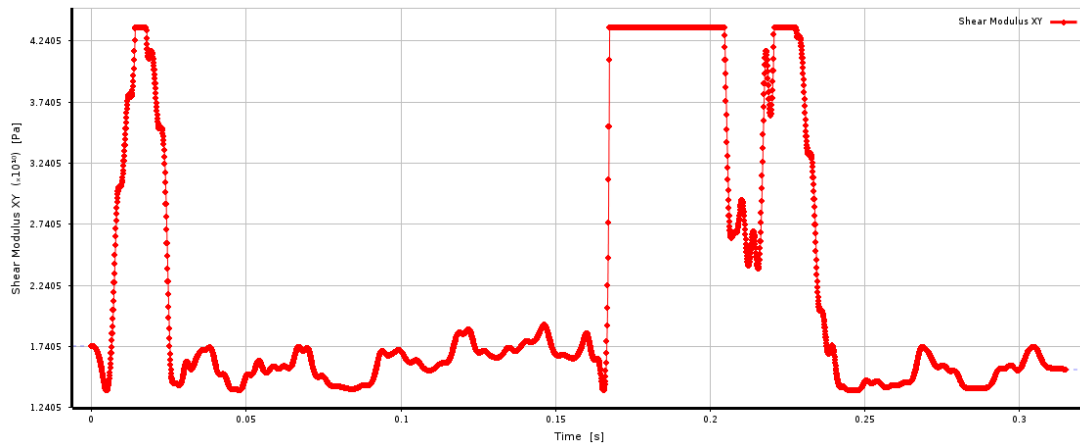


Figure 7.14: Shear modulus vs. time curve for coupling material for transient analysis of 3DFE engine genset

Since the modal superposition method does not account for full non-linear behaviour, the full transient method is used in this analysis. Figures 7.16 and 7.17 show the torque and speed results from the full transient analyses with the non-linear material assigned to the coupling shaft in the diesel engine genset model. Viscous damping is included in this analysis and the damper at the non-drive end of the engine is represented as follows. The end shaft section contributes the torsional stiffness of the damper hub connected to the drive shaft and the hollow cylinder that orbits this section contributes the inertia of the inertia ring. A cylindrical joint between the two is set to provide the 67.8 Nms/rad viscous damping associated with the fluid filled medium between the damper hub and inertia ring. In addition, the outer surface of the inertia ring is fixed to a single degree of freedom, rotation about the z axis with a cylindrical body to ground joint.

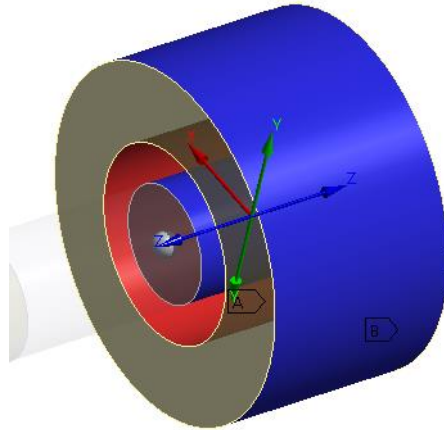


Figure 7.15: Equivalent geometry of inertia ring in engine damper hub and applied joint boundary conditions. (A) Inertia ring to damper hub joint, (B) inertia ring to ground joint

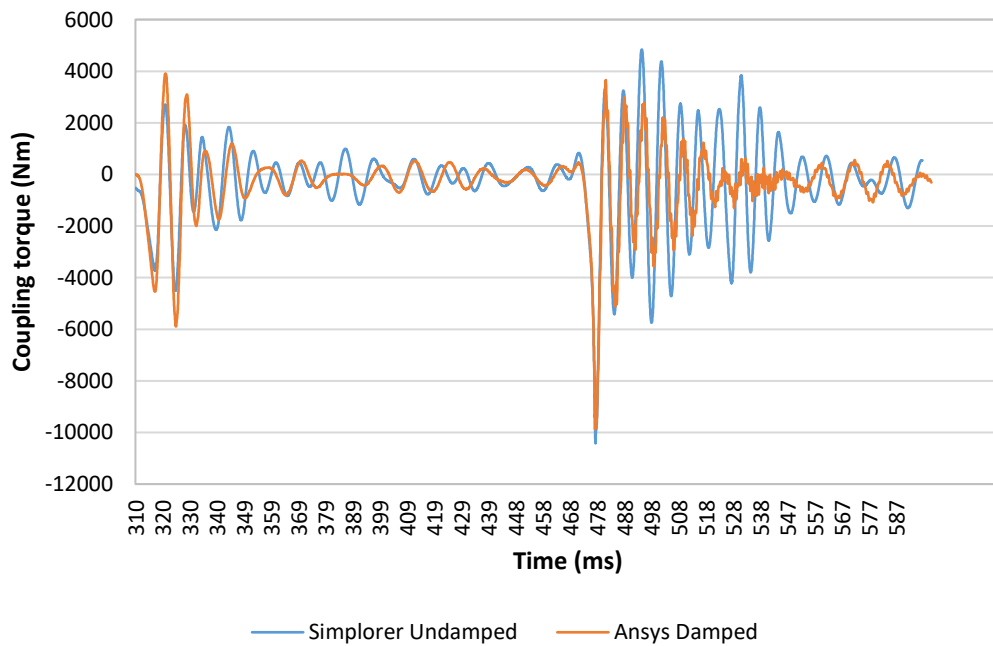


Figure 7.16: Full transient analysis results of coupling torque for the engine generator set with flexible coupling

The damping value of 20 Nms/rad at the coupling hub between the engine and generator rotor is again applied using a cylindrical body to body joint between the connecting shaft sections.

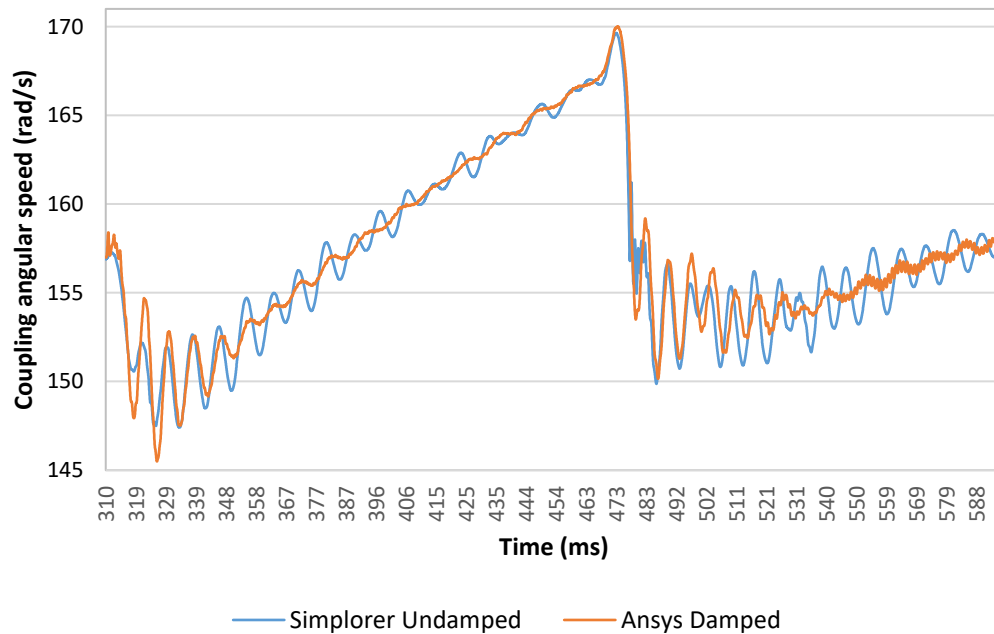


Figure 7.17: Full transient analysis results of coupling angular speed for the engine generator set with flexible coupling

The ANSYS model of the engine generator set responds with broadly similar torque and angular speed results measured at the flexible coupling when the external electromagnetic and engine torques from the Simplorer model are applied to the structure. No configuration of model and analysis settings could reproduce precisely the same results as for the Simplorer model owing to the additional simulation complexity introduced with a 3D mesh, including the influence of bonded contact stiffness and simulation of non-linear elastic behaviour included in the full transient analysis solver.

7.1.5 Impact of coupling stiffness on modal results

As previously observed, the magnitude of torsional vibration varies with torsional stiffness of the coupling. It is already known that the resulting shift in frequency of the torsional modes is at least partially responsible for this behaviour. In order to investigate this further, modal analysis is performed on the equivalent 1D model of the genset. This modal analysis is performed under free-free support conditions, the bearing connections to the ground are not included here. Modal analysis is carried out on both 3DFE generator set models for various values of coupling stiffness. The results for both models are shown in Table 7.1 and 7.2. Node 1 designates the non-drive end of the generator and node 13 and 20 designates the end of the diesel engine.

Table 7.1: Torsional modes for the 3DFE equivalent motor driven generator set - modal frequencies and shapes for various coupling stiffness

Coupling stiffness (kNm/rad)	Torsional mode number	Un-damped frequency (Hz)
50	1	50.98
50	2	476.95
100	1	66.421
100	2	490.18
200	1	82.517
200	2	509.3
300	1	91.293
300	2	522.47
400	1	96.802
400	2	531.88
500	1	100.71

500	2	539.12
600	1	103.55
600	2	544.71
700	1	105.78
700	2	549.27
800	1	107.52
800	2	552.95
900	1	108.96
900	2	556.08
1000	1	110.14
1000	2	558.69

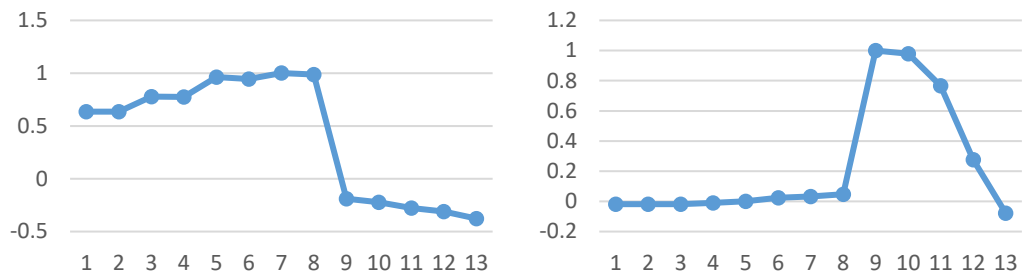


Figure 7.18: Mass normalised torsional mode shapes for 50 kNm/rad coupling stiffness (T1 left, T2 right)

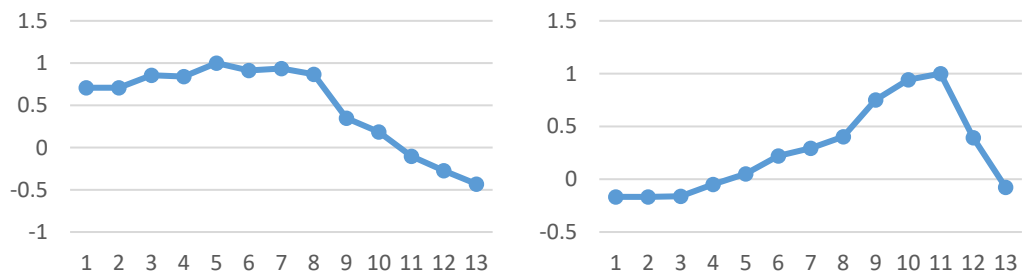


Figure 7.19: Mass normalised torsional mode shapes for 1000 kNm/rad coupling stiffness (T1 left, T2 right)

Table 7.2: Torsional modes for the 3DFE equivalent engine driven generator set -
modal frequencies and shapes for various coupling stiffness

Coupling stiffness (kNm/rad)	Torsional mode number	Un-damped frequency (Hz)	Damped frequency (Hz)
50	1	52.855	53.206
50	2	111.72	105.53
50	3	242.03	240.38
50	4	554.66	554.66
100	1	71.706	73.049
100	2	112.83	105.68
100	3	242.19	240.54
100	4	554.69	554.7
200	1	92.169	98.931
200	2	117.06	104.51
200	3	242.49	240.86
200	4	554.75	554.76
300	1	100.56	102.51
300	2	124.77	117.04
300	3	242.77	241.15
300	4	554.79	554.8
400	1	103.56	101.95
400	2	133.29	129.12
400	3	243.03	241.43
400	4	554.83	554.83
500	1	104.88	101.84
500	2	140.91	138.15
500	3	243.28	241.69
500	4	554.86	554.86
600	1	105.57	101.84

600	2	147.3	145.23
600	3	243.52	241.94
600	4	554.88	554.89
700	1	105.99	101.87
700	2	152.6	150.9
700	3	243.73	242.16
700	4	554.91	554.91
800	1	106.27	101.91
800	2	157.13	155.67
800	3	243.94	242.38
800	4	554.92	554.93
900	1	106.47	101.94
900	2	160.96	159.65
900	3	244.13	242.59
900	4	554.94	554.94
1000	1	106.62	101.98
1000	2	164.3	163.1
1000	3	244.32	242.78
1000	4	554.95	554.96

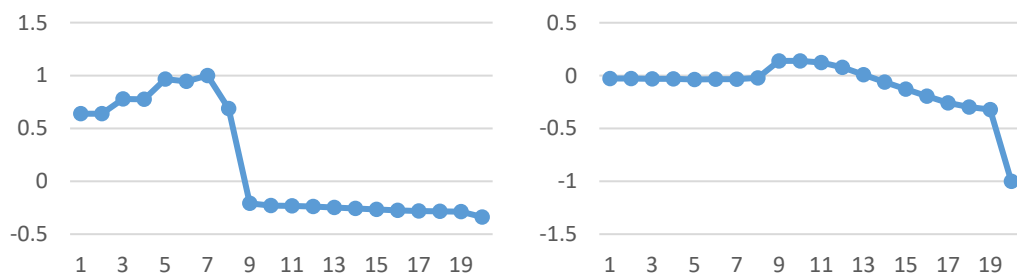


Figure 7.20: motor genset mass normalised torsional mode shapes for 50 kNm/rad coupling stiffness (T1 left, T2 right)

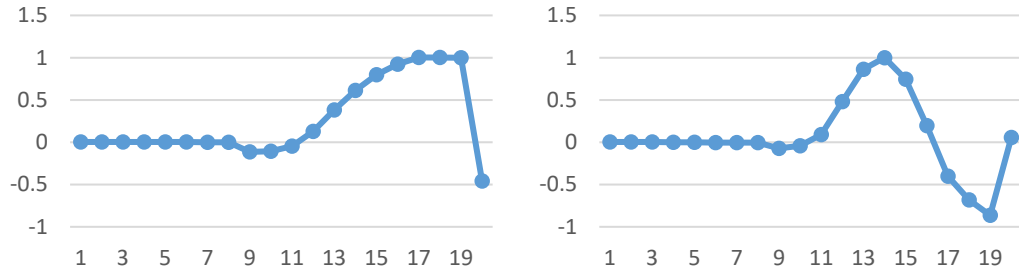


Figure 7.21: Motor gendset mass normalised torsional mode shapes for 50 kNm/rad coupling stiffness (T3 left, T4 right)

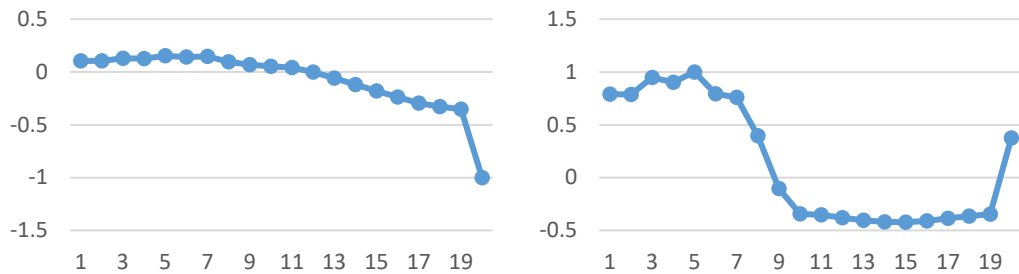


Figure 7.22: Engine gendset mass normalised torsional mode shapes for 1000 kNm/rad coupling stiffness (T1 left, T2 right)

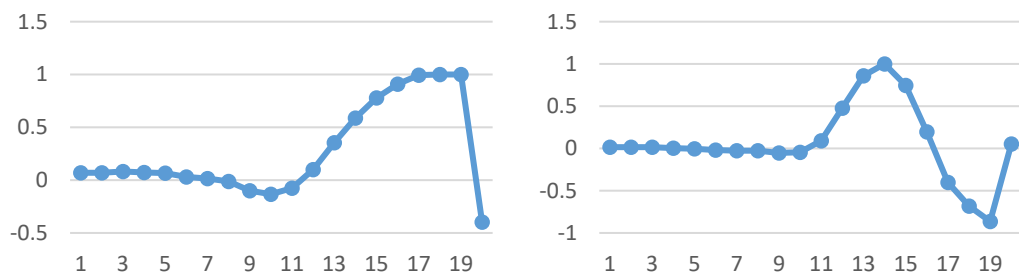


Figure 7.23: Engine gendset mass normalised torsional mode shapes for 1000 kNm/rad coupling stiffness (T3 left, T4 right)

Using a constant coupling stiffness of 50 kNm/rad, the first torsional mode for both the motor driven and the engine driven generator sets is near 50 Hz at 50.98 Hz and 53.02 Hz respectively. With such a low torsional stiffness, the first mode will be excited by

the dominant 50 Hz torsional component applied by the grid voltage supply. For both gensets, the first torsional mode shape is characterised by a large rotational displacement of entire generator rotor relative to the prime mover. As the coupling stiffness is increased above 50 kNm/rad, the first torsional mode of the diesel engine genset quickly increases in frequency as the displacement of the inertia ring at the end of the engine increase relative to the displacement of all other inertia elements. The torsional stiffness between the inertia ring and the damper hub is 90.38 kNm/rad and so it becomes the least stiff connection in the torsional train once the coupling stiffness is increased to 100 kNm/rad. Note that the mode shape switches to show displacement of the component with the next lowest torsional stiffness in the train when the coupling stiffness exceeds is increased.

7.2 Dynamic Stress analysis

As discussed in Chapter 3, the true torsional behaviour of the generator set is somewhat more complex than what an equivalent shaft or 1D beam element model is capable of replicating. The equivalent torsional stiffness models are also incapable of producing meaningful stress results for LVRT simulations since the geometry lacks in detail.

In order to analyse the stress in the generator rotor during an LVRT event, the full detail 3D rotor model is utilised. The modal properties of this model were validated earlier in this chapter. This detailed rotor model is now coupled to the equivalent shaft model representing the diesel engine, these parts remain unchanged from the previous analysis. Note that the stress/strain response of the engine components is not included in this analysis. The coupling geometry is altered to include a keyway which supports a key between it and the generator shaft. This area of the assembly is most susceptible to damage due to high magnitude, fast transient loading and is of primary interest for the stress analysis. The mesh quality and density is significantly increased here in order to capture the detailed features of the geometry so that it is possible to obtain the distribution of stress throughout the key and keyways. The key is also fully bonded to all contact surfaces in both keyways. The elastic properties of the coupling section that contains the upper keyway are the same as for the shaft steel.

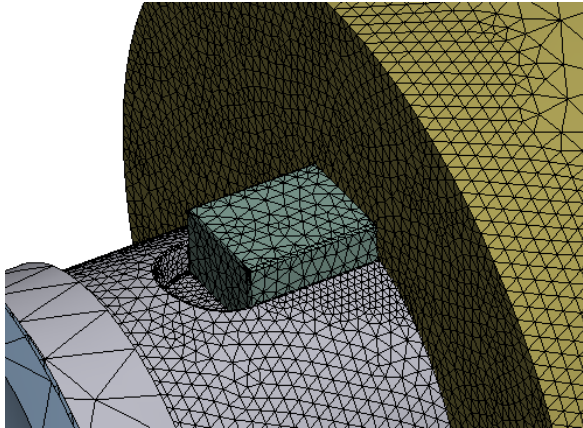


Figure 7.24: View of generator shaft connected to the engine coupling with extended key.

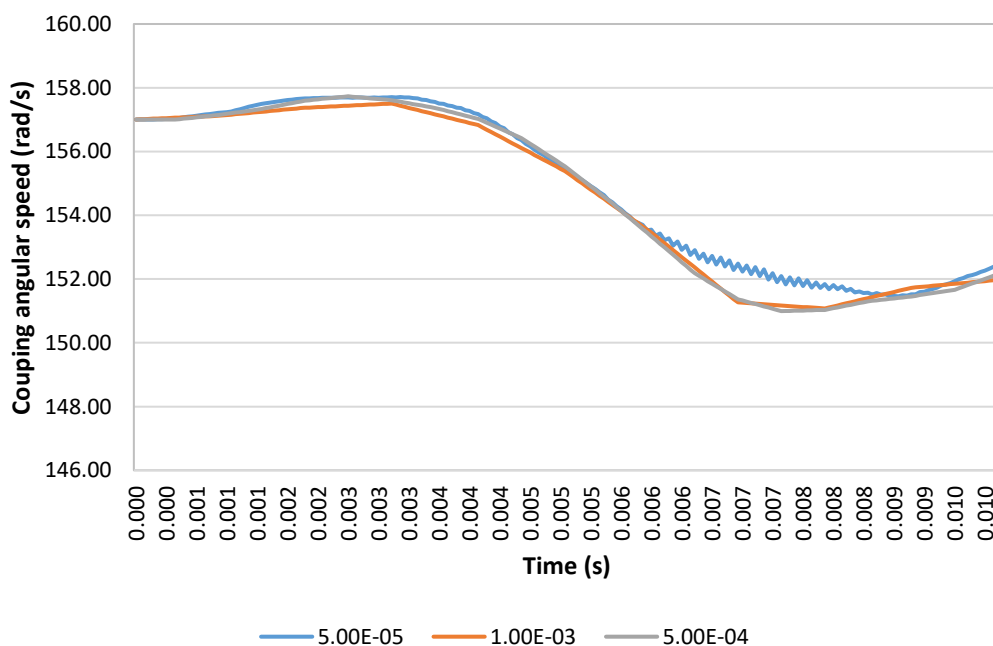
7.2.1 Full transient analysis of the engine generator set with a flexible coupling

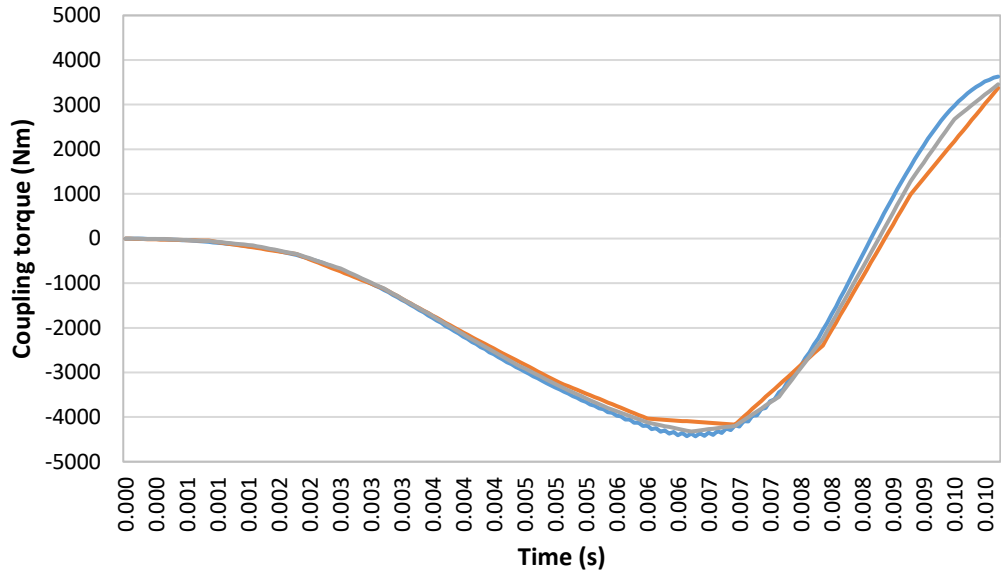
The same electromagnetic torque and engine torque used in the equivalent shaft model and Simplorer model are applied to the full detail 3DFE model of the engine generator set. The electromagnetic torque is applied to the outer surface of the generator rotor poles, thus distributing the full torque across the entire area.

Since it has been documented in existing LVRT tests that the shaft and coupling can sustain significant damage including bending and crack formation, it is important to determine if such an event could occur for this generator model. If so, what rotor angle shift would cause structural failure and what is the likely stress the rotor would experience under the minimum specified FRT period of 140 ms. The following simulations are performed to analyse the stress in the coupling keyways and better understand the physical impact of low voltage fault ride through on the rotor;

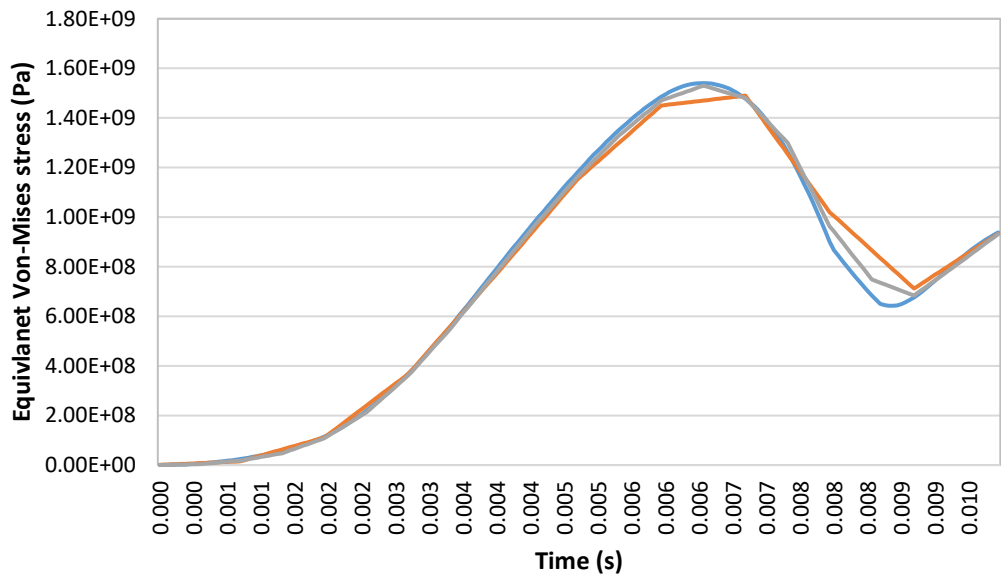
7.2.2 Initial disconnection transient torque

The initial disconnection transient torque is the same regardless of ride through time, it is largely determined by the circuit reactance and to a lesser extent, the electrical angle of stator current at the point of disconnection. The disconnection torque and therefore the coupling stress is considered to be constant in the following ride through simulations, it can therefore be analysed separately from them. First, the disconnection simulation is performed with a time step of 0.05 ms. The results are then compared against those from the same simulation utilising larger time steps of 1 ms and 0.5 ms. As the solver for this model demands a large amount of dedicated memory and CPU resources (far in excess of the equivalent 1D model) a time step of 0.05 ms requires several hours (~15 hours) to complete even a 10 ms time period. In comparison, a 10 ms simulation period with a time step of 1 ms requires 1 hour to complete. Figure 7.25 shows the difference between the angular speed, torque and stress results when simulating with the three different time steps of 0.05 ms, 0.5 ms and 1 ms. Figure 7.26 shows the equivalent stress results in the key/keyway for the 0.5 ms time step.



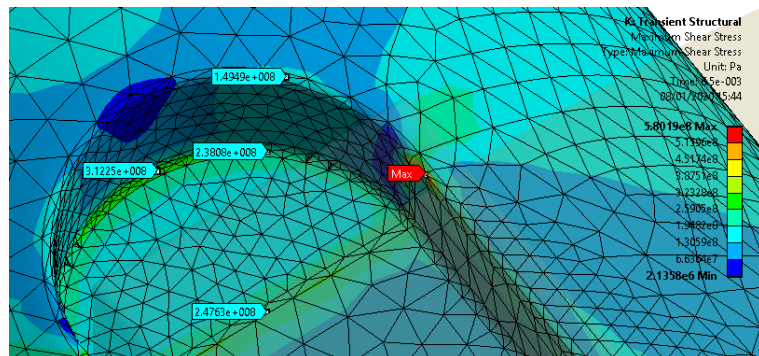
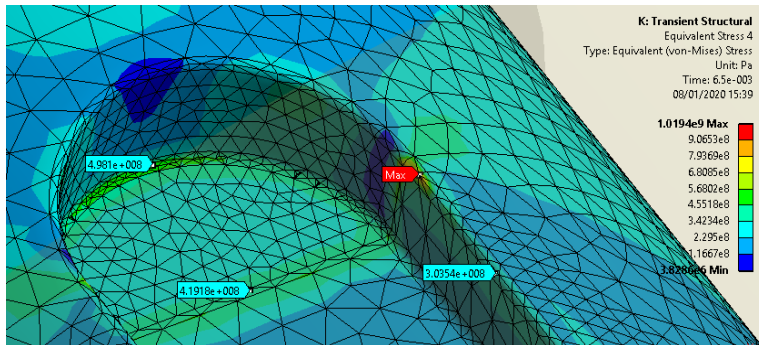
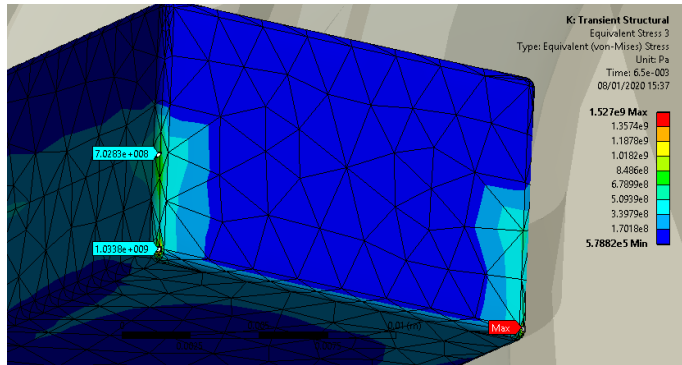
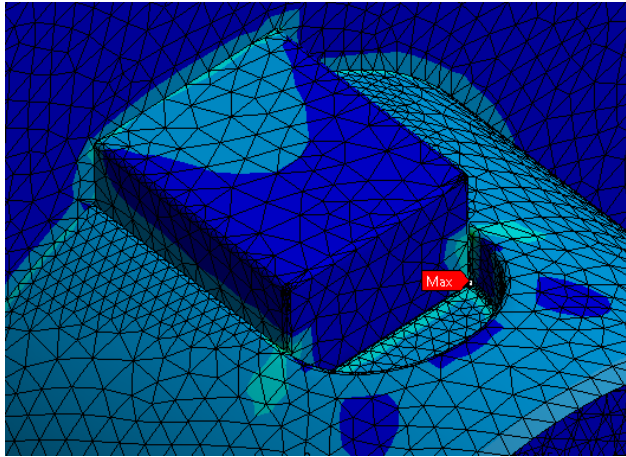


— 5.00E-05 — 1.00E-03 — 5.00E-04



— 5.00E-05 — 1.00E-03 — 5.00E-04

Figure 7.25: Coupling torque (moment reaction), angular speed and average von Mises stress in the keyway during grid disconnection over 10ms period. Comparison of results with 0.05ms, 0.5ms and 1ms time steps



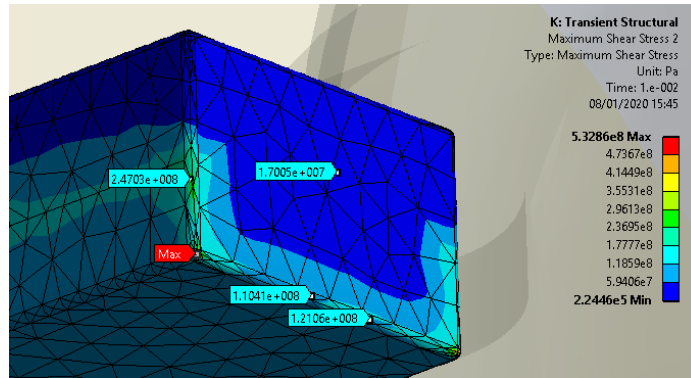


Figure 7.26: Equivalent von Mises and shear stress in the key/keyway at 10 ms following during grid disconnection.

The results from this sensitivity analysis suggest that the time step of $5e^{-4}$ s (0.5 ms) is suitable for stress analysis results for applied transient peak torques over short periods of time. Although the reported stress results are expected to be slightly below the true maximum stress magnitude due to the increased step period. Initial observations from the key and keyways of the rotor indicate that at the time that the peak coupling torque of 4.3 kNm occurs (6.5 ms), the average equivalent stress at the contact edges of the key is $3e^8$ Pa. A maximum equivalent stress of $1.53e^7$ Pa is measured at the corners of the key.

The corners of the geometry are meshed with increased mesh density to reduce erroneous stress concentration effects. Regarding the stress measured at the contact edges, it is these areas that are most likely to deform during grid reconnection as evident in the damaged key example shown in Figure 2.8. Once this section of shaft yields, the next component in line to take the full fault torque is the coupling itself which will fail likely immediately.

7.2.3 Equivalent stress and maximum shear stress over 40 ms with 0.5 ms time step

This analysis is extended over a time period of 40 ms, note that this would not be possible with a time step of 0.05 ms due to hardware limitations. The equivalent stress plot at for the point at which the peak coupling torque occurs (14 ms) is shown in Figure 7.27, the coupling torque plot is shown in Figure 7.28 and the electromagnetic torque applied to the rotor is shown in Figure 7.29.

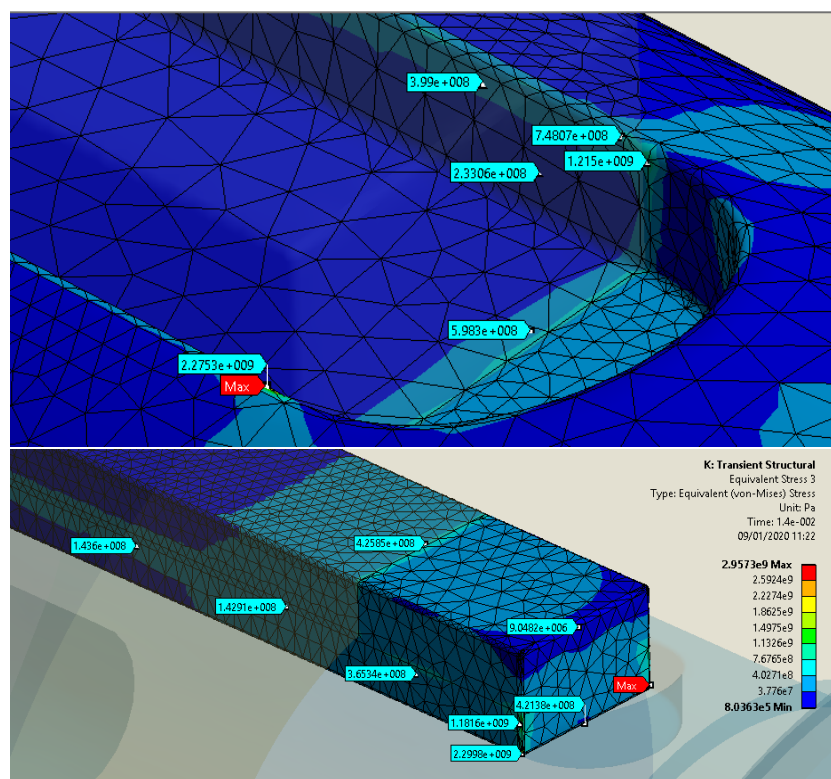


Figure 7.27: Equivalent stress at peak coupling torque (14 ms)

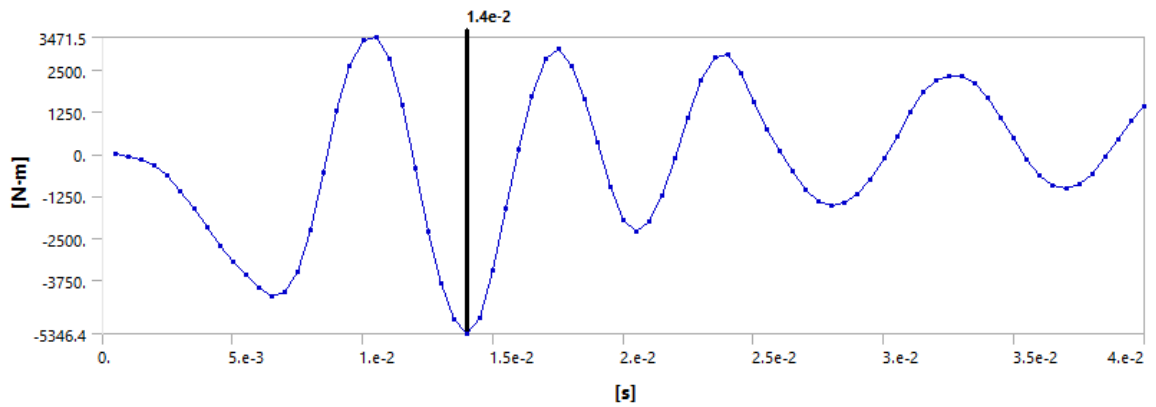
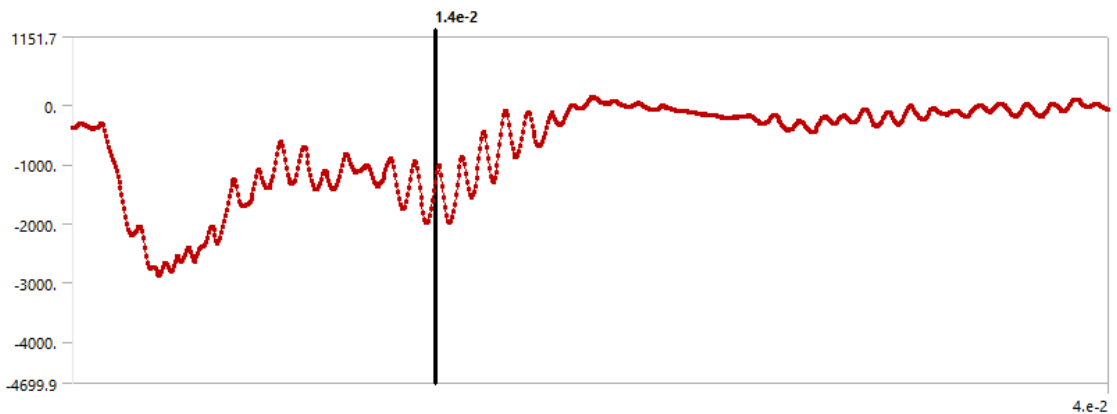


Figure 7.28: Peak disconnection coupling torque over 40 ms time period



Time [s]	✓ Moment [N·m]
1.38e-002	-1879.4
1.385e-002	-1755.8
1.39e-002	-1610.6
1.395e-002	-1455.2
1.4e-002	-1291.9
1.405e-002	-1146.
1.41e-002	-1047.1

Figure 7.29: Magnitude of electromagnetic torque at 14 ms

Note that due to 'wind up'/angular twisting of the shaft caused by the inherent elasticity of the structure, the peak coupling torque is effectively delayed following the peak applied electromagnetic torque. The resulting equivalent stress through the key and keyway at the point of maximum coupling torque peaks at $2.96e^9$ Pa at the bottom corner of the key as it is compressed against the keyway of the generator shaft. The

contact between the bottom half of the key and the lip of the shaft keyway is the second most highly stressed region. The value of equivalent stress here peaks at around 3.65×10^8 Pa.

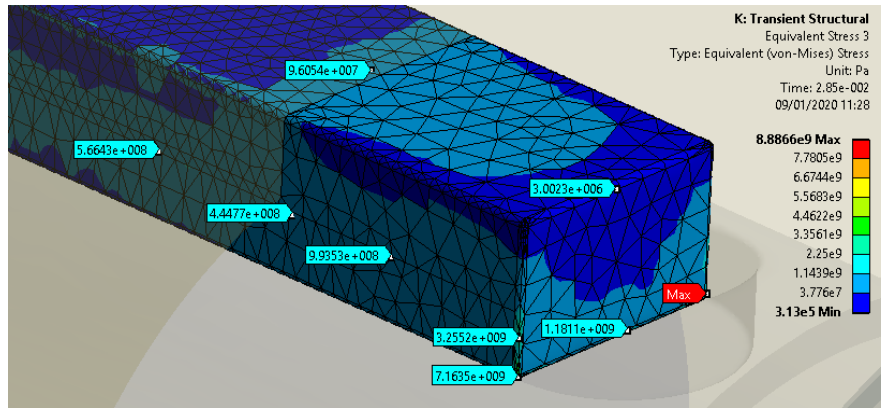


Figure 7.30: Equivalent stress at 28.5 ms

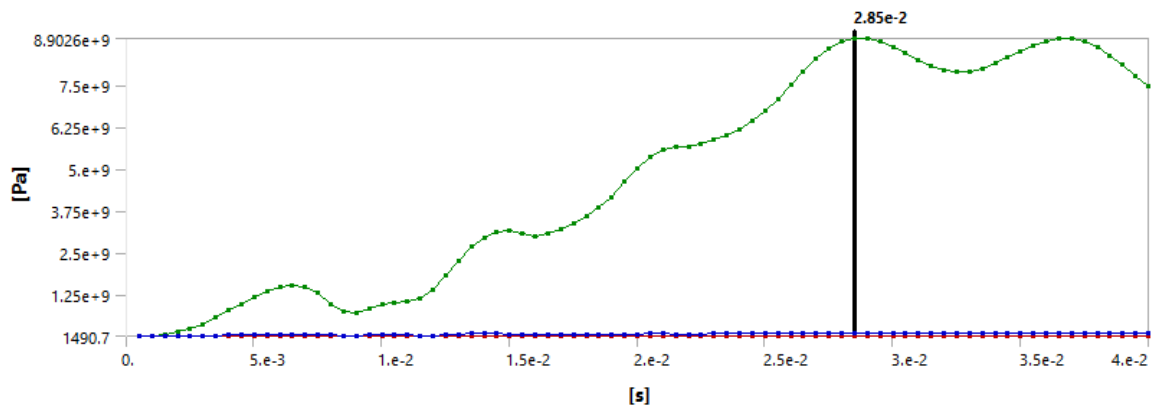


Figure 7.31: Plot of maximum equivalent stress over 40 ms time period

The peak stress also depends upon the relative rotational displacement (twist) between the coupling and the generator shaft as well as the instantaneous coupling torque. As a result, the peak stress occurs at 28.5 ms as shown in Figure 7.30 and Figure 7.31, 14.8 ms after the peak coupling torque is applied. The resulting stress increases to 8.89×10^9 Pa at the leading corner of the key and 9.94×10^8 Pa at the area of contact with the keyway lip. The shear stress results at this time as shown in Figure 7.32 and Figure 7.33 below

show more clearly the shearing action experienced by the keyway. One can visualise how the engine torque is applied in counter direction to the generator torque through the coupling and generator rotor shaft.

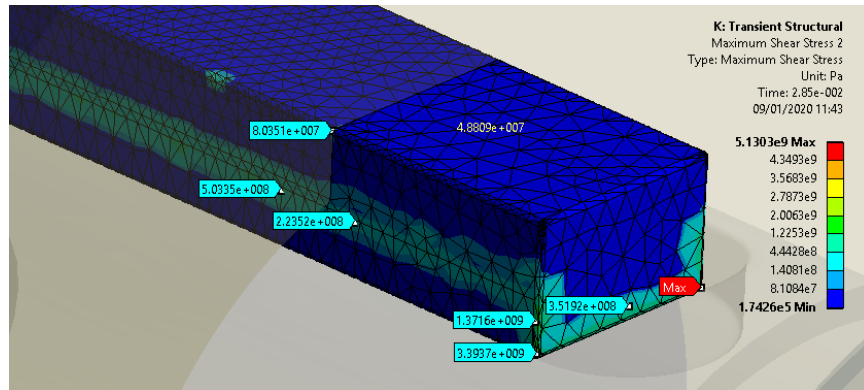


Figure 7.32: Maximum shear stress in the key at 28.5 ms

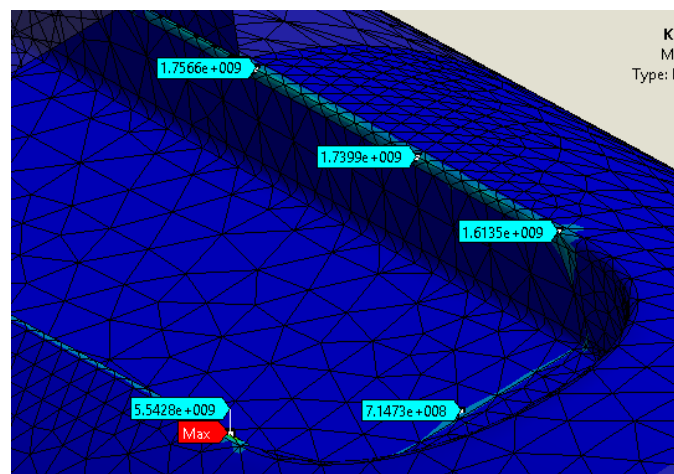


Figure 7.33: Maximum shear stress in the shaft keyway at 28.5 ms

Additionally, the stress in the coupling keyway at the instant the peak electromagnetic torque is produced can be simulated using a static structural analysis which solves substantially faster. The static structural analysis does not simulate non-linearity however and is not a suitable substitute for analysis of sustained transient faults.

7.2.4 Stress analysis for grid reconnection at 140 ms

The electromagnetic generator torque (Figure 7.34) and engine torque (Figure 7.35) from the 140 ms LVRT Simulink model is applied to the 3DFE model and the coupling stress is analysed over an 80 ms time period from the point of grid reconnection. Corners and edges are considered as potential failure locations where large stress concentrations are present, but this would not lead to any significant deformation of the key/keyway geometry following a single fault ride through event, only localised damage is expected. The resulting coupling torque in the 3DFE transient stress analysis shown in Figure 7.36 closely matches the coupling torque obtained from the 1D torsional model (Figure 7.35).

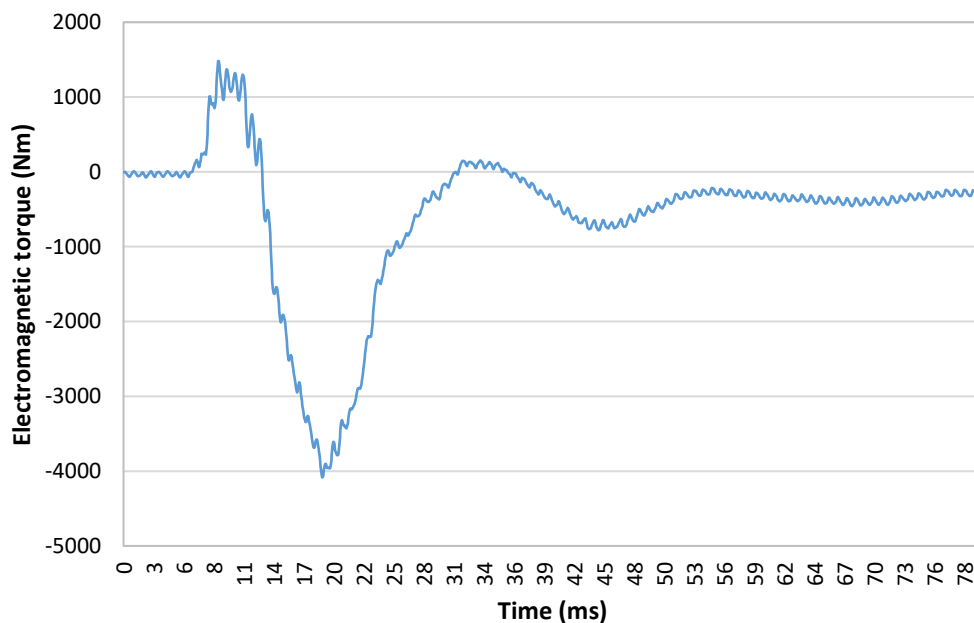


Figure 7.34: Electromagnetic torque applied to the generator core over 80 ms.

Obtained from 140 ms LVRT Simplorer simulation of the engine genset

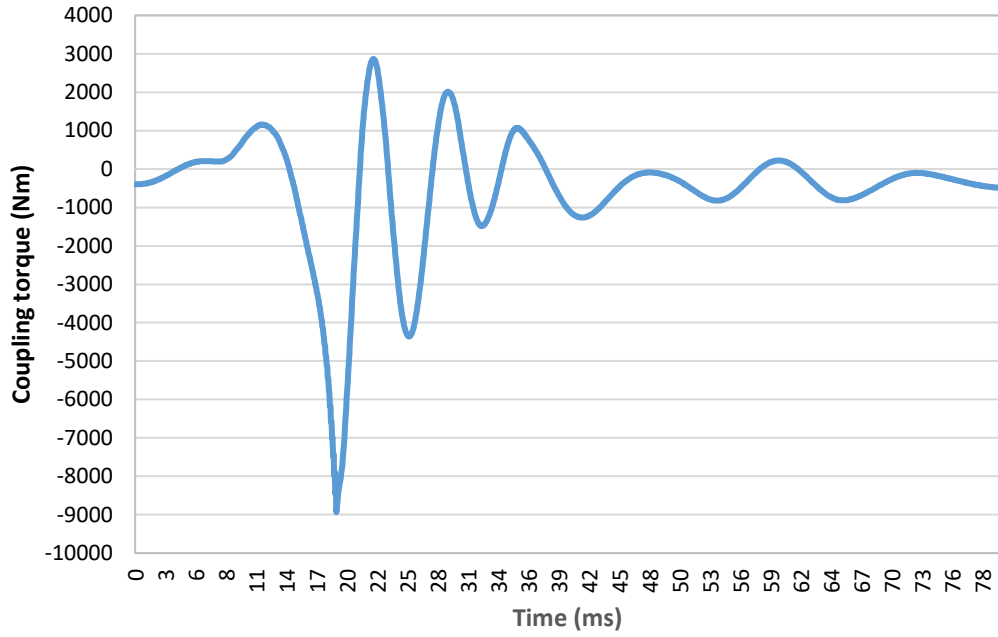


Figure 7.35: Coupling torque over 80 ms obtained from 140 ms LVRT Simplorer simulation of the engine genset.

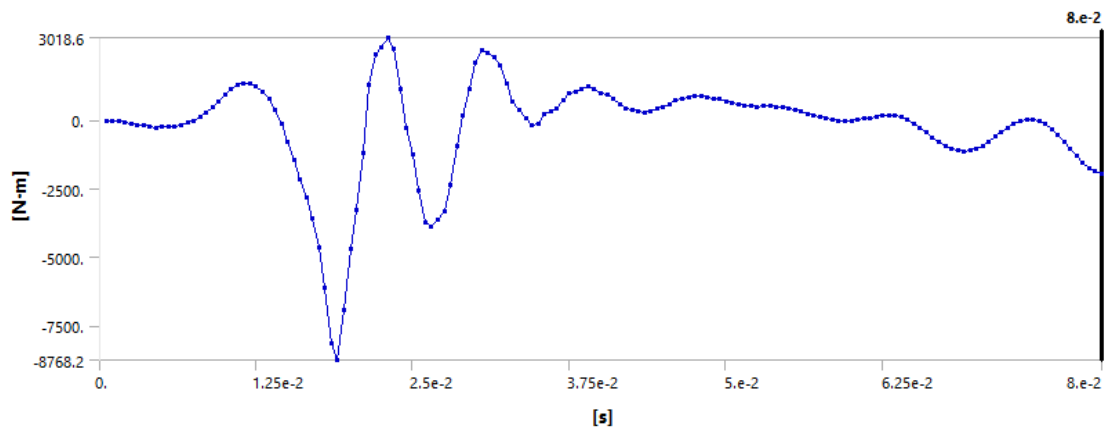


Figure 7.36: Coupling torque in the 3DFE transient model over 80 ms following grid reconnection

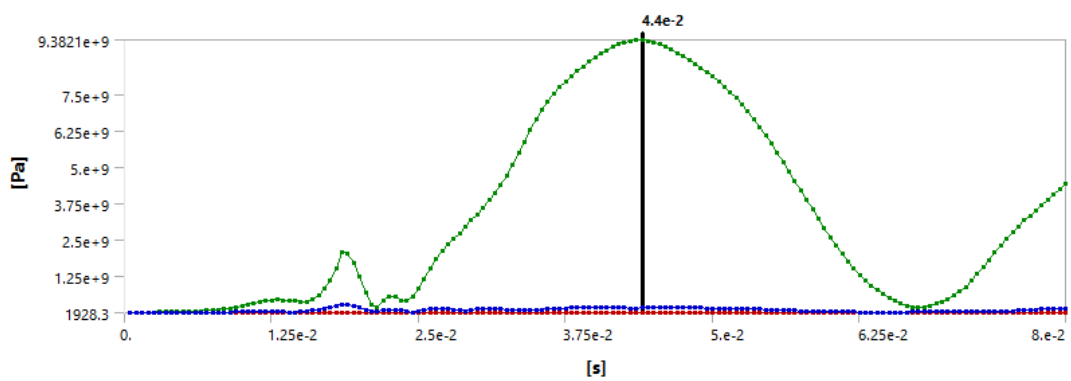
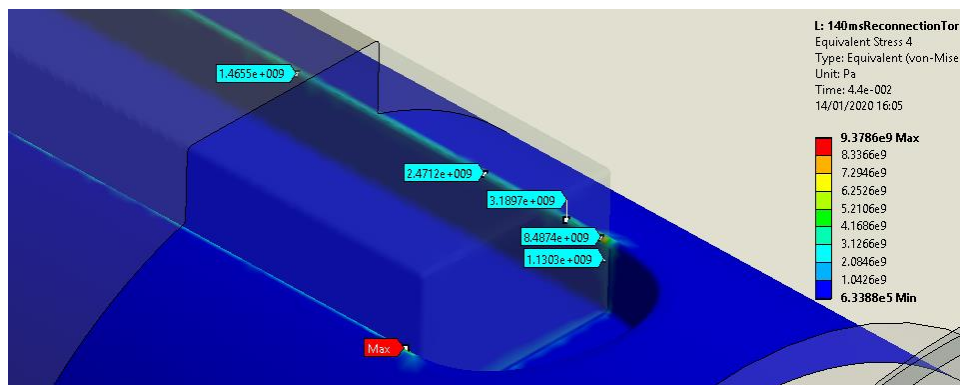
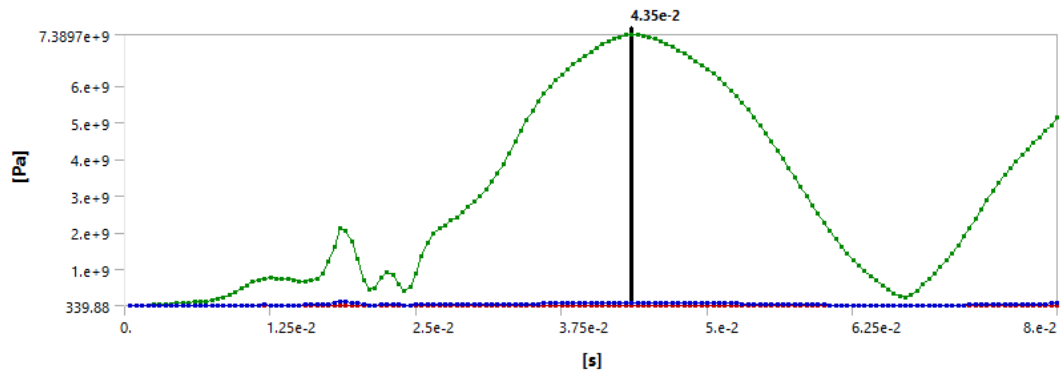
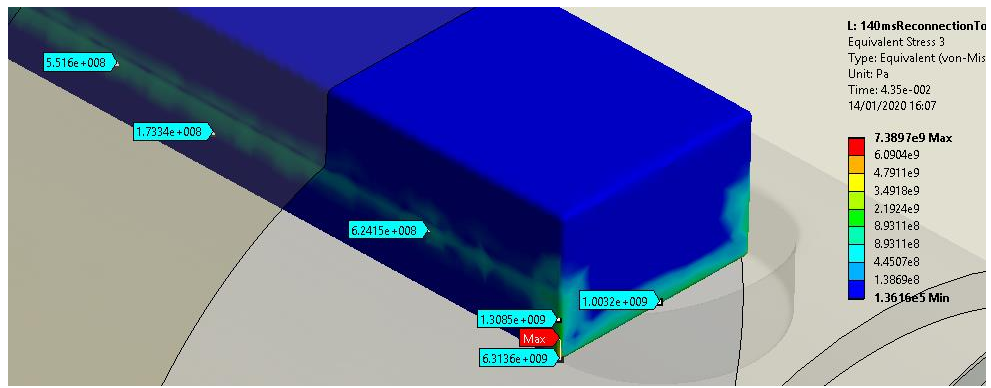


Figure 7.37: Equivalent stress in the key and keyway over 80 ms following grid reconnection

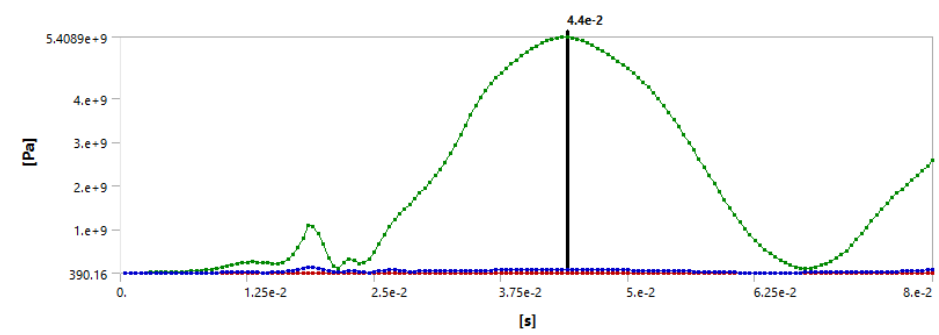
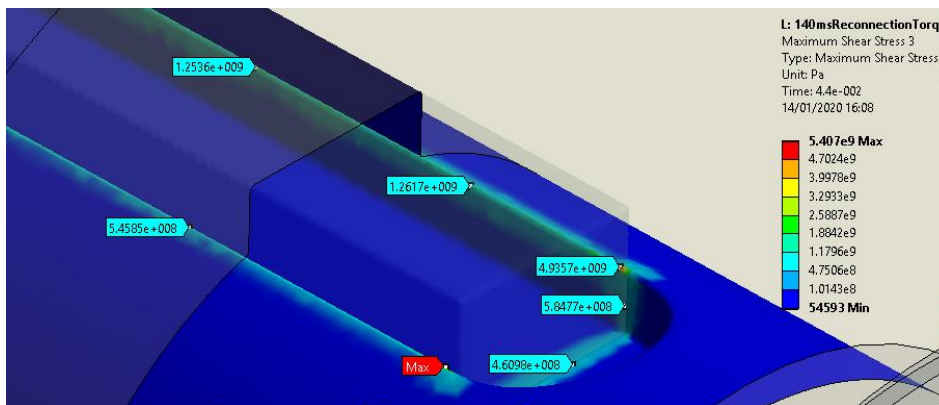
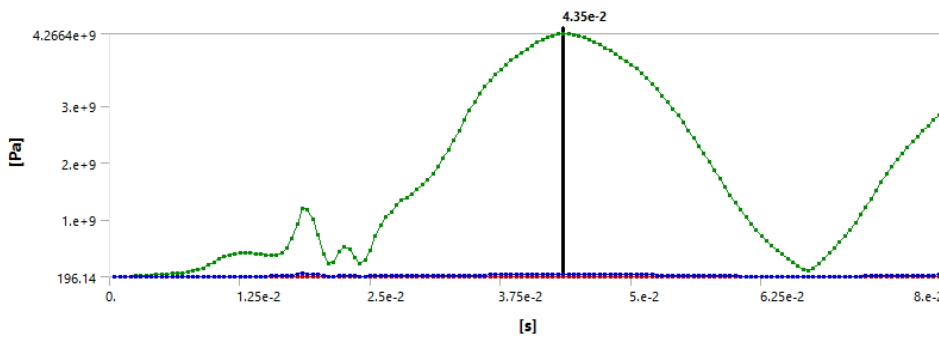
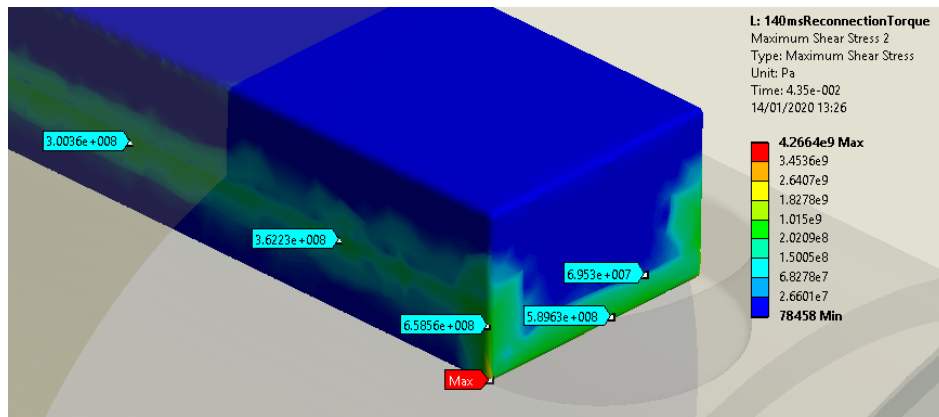


Figure 7.38: Maximum shear stress at the key and keyway over 80ms following grid reconnection.

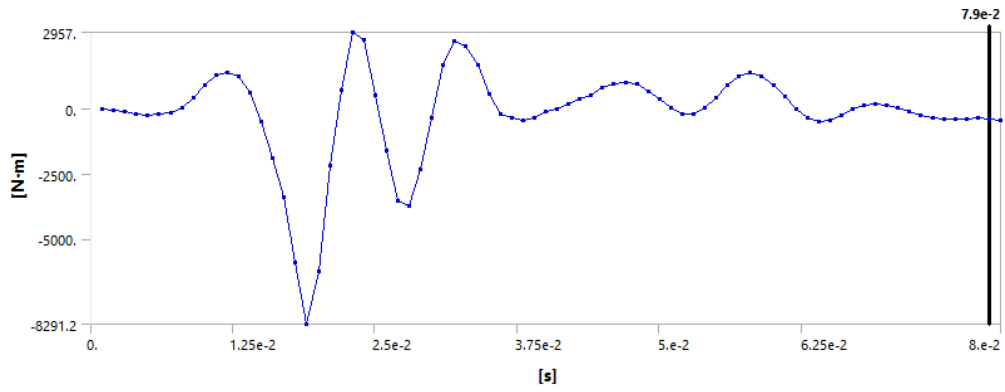


Figure 7.39: Coupling moment reaction over 80 ms, torque applied at the shaft instead of the core. (Time step increased to 1 ms)

Note that the torque following reconnection as measured at the coupling point inertia begins to increase again towards a value of -2 kNm. This phenomenon should not occur, rather the torque should reach steady state around -365 Nm. Upon further investigation this appears to be caused by the application of electromagnetic air gap torque to the poles of the generator main core. As shown in Figure 7.39 above, the coupling torque settles to -365 Nm when the torsional stiffness of the rotor core is bypassed and the electromagnetic torque is applied directly to the shaft (core inertia is still present). This suggests that, despite the accuracy of the equivalent torsional stiffness of the core section in the 1D model, the real geometry of the core experiences increased twisting displacement. As previously discussed, the 1D equivalent model does not perfectly represent the elastic behaviour of a rotor core. Especially when core windings, damper bars and support bars are considered.

Since the applied electromagnetic torque is obtained from the Simplorer model, it does not change in response to the angular position of the rotor poles in the transient analysis. Thus, over an extended period of time, the mismatch in generator and motor torque can produce anomalies such as the period of increased coupling torque seen here. Ideally,

the generator and motor torque calculated from experimental testing of the real engine generator set, alongside torque measured close to the coupling would be used to inform the transient stress analysis. Despite this observation, the coupling torque over the period of ~40 ms is a close match to that from the Simplorer results.

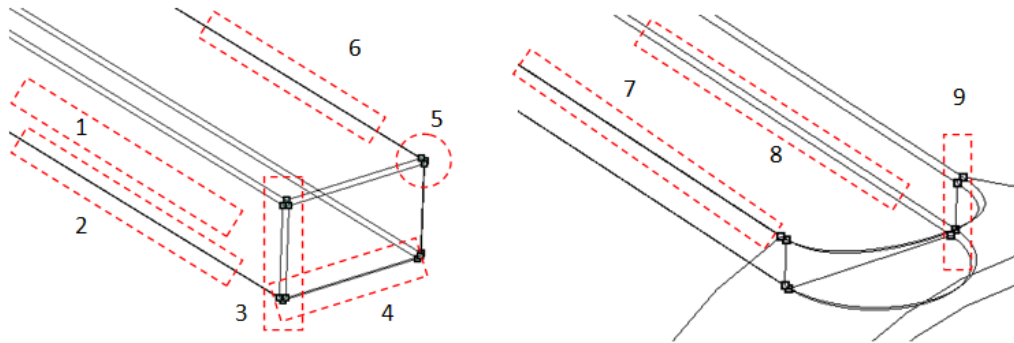


Figure 7.40: Stress locations on the key and keyway

Table 7.3: Peak equivalent stress and shear stress in the coupling key/keyway following reconnection after 140 ms FRT

Location	Maximum Shear Stress (Pa)	Equivalent Stress (Pa)
1, under coupling	$3e^8$	$5.51e^8$
1, free	$3.6e^8$	$6.28e^8$
3 (average)	$6.59e^8$	$1.31e^9$
5	$4.27e^9$	$7.39e^9$
7, under coupling	$1.25e^9$	$1.47e^9$
7, free	$1.26e^9$	$2.47e^9$

Again, note that the peak shear and equivalent stress in the coupling keyway occurs later in time following peak coupling torque. Occurring at 44 ms in the simulation or 25.3 ms after the point of peak electromagnetic torque at 18.7 ms. Stress results from

the free end of the key are of primary interest here since the top of the key is not held in position allowing for potential bending under high torque.

The stress results in the keyway are strongly influenced by the contact settings applied between the assembled components. In this case the key was fully bonded with all surrounding faces of the coupling and the shaft, the inner race of the coupling is also fully bonded with the outer surface of the generator shaft. In the event of coupling slip where the coupling moment exceeds the circumferential pre-load of the shaft to coupling fitting (determined by clamping pressure), the fault torque will be transferred directly to the key alone. Although this would constitute component failure even if the key sustained no damage, the assembly would at least remain intact for the remainder of the fault.

7.2.5 Keyway and key contact stress

As mentioned in section 1.3.6 of the literature review, it is possible to calculate the stress in the keyway geometry by multiplying the associated stress concentration factor (SCF) with the nominal maximum shear stress or nominal maximum von Mises stress in the shaft. In this case, the shaft diameter is 55 mm, the polar moment of inertia is $8.98e^{-7} \text{ m}^4$ and the peak torque acquired in the ANSYS transient stress analysis is 8768 Nm. The resulting peak shear stress for the solid shaft is 268 MPa. In torsion, the peak shear stress in the keyway (no key included) is found at the bottom edges (location 8 in Figure 7.40). The stress concentration factor varies around 2 to 3 depending on the keyway geometry, thus a maximum shear stress of at least 536 MPa is expected in the

lower edges of the keyway. In this case, the peak shear stress in this region is lower than 100 MPa as shown in Figure 7.38 by the dark blue shading at these edges.

The stress concentration factor in the keyway is valid only for the keyway by itself, not including for contact with a key. As noted in (24), there is no general solution for calculating the contact stress between the keyway and key, experimental validation would be required to obtain a comparable stress. The presence of the key reduces the angle of twist in the keyway geometry and the stress is instead concentrated at the contact surfaces between the key and the keyway. In addition, due to the geometry of the keyway and key, the peak value of contact stress is not wholly reliable by itself and will not perfectly reflect the stress conditions in the real coupling.

Ultimately, this analysis is conducted to obtain peak stress values for comparison with the modified genset stress analysis performed in Chapter 8 to demonstrate the relative reduction in stress obtained by the modified genset. Further testing and analysis are required to validate the magnitude of stress obtained from this stress analysis.

7.2.6 Chapter 7 summary

In this chapter, the electromagnetic torque and prime mover torque obtained in Chapter 6 are applied to 3DFE models of the complete motor driven and engine driven generators sets using the transient analysis solver in ANSYS. The resulting stress in the keyway is obtained for later comparison with the modified genset in Chapter 8.

The steps taken in this chapter are as follows:

- Equivalent 3D models of the torsional models for both gensets are built and imported into the modal solver. The modal results for the first three torsional modes are compared with those for the 1D torsional model obtained using the Matlab script shown in Appendix B. The modes closely match for both 3D genset models, confirming that the inertia/stiffness properties of the 3D model match those of the 1D model.
- The torque and speed results taken at the coupling of the 3DFE models are compared with those obtained from the 1D mechanical model when the same electromagnetic torque and prime mover torque is applied.
- The same process is repeated with the flexible coupling included in the ANSYS model. The flexible coupling is defined with a curve of shear modulus for the coupling element that produces an equivalent torsional stiffness depending on the applied load.
- The impact of the torsional stiffness of the coupling on the modes of the structure is explored.
- The detailed 3DFE model of the generator rotor is then coupled to the equivalent shaft model of the diesel engine and its couplings.
- A full transient analysis of the structure is performed. The fault torque for a 140 ms LVRT event is applied to the generator rotor core (electromagnetic torque) and the inertia elements for each engine piston (prime mover torque). The stress in the keyway/key between the generator shaft and the engine couplings is obtained for further use in Chapter 8 to compare with the keyway/key stress in the modified generator set.

The key points from this chapter as follows:

- The coupling speed and torque results from the transient analysis of the 3DFE genset rotors closely match those from the 1D torsional models, thus validating the use of these models for stress analysis.
- Extremely high peak stress is obtained for the applied torque (4 kNm peak electromagnetic torque). The peak stress is in the order of 700 MPa (excluding the peak stress in the very corners of the model). Far exceeding the yield strength of EN8 steel, 280 MPa and the ultimate tensile strength of 550 MPa.
- Even at a FRT time of 140 ms, the key is likely to experience permanent deformation at the very least and potentially catastrophic failure. This LVRT fault is for an extreme case where there is no protection at all for the generator, the engine inertia is significantly greater than the generator inertia and when the grid is reconnected, the voltage is restored to 100% instantaneously.

The work completed here is used in the following chapters are as follows:

- The validated 3DFE model of the generator rotor connected to the equivalent shaft model of the diesel engine produced in this chapter is used in Chapter 8 for further stress analysis comparisons between the modified and un-modified generator sets.
- The examples simulated here indicate that even an electromagnetic fault torque of 4 kNm would severely damage the generator coupling. This observation is considered in Chapter 8 where the generator set is modified to reduce the peak fault torque.

Chapter 8 Design optimisation for low voltage ride through performance improvement

8.1 Generator set modifications

This chapter explores the electromechanical performance of the UC22F generator rotor as determined from the previous simulation and experimentation chapters. The target performance parameters are firstly, minimising the rotor angle, which is achieved by reducing the acceleration of the rotor during fault ride through. Secondly, reducing the stress applied to the rotor structure thereby extending the life of the machine which is achieved by reducing the peak torque applied to the highlighted areas on the rotor.

It is likely that grid code requirements for fault ride through time will become ever more demanding, new generators being connected to the grid will be expected to become more robust over time (analogous to diesel engines and emissions regulations) and the required fault ride through time for 100% voltage drop will increase to suit. Minimising the rotor speed is therefore an important objective of this for potential design improvements.

As previously investigated in section 6.4.2, the maximum speed reached does not significantly impact the peak electromagnetic torque (disregarding the rotor angle shift that happens to be present at reconnection) but it does influence the time required for resynchronisation to occur. A high rotor speed increases the time over which the rotor is subjected to elevated torque before steady state is achieved (-364 Nm), thus increasing the time period over which the rotor is highly stressed. Excessive post fault rotor speed also increases the chance of physical rotor slip events.

Whilst the keyed coupling is most at risk of failure due to high transient fault torque, all other components attached to the generator rotor and engine train experience significant stress during LVRT events. Sudden accelerations induce high inertial force on the secondary rotor components, particularly the fan blades and rotor windings. Stator and rotor windings bend and warp under the immense inrush fault current and are sensitive to both the torsional vibrations that follow disconnection/reconnection and electrical harmonics. Both are fastened to their cores under tension and hardened with insulating resin, making them substantially weaker compared to the steel structures surrounding them and more difficult to analyse with FE models alone. When modifying the rotor for LVRT performance improvement, transient torque and rotor acceleration should be reduced as much as possible, not just to within safe levels for the coupling. The main objectives for the following design optimisations are:

- Reduce peak reconnection/disconnection stator current (reduce thermal and mechanical load on the windings, also determines electromagnetic torque)
- Reduce the electromagnetic torque (reduce stress on all rotor components)
- Reduce the coupling torque (reduce stress in the coupling keyway)
- Reduce the maximum angular speed of the generator rotor (reduce resynchronisation time, reduced probability of rotor slip/crash resynchronisation).

The modifications are limited to options that do not alter the existing design of the generator rotor or significantly impact the existing steady state performance of the generator. For example, as previously discussed in section 2.1.9.3 the magnitude of

stator fault current could be reduced by reducing the sub-transient reactance of the machine, although this would require physical modification of the windings that would negatively impact the efficiency of the generator. All simulations are performed on the grid connected diesel engine driven generator set model.

8.1.1 Braking resistors

As identified in the literature review, braking resistors can significantly reduce the magnitude of peak fault current and thus electromagnetic air gap torque during LVRT. It should be noted that the generator circuit used in the Simplorer model does not contain any connection equipment between it and the grid and is directly connected to it, thus the system impedance is significantly lower (only the stator winding resistance of 0.065Ω per phase is included) than that of a real grid connected genset.

The existing three-phase short circuit lines are repurposed as braking resistors (Figure 8.1) which connect between the three phases in parallel with the voltage supply lines that represent the terminal connection to the grid. In practise the braking resistors will require a control signal to determine when a low voltage fault occurs, this could be a voltage signal from the stator circuit (18). In this case, an ideal scenario is simulated as the switches are set to open at the instant that the low voltage fault occurs and close at the instant the grid is reconnected. The peak field current remains unchanged here and a 140 ms, 100% voltage drop FRT is simulated.

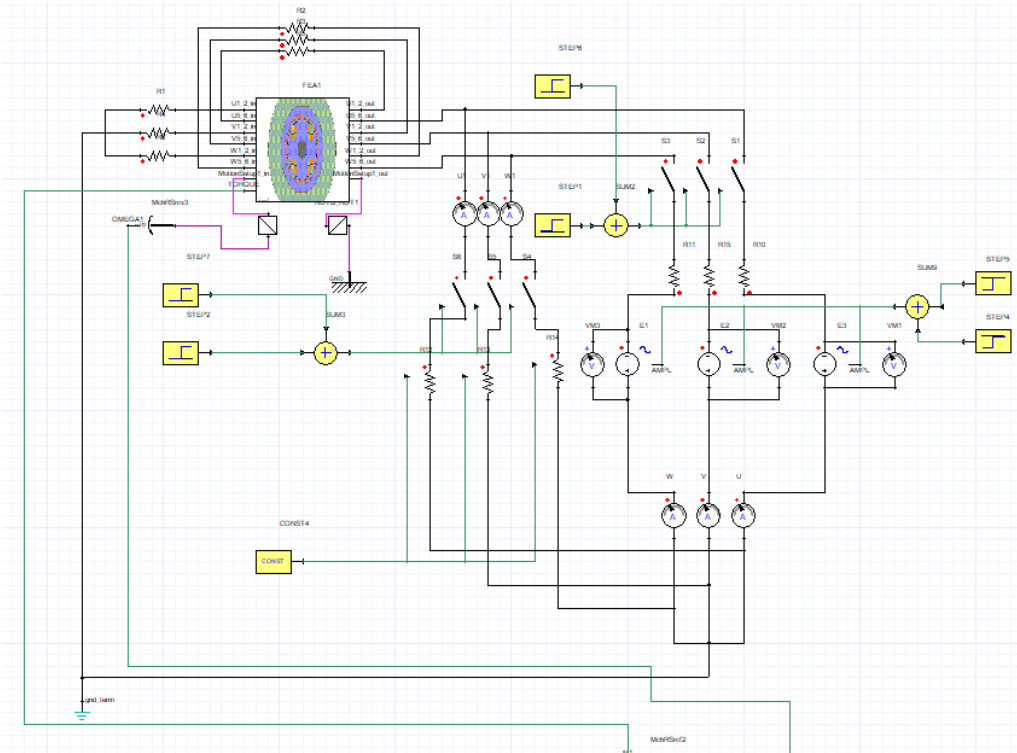


Figure 8.1: Simplorer generator circuit with braking resistor branches

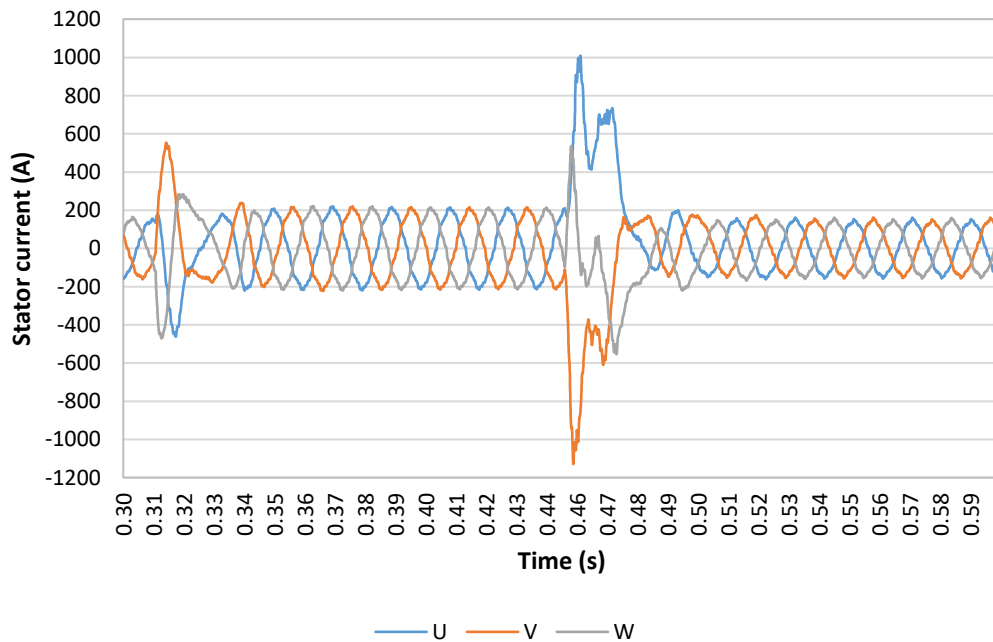


Figure 8.2: Stator current with braking resistors 0.5 Ω per phase

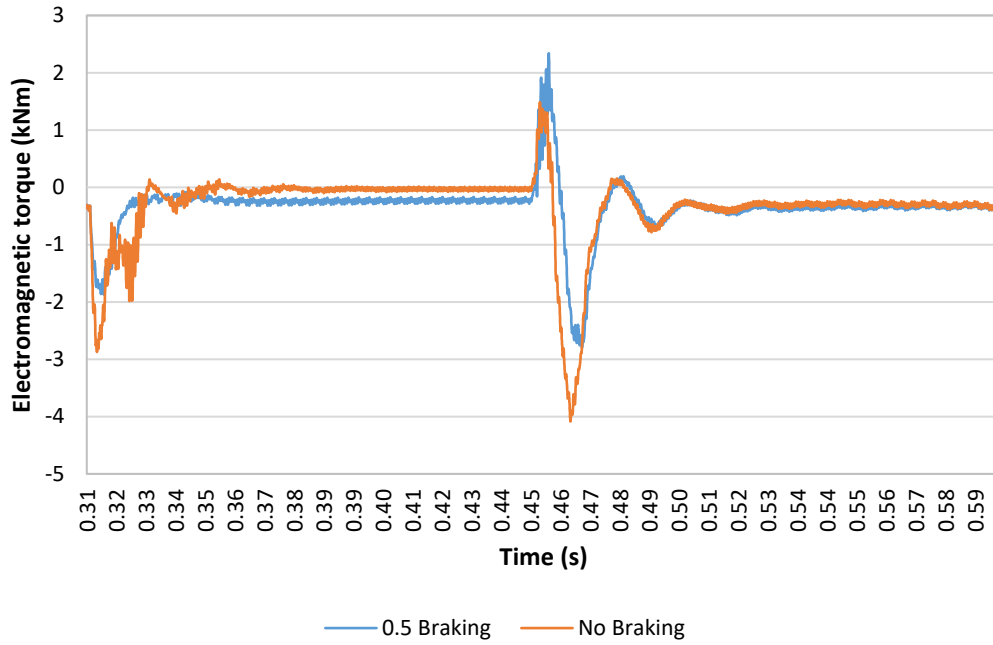


Figure 8.3: Electromagnetic torque with braking resistors 0.5 Ω per phase

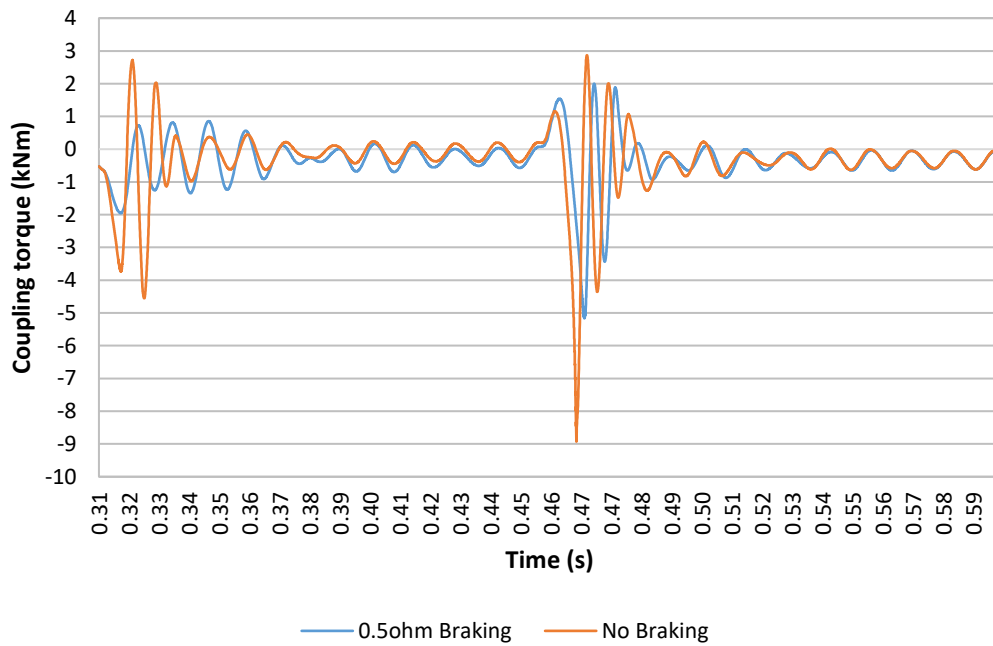


Figure 8.4: Coupling torque with braking resistors 0.5 Ω per phase

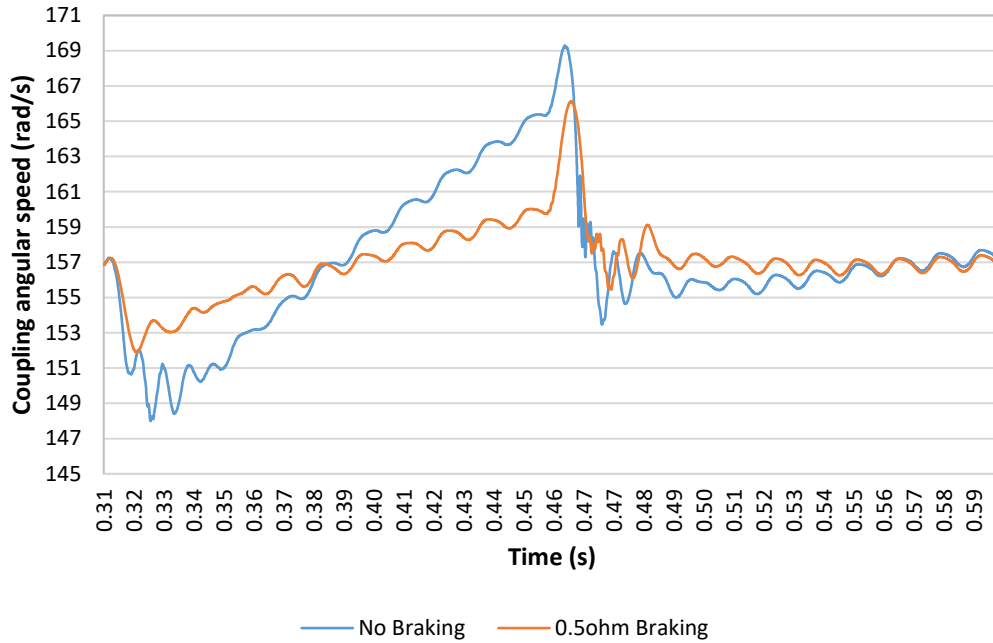


Figure 8.5: Coupling angular speed with braking resistors 0.5 Ω per phase

The peak disconnection/reconnection stator current (Figure 8.2) is reduced. Instead of the energy stored in the magnetic field being converted to circulating current in the stator as it collapses, it is sustained by the resistive load now present in the active braking resistor line. The fault behaviour is now similar to that of a partial voltage drop rather than a 100% drop as the braking resistor acts as a new load which, while smaller than the grid load in this instance, still sustains a steady state three phase current in the machine of 118 A (205 A peak).

Like the load bank used in the initial short circuit testing, the braking resistor provides a resistive load to which the generator can maintain a steady state power supply, albeit on a smaller scale and for only a very limited time before the braking resistors suffer heat damage. In practise, the braking resistors would need to be disconnected over longer FRT periods or switched to an additional backup branch. Where the braking

resistor is disconnected during FRT, the resistance would need to be reduced gradually to prevent increased stator current transients.

Since a load is sustained by the braking resistors during the fault, the rate of increase in rotor angular speed is reduced. As a result of this, the shift in rotor angle is altered at the point of grid reconnection as compared with the model without braking resistors. The peak positive reconnection electromagnetic torque is increased at this rotor angle so that, whilst the peak-to-peak electromagnetic torque is reduced, the final rotor angular speed (Figure 8.5) is only ~ 3 rad/s slower. Note that should the two simulations be compared when reconnecting at the same rotor angle shift rather than fault ride through period, the braking resistor performance would improve further. The coupling torque (Figure 8.4) is also significantly reduced (almost halved) at the point of grid disconnection and reconnection, more so than the comparatively small drop in transient electromagnetic torque (Figure 8.3) would suggest.

8.1.2 Increased braking resistance: 1Ω per phase

The same simulation as in section 8.1.1 is repeated, but with the braking resistance increased to 1Ω per phase. The results are shown below in Figure 8.6 to Figure 8.9.

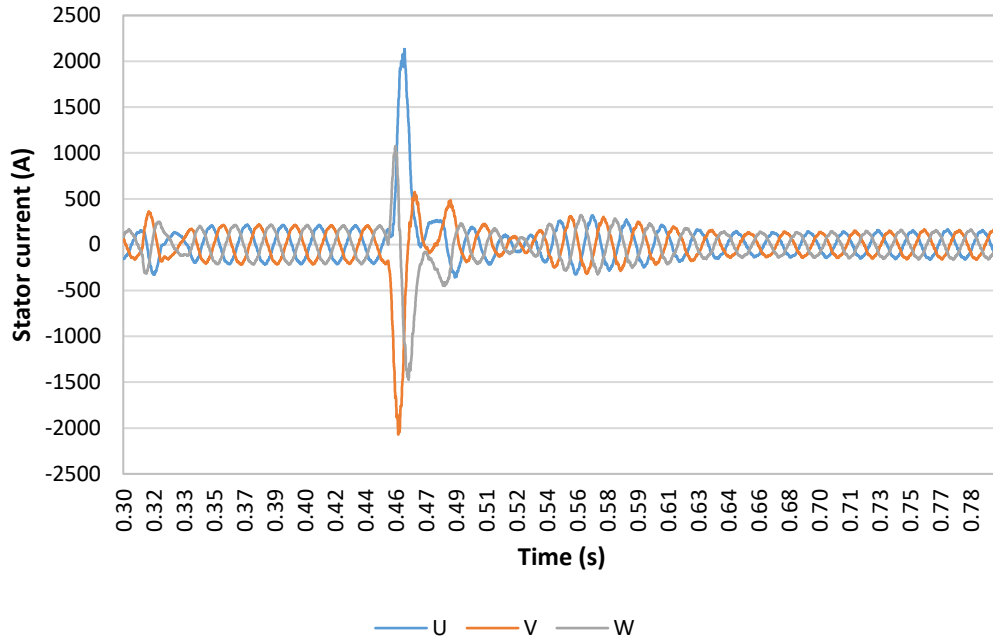


Figure 8.6: Stator current with braking resistors, 1 Ω per phase

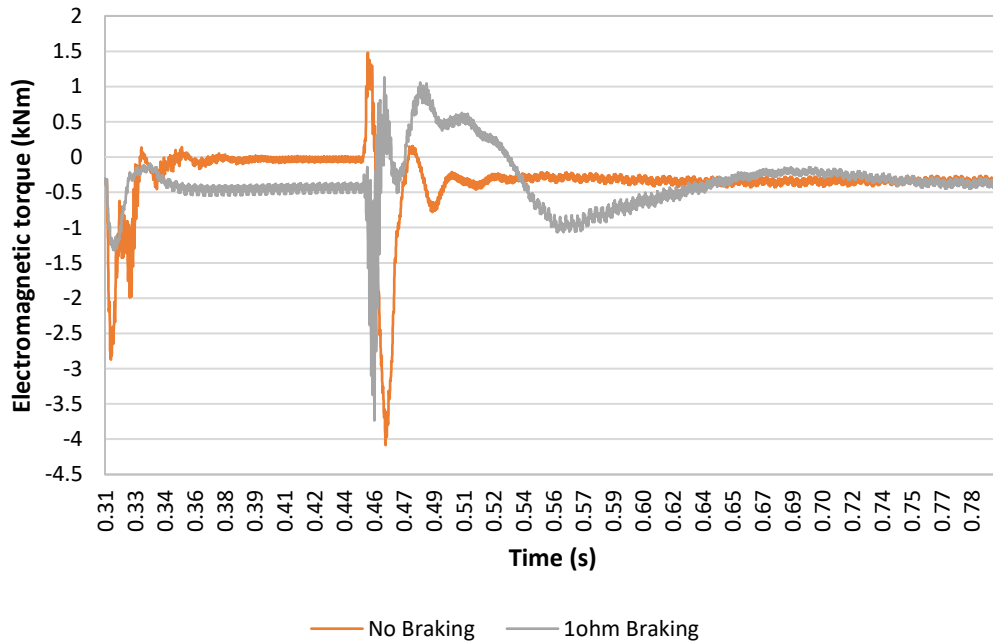


Figure 8.7: Electromagnetic torque with braking resistors, 1 Ω per phase

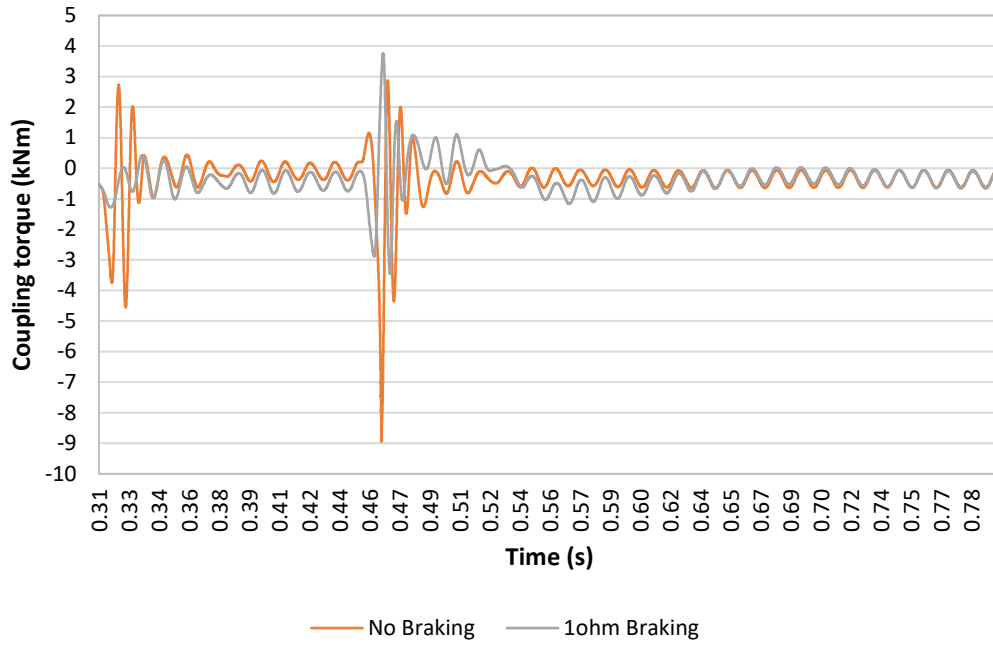


Figure 8.8: Coupling torque with braking resistors, 1 Ω per phase

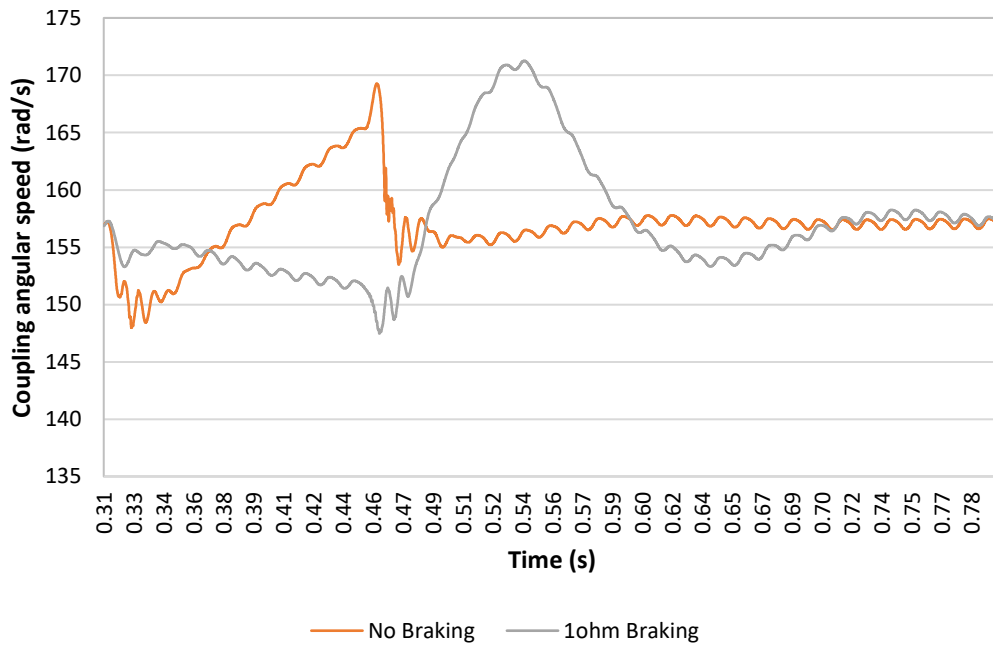


Figure 8.9: Coupling angular speed with braking resistors, 1 Ω per phase

Further increasing the resistance of the braking resistors to 1 Ω results in the following:

- Reduced coupling torque at grid disconnection.
- Reduced peak coupling torque at grid reconnection, now acts in the positive direction as motor accelerates.
- Half the peak disconnection current and electromagnetic torque.
- Double peak reconnection stator current, when the grid is reconnected, the braking resistors are immediately shut off and 100% of the sustained load energy now circulates around relatively low resistance stator circuit only.
- Similar initial peak to peak electromagnetic torque, but contains a second, sustained period of increased electromagnetic torque.
- Speed steadily decreases as the sustained load is greater than the steady state load (215 A vs 150 A peak per phase). When the grid is reconnected the rotor speed suddenly increases as the generator current is greater than that demanded by the grid load.

Note that whilst the stator current determines the electromagnetic torque in the generator, and this holds true during grid disconnection/reconnection, the peak-to-peak electromagnetic torque produced by the initial peak current only increases by ~1 kNm when the peak current is doubled. This behaviour is attributed to the additional resistive load and highlights the need to pay close attention to both the stator current and the electromagnetic torque when performing LVRT tests. It should not be assumed that because the electromagnetic torque remains largely unchanged with the addition of control equipment to the generator circuitry that the stator current has not changed significantly either.

Since the disconnection electromagnetic torque is already of lesser concern than the reconnection electromagnetic torque, the benefit of reduced disconnection torque with a 1 Ω braking resistance is greatly diminished by the reduced post reconnection performance that it brings.

Ultimately, this fails the requirement to reduce the post reconnection resynchronisation time but does achieve a small improvement to reducing the peak mechanical torque over the 0.5 Ω braking resistor. The greatly increased reconnection fault current certainly fails the requirement to reduce fault current. As the rotor speed both increases in maximum magnitude and requires an additional ~ 200 ms to achieve resynchronisation with the grid frequency, the 1 Ω braking resistor fails the requirement to reduce maximum angular speed and resynchronisation time.

8.1.3 Series braking resistors: 0.5 Ω per phase

The previous braking resistor simulations are activated in parallel with the grid supply. In reality, the generator must not be disconnected from the grid during FRT as specified in grid codes. Therefore, the 0.5 Ω braking resistors are connected in series with the supply as shown in Figure 8.10 below. Note that the shift in rotor angle will be altered due to the braking resistors sustaining a load in the generator during the ride through period. For the standard generator set model, the rotor angle shift at the point of reconnection (140 ms FRT) is 7.67° , the same rotor angle shift for the model with braking resistors engaged occurs at 431.85 ms

The braking resistors are connected at the instant the grid is disconnected at 311 ms and remain connected following grid reconnection at 431.85 ms, at which point the resistance remains connected for an additional 50 ms 481.85 ms before the braking resistors are switched off.

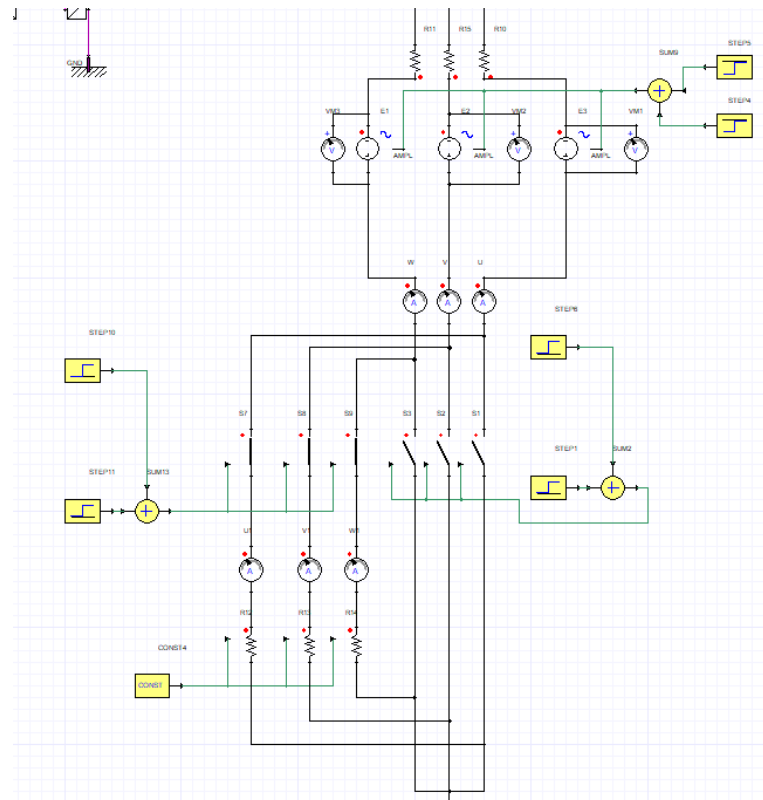


Figure 8.10: Braking resistors connected with series with grid supply

If the braking resistors are disconnected at the moment the grid voltage is restored, then the additional resistance will not be present to reduce the peak stator current and electromagnetic torque in the generator. Also, if the resistors are disconnected after grid reconnection, the sudden load step will induce an additional current transient. This may be improved by using variable resistors or including capacitors in a similar manner to a snubber circuit in order to slowly reduce the load through the braking resistors following the fault.

Alternatively, rather than connecting and disconnecting the braking resistors lines during FRT, the existing resistors can be swapped out for variable resistors. The braking resistors are still switched into the circuit at the point of grid disconnection but remain connected following grid connection. The resistance of the circuit is reduced from 0.5 Ω per phase to 0 Ω over a period of 200 ms, which begins 50 ms after the grid is reconnected. The resulting reconnection electromagnetic torque follows a gentler curve, and the peak torque is reduced. The downside of this arrangement is that the resynchronisation time is increased, and the rotor coupling will be exposed to the increased torque for a longer period of time. The variable resistance may be decreased at a faster rate and begin immediately following grid reconnection to improve this result at the expense of increased peak electromagnetic torque.

Compared to the model with no braking resistors present, the peak electromagnetic torque at the beginning of the fault is reduced from 2.87 kNm to 1.7 kNm (-40.77 %) and at the point of fault clearance is reduced from 4.08 kNm to 1 kNm (75.49%). The observation of reduced rotor acceleration due to the addition of series braking resistors is similar to that made in existing literature (19). With the series braking resistors optimised and controlled as performed in (19), the rotor speed could be managed at near pre-fault levels throughout the LVRT fault. As shown later in Section 8.2 when the braking resistors are controlled, the short circuit current is dramatically reduced which helps to achieve a lower rotor acceleration as shown in the speed results in Figure 8.30.

8.1.4 Increased inertia

Increasing the inertia of the generator set is perhaps the simplest alteration that can be made in order to address FRT performance. In the following simulations, the coupling inertia is increased, and an additional inertia is added to the NDE of the generator rotor. The main disadvantages of additional inertia on the performance of the generator are:

- Start-up is slower, requires more time or more torque to accelerate at the same rate prior.
- Additional material cost.
- Shifts the torsional frequencies of the genset, requires additional modal analysis before implementation.

8.1.4.1 Increased coupling inertia of 0.67 kgm^2

The inertia of the coupling in the model is increased to 0.67 kgm^2 , the simulation results for this modification are shown in Figure 8.11 to Figure 8.13.

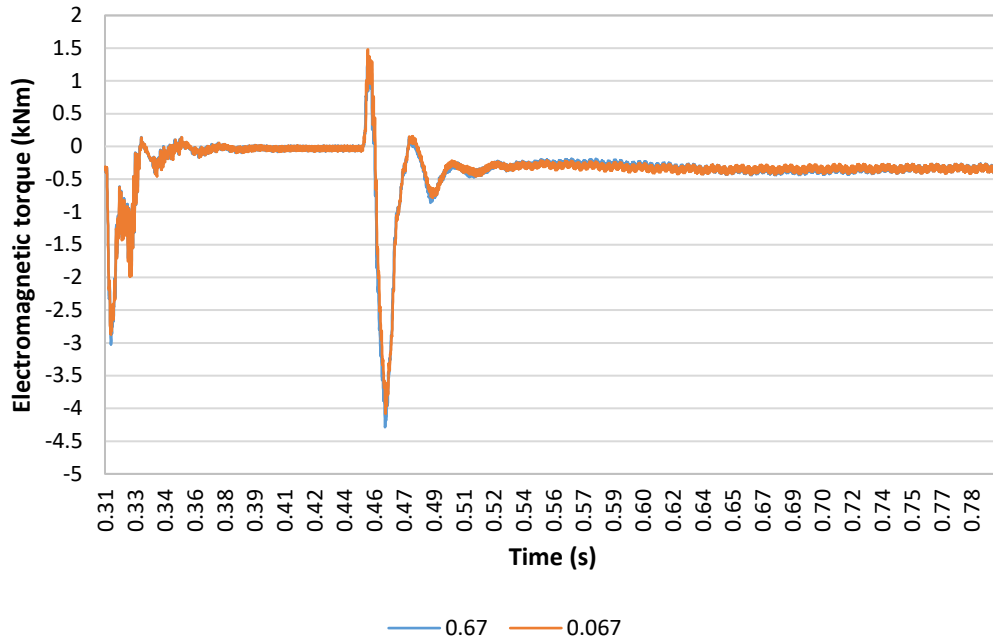


Figure 8.11: Electromagnetic torque for increased inertia (0.67 kgm^2) vs. original inertia (0.067 kgm^2)

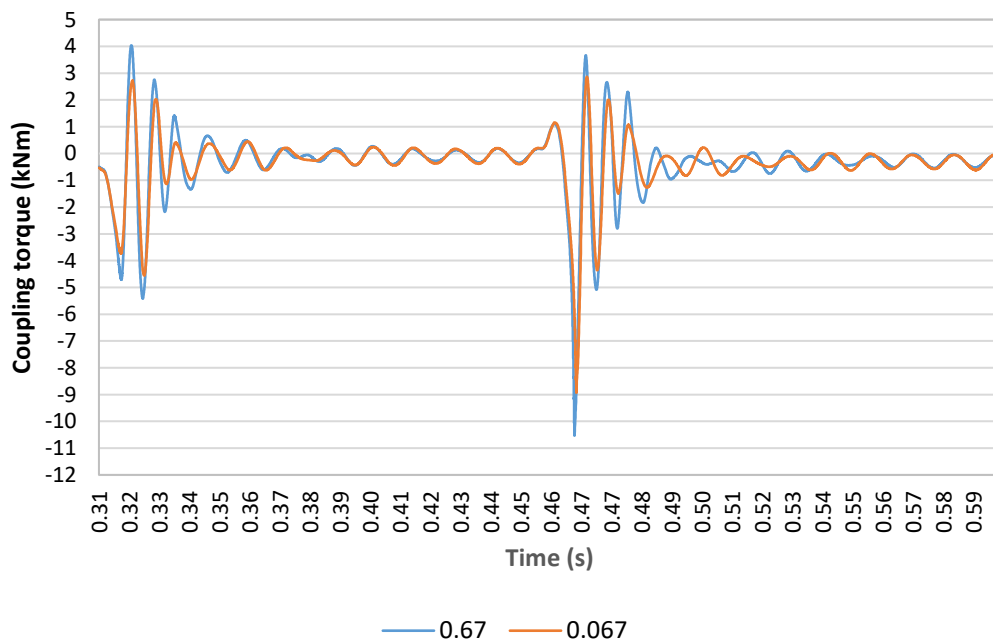


Figure 8.12: Coupling torque with increased inertia (0.67 kgm^2) vs. original inertia (0.067 kgm^2)

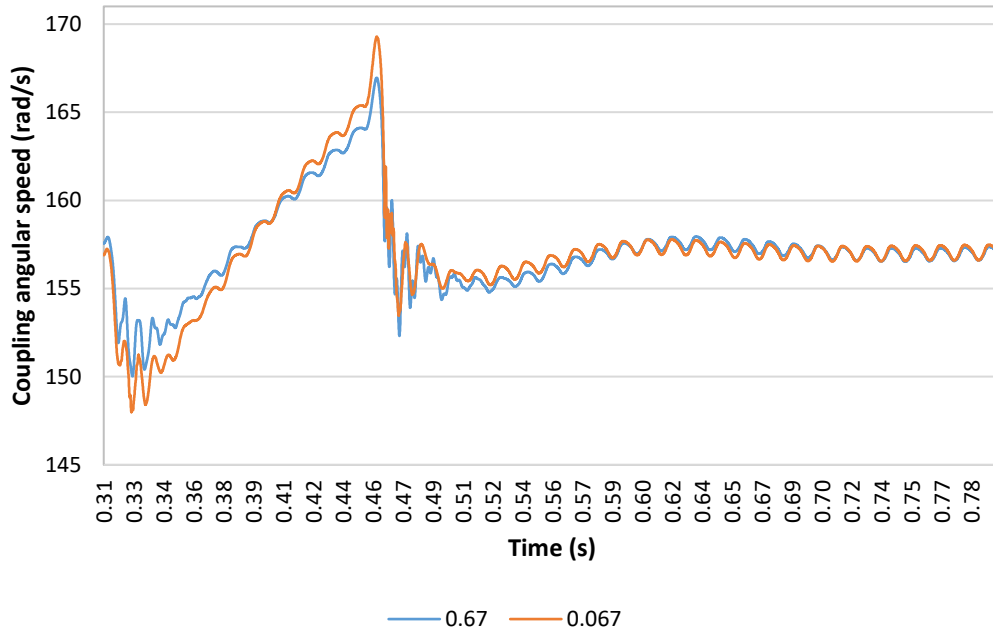


Figure 8.13: Coupling angular speed with increased inertia (0.67 kgm²) vs. original inertia (0.067 kgm²)

With the flexible coupling present in the assembly, the increased coupling inertia results in a mild improvement to LVRT performance. The peak coupling torque is reduced, as is the peak maximum rotor speed and average rotor speed during FRT. It must be noted that increasing the coupling inertia further can result in an increase in coupling torque, therefore the focus for this solution is placed on increasing the inertia of the generator and engine as well as balancing the inertia of both machines.

8.1.4.2 Adding inertia to the generator and engine and auxiliary inertia components

Note this would need to be a large diameter mass and would therefore need to be housed outside of the generator casing in a similar manner to how a permanent magnet generator is attached to the end of the rotor shaft outside of the casing. In practise, the

inertia could be a simple solid steel cylinder, or the system could make use of an additional large or high-speed flywheel similar to that used on the diesel engine.

In this case the inertia is positioned closer to the rotor core than the flexible coupling and the torsional stiffness of the shaft between it and the rotor core is greater than that between the coupling and the rotor core. Increasing the inertia attached directly to the generator rotor shaft will therefore have a greater impact on changes in rotor angular speed.

As highlighted in Chapter 2, the magnitude of increased fault torque at the coupling resulting from an LVRT event depends on the ratio of inertia between the generator and prime mover. If for example the generator inertia is several times larger than the diesel engine inertia, the coupling torque will be significantly increased following grid reconnection.

To reduce the coupling torque, the inertia on both sides of the coupling should be equal and the total inertia should be increased in order to reduce acceleration of the whole genset during the FRT period. The inertia of the generator rotor about its axis of rotation is 0.558 kgm^2 and the inertia of the engine is 1.6 kgm^2 . A rotational inertia of 1.042 kgm^2 is added to the NDE bearing element at the end of generator model so that the ratio of inertias between both machines is equal to 1. An additional 0.5 kgm^2 is added to the end of the engine rotor train at the damper hub (shaft side) and the generator rotor to bring the total inertia of the generator set to 4.2 kgm^2 , almost twice the original total inertia. The LVRT simulation is repeated with these modifications made to the rotor inertia and the results are shown in Figure 8.14 to 8.15.

Although the rotor angle will have shifted for the increased inertia model versus the standard diesel genset model, the same electromagnetic torque is used in both simulations to compare the coupling speed and torque.

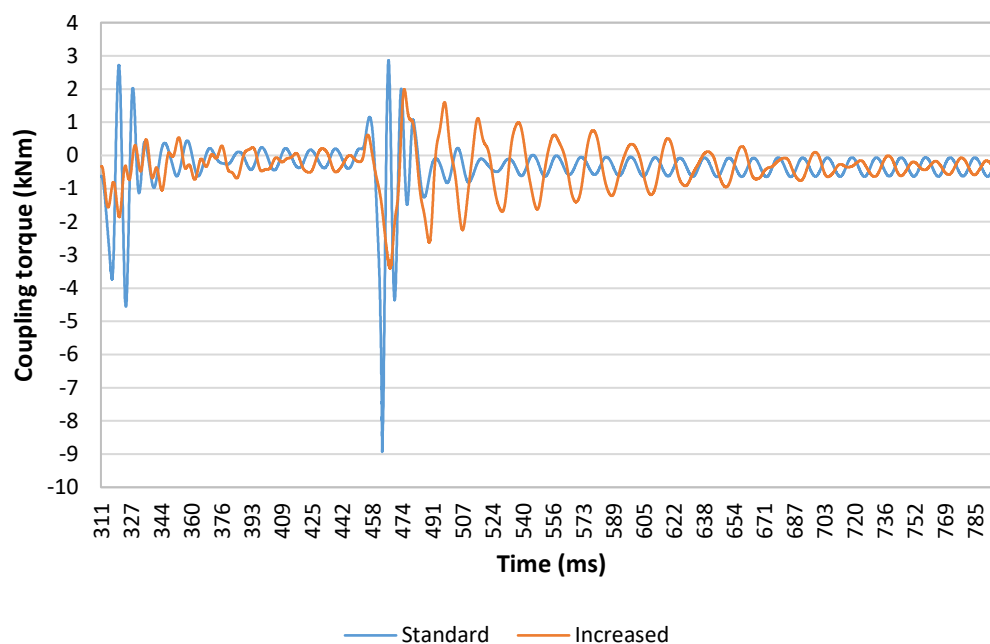


Figure 8.14: Coupling torque for the increased inertia generator set and balanced inertia ratio to 1 vs. standard genset model

Whilst the peak coupling torque and angular speed is significantly reduced at both the point of grid disconnection and reconnection, the post fault performance is somewhat degraded by the presence of the increased rotor inertia. The additional inertia results in a high magnitude torsional oscillation following grid reconnection.

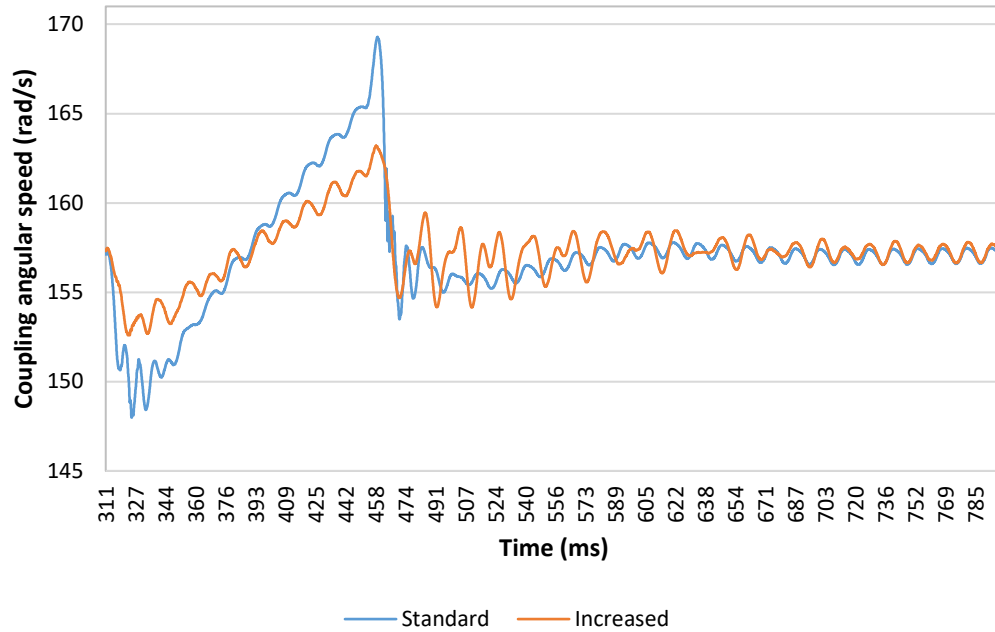


Figure 8.15: Coupling angular speed for the increased inertia generator set and balanced inertia ratio to 1 vs. standard genset model.

Compared with existing research into the impact of increasing generator set inertia on LVRT performance (20), (19), the results from this simulation reproduce the expected reduction in rotor acceleration. With the inertia of the system doubled, the time required to reach the same peak speed as the standard genset model is increased by 127 ms, thus the rate of acceleration is reduced by almost 50%.

If the additional 0.5 kgm^2 inertias added to the generator and engine rotors is instead connected to the NDE bearing and damper hub components by separate stiffness branches then the torsional oscillations can be reduced when these branches are disconnected in a similar manner to the clutch solution discussed in the following section. The coupling torque and speed results for the genset with auxiliary inertias connected throughout the LVRT period and disconnected 50 ms after the grid is reconnected are shown in Figure 8.17 and Figure 8.18 respectively.

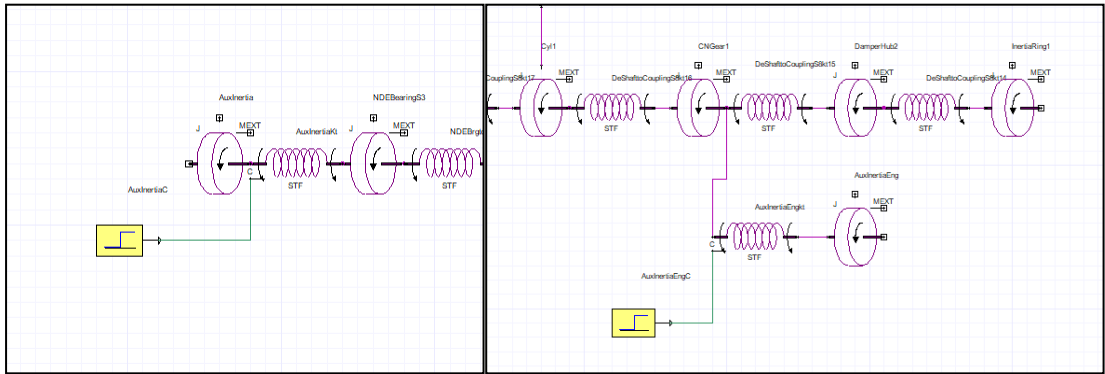


Figure 8.16: Auxiliary 0.5 kgm² inertias, end of generator shaft (left) and connected in parallel with the damper hub of the engine (right)

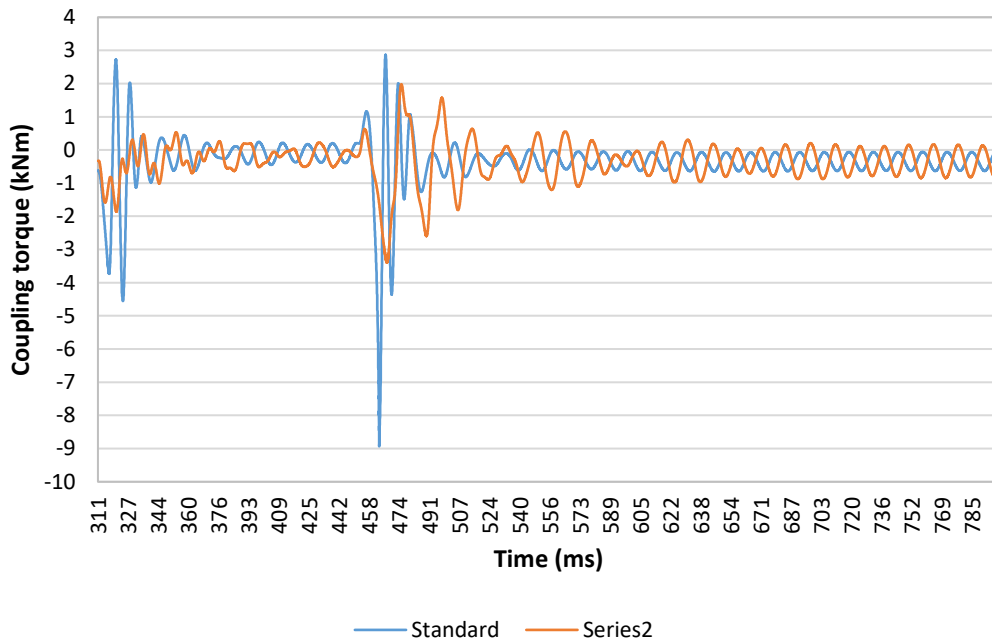


Figure 8.17: Coupling torque for the increased inertia generator set (Series2) and balanced inertia ratio to 1 vs. standard genset model. 0.5 kgm² inertias removed 50 ms after grid reconnection

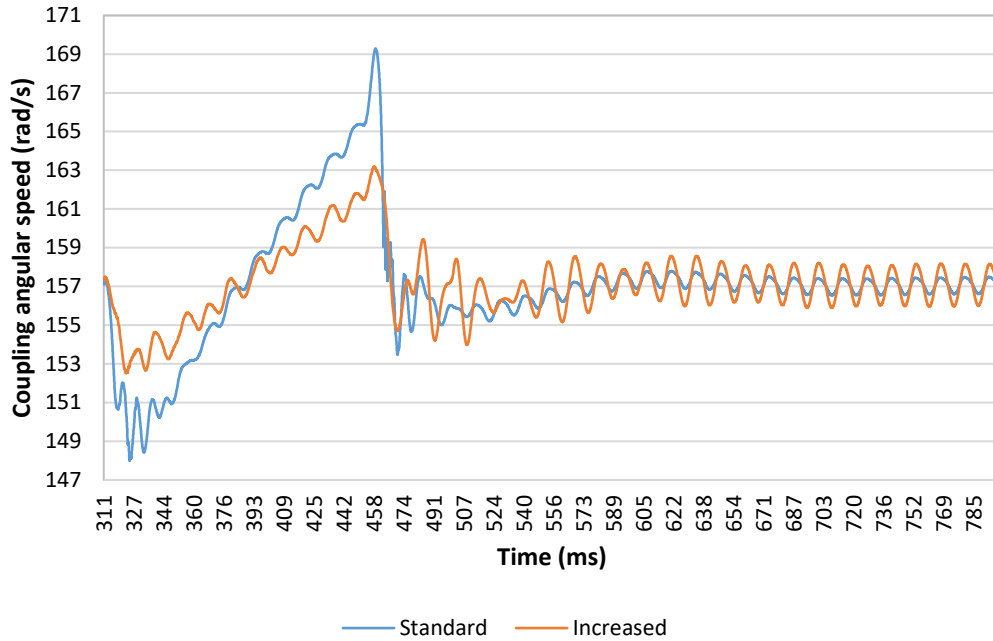


Figure 8.18: Coupling angular speed for the increased inertia generator set and balanced inertia ratio to 1 vs. standard genset model. 0.5 kgm^2 inertias removed 50 ms after grid reconnection

Note that removal of the 0.5 kgm^2 inertias following the fault alters the modal results for the generator set. In this case the amplitude of torsional oscillations has increased slightly at steady state as torsional modal frequencies are shifted closer to the grid frequency (50 Hz).

With all the inertia modifications combined, the peak electromagnetic torque is reduced at the point of grid disconnection and reconnection by 4.54 kNm to 1.85 kNm and 8.93 kNm to 3.38 kNm respectively.

8.1.5 Increased rotor to generator stiffness: Coupling clutch

This simulation utilises an additional torsional stiffness element which effectively bypasses the flexible coupling when activated due to possessing a significantly higher torsional stiffness (set to $5e^6$ Nm/rad). This torsional clutch component would surround the flexible coupling and directly connect the generator shaft to the engine flywheel. The intended effect is that the increased torsional stiffness between the generator and engine will reduce the coupling torque during FRT, thus reducing the keyway stress (since the angle of twist is reduced) and will also reduce the maximum speed reached by the generator rotor, thus increasing the FRT time required before rotor slip occurs. The device is coupled to the generator shaft using the same keyed joint.

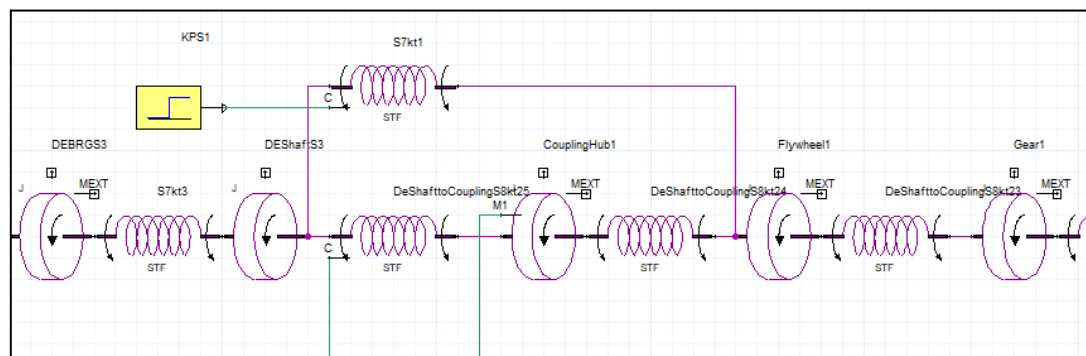


Figure 8.19: Simplorer torsional model with 'clutch' torsional stiffness element

(S7kt1)

Activation of the additional stiffness component could be controlled by magnetic actuation, using measured terminal voltage as a control signal to determine the level of voltage drop and thus the potential severity of the disconnection fault torque. The arrangement would allow the system to engage only at levels of voltage drop that could result in damage to the generator set. Lower voltage drops, for example a 10% reduction to 198 V, have very little impact on the electromagnetic air gap torque relative to a

100% reduction. This fault torque would be permitted to act upon the flexible coupling alone since the resulting speed increase is negligible over the minimum fault ride through period. In order to determine the safe levels of voltage drop, the reconnection fault torque would need to be simulated for intervals of potential voltage drop (i.e. 10%, 20% and so on) with the maximum rotor shift angle at the point of grid reconnection as performed in section 6.4.2. Ideally the system will also disengage after use, returning the benefits of vibration protection that the flexible coupling provides.

In this case, the stiffness of the 'clutch' element is instantaneously added to the system at the point in time (311 ms) that the grid voltage is reduced to 0V. The FRT time period is 140ms and the results are compared with those from the flexible coupling simulation over the same FRT time period. Torque (Figure 8.21) and angular speed (Figure 8.22) measurements are obtained at the engine flywheel since the torque in the flexible coupling is reduced to ~0 Nm. The clutch remains engaged after grid reconnection in this simulation.

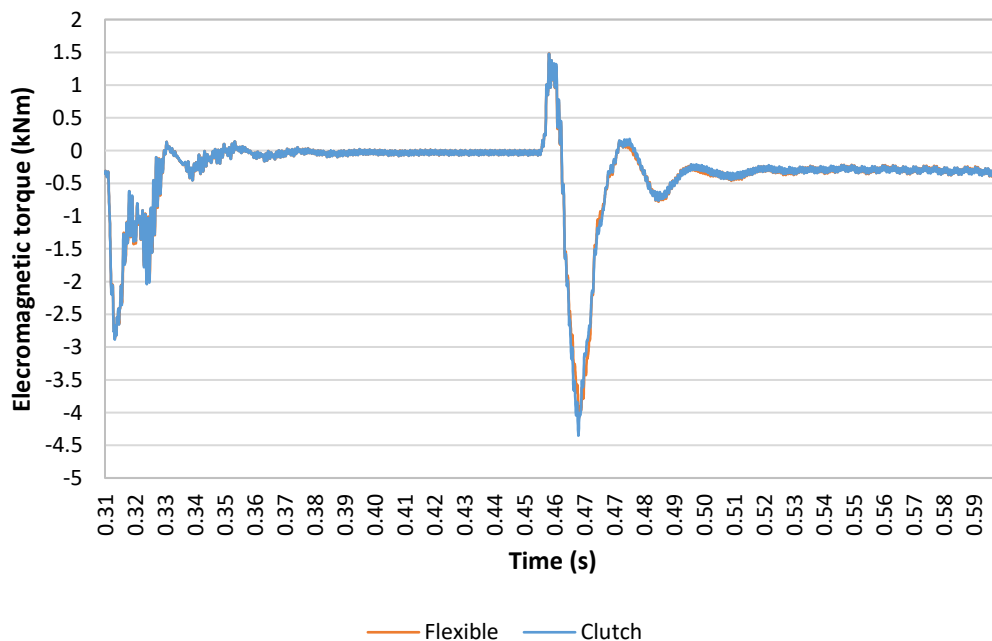


Figure 8.20: Electromagnetic torque for coupling with clutch vs. electromagnetic torque for standard flexible coupling

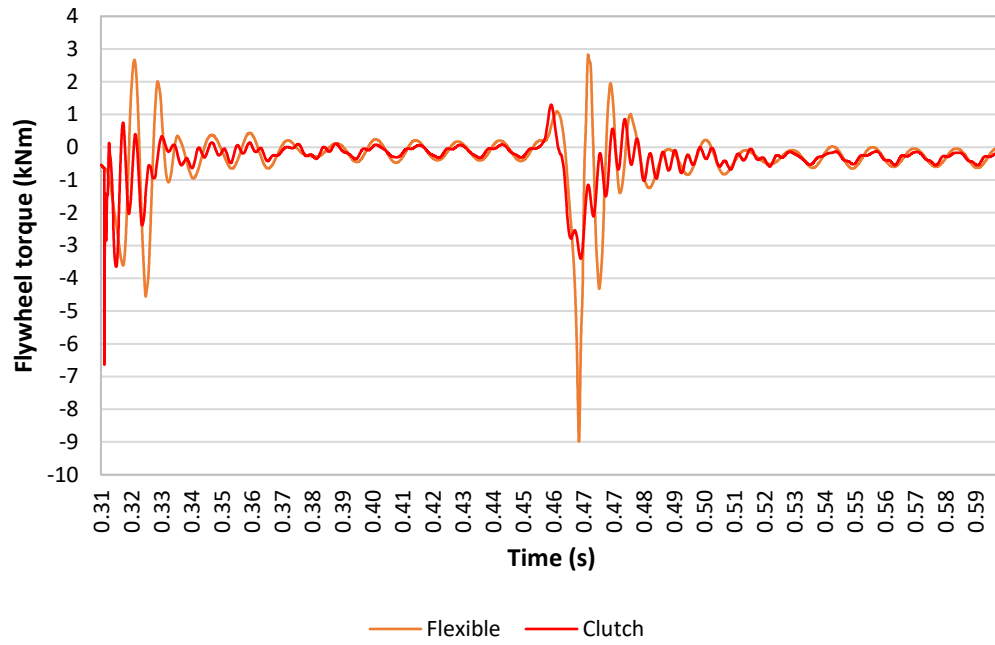


Figure 8.21: Engine flywheel torque for coupling with clutch vs. engine flywheel torque standard flexible coupling

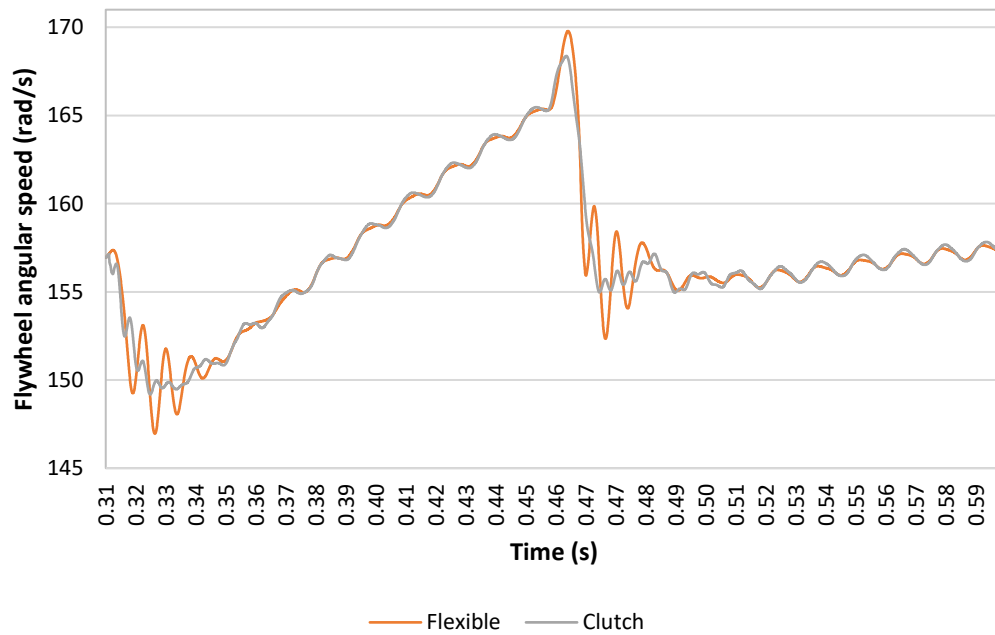


Figure 8.22: Engine flywheel speed for coupling with clutch vs. engine flywheel speed standard flexible coupling

Note that due to the reduction in angular speed here, the rotor shift angle is not the same at the point of reconnection between the clutch system and the flexible coupling system. What can be compared is the maximum rotor speed which is reduced to 168.32 rad/s from 169.51 rad/s, the flywheel torque is also significantly reduced from -8.99 kNm to -3.40 kNm at the point of grid reconnection. Even if reconnected at the exact same rotor shift angle, the stress at the generator coupling keyway is reduced. Note that the 'flywheel speed' refers to the angular speed of the system at this point and is considered to be equal to the shaft speed.

These results are effectively the same as the stiff coupling results, with the exception that at steady state the engine drive train does not experience high frequency vibration. This solution incorporates the benefits of the flexible coupling whilst improving LVRT performance. High frequency torsional vibration does appear during grid disconnection and reconnection although the amplitude is significantly reduced.

In practise, the performance of the coupling clutch will be degraded depending on the length of time between the fault signal being received and the clutch engaging. As the initial fast transient torque occurs over a period of 30 ms, the system would need to react very fast to engage at the beginning of the fault and it would not be realistic to expect it to be able to do so. However, for a FRT of 140 ms, the system should have enough time to engage the clutch before the second fast transient occurs at the point of

grid reconnection. Since it is only important to reduce the magnitude of the second transient, the clutch will still achieve the objective of reducing the peak coupling torque. The clutch will only reduce the peak transient torque if it can be engaged before the peak torque is reached. If for example the clutch was engaged 3 ms after the second transient occurs it would still reduce the peak torque reached, but not by as much as an engagement before the transient would achieve.

8.1.5.1 Clutch engaged at the point of grid reconnection only

An additional simulation is performed to analyse the LVRT performance when the clutch is engaged only at the point of grid reconnection. The following torque and speed results are obtained as shown in Figure 8.23 to Figure 8.25 when the clutch is engaged at 451 ms, the additional stiffness remains connected until the simulation end time is reached.

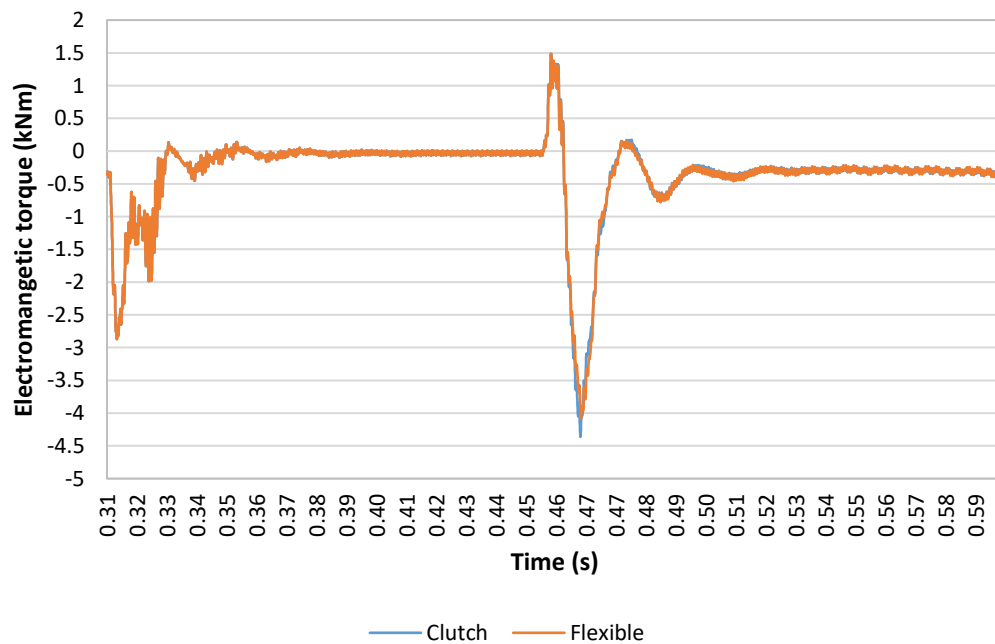


Figure 8.23: Electromagnetic torque for coupling with clutch vs. electromagnetic torque for standard flexible coupling. Activated at the point of reconnect

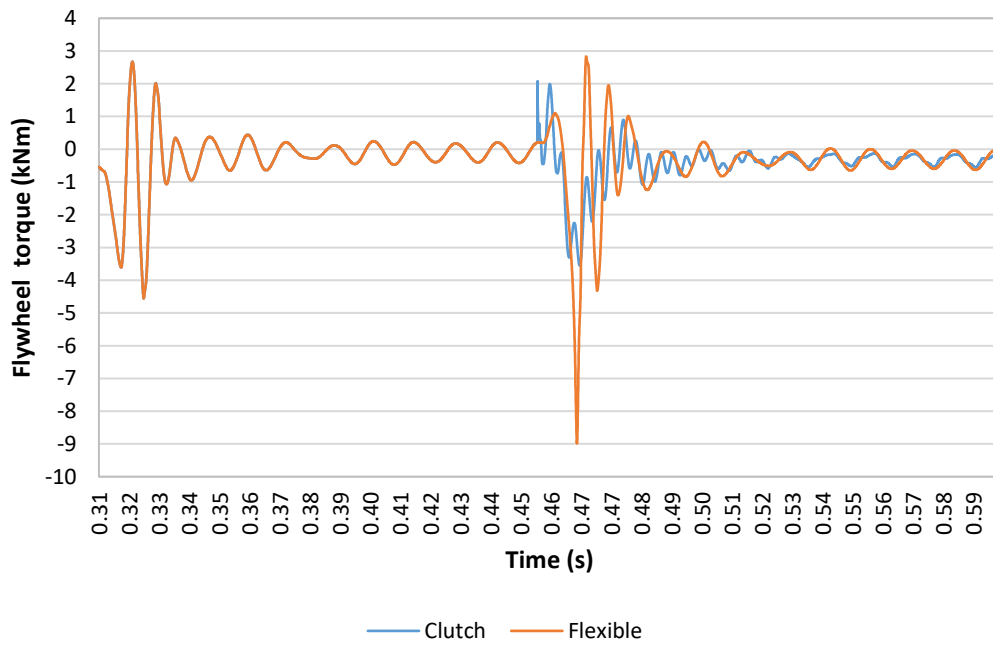


Figure 8.24: Engine flywheel torque for coupling with clutch vs. engine flywheel torque standard flexible coupling. Activated at the point of reconnect

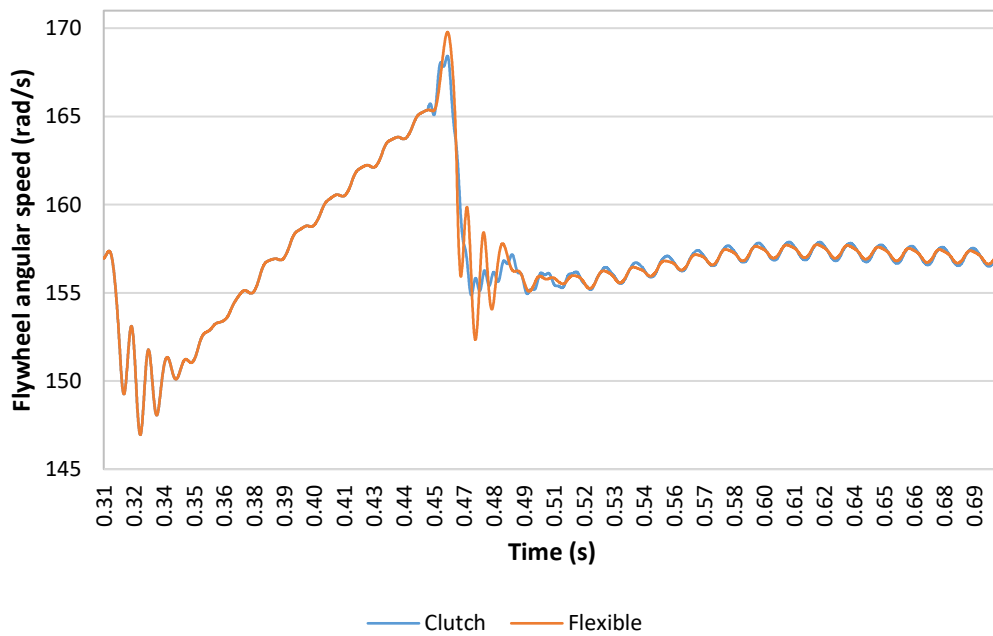


Figure 8.25: Engine flywheel speed for coupling with clutch vs. engine flywheel speed standard flexible coupling. Activated at the point of grid reconnection

Due to the reduction in generator to motor torsional stiffness, the maximum angular speed measured at the flywheel is decreased as expected, though only by a small margin of 1.19 rad/s. The peak flywheel torque at the point of grid disconnection reaches -6.64 kNm but the half cycle period is only 0.35 ms long. As a result the minimum angular speed, angle of rotor twist and thus keyway stress during disconnection is still reduced when compared with the flexible coupling.

8.2 Combined fault ride through modifications

The modifications for increased inertia, increased coupling stiffness (clutch) and increased circuit resistance (braking resistors) are all combined in one Simplorer model. The worst-case scenario for grid reconnection is selected for comparison of LVRT performance with and without these modifications. As identified in section 6.4.2, a 360° rotor angle shift produces the most challenging known reconnection conditions. During initial simulations for the combined LVRT improvements model it was found that the model would take several times longer to reach a rotor shift angle of 360°. It took 980 ms to reach only 180° and the rotor speed had levelled out which means that the rate of rotor angle shift was also decreasing at the point and would continue to decrease further as the engine torque is increased to correct the angular speed. Whilst this does confirm that the maximum fault ride through / CCT is certainly increased, it also suggests that the rotor speed will be much closer to its steady state value at the point of reconnection than for the standard model.

The grid is instead reconnected at 15°, which as shown in section 6.4.2 has a similar peak electromagnetic torque to the 360° rotor angle shift. For the standard generator

set, this angle occurs at 489.7 ms, an FRT time of 178.7 ms. For the combined improvements model the angle occurs at 587.35 ms, an FRT of 276.35 ms.

This model utilises the additional inertia added to the NDE end of the generator and auxiliary 0.5 kgm^2 inertias which are again disconnected via reduction of the connecting torsional stiffness 50 ms following grid reconnection. The series 0.5Ω braking resistors are also included, engaging at 311 ms and dropping to 0Ω over 100 ms following grid reconnection. Mechanical shaft torque and angular speed is once again measured at the flywheel and coupling.

If the clutch is not released following grid disconnection the resulting stiff coupling between rotors, combined with the increased inertia results in a very high magnitude, sustained torsional oscillation through the shaft. This highlights the problem with simply using a stiff coupling to improve LVRT performance. A flexible coupling is still required, especially when the inertia of the assembly is increased. The clutch is therefore activated by measurement of the electromagnetic torque. When the electromagnetic torque exceeds 600 Nm the clutch is activated. At any torque below this value the clutch will remain disconnected, redirecting the torque through the flexible coupling. In addition, if the additional inertia remains constant throughout the fault ride through period, the post reconnection performance is degraded.

The final LVRT simulation results are shown in Figure 8.26 to Figure 8.32. This simulation combines all of the modifications discussed in this chapter into one model.

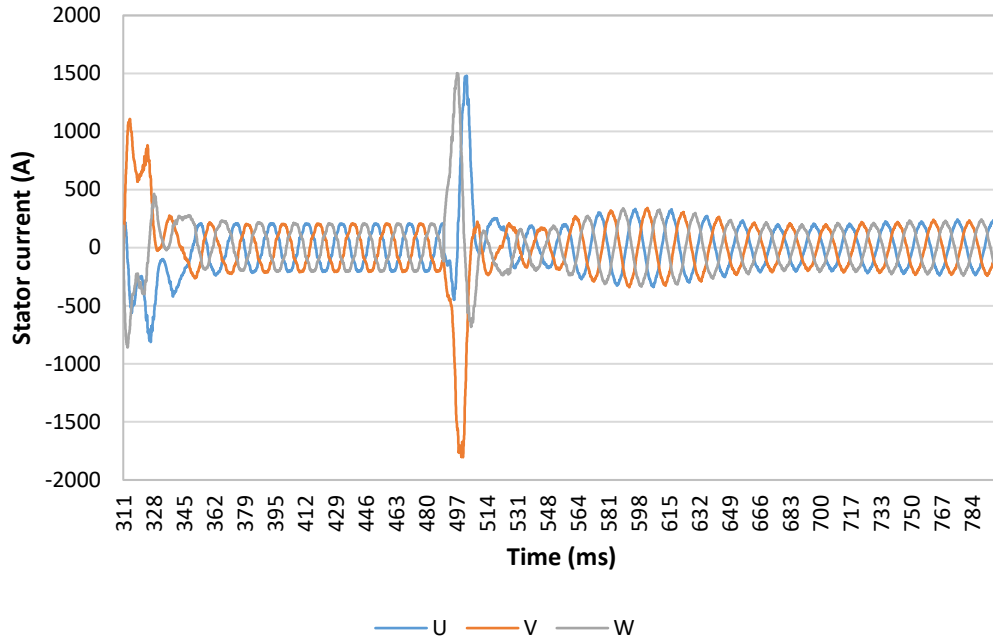


Figure 8.26: Standard genset stator current (A) reconnection at rotor angle shift of 15°
(178.8 ms FRT)

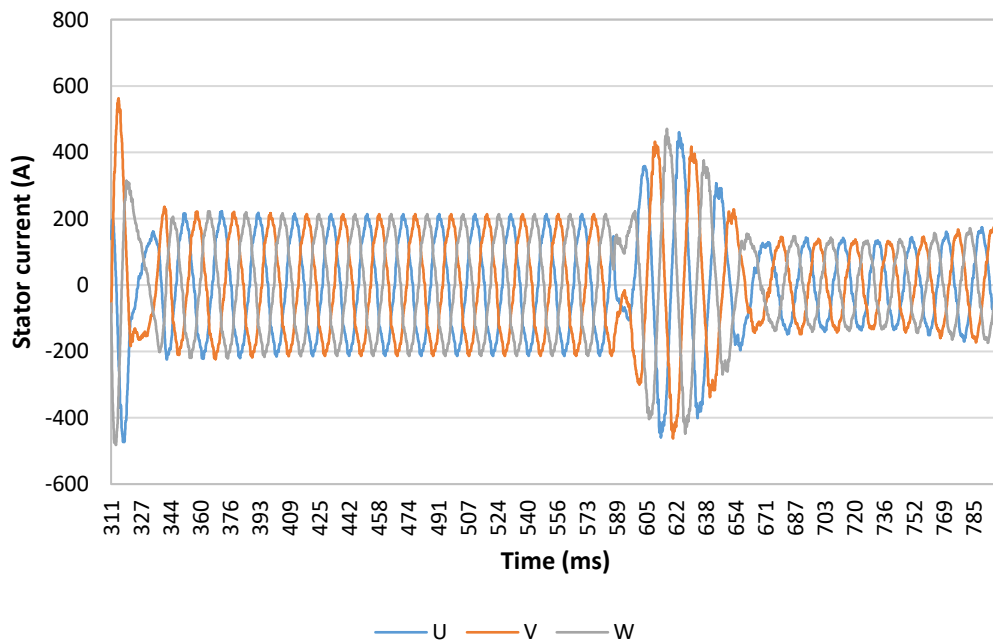


Figure 8.27: Combined FRT improvements genset stator current (A) reconnection at
rotor angle shift of 15° (276.35 ms FRT)

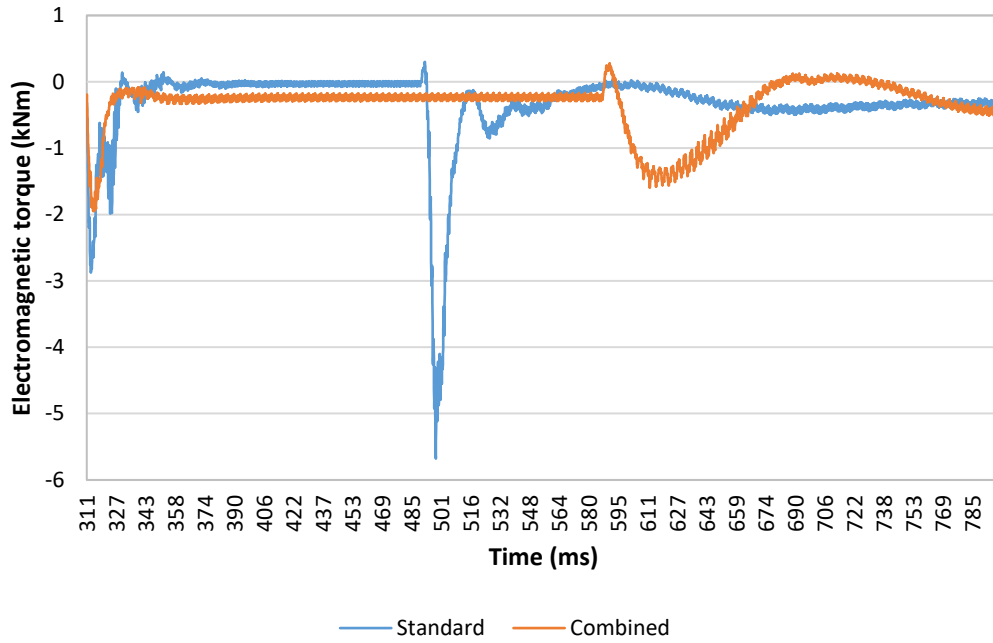


Figure 8.28: Combined fault ride through improvements versus standard genset electromagnetic torque (kNm) at 15° rotor angle shift

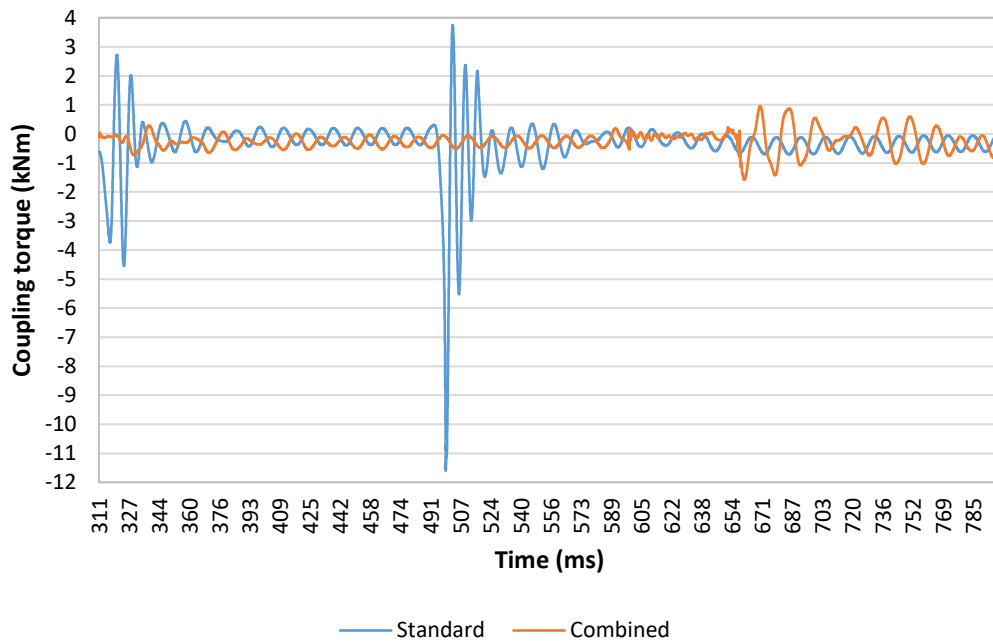


Figure 8.29: Combined fault ride through improvements versus standard genset coupling torque (kNm) at 15° rotor angle shift

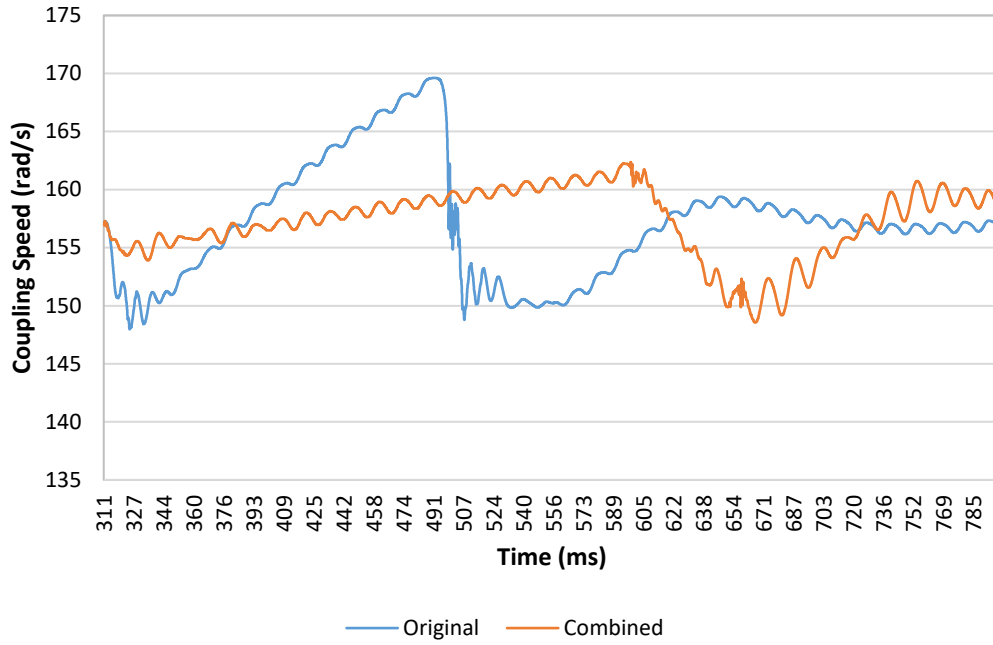


Figure 8.30: Combined fault ride through improvements versus standard genset coupling speed (rad/s) at 15° rotor angle shift

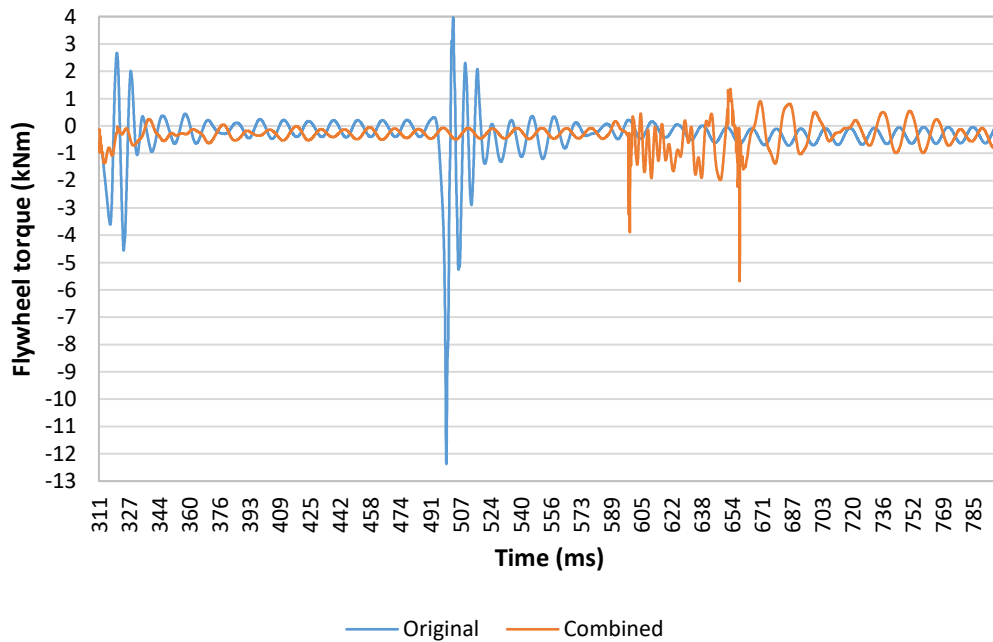


Figure 8.31: Combined fault ride through improvements versus standard genset flywheel torque (kNm) at 15° rotor angle shift

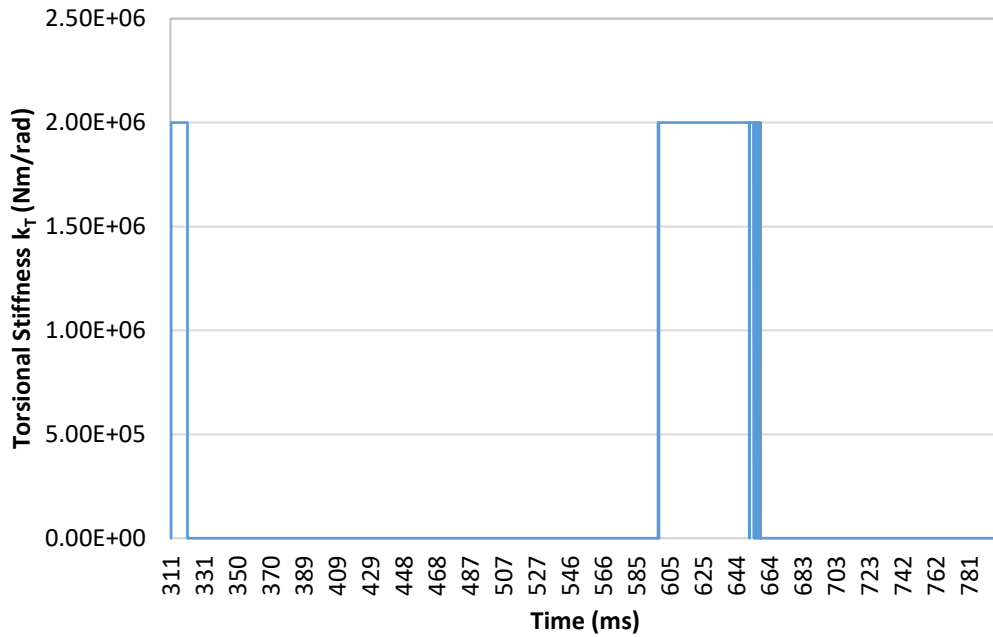


Figure 8.32: Combined fault ride through improvements versus standard genset clutch torsional stiffness (Nm/rad) at 15° rotor angle shift

The full Simplorer model for the final combined improvements model is included in Appendix E. With the braking resistors, increased inertia, auxiliary inertias and coupling clutch included in the diesel engine generator set, LVRT performance is significantly improved.

8.2.1 Dynamic stress analysis for the improved LVRT performance generator set versus the standard generator set

The resulting keyway stress is analysed in the 3DFE model of the standard generator set and improved generator set when the grid is restored at a rotor shift angle of 15°. The maximum equivalent von Mises stress in each of the areas subjected to high stress is collected in Table 8.1. The measurement locations are the same as those shown in Figure 7.40. The stress contour plots are shown in Figure 8.33 to Figure 8.40.

Table 8.1: Peak equivalent stress and shear stress in the coupling key/keyway following reconnection at 15° rotor angle shift for the standard genset and the improved genset

Location	Standard genset maximum equivalent stress (Pa)	Improved genset maximum equivalent stress (Pa)
1	1.14e ⁹	7.56e ⁸
3	6.63e ⁹	9.67e ⁸
4	3.04e ⁹	6.87e ⁸
5 (corner)	1.41e ¹⁰	3.15e ⁹
7	5.27e ⁹	2.84e ⁹
9	2.31e ⁹	7.47e ⁸

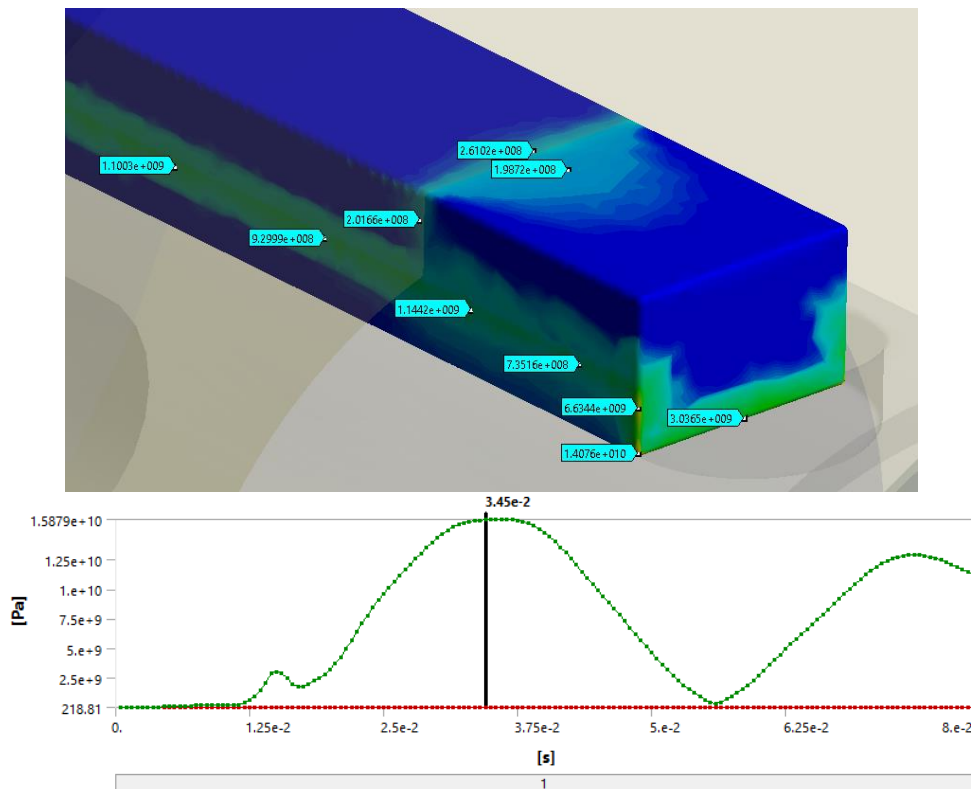


Figure 8.33: Maximum equivalent stress in standard genset key at 15° rotor angle shift

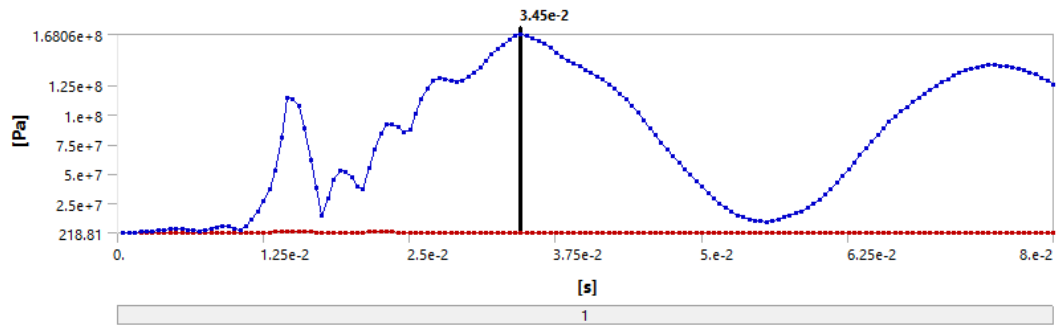


Figure 8.34: Average equivalent stress in standard genset key at 15° rotor angle shift

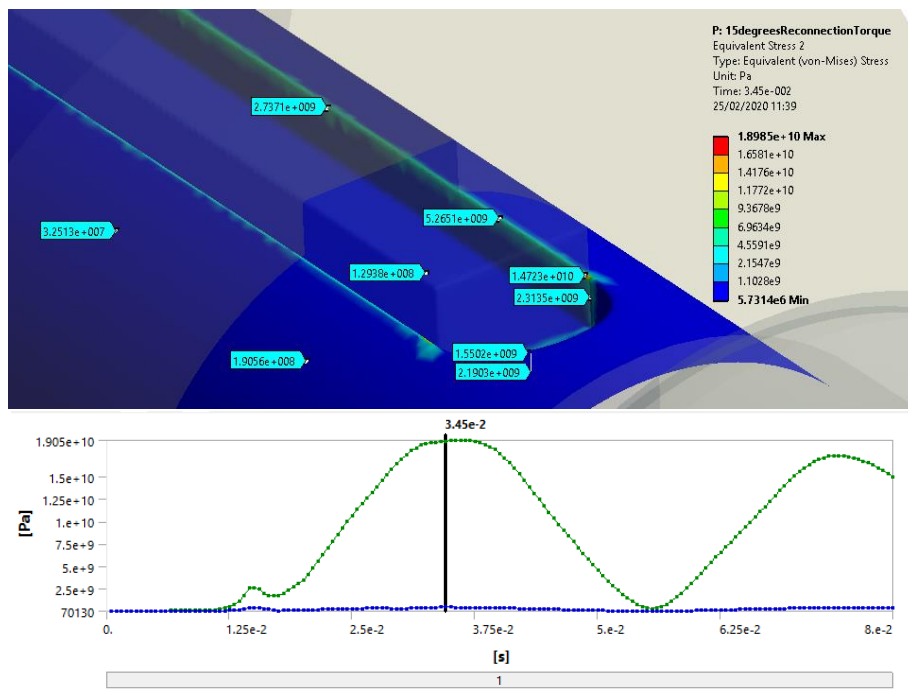


Figure 8.35: Maximum equivalent stress in standard genset keyway at 15° rotor angle shift

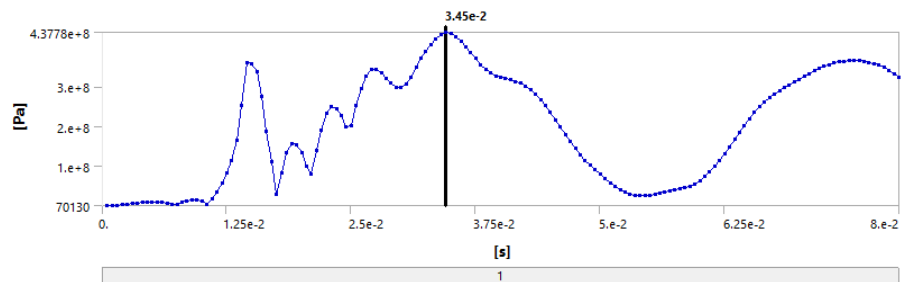


Figure 8.36: Average equivalent stress in standard genset keyway at 15° rotor angle shift

The 3DFE model of the standard generator set is modified to match the configuration of the improved generator set. The additional balancing inertia is added to the end of the generator shaft and the auxiliary inertias are added at the NDE of the generator and to the gearing inertia near the end of the engine. The coupling clutch stiffness is combined with the flexible coupling stiffness here, since the keyway supporting section is a separate element and not part of the flexible coupling stiffness element.

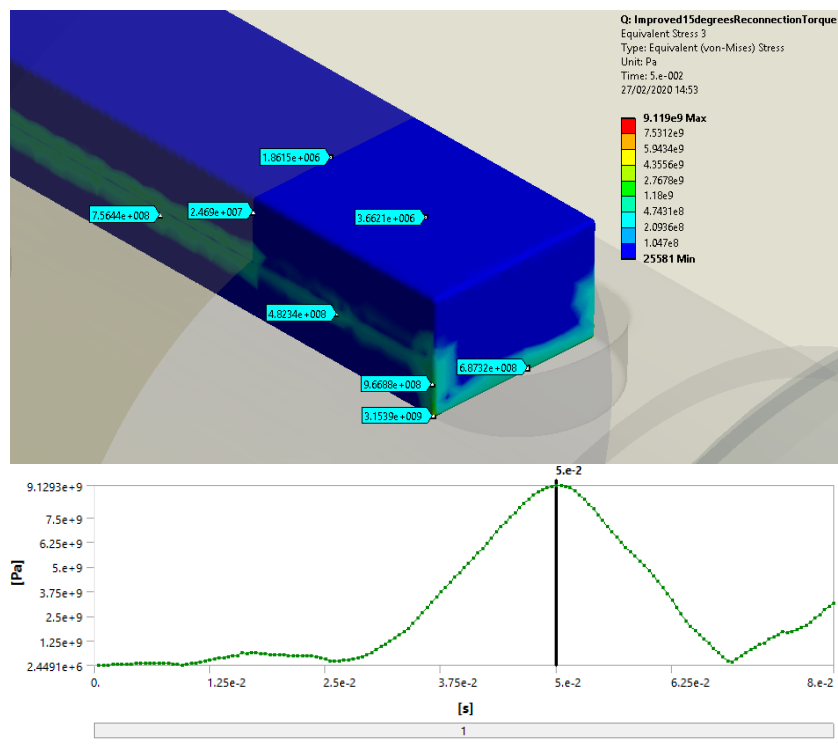


Figure 8.37: Maximum equivalent stress in improved genset key at 15° rotor angle shift

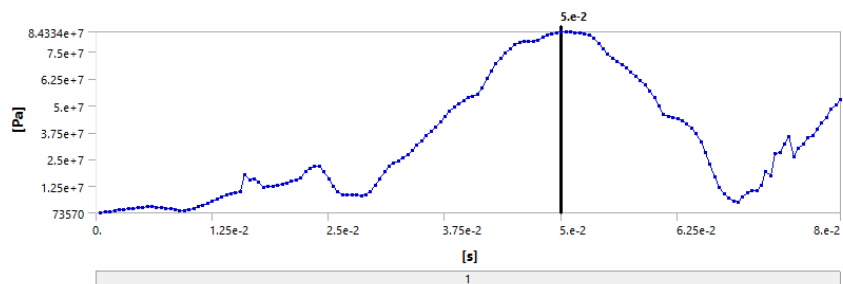


Figure 8.38: Average equivalent stress in improved genset key at 15° rotor angle shift

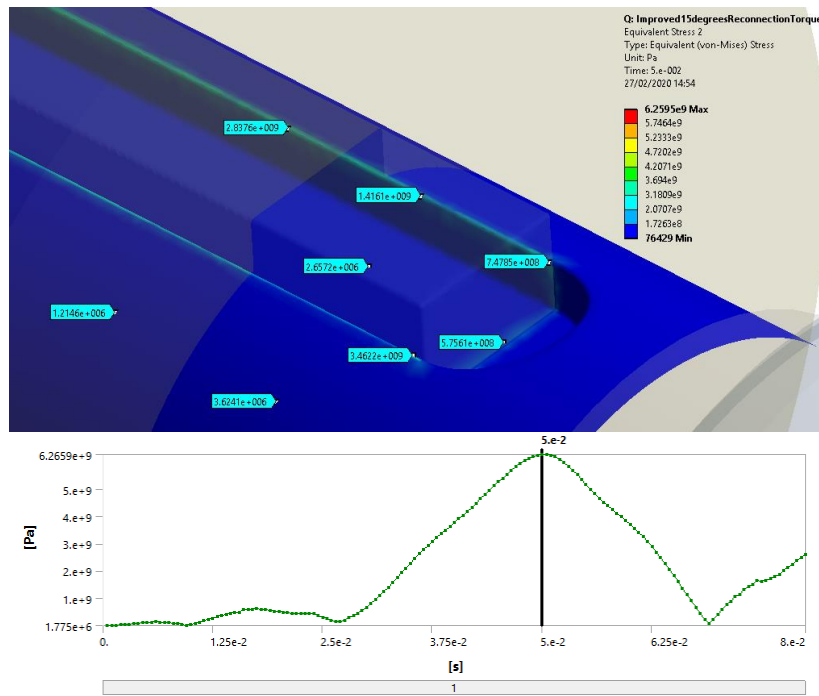


Figure 8.39: Maximum equivalent stress in improved genset keyway at 15° rotor angle shift

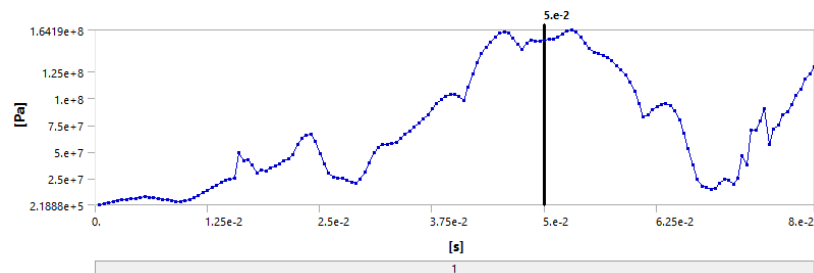


Figure 8.40: Average equivalent stress in improved genset keyway at 15° rotor angle shift

With reduced coupling torque applied to the keyway, the maximum equivalent stress across all surfaces is significantly reduced. The peak average stress for both the key and keyway is reduced below the yield strength of the shaft material, (EN8 steel) $2.80e^8$ Pa, although the maximum stress exceeds this in all measured areas. As the peak stress is localised to the contact edges between the key and keyways and considering the time period over which the stress exists above yield strength, there is little to suggest that any permanent deformation will occur over a single LVRT fault cycle for the improved

genset model. The peak average stress results for the standard model are much closer to the yield stress and even exceed it in the keyway, however the most telling feature is the maximum stress at the edges of the key in contact with the end edges of the coupling keyway. A peak stress of $2.02e^8$ Pa is measured at the vertical edge where the assembly is expected to yield in the event of coupling key failure. This peak stress is almost ten times greater than that measured in the same region of the improved genset, although it is still lower than the yield stress of the material. Given the high peak stress recorded elsewhere for the standard genset it is likely that the key and keyway will experience plastic deformation following a single LVRT fault cycle and highly likely that the crack formation will occur at the edges of the keyway over repeated LVRT events leading to low cycle fatigue failure.

When considering the flywheel torque results it is evident that the peak oscillatory torque, whilst lower than the maximum peak recorded for the standard genset configuration, is sustained over an extended period of time. The improved genset is subjected to several more torsional oscillation cycles that peak at -2 kNm or 5.5 pu, thus the potential for fatigue failure still exists as the peak stress exceeds the yield stress in several locations.

8.2.2 Additional design alterations

Additional stress reduction could easily be achieved by adding at least one additional keyway to the other side of the generator shaft in order to share the applied torque across the structure. Existing coupling configurations that utilise multiple keys or machined

locking surfaces may be more suitable under these conditions but would require additional cost justification.

8.2.3 Chapter 8 summary

In this chapter, the engine driven synchronous generator set model is modified to improve its fault ride through performance. This is achieved by implementing the suggested modifications discussed in the literature review (braking resistors, increased rotor inertia) as well as some new modifications (auxiliary inertia and coupling clutch components) considered specifically for this application. The modifications made to the model successfully reduce the peak current, electromagnetic torque, rotor speed associated with reconnecting to the grid following a LVRT event. The torque in the coupling, and therefore the stress on the keyway assembly is significantly reduced as a result.

The steps taken in this chapter are as follows:

- Firstly, the braking resistor modification is tested. The braking resistors are first introduced in parallel to the grid voltage supply with a resistance per phase of 0.5Ω . The resistors are switched in immediately following a voltage drop fault and significantly reduce the peak disconnection/reconnection stator currents.
- Immediately disconnecting the braking resistors at the point of grid reconnection is found to increase the peak stator current. The braking resistors are altered to operate in series with the grid supply (as the generator is required

to remain connected to the grid throughout LVRT) and the need to slowly ramping down the resistance following reconnection is highlighted.

- An increase to the coupling inertia is tested.
- The inertia of the generator is increased so that the ratio of inertias between the generator and prime mover is 1:1 and an addition 0.5 kgm² inertia is added to both machines. The coupling torque is greatly reduced.
- The 0.5 kgm² inertia elements are altered so that they are coupled to the generator and engine with variable torsional stiffness elements. They are then effectively disconnected from their machines following FRT to reduce the magnitude of torsional oscillations following grid reconnection.
- The coupling clutch modification is then tested to reduce the angular displacement that occurs during disconnection/reconnection and thus greatly reduce the peak coupling torque.
- All of the modifications are then combined into one final modified version of the multi-physics genset model and the current, torque, speed and key stress results are compared for the unmodified and modified multi-physics models.

The key points from this chapter as follows:

- The braking resistors greatly reduce the peak current, electromagnetic torque, coupling torque and rotor acceleration, at the cost of temporarily increased stator current following reconnection (and increased time to reach full synchronisation). This modification provides the best theoretical improvement to LVRT performance for the genset, though in practise such a solution requires advanced feed forward prediction of upcoming LVRT events.

- Increasing the inertia of the system, and more importantly, ensuring that the ratio of inertia between the two machines is as close to 1:1 as possible, provides a significant reduction in peak torque at the coupling and angular acceleration.
- In the absence of increased inertia, the coupling clutch significantly reduces the peak torque at the coupling during grid reconnection and is particularly effective when engaged mid-way through the FRT time period, allowing the system time to respond to the fault.
- The stress analysis reveals that the reduction in peak coupling torque results in a reduction in equivalent stress of almost 10 pu in the expected region of key failure.

The work completed here is used in the following chapters are as follows:

Further work is recommended in Chapter 9 to design and build a prototype of the flexible coupling clutch, auxiliary inertia components and investigate the implementation of braking resistors within the stator circuit of a physical test generator.

8.2.4 Chapter 8 contributions to the literature

The main contributions to the literature reviewed in section 1.3.5 are as follows:

- Performance improvements provided by the addition of braking resistors is explored in the literature review and analytical results from (19) demonstrate a significant reduction in fault current and rotor acceleration throughout the simulated LVRT period. The impact on the peak electromagnetic torque at the

point of grid reconnection is however not explored here. In this chapter the braking resistors were simulated, and the fault current and rotor acceleration did indeed drop in a similar manner. In addition, the electromagnetic torque was obtained here for comparison with the non-modified generator set model to demonstrate the relative reduction in the shaft/coupling stress that the genset experiences during grid reconnection. The results of this chapter show how the addition of braking resistors reduces the shaft/coupling stress significantly and how the mechanical response behaviour changes with the selection of resistance and engagement time of the braking resistors.

- The research also indicates that additional inertia added to the rotor could reduce the rotor acceleration during LVRT, but that a very large inertia would need to be added to the genset. In this chapter, the inertia of the generator and engine is increased to almost double its original value, with most of the inertia added to the end of the generator to increase its inertia to equal that of the engine. The torque at the coupling resulting from the applied LVRT is greatly reduced but the magnitude of torsional oscillations following reconnection is increased significantly. This chapter proposes that the additional inertia should have some element of control so that it can be disengaged following grid reconnection to allow the rotor speed to be corrected faster. The auxiliary inertia modification provides an additional contribution to the literature and demonstrates that any LVRT design solution looking to increase the rotor inertia should consider using the auxiliary inertia concept to prevent an increase in the post fault resynchronisation time.

Chapter 9 Conclusions

In this section an overview of the work completed in this thesis is provided which summarizes the key results from each chapter. A summary of the contributions to knowledge is also included and potential future work is outlined.

This thesis aims to address the problem of mechanical failure in grid connected synchronous generator sets subjected to low voltage faults by observing the electromechanical response to such faults and the resulting stress that occurs in the generator rotors and couplings. This work seeks to reduce the peak stress to extend the life of synchronous generator sets and ensure they are physically capable of meeting increasingly demanding grid code requirements.

For the first part of this aim, the work completed here seeks to obtain simulated torque, speed and stress results for a multi-physics generator set model subjected to several 100% voltage drop faults. This is done to determine the likelihood of reconnection at a relative angular position that produces the peak fault torque and to obtain the resulting maximum stress in the genset rotors. For the second part of this aim, the work seeks to incorporate new and existing modifications to the generator set model to improve its LVRT performance and reduce the peak torque and the maximum stress in the generator set.

9.1 Overview of Work

A 72.5 kVA, four pole synchronous generator (UC22F) was selected, and modal testing and analysis was performed to obtain the stiffness properties of the rotor core in Chapter 3. The rotor core stiffness properties were found to be reduced to the following: $E_{zz} = 1.5e^{11}$ and $G_{yz}/G_{xz} = 1.56e^{10}$. The parametric mode matching technique applied here proved capable of obtaining the first 8 modes, including torsional modes, within an average margin of error of 1.3% between the analytically and experimentally obtained modal frequencies. The corrected stiffness properties are used to obtain the torsional stiffness values for the generator rotor for use in the 1D torsional model of the generator sets in Chapter 5 and beyond.

The electromagnetic model of the generator set is built in Chapter 4 and the steady state results are compared with those obtained from the test machine to validate the model. A close match between the steady state voltage, current and torque results is obtained. The electromagnetic model is combined with a 1D torsional model of the test generator set and a diesel generator set in Chapter 5. Three-phase short circuit tests are performed on the test machine and simulated using the electro-mechanical (multi-physics) model. Fault current, torque and speed results are closely matched in the model, validating it for use in 100% voltage drop LVRT simulations in Chapter 6.

In Chapter 6, a range of different LVRT simulations are performed which ultimately lead to the characterisation of the relationship between relative rotor angle at the point of grid reconnection and peak electromagnetic torque in the generator. The electromagnetic torque is found to follow a sinusoidal curve and peak 5 times over a

relative angular shift range of 360° . The maximum peak torque achieved in this analysis is 6.02 kNm or 16.5 pu of the steady state torque at a relative shift angle of 360° .

In Chapter 7, stress analysis is performed using the electromagnetic and prime mover torque curves obtained for the 140 ms FRT simulation performed in Chapter 6 on the case study model. A peak stress is obtained of over 700 MPa, far exceeding the yield strength of the shaft material, confirming that a reconnection at a peak relative rotor angle will likely damage or destroy the generator shaft.

In the final combined model that includes all the modifications made in Chapter 8, the peak stator phase currents at the beginning of the low voltage fault and at the point of reconnection are reduced by 539 A (50.2%) and 1290 A (73.8%) respectively. The peak electromagnetic torque is reduced by 0.88 kNm (32.2%) and 4.17 kNm (73.8%) respectively. Ultimately, the peak stress in the generator shaft keyway is reduced by 77.4%.

9.2 Contributions to knowledge

The three main contributions to knowledge produced in this thesis are listed below, further details are provided in Section 9.2.1, 9.2.2 and 9.2.3.

1. Determination of the relationship between the relative angular position of the rotor and stator fields and the magnitude of peak fault electromagnetic torque at the point of grid reconnection.
2. Simulation of combined generator modifications for the reduction of LVRT fault severity.

3. Parametric modal analysis of a generator rotor for the determination of the orthotropic elastic properties of a laminated core and correction of modal frequencies.

9.2.1 Contribution 1: Relationship between the relative angular position and fault torque for a synchronous generator during a LVRT fault.

This research action addresses a gap in the knowledge regarding LVRT for engine driven, grid connected generator sets in which the precise rotor angle at the point of grid reconnection is not considered in existing simulations. Twenty-five low voltage fault simulations were performed using the multi-physics model of an engine driven generator set to determine the relationship between the electromagnetic torque following FRT and the relative angular position of the rotor. The grid voltage was restored at intervals of 15° angular shift between the magnetic field of the rotor and the stator. It was found that the maximum peak electromagnetic torque occurred at relative angular positions of 15° , 195° and 360° , repeating every 180° and increasing in magnitude as the fault ride through time is extended. Similarly, the minimum peak electromagnetic torque occurs at 45° , 135° , 225° and 315° , repeating every 90° . The magnitude of peak electromagnetic torque also increases with FRT time. The conclusion of this observation is vital for future LVRT simulations as it indicates that the peak electromagnetic torque that the generator set is subjected to can vary by as much as 3.64 kNm or 60.5% of the maximum torque observed (for just the first 360° shift in relative angular position) depending on the relative angular displacement of the rotor at the point of fault clearance. This highlights the need to analyse the electromagnetic torque at the point of grid reconnection over at least 180° shift in rotor

angle for any four-pole synchronous generator if the maximum possible fault torque is to be determined. Generator sets are typically simulated for specific FRT times, when in practise, reconnection can occur at any point in time between the initial loss of voltage and the rated FRT time, thus a single LVRT test or analysis is not enough to determine the maximum possible fault torque. The full details of the observations made for this behaviour can be found in section 6.4.

9.2.2 Contribution 2: Modifications to improve LVRT performance.

The work carried out in Chapter 8 advances the research into improving the fault ride through capability of grid connected generator sets outlined in section 1.3.5 by implementing the suggested potential solutions in the multi-physics generator set model to gauge how effective they are in reducing the peak torque, current, rotor acceleration and structural stress in the generator rotor. The existing research highlights two main solutions, braking resistors (and similar in-rush current protection schemes) and increased rotor inertia. The following modifications to the generator set model are analysed; an increase in the engine and generator rotor inertia and the addition of coupled auxiliary inertias (8.1.4), the addition of variable braking resistors (8.1.1) and the addition of a coupling clutch (8.1.5).

An analytical solution to the chosen 'worst-case' low voltage fault scenario was developed, combining modifications that do not alter the electro-mechanical performance of the machine under normal steady state operating conditions but does substantially improve transient performance during disconnection and reconnection to the grid.

The braking resistors have the greatest impact on fault ride through performance as they target the root of the problem, elevated stator currents. Rather than modifying the generator to alter its synchronous reactance or oversize the machine, an external bank of resistors can be used to effectively increase the circuit resistance during fault ride through. In the final combined modifications model, the peak stator phase current at grid disconnection and reconnection is reduced by 539 A (50.2%) and 1290 A (73.8%) respectively. The electromagnetic torque drops correspondingly by 0.88 kNm (32.2%) and 4.17 kNm (73.8%) respectively. The braking resistance is reduced from 0.5 Ω to 0 Ω over 100 ms following grid reconnection, whilst this prevents any additional high current peaks from appearing as a result of a sudden load change during resynchronisation, it also sustains an elevated stator current and electromagnetic torque following grid reconnection.

The time period over which the resistance falls may be reduced at the expense of increased reconnection current and electromagnetic torque if using the same linear ramp behaviour. Alternatively, the rate of change of resistance could be determined by the stator current with additional power electronics control systems thus only maintaining elevated braking resistance during the sub-transient peak current period. Note that the braking resistance is below that required to maintain full load in the generator following the 100% voltage drop, if the maximum resistance is increased until the resistive load is equal to the full load then the minimum peak stator current will be produced on grid disconnection/reconnection.

The coupling clutch does not greatly impact the rotor speed during disconnection and reconnection events aside from reducing the magnitude of torsional oscillations and

slightly reducing the peak rotor speed. The clutch does however significantly reduce the amplitude of the peak torque measured at the flywheel by 5.59 kNm (62.1% reduction) when applied as the only rotor modification. Whilst the flexible coupling does remain connected when the clutch is engaged (when shaft torque exceeds 600 Nm), its average torsional stiffness of 250 kNm is but a small fraction of the 2 MNm possessed by the clutch thus the torque is largely transferred through the clutch. The important outcome is that the torque applied to the generator shaft and keyway is reduced and therefore the resulting stress in these areas is reduced. In practise such a device would need to be positioned to surround the flexible coupling or alternatively be incorporated into the design of the coupling, although this would require extensive redesign of the coupling.

The additional inertia added to the non-drive end of the generator achieves the 1:1 ratio of generator and prime mover inertias that is required to minimise the peak shaft torque during LVRT. When combined with the additional auxiliary inertias, these modifications alone are capable of reducing the peak rotor speed by 6.5 rad/s, effectively almost doubling the maximum allowable fault ride through time. The peak coupling torque is also reduced by 4.8 kNm (60% reduction). If the auxiliary inertias are permanently connected to the system, the increased inertia results in an increased time to resynchronisation and an increase in the magnitude of torsional oscillations. These inertias are instead connected to the generator set shafts with torsional stiffness elements in a similar fashion to the coupling clutch, allowing the inertias to be disconnected from the system following grid reconnection.

With all three modifications combined, the peak stator current, electromagnetic torque, coupling/shaft torque and rotor speed are all greatly reduced. The equivalent stress in the keyway is reduced accordingly as shown in the stress analysis results in section 8.2.1.

9.2.3 Contribution 3: Parametric modal analysis method for laminated rotors

Research on the dynamic analysis of electrical machine rotors immediately highlighted the need to determine the correct elastic properties of the main rotor core. The research covered in Section 1.3.3 indicated that it was possible to use modal analysis results from a 3D model of the rotor core to obtain its elastic properties if the modal frequencies and shapes matched those obtained from experimental modal analysis of the real rotor core. A parametric analysis was performed with several hundred possible combinations of Young's modulus and shear modulus and the solution with the smallest margin of error between all modal frequencies and the experimentally obtained frequencies was obtained. The method applied here proved capable of obtaining the first 8 modes, including torsional modes, within an average margin of error of 1.3%. This contributes to the existing research by validating that the parametric modal analysis method can be used to correct the modal frequencies and shapes of a complete 3DFE synchronous generator rotor model to within a small margin of error. This method reduces the need for building equivalent models and can instead be used directly with detailed geometries. Full details of the analysis that lead to this conclusion can be found in Chapter 3.

9.3 Future work

Future work that can directly build off the work completed in this thesis, as well as potential areas of future work are identified in this section.

9.3.1 Direct future work

- Run the multi-physics model with different sized generators, particularly larger synchronous generators.

The 1D torsional model and the electromagnetic model can be replaced with that of any other electrical machine provided the geometry and mass properties are known. It would be of significant interest to analyse a wide range of synchronous generators and determine the fault ride through performance of each to better understand the relationship between generator size and FRT performance.

- Test the parametric modal analysis method on different rotor geometries and measure the error associated with each.

The parametric modal analysis method was effective in obtaining closely matching modal frequencies and shapes for both the UC22F and UC22G rotor geometries. How effective the method would be for different rotor geometries is unknown and should be validated.

- Experimental testing of the braking resistors.

The addition of braking resistors to the generator circuit would be a simple experiment and could be done with a grid connected LVRT test on a diesel engine generator set if the facilities are available or can be tested using a controlled three-phase short circuit test. If a control circuit for adjusting the braking resistance both during and after the fault is designed and included in the test, the impact on LVRT performance can be fully validated.

- Experimental testing of various levels of voltage drop and FRT time using a diesel engine generator.

Experimental validation of the multi-physics generator model set should be performed using a real diesel engine as the prime mover. Applying a range of different LVRT faults (different voltage drop curves, gradual recovery in voltage/frequency etc.) to this genset would enable a wider range of grid fault conditions to be considered other than a 100% voltage drop with immediate grid recovery. For each different LVRT fault, the full range of current, torque and speed results can be predicted using the multi-physics model and compared with the experimental result. With this additional model validation complete it would be possible to make life estimates for the genset based on the average frequency and severity of LVRT faults.

9.3.2 Potential future work

- LVRT performance with magnetic couplings

It would be of scientific interest to characterise the LVRT performance of a genset with magnetic couplings. Magnetic couplings can eliminate high torque transients between machines as the rotors will slip when their peak torque capacity is exceeded but return

to a coupled state once the load torque has dropped back to normal. Permanent magnet couplings are being increasingly used for torque transmission between high power machines, proving one for use under severe LVRT fault conditions would be a valuable scientific contribution.

- Design and testing of the auxiliary inertia and coupling clutch devices to prove the concept with experimental testing.

The auxiliary inertia concept can reduce rotor acceleration during LVRT and automatically disconnect once the voltage is restored to prevent an increase in the resynchronisation time. The device requires additional couplings and a control system to be developed to test how effective the physical device could be taking into account limitations in response speed. The coupling clutch device concept could also be designed and tested for use with flexible couplings to reduce the severity of the electromagnetic torque transient. If such a device were to be manufactured as part of a new flexible coupling design, the benefits of a flexible coupling could be retained without the excessive angular displacement that occurs during very high torque transients.

9.3.3 Concluding remarks

As discussed in Chapter 2, the research problem that is addressed in this thesis is the existence of increasingly demanding grid code regulations that require generator sets to remain connected during LVRT faults and maintain longer FRT times with greater drops in voltage. The main objective of the research was to model the electromechanical

response behaviour of a synchronous generator set subjected to LVRT faults and address the problem of the resulting mechanical failures.

The aim of this work was to improve understanding of the impact of LVRT faults on grid connected synchronous generators, particularly the transient mechanical responses of rotor acceleration, torque and rotor angular position, in order to determine the stress that the rotors and couplings are subjected to. To address the problem of mechanical damage to the system, the research also aimed to develop modifications to the generator to reduce LVRT fault severity and extend the life of new and existing generator sets.

The first main research outcome was the creation and validation of a multi-physics model of a diesel engine driven synchronous generator set which was used to determine the most severe LVRT fault. The resulting stress on the generator shaft keyways due to this magnitude of fault significantly exceeded the yield stress of the steel. This confirmed the possibility of a catastrophic failure in an unprotected generator set subjected to severe LVRT faults and also highlighted the importance of the relationship between the relative angular position of the generator rotor at the point of grid reconnection and the chance of rotor failure. It was found that the peak electromagnetic torque varied significantly depending on the relative angular position of the generator rotor which could easily mislead any conclusions made about the severity of the fault (i.e. stress in the machine couplings, peak current in the windings) from a LVRT test.

The second research outcome was a performance analysis of three conceptual devices, auxiliary inertias, internal braking resistors and a flexible coupling clutch, the first two of which build on existing research into reducing the impact of electrical faults in

generators. The third device was conceived in response to the observation made during the LVRT testing phase of the multi-physics model where a flexible coupling was found to dramatically increase the peak electromagnetic fault torque. The improvement to LVRT performance that is achieved using ideal versions of these devices on an otherwise unprotected generator is promising. Although real generator sets will rarely, if ever, be subjected to the worst-case magnitude faults simulated here since they are connected to the grid through additional electrical components that contain fault protection systems, the device concepts explored here will certainly increase the maximum FRT period for synchronous generators.

The suggested further work notes potential actions to be taken to build on the research conducted here. With the theme of implementing the LVRT performance improving devices and exploring the practicality and relative impact of other special devices such as magnetic couplings. As the complexity of electricity grids and the proportion of distributed electricity generation continues to increase, the chance of grid disruptions and the demand on grid connected generators grows too. Without relying on widespread adoption of energy storage or smart power distribution systems to plug the gap, it is vital that grid connected standby generators stay ahead of minimum fault ride through requirements around the world to maintain grid stability. Multi-physics modelling of generator sets enables the development of both electrical and mechanical design modifications/enhancements and will play a key part in the future development of synchronous generators that will enable them to stay ahead of future design demands.

References

1. Mudau T, Murray Field R. Rotordynamic Analysis of the AM600 TurbineGenerator Shaftline. *Energies*. 2018;11(12):3411.
2. Bellamy RA, Jonson CP, Gaffney R. Developing Concepts in the Rotordynamic Analysis of Aero Gas Turbines. ASME 1985 International Gas Turbine Conference and Exhibit. 1985;4:V004T13A014.
3. Rao JS, Sreenivas R. Dynamics of Asymmetric Rotors using Solid Models. In: International Gas Turbine Congress. Funabori, Tokyo, Japan; 2003.
4. Ma WM, Wang JJ. 3D Solid Finite Element Modeling and Rotordynamics of Large Rotating Machines: Application to an Industrial Turbo Engine. *Advanced Materials Research*. 2012;591–593:1879–85.
5. Jalali MH, Ghayour M, Ziaei-Rad S, Shahriari B. Dynamic analysis of a high speed rotor-bearing system. *Measurement*. 2014;53:1–9.
6. Cao H, Niu L, Xi S, Chen X. Mechanical model development of rolling bearing-rotor systems: A review. *Mechanical Systems and Signal Processing*. 2018 Mar;102:37–58.
7. Garvey SD, Penny JET, Friswell MI, Lees AW. The Stiffening Effect of Laminated Rotor Cores on Flexible-Rotor Electrical Machines. In: 8th International Conference on Vibrations in Rotating Machinery. Swansea, UK; 2004. p. 193–202.
8. LV. Santos H, A. Luerson M, A. Bavastri C. Experimental Evaluation of Numerical Models to Represent the Stiffness of Laminated Rotor Cores in Electrical Machines. *Journal of Engineering Science and Technology*. 2013;8:457–71.
9. Kim Y-C, Kim K-W. Influence of Lamination Pressure upon the Stiffness of Laminated Rotor. *JSME International Journal Series C*. 2006;49(2):426–31.
10. Garvey SD. The Vibrational Behaviour of Laminated Components in Electrical Machines. In: 1989 Fourth International Conference on Electrical Machines and Drives. London, UK; 1989. p. 226–31.
11. Chen S-Y, Kung C, Liao T-T, Chen Y-H. Dynamic Effects of the Interference Fit of Motor Rotor on the Stiffness of a High Speed Rotating Shaft. *Transactions of the Canadian Society for Mechanical Engineering*. 2010;34(2):243–61.
12. Chen S-Y. An equivalent direct modeling of a rotary shaft with hot-fit components using contact element modal analysis results. *Computers & Mathematics with Applications*. 2012;64(5):1093–9.

13. Michaelides A, Brown NL. CyberGen: modelling the design challenges for small embedded synchronous generators connected to increasingly unstable networks. In: 5th IET International Conference on Power Electronics, Machines and Drives (PEMD 2010). Brighton, UK: Institution of Engineering and Technology; 2010. p. 435–435.
14. Brown NL, Mebarki A, Narayanan S. Low voltage ride through performance of a 4MVA synchronous generator – measurements and simulations. In: 7th IET International Conference on Power Electronics, Machines and Drives (PEMD 2014). Manchester, UK: Institution of Engineering and Technology; 2014. p. 497.
15. Östman M, Wägar N, Ristolainen I, Klimstra J. The impact of grid dynamics on low voltage ride through capabilities of generators. In: PowerGrid Europe 2010. Amsterdam, Netherlands; 2010.
16. Ristolainen I, Simolin J, Wägar N, Östman M. Considerations for Fault Ride Through Simulation and Testing. In: PowerGrid Europe 2015. Amsterdam, Netherlands; 2015.
17. Abed NY, Kabsha MM, Abdlsalam GM. Low Voltage Ride-Through Protection Techniques for DFIG Wind Generator. In: 2013 IEEE Power & Energy Society General Meeting. Vancouver, BC: IEEE; 2013. p. 1–6.
18. Shicong Y, Shagar GV, Ukil A, Jayasinghe SDG, Gupta AK. Evaluation of Low Voltage Ride-Through capability of synchronous generator connected to a grid. In: 2015 IEEE Power & Energy Society General Meeting. Denver, CO, USA: IEEE; 2015. p. 1–5.
19. Essl N. Dynamic Behavior of Synchronous Machines Relating to LVRT Requirements [Internet] [Doctoral Thesis]. Graz University of Technology; 2016. Available from: <https://diglib.tugraz.at/download.php?id=58e2caa9c1f54&location=browse>
20. Johal H, Konopinski R, Skliutas J, Eitzmann M, Leonard D. Solutions to Improve Grid Code Compliance of Synchronous Generation. In: 2014 Grid of the Future Symposium. Houston, Texas, USA; 2014.
21. Ulbig A, Borsche TS, Andersson G. Impact of Low Rotational Inertia on Power System Stability and Operation. IFAC Proceedings Volumes. 2014;47(3):7290–7.
22. Narayanan S, Berridge G, Biebighaeuser A, Brown NL. Fault Ride through Effects on Alternators Connected to the Grid. [Internet]. Cummins Generator Technologies; 2012 [cited 2020 Mar 4]. Available from: http://www.gridcodegenerators.com/library/LVRT_Grid_White_Paper_EN_LR.pdf
23. Le X, Le Z. Stress concentration factors due to typical geometric discontinuities for shaft design by numerical simulation. In ASEE Conferences; 2013 [cited

2021 Apr 28]. p. 23.1091.1-23.1091.16. Available from:
<http://peer.asee.org/22476>

24. Hearn EJ. Contact Stress, Residual Stress and Stress Concentrations. In: *Mechanics of Materials 2* [Internet]. Elsevier; 1997 [cited 2021 Apr 28]. p. 381–442. Available from:
<https://linkinghub.elsevier.com/retrieve/pii/B9780750632669500111>
25. Wenske J, Beckert U. Voltage-induced stresses during Low Voltage Ride Through (LVRT) in the drive train of wind turbines with DFIG. In: *International Conference on Renewable Energies and Power Quality*. Santiago de Compostela, Spain; 2012.
26. Jiang DX, Hong LY, Huang Q. Shaft Crack Analysis and Diagnosis for the 600MW Steam Turbine. *Key Engineering Materials*. 2009;413–414:591–8.
27. Pillai R, Narayanan S, Swindale G. Benefits and challenges of a grid coupled wound rotor synchronous generator in a wind turbine application [Internet]. Cummins Generator Technologies; 2012 [cited 2020 Mar 4]. Available from:
https://www.stamford-avk.com/sites/stamfordavk/files/2019-03/WP_WIND_S_EN_GS_01_0.pdf
28. Fogarty JM. Connections between generator specifications and fundamental design principles. In: *IEEE International Electric Machines and Drives Conference*. Cambridge, MA, USA: IEEE; 2001. p. 51–6.
29. Ruester C, Hoppert S, Blum J. Power Quality and Stability Issues in Modern Distribution Grids: Identification and Mitigation. In: *Challenges of Implementing Active Distribution System Management*. Rome, Italy: Cired; 2014.
30. Popovic D, Wallace I. International Review of Fault Ride Through for Conventional Generators [Internet]. EirGrid; 2010 [cited 2020 Mar 4]. Available from: http://www.eirgridgroup.com/site-files/library/EirGrid/MPID215_FRT_KEMA_Report_16010829.pdf
31. Fault Ride Through [Internet]. National Grid; 2016 [cited 2020 Mar 4]. Available from:
<https://www.nationalgrid.com/sites/default/files/documents/8589935658-Report%20to%20the%20Authority%20v2.pdf>
32. Establishing a network code on requirements for grid connection of generators. [Internet]. European Commission; 2015 [cited 2020 Mar 4]. Available from:
https://ec.europa.eu/energy/sites/ener/files/documents/RfG_100615.pdf
33. Mohseni M, Masoum M, Islam S. Low voltage ride-through of DFIG wind turbines complying with Western-Power grid code in Australia. In: *IEEE Power and Energy Society General Meeting*. Detroit, MI, USA: IEEE; 2011. p. 1–8.
34. Grid Code Short Circuit Ratio requirement in respect of Very Large Synchronous Generating Units. [Internet]. National Grid; 2009 [cited 2020 Mar 4]. Available from:

<https://www.nationalgrid.com/sites/default/files/documents/15380-Short%20Circuit%20Ratio.pdf>

35. Stephan CE, Baba Z. Specifying a turbogenerator's electrical parameters guided by standards and grid codes. In: IEEE International Electric Machines and Drives Conference. Cambridge, MA, USA: IEEE; 2001. p. 63–8.
36. An explanation of the origin of a generator's subtransient reactance. [Internet]. The Nuclear Electrical Engineer. 2014 [cited 2020 Mar 4]. Available from: <http://www.nuclearelectricalengineer.com/explanation-origin-generators-subtransient-reactance/>
37. HCI 434F/444F – Winding 311 Technical Data Sheet [Internet]. Cummins Generator Technologies; Available from: http://stamford-avk.com/sites/default/files/literature/all/HCI4F-311-TD-EN_Rev_A.pdf
38. Grid Code Ready Alternators. Available from: http://news.stamford-avk.com/wp-content/uploads/2015/05/Grid-Code-Ready-Alternators_EN_LR_Rev-3.0.pdf
39. RC Snubbers (SMPS). [Internet]. Illinois Capacitors; [cited 2020 Mar 4]. Available from: http://www.illinoiscapacitor.com/pdf/papers/rc_snubber.pdf
40. Patel D, Baker DE. Synchronous Generating Machine With Rectifier Snubber Circuit. US 8450892 B2.
41. Narayanan S. Critical parameters of a synchronous alternator for a grid code compliant generating set [Internet]. Cummins Generator Technologies; 2012 [cited 2020 Mar 4]. Available from: https://www.amps.org.uk/sites/default/files/uploads/Grid_Code_Compliance_White_Paper_LR.pdf
42. Moore B, Maughan C. Generator Stator End Winding Resonance: Problems and Solutions. In: Volume 1: Fuels and Combustion, Material Handling, Emissions; Steam Generators; Heat Exchangers and Cooling Systems; Turbines, Generators and Auxiliaries; Plant Operations and Maintenance [Internet]. Boston, Massachusetts, USA: American Society of Mechanical Engineers; 2013 [cited 2020 Mar 4]. p. V001T04A010. Available from: <https://asmedigitalcollection.asme.org/POWER/proceedings/POWER2013/56055/Boston,%20Massachusetts,%20USA/279207>
43. Stone G, Boulter EA, Culbert I, Dhirani H. Off-line Rotor and Stator Winding Tests. In: Electrical Insulation for Rotating Machines. 1st ed. Hoboken, NJ, USA: John Wiley & Sons, Inc.; 2004. p. 235–83.
44. How damper windings provide smooth starting to synchronous machines. [Internet]. Electrical Blog. [cited 2020 Mar 4]. Available from: <http://eblogbd.com/what-is-damper-winding/>
45. Nuzzo S, Degano M, Galea M, Gerada C, Gerada D, Brown NL. Improved Damper Cage Design for Salient-Pole Synchronous Generators. IEEE Transactions on Industrial Electronics. 2017;64(3):1958–70.

46. Synchronous Machine Armature Winding. [Internet]. Electric machines. [cited 2020 Mar 4]. Available from:
https://people.ucalgary.ca/~aknigh/electrical_machines/synchronous/s_armature.html
47. Stand Alone Phasor Diagrams. [Internet]. Electric machines. [cited 2020 Mar 4]. Available from:
https://people.ucalgary.ca/~aknigh/electrical_machines/synchronous/sg_standalone.html
48. Wagner MB, Younan A, Allaire P, Cogill R. Model Reduction Methods for Rotor Dynamic Analysis: A Survey and Review. *International Journal of Rotating Machinery*. 2010;1–17.
49. EDG Vibrations and Mitigation [Internet]. Energiforsk; [cited 2020 Mar 4]. Available from:
https://energiforskmedia.blob.core.windows.net/media/21641/lindholm_edg.pdf
50. Causes of an Unbalanced Rotor [Internet]. Unbalance - The Common Cause of Vibration & Premature Bearing Destruction within Rotating Machinery Equipment. 2017 [cited 2020 Mar 4]. Available from:
http://www.irdbalancing.com/unbalance---cause-of-vibration.html#causes_of_an_unbalanced_rotor
51. Whirl Speed and Stability Results [Internet]. 2017 [cited 2020 Mar 4]. Available from: <https://dyrobes.com/help1800/Rotor/html/dyro4a0d.htm>
52. Rao JS. Transient Forward and Backward Whirl of Beam and Solid Rotors With Stiffening and Softening Effects. In: *23rd Biennial Conference on Mechanical Vibration and Noise*. Washington, DC, USA: ASMEDC; p. 911–20.
53. Effects of Spin Softening and Stress Stiffening [Internet]. Spin Softening. [cited 2020 Mar 4]. Available from:
http://www.mm.bme.hu/~gyebro/files/ans_help_v182/ans_thry/thy_geo4.html
54. Swanson E, Powell CD, Weissman S. A Practical Review of Rotating Machinery Critical Speeds and Modes. *Sound and Vibration*. 2005;39:10–7.
55. Brown RN. Torsional Damping - Transient and Steady State. In: *Proceedings of the Thirteenth Turbomachinery Symposium* [Internet]. Texas USA: Texas A & M Univ. Press; 1984. Available from:
<https://oaktrust.library.tamu.edu/bitstream/handle/1969.1/163659/T13203-208.pdf?sequence=1&isAllowed=y>
56. Options for Attaching Rotor to Shaft (Electric Motors) [Internet]. What-when-how. [cited 2020 Mar 4]. Available from: <http://what-when-how.com/electric-motors/options-for-attaching-rotor-to-shaft-electric-motors/>
57. Marscher WD, Boyadjis PA, Gamarra JD, Gruener JO. Effect of Component Interference Fit and Fluid Density on the Lateral and Torsional Natural Frequencies of Pump and Turbomachinery Rotor Systems. In: *Proceedings of the Twenty-Ninth Pump Symposium* [Internet]. Houston, Texas, USA; 2013

- [cited 2020 Mar 4]. Available from:
<https://pdfs.semanticscholar.org/cfea/01df8b23c2fad4b7af1fbd75ce64975acfe1.pdf>
58. H. Kloutsey AE, Diniz ACGC, Viana Serra Villa C. Finite Element Model Updating of a Rotor-Generator Unit. In: Proceedings of COBEM 2007 [Internet]. Brazil: AVCM; 2007. Available from:
<http://www.abcm.org.br/anais/cobem/2007/pdf/COBEM2007-1810.pdf>
 59. Introduction to Finite Element Analysis (FEA) or Finite Element Method (FEM) [Internet]. [cited 2020 Mar 4]. Available from:
https://www.engr.uvic.ca/~mech410/lectures/FEA_Theory.pdf
 60. COMBIN14 Spring-Damper [Internet]. [cited 2020 Mar 4]. Available from:
http://mechanika2.fs.cvut.cz/old/pme/examples/ansys55/html/elem_55/chapter4/ES4-14.htm
 61. COMBI214 2-D Spring Damper Bearing [Internet]. [cited 2020 Mar 4]. Available from:
http://www.mm.bme.hu/~gyebro/files/ans_help_v182/ans_elem/Hlp_E_COMBI214.html
 62. Wu JS, Chen CH. Torsional Vibration Analysis of Gear-Branched Systems by Finite Element Method. *Journal of Sound and Vibration*. 2001;240(1):159–82.
 63. Ramirez-Nino J, Pascacio S A. Novel Method for Stator Core Interlamination Short-circuits Detector Based on Eddy-current Losses Measurement in Power Generators. *IEEE Computer Applications in Power*. 2001;14(4):39–42.
 64. ANSYS Maxwell V16 Training Manual [Internet]. ANSYS; Available from:
http://ansoft-maxwell.narod.ru/en/Maxwell_v16_L05_Transient_Solvers.pdf
 65. Hosain ML, Fdhila RB, Rönnerberg K. Air-gap Flow and Thermal Analysis of Rotating Machines using CFD. *Energy Procedia*. 2017;105:5153–9.
 66. Fault Currents and Short Circuit Decrement Curves [Internet]. Cummins Generator Technologies; [cited 2020 Mar 4]. Available from:
https://www.stamford-avk.com/stamford-avk/sites/stamfordavk/files/AGN005_D.pdf
 67. GC0062 – Fault Ride Through [Internet]. National Grid; [cited 2020 Mar 4]. Available from: <https://www.nationalgrideso.com/document/13246/download>
 68. Johnson A. Fault Ride Through. RfG - Compliance [Internet]. National Grid; [cited 2020 Mar 4]. Available from:
<https://www.nationalgrideso.com/document/13361/download>
 69. HTB-GS, DCB-GS and RB Superior Coupling Technology. Hi-Tec Generator and Pump Set Couplings [Internet]. HTB; Available from:
https://www.renold.com/media/162089/htb_gs_dcb_gs_rb_new.pdf

70. Keller J, Kroposki B. Understanding Fault Characteristics of Inverter-Based Distributed Energy Resources [Internet]. National Renewable Energy Laboratory; 2010 [cited 2020 Mar 4]. Available from: <https://www.semanticscholar.org/paper/Understanding-Fault-Characteristics-of-Distributed-Keller-Kroposki/b34bb1df4ffbc09e67af62b22da26195e5c5d220>

Appendix A: Raw frequency analyser results for UC22F/G rotors

The imaginary frequency response plots for the UC22F and disassembled UC22G rotors are included here. These plots are used to determine the direction and relative magnitude of displacement at each impact point along the rotor.

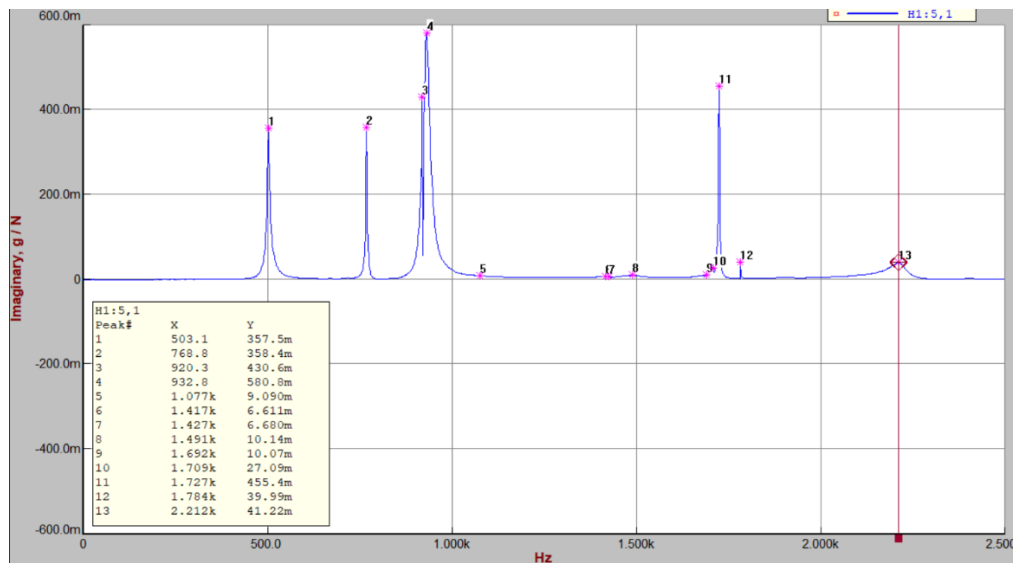


Figure A.1: FRF plot for UC22F rotor. Lateral modes measured at impact point 2

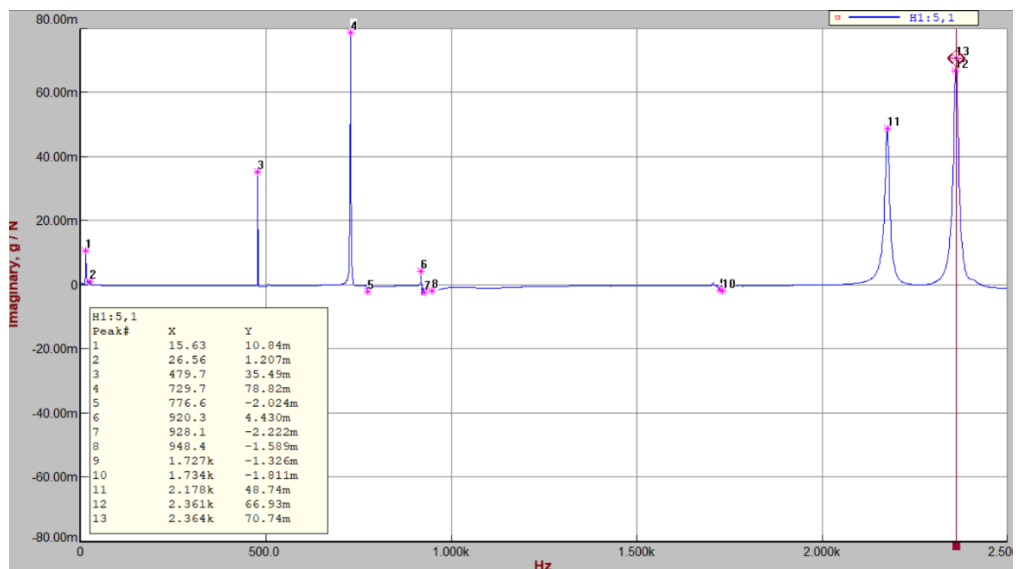


Figure A.2: FRF plot for UC22F rotor. Torsional modes measured at impact point 5
(end of core)

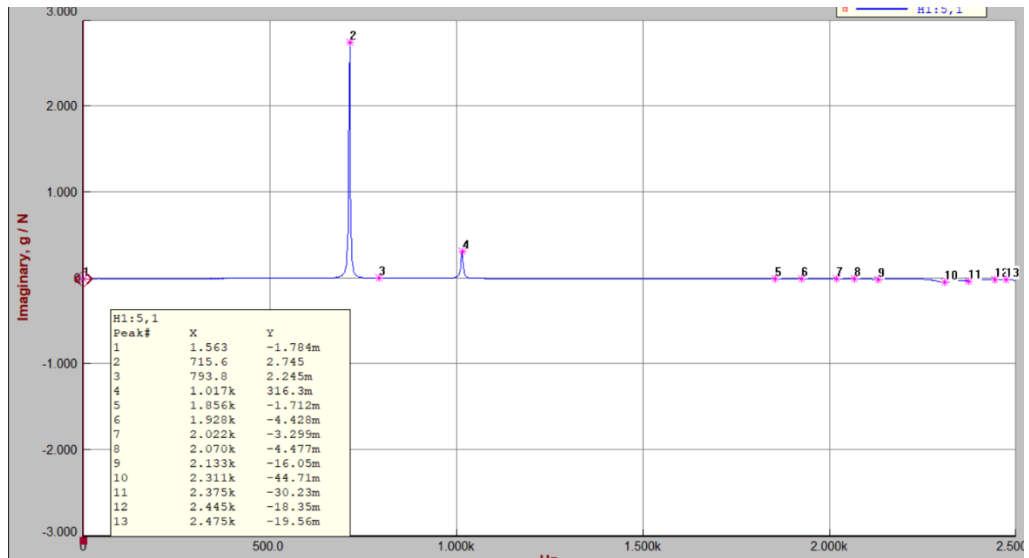


Figure A.3: FRF plot for UC22G rotor. Lateral modes measured at impact point 2

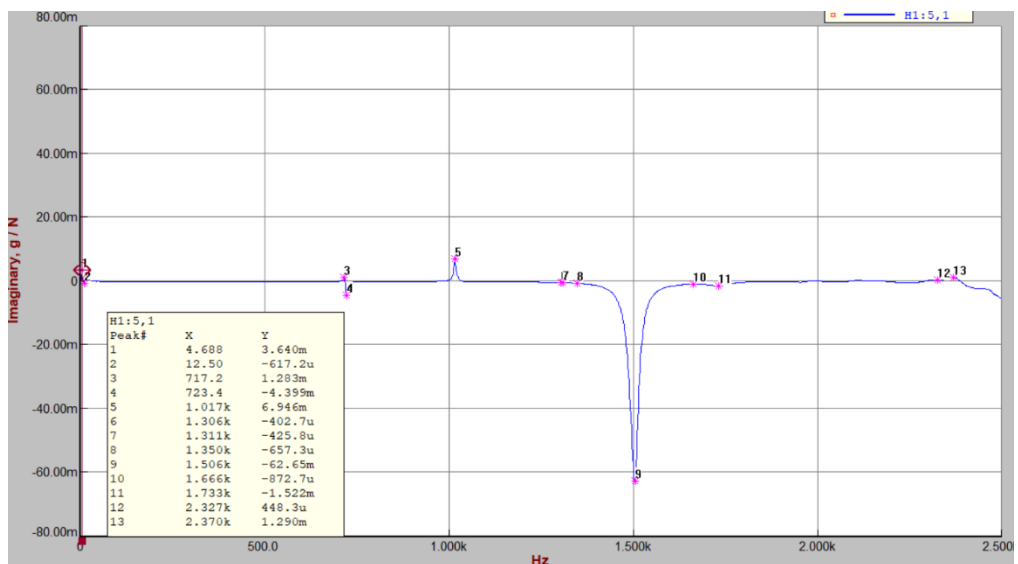


Figure A.4: FRF plot for UC22F rotor. Torsional modes measured at impact point 5
(end of core)

Note that the response peaks vary in magnitude depending on the measured impact location. For example in Figure A.3, the third lateral mode at peak number 10 (2311 Hz) is low at this impact location but increases in magnitude the closer the impact location is moved towards the node of greatest acceleration for the third mode. The raw FRF results for each impact location and each modal peak within are normalised

before they are compared to the mode shapes obtained from the modal analysis. The normalised torsional modes are multiplied by -1 in this case to match the modal analysis shapes as the direction of measurement was reversed in the modal analysis.

Appendix B: Torsional mode calculation for equivalent shaft model of the motor driven generator set

```

I1 = 0.0001;
I2 = 0.0511;
I3 = 0.0026;
I4 = 0.4720;
I5 = 0.0021;
I6 = 0.0280;
I7 = 0.001255;
I8 = 0.000922;
I9 = 0.0086995;
I10 = 0.0045;
I11 = 0.0687;
I12 = 0.039706;
I13 = 1.2;

```

```

k1 = 537000;
k2 = 2890000;
k3 = 1200000;
k4 = 4420000;
k5 = 3020000;
k6 = 8130000;
k7 = 3890000;
k8 = 559000;
k9 = 1165000;
k10 = 1165000;
k11 = 1176000;
k12 = 2000000;

```

%Inertia Matrix

```

I = [I1 0 0 0 0 0 0 0 0 0 0 0 0 0
0 I2 0 0 0 0 0 0 0 0 0 0 0 0
0 0 I3 0 0 0 0 0 0 0 0 0 0 0
0 0 0 I4 0 0 0 0 0 0 0 0 0 0
0 0 0 0 I5 0 0 0 0 0 0 0 0 0
0 0 0 0 0 I6 0 0 0 0 0 0 0 0
0 0 0 0 0 0 I7 0 0 0 0 0 0 0
0 0 0 0 0 0 0 I8 0 0 0 0 0 0
0 0 0 0 0 0 0 0 I9 0 0 0 0 0
0 0 0 0 0 0 0 0 0 I10 0 0 0 0
0 0 0 0 0 0 0 0 0 0 I11 0 0
0 0 0 0 0 0 0 0 0 0 0 I12 0
0 0 0 0 0 0 0 0 0 0 0 0 I13];

```

%Stiffness Matrix

```

K = [k1 -k1 0 0 0 0 0 0 0 0 0 0 0 0
-k1 (k1 + k2) -k2 0 0 0 0 0 0 0 0 0 0 0
0 -k2 (k2+k3) -k3 0 0 0 0 0 0 0 0 0 0 0
0 0 -k3 (k3+k4) -k4 0 0 0 0 0 0 0 0 0 0
0 0 0 -k4 (k4+k5) -k5 0 0 0 0 0 0 0 0 0
0 0 0 0 -k5 (k5+k6) -k6 0 0 0 0 0 0 0 0
0 0 0 0 0 -k6 (k6+k7) -k7 0 0 0 0 0 0 0
0 0 0 0 0 0 -k7 0 0 0 0 0 0 0 0

```

```

0  0  0  0  0  0  -k7 (k7+k8) -k8 0  0  0  0
0  0  0  0  0  0  0  -k8 (k8+k9) -k9 0  0  0
0  0  0  0  0  0  0  0  -k9 (k9+k10)  -k10  0  0
0  0  0  0  0  0  0  0  0  -k10  (k10+k11)  -k11  0
0  0  0  0  0  0  0  0  0  0  -k11  (k11+k12)  -k12
0  0  0  0  0  0  0  0  0  0  0  -k12  k12];

```

```
lam=eig(K,I);
```

```
Hz = sort(sqrt(lam)/6.2831);
```

```
[V, D] = eig(K,I);
```

```
Hz =
```

```
1.0e+04 *
```

```

0.0000
0.0107
0.0561
0.0674
0.1272
0.1493
0.1791
0.3924
0.6394
0.8750
0.9554
1.1675
1.7186

```

Appendix C: Torsional mode calculation for equivalent shaft model of diesel engine driven generator set

```

I1 = 0.0001;
I2 = 0.0511;
I3 = 0.0026;
I4 = 0.472;
I5 = 0.0021;
I6 = 0.028;
I7 = 0.001255;
I8 = 0.000922;
I9 = 0.06711;
I10 = 1.2;
I11 = 0.0101;
I12 = 0.039706;
I13 = 0.027523146;
I14 = 0.03796296;
I15 = 0.03796296;
I16 = 0.026223819;
I17 = 0.038912034;
I18 = 0.003039297;
I19 = 0.054696039;
I20 = 0.1242835;

```

```

k1 = 537000;
k2 = 2890000;
k3 = 1200000;
k4 = 4420000;
k5 = 3020000;
k6 = 8130000;
k7 = 3890000;
k8 = 2011330;
k9 = 2011330;
k10 = 5106922;
k11 = 1751267.5;
k12 = 1175044;
k13 = 1175044;
k14 = 1175044;
k15 = 1175044;
k16 = 1175044;
k17 = 1852954;
k18 = 2689043;
k19 = 90388;

```

```
%Inertia Matrix
```

```

I = [I1 0 0 0 0 0 0 0 0 0 0 0 0 0 0 0 0 0
0 0 0
0 I2 0 0 0 0 0 0 0 0 0 0 0 0 0 0 0 0
0 0
0 0 I3 0 0 0 0 0 0 0 0 0 0 0 0 0 0 0
0 0
0 0 0 I4 0 0 0 0 0 0 0 0 0 0 0 0 0 0
0 0
0 0 0 0 I5 0 0 0 0 0 0 0 0 0 0 0 0 0
0 0
0 0 0 0 0 I6 0 0 0 0 0 0 0 0 0 0 0 0
0 0

```

```

0 0 0 0 0 0 I7 0 0 0 0 0 0 0 0 0 0 0
0 0
0 0 0 0 0 0 0 I8 0 0 0 0 0 0 0 0 0 0
0 0
0 0 0 0 0 0 0 0 I9 0 0 0 0 0 0 0 0 0
0 0
0 0 0 0 0 0 0 0 0 I10 0 0 0 0 0 0 0 0
0 0
0 0 0 0 0 0 0 0 0 0 I11 0 0 0 0 0 0 0
0 0
0 0 0 0 0 0 0 0 0 0 0 I12 0 0 0 0 0
0 0
0 0 0 0 0 0 0 0 0 0 0 0 I13 0 0 0 0
0 0
0 0 0 0 0 0 0 0 0 0 0 0 0 I14 0 0 0
0 0
0 0 0 0 0 0 0 0 0 0 0 0 0 0 I15 0 0
0 0
0 0 0 0 0 0 0 0 0 0 0 0 0 0 0 I16 0
0 0
0 0 0 0 0 0 0 0 0 0 0 0 0 0 0 0 I17 0
0 0
I18 0 0
0 0 0 0 0 0 0 0 0 0 0 0 0 0 0 0 0
I19 0
0 0 0 0 0 0 0 0 0 0 0 0 0 0 0 0 0
0 I20];

```

```
%Stiffness Matrix
```

```

K = [k1 -k1 0 0 0 0 0 0 0 0 0 0 0 0 0 0 0
0 0 0
-k1 (k1 + k2) -k2 0 0 0 0 0 0 0 0 0 0 0 0 0
0 0 0
0 -k2 (k2+k3) -k3 0 0 0 0 0 0 0 0 0 0 0 0
0 0 0
0 0 -k3 (k3+k4) -k4 0 0 0 0 0 0 0 0 0 0
0 0 0
0 0 0 -k4 (k4+k5) -k5 0 0 0 0 0 0 0 0 0
0 0 0
0 0 0 0 -k5 (k5+k6) -k6 0 0 0 0 0 0 0 0
0 0 0
0 0 0 0 0 -k6 (k6+k7) -k7 0 0 0 0 0 0 0 0
0 0 0
0 0 0 0 0 0 -k7 (k7+k8) -k8 0 0 0 0 0 0 0
0 0 0
0 0 0 0 0 0 0 -k8 (k8+k9) -k9 0 0 0 0 0 0
0 0 0
0 0 0 0 0 0 0 0 -k9 (k9+k10) -k10 0 0 0 0
0 0 0 0 0 0 0 0 0 -k10 (k10+k11) -k11 0 0
0 0 0 0 0 0 0 0 0 0 -k11 (k11+k12) -k12 0
0 0 0 0 0 0 0 0 0 0 0 -k12 (k12+k13) -k13
0 0 0 0 0 0 0 0 0 0 0 0 -k13 (k13+k14) -
k14 0 0 0 0 0

```

```

0 0 0 0 0 0 0 0 0 0 0 0 0 0 -k14 (k14+k15)
-k15 0 0 0 0
0 0 0 0 0 0 0 0 0 0 0 0 0 0 -k15
(k15+k16) -k16 0 0 0
0 0 0 0 0 0 0 0 0 0 0 0 0 0 -k16
(k16+k17) -k17 0 0
0 0 0 0 0 0 0 0 0 0 0 0 0 0 0 -k17
(k17+k18) -k18 0
0 0 0 0 0 0 0 0 0 0 0 0 0 0 0 0 0 -
k18 (k18+k19) -k19
0 0 0 0 0 0 0 0 0 0 0 0 0 0 0 0 0 0
-k19 k19];

```

```
lam=eig(K,I);
```

```
Hz = sort(sqrt(lam)/6.2831);
```

```
[V, D] = eig(K,I);
```

```
Hz =
```

```
1.0e+04 *
```

```

0.0000
0.0107
0.0183
0.0246
0.0555
0.0675
0.0919
0.0987
0.1175
0.1417
0.1686
0.1765
0.1860
0.4194
0.6253
0.6394
0.9526
1.0316
1.1675
1.7474

```

Appendix D: Shear modulus values used in the 3DFE model

The shear modulus is adjusted for each component in the 3DFE diesel engine to match the required torsional stiffness as per table 5.2. The equivalent shaft model of the diesel engine is constructed from solid cylinders 120 mm in diameter and 100 mm in length.

Table D.1: Shear modulus values for full 3DFE equivalent stiffness engine model

Component	Length (m)	J (m ⁴)	Diameter (m)	k _T (Nm/rad)	G (Pa)
NDE Bearing	0.1	2.04E-05	0.12	0	0.00E+00
Exciter	0.1	2.04E-05	0.12	537000	2.64E+09
Shaft 1	0.1	2.04E-05	0.12	2890000	1.42E+10
Main Core	0.1	2.04E-05	0.12	1200000	5.89E+09
Shaft 2	0.1	2.04E-05	0.12	4420000	2.17E+10
Fan	0.1	2.04E-05	0.12	3020000	1.48E+10
DE Bearing	0.1	2.04E-05	0.12	8130000	3.99E+10
Shaft 3	0.1	2.04E-05	0.12	3890000	1.91E+10
Coupling Hub	0.1	2.04E-05	0.12	2011330	9.88E+09
Flywheel	0.1	2.04E-05	0.12	2011330	9.88E+09
Gear	0.1	2.04E-05	0.12	5106922	2.51E+10
Cylinder 6	0.1	2.04E-05	0.12	1751268	8.60E+09
Cylinder 5	0.1	2.04E-05	0.12	1175044	5.77E+09
Cylinder 4	0.1	2.04E-05	0.12	1175044	5.77E+09
Cylinder 3	0.1	2.04E-05	0.12	1175044	5.77E+09
Cylinder 2	0.1	2.04E-05	0.12	1175044	5.77E+09
Cylinder 1	0.1	2.04E-05	0.12	1175044	5.77E+09
CNGear	0.1	2.04E-05	0.12	1852954	9.10E+09

DamperHub	0.1	2.04E-05	0.12	2689043	1.32E+10
Inertia Ring	0.1	2.04E-05	0.12	90388	4.44E+08

Appendix E: Simpler model of the improved diesel engine generator set

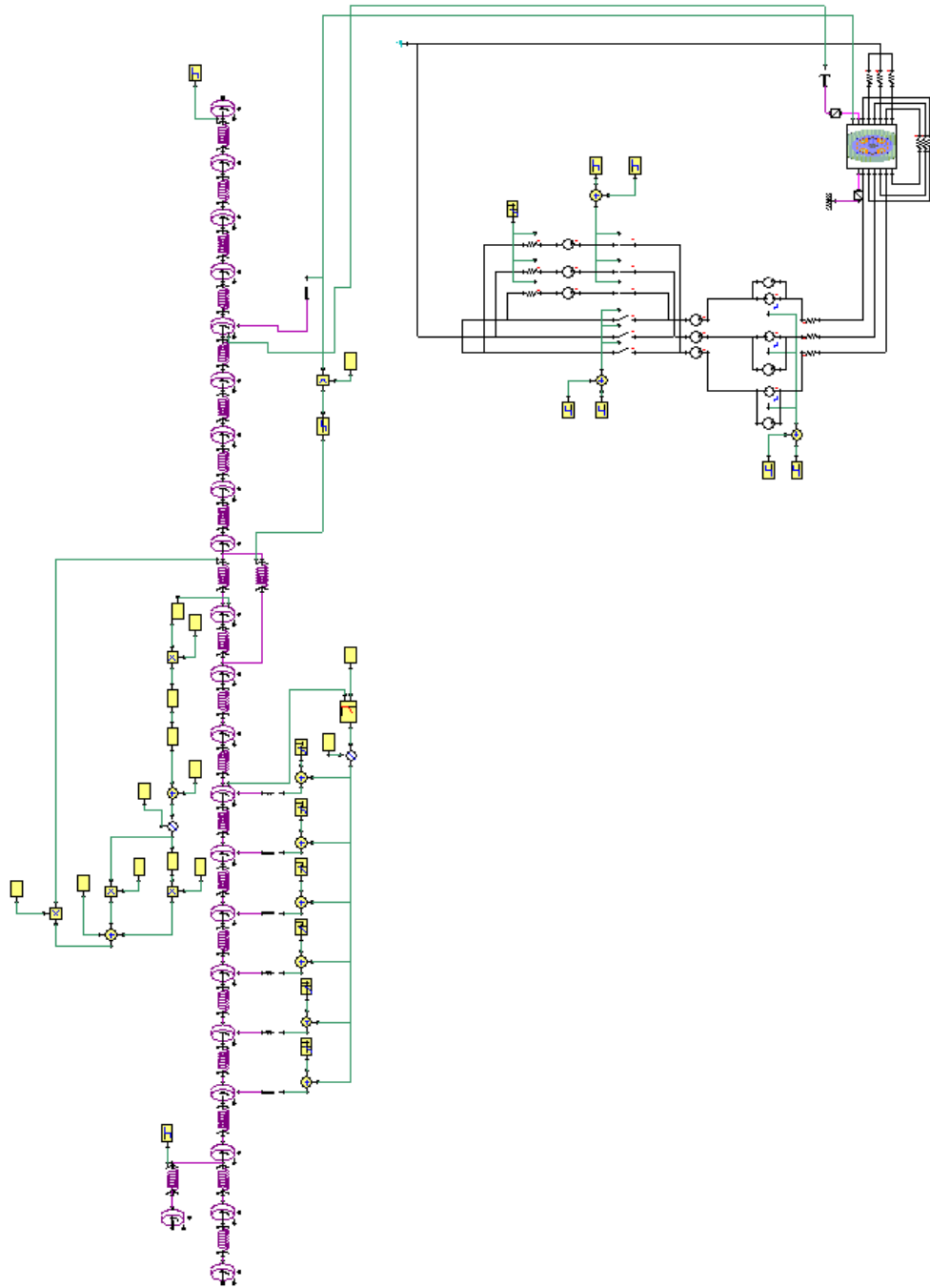


Figure E.1: Complete Simpler model of the improved generator set

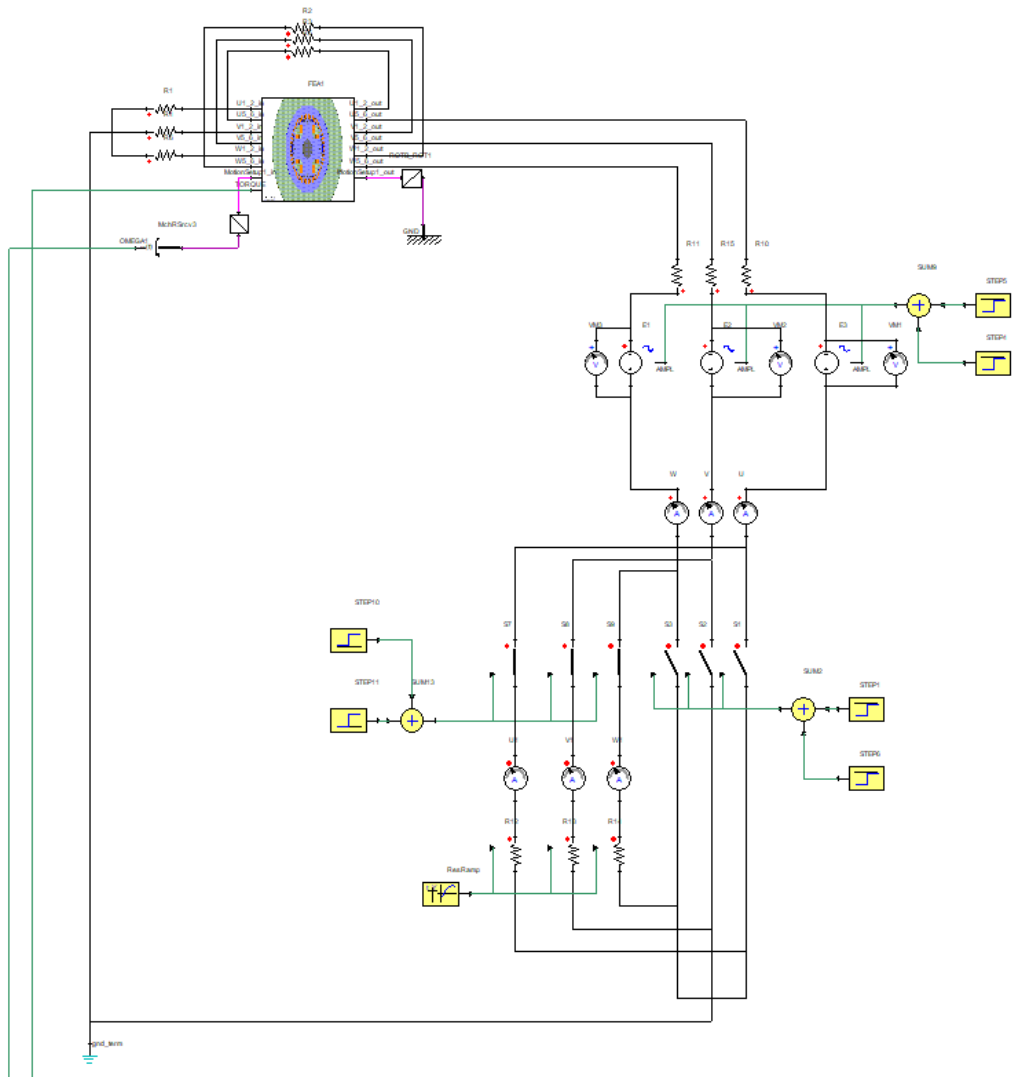


Figure E.2: Electromagnetic generator model connected to stator/terminal circuit in the improved generator set model

Figure E.3: Torsional model within the improved generator set model

